

PhD Comprehensives, Monday March 28 @ 1pm, Room 1027

**Examining Committee: Dr. Norm Duke, Dr. Desmond Moser, Dr. Keith Barron,
Dr. Craig Finnigan**

Chair: Dr. William Church

PhD Candidate: Jim Renaud

**Prospectus for PhD Thesis:
Mineralogical Zoning of the U3O8 Corp. Aricheng Basement-Hosted Uranium Deposit,
Roraima Basin, British Guyana, South America**

Objectives:

The surface mapping and drilling carried out to date on the Pakaraima Escarpment area of the Roraima Basin has established a geological look alike to the Athabasca Basin in Saskatchewan, with recent discovery of both basement-hosted and unconformity related uranium deposits. The basement-hosted uranium mineralization occurs in albitized granite breccias proximal to the Pakaraima Escarpment. These occurrences have associated zircon veining and intense hematite-chlorite-albite alteration along faults and shear zones. The sodic alteration, hydrothermal zircon, and U-mineralization at Aricheng shares features characteristic of the Valhalla U-deposit in Australia (Polito et al., 2009).

The primary objective of this PhD investigation will be to document the hydrothermal zoning in uranium mineralized basement granite breccia. This will be accomplished by determining the mineral chemistry of the intense hematite-chlorite-albite alteration assemblage as well as the vein zircon. The study will refine the original working hypothesis that U, P, Ti, and Zr were transported in oxidized brines and precipitated in basement faults well below the unconformity. It is now proposed that the shear-hosted U mineralization is linked to post collisional extension that characterized the 2.1-1.96 Ga Orosirian phase of the Transamazonian orogenic event. Mylonitic shears in the basement were mineralized well before Roraima deposition. A brief synopsis is given of the microprobe results to date on: (a) a retrograde cpx-hb-act-bio-mt-chl(1) assemblage; (b) relict plagioclase versus secondary metasomatic K-feldspar-albite alteration; and (c) the chl(2)-zircon-brannerite-specularite speciation occupying U-mineralization.

Methodology:

The study is based on sampling strategic drill core intersections that outline the complex hydrothermal zoning patterns. The analytical work will involve limited bulk rock geochemistry to supplement detailed microprobe investigations. Mineral chemistry will be used to detail the alteration assemblages and the growth zoning patterns of the vein zircon. The study of hydrothermal vein zircon, igneous zircon in the host granite, and detrital zircon in overlying

Roraima sandstone will be carried out through collaboration with the Dr. Desmond Moser. Dating of the coarse grained spenes (date of metamorphism) and perhaps K-Ar or Ar-Ar dating to tie in megacrystic K-feldspar to early stages of mineralization. Limited stable and radiogenic isotope determinations will be used to establish the fluid source of the alteration assemblages.

Regional Setting:

The Aricheng U District is situated within the west-dipping Kurupung Mylonite Zone, overprinting the low grade southwestern edge of the juvenile 2.25-2.20 Ga Transamazonian volcanic-TTG arc terrane adjacent to the Roraima sandstone and Uatuma ash tuff cover sequences. The Kurupung Mylonite Zone terminates in large 2-mica granite bodies exposed to the northwest and southeast of the Uatuma ash tuff field. These are the intrusive/extrusive counterparts defining the post-collisional peraluminous 2.1-1.96 Ga Orosirian magmatic episode. The Kurupung clinopyroxene granodiorite also dates as 2.1 Ga and is a member of initial collisional Mg-suite granitoids of "primitive sanukitoid affinity". The southern boundary of the Uatuma ash tuff field is the Bakhuis ultra high pressure metamorphic complex whose metamorphic history directly coincides with the 2.1-1.96 Ga age of the peraluminous magmatism. The UHP separates juvenile Transamazonian crust to the north from Mesoarchean basement to the south.

Aricheng U District:

The numerous U prospects of the Aricheng District focus on the margin of the Kurupung batholith. Detailed study of the Kurupung batholith reveals mafic assemblages defined by Cr-Na clinopyroxene mantled by Cr-hornblende, mantled by more retrograde actinolite, overgrown by biotite-magnetite. This assemblage is partially to completely irradiated within chlorite (1) altered mylonitic shears. These same shears are variably overgrown by coarse growth-zoned K-feldspar, clearly demonstrating that secondary K-metasomatism postdates pale green chlorite(1) retrogression. The cores of K-feldspar altered shears shows local development of jet black chlorite(2) cemented albitite breccia that hosts the disseminated to vein style Zr-U mineralization.

The Kurupung Mylonite Zone was active between the 2.1 Ga age of the Kurupung batholith and the 1995 Ma age of the hydrothermal zircon coexisting with the U mineralization. The Kurupung clinopyroxene granodiorite originated by melting of metasomatized peridotitic mantle. Tectonic unroofing of the Kurupung, accommodated by the mylonitic shearing, juxtaposes this intrusive against low grade Transamazonian volcanics (Himaraka). When coupled with the available geochron, the textural evidence for retrograde cpx-hb-act-bio-mt-chl(1) assemblages suggests tectonic unroofing. Similar unroofing structures are noted in extensional environs related to dome and keel structures.

A key factor regarding the U mineralization regards the origin of secondary potassium feldspar growth. Where exposed at Accori, and drilled at Meamu, the western margin has not been as subject to retrograde shearing as the eastern margin and there appears to be consistent 25-35 % replacement of hornblende (amphibolite-facies) granodiorite by coarse growth-zoned

K-feldspar. Albite overgrows and chlorite(2) cements still magnetic hydrothermal cataclasite at Accori N. On the well sheared eastern margin variable minor to wholesale coarse K-feldspar overgrows chlorite(1) retrograde shears. Within these domains, the cores of shears show development of coarse red albitite, typically forming reticulate textured cataclasite cemented by jet black chlorite(2). The Zr-U mineralization is hosted within the chlorite(2) cemented albitite breccia. It therefore appears that the geothermal gradient, with still hot intrusive against cold footwall volcanoclastics played a key role in albitite development. It is likely that the footwall low grade phyllites hydrated the intrusive, giving rise to the retrograde chlorite(1) shears. The Na liberated by wholesale K-feldspar growth partitioned into the hydrous fluid phase within active shears.

Interestingly, an internal report for U3O8 Corp., suggests isotope signatures indicate albite and zircon have magmatic affinity while chlorite(2) has meteoric affinity. This suggests high temperature potassium metasomatism supplied the Na and associated metals, while the jet black chlorite indicates ingress of meteoric fluid from surface. Possibly, the source of the voluminous potassium alteration along the structurally active margins of the Kurupung is from degassing of peraluminous melts emplaced below the cpx-hb granodiorite.

Host Foliated Kurupung Granodiorite:

The host Kurupung granodiorite is a granular clinopyroxene-hornblende rock composed of coarse clots of Na-Cr-diopsidic clinopyroxene (replaced by chromian-edenite to magnesio-hornblende), coarse grained plagioclase, white microcline, quartz, biotite, chlorite, sphene, Cr-Ti magnetite, magnetite and hematite. The dominant mineral assemblage of Cr clinopyroxene-Cr amphibole-plagioclase-microcline is glomerophyric in texture. Marginal samples show a strong to weak foliation defined by mafics overgrown by euhedral secondary K-feldspar. The Na-Cr-diopside formed in deep crust/upper mantle conditions where significant pressures are required to induce the Na-Cr substitution. During exhumation, the body cooled to amphibolite facies to form Cr-amphibole and then to greenschist to form biotite-chlorite-sphene assemblages.

Secondary Oscillatory Zoned Ba-K-Feldspar:

Millimeter to centimeter K-feldspar megacrysts occur randomly in the K-metasomatized domains and overgrow the dominant D1 fabric of the Kurupung batholith. The cores of the megacrysts are occupied by relict Ca-plagioclase altered to albite+epidote+muscovite. This core acted as the nucleating kernel for development of the surrounding Ba-K-feldspar growth zones. The compositional oscillatory growth zoning in the Ba-K-feldspar is due to the variation in barium content of the alternating zones. The barium content peaks at 6% but most commonly ranges from 1.38 wt% BaO near the core to 0.16 wt% BaO at the outermost margin. Plagioclase inclusions of micron to millimeter size have their long axes preferentially aligned parallel to the Ba-K-feldspar growth zones. They are essentially albite (An 1.37). These albite grains grew with the secondary K-feldspar, periodically attaching to the faces of the growing crystal. The alternating oscillatory compositional banding of the Ba-K-feldspar reflects changing chemistry of the metasomatic fluid system, evolving from a K-rich to a Na-rich system within the mineralized zones (i.e. breakdown of plagioclase partitioned Na into the fluid phase).

Hydrothermal Zircon and U-Mineralization:

Red-pink blocky cataclasite with both microgranular zircon and hematite+Zr veins hosts U-mineralization. Zones of microbreccia, variably cemented by black chlorite, have Fe-Ti-U oxides disseminated throughout. The groundmass minerals are dominantly coarse grained albite+quartz+chlorite+calcite and fine grained apatite+barite+ granular zircon+U/Th-monzite+rutile. Mineralized samples host anastomosing brown veinlets of zircon and ramifying red veinlets of hematite. Zircon occurs in two forms: (a) as anastomosing hydrothermal veinlets associated with U-mineralization; and (b) as euhedral and subhedral granular grains in the matrix which are relatively U-depleted. The Zr-veinlets are 50-400 microns wide and tend to host the majority of the U-bearing minerals. The centre of Zr-veinlets contain Zr+carbonate+hematite+U bearing minerals. The margins of the veinlets are mainly chlorite+calcite+epidote and a consortium of uranium minerals. Backscatter imaging of the hydrothermal zircon veins reveals a heterogeneous compositional variation evident by domains of dark, intermediate and bright zones representing the variations in U content within the zircon structure. Electron microprobe analysis reveals that the brightest domains contain up to 5.83% UO₂, intermediate domains 2.01% UO₂, and dark domains 0.79%.

The isolated granular grains of zircon have well defined crystal boundaries where disseminated throughout the sections. They occur as euhedral inclusions in hematite and are relatively U-depleted. The most obvious chemical difference between these granular grains and the zircon veins is the lack of UO₂ in the zircon structure of the granules.

Uranium Minerals:

The uranium species, occurring as yellow-brown and red-brown minerals in plane light, grow within zircon veins in samples C5 and C5B, and within hematite-chlorite-albite-apatite domains of sample C13. The species are branneritic (rarely coffinitic) U-silicates and oxides. Many are difficult to classify as they don't match compositions detailed in the literature. Uraninite was only observed in fractured albite. Locally, Pb-U-Si and Ti-U-Pb species also infill fractures within albite, coexisting with calcite. The U-bearing minerals so far identified are brannerite, uraninite, coffinite, thorite/ekenite.

Working Hypotheses:

The available geochron on the Kurupung clinopyroxene granodiorite and associated U mineralization ties both emplacement and mineralization to the post collisional 2.1-1.96 Ga Orosirian phase of the Transamazonian orogeny. Rapid unroofing accommodated by mylonitic shearing, commonly associated with dome and keel structures (Tinkham and Marshak, 2004), subjected the intrusion to retrograde amphibolite then greenschist facies metamorphic overprints during subsolidus cooling. The western margin remained at amphibolite grade. The eastern contact at Aricheng was juxtaposed against low grade phyllites after Transamazonian volcanoclastics. Mylonite zones within the margin of the intrusion became pervasively chloritized. Both the west and east margins of the body were strongly alkali metasomatized, possible by degassing from deeper seated 2-mica granite.

References:

Polito, P., Kyser, K., and Stanley, C., 2009. The Proterozoic, albitite-hosted, Valhalla uranium deposit, Queensland, Australia: a description of the alteration assemblage associated with uranium mineralization in diamond drill hole V39. *Miner Deposita*, 44, pp. 11-40.

Tinkham, D., and Marshak, S., 2004. Precambrian dome-and-keel structure in the Penokean orogenic belt of northern Michigan, USA. *In: Gneiss domes in orogeny*, The Geological Society of America, Special Paper 380, pp. 321-338.

Other References of Interest:

Heilimo, E., Mikkola, P., and Halla, J., 2007. Age and petrology of the Kaapinsalmi sanukitoid intrusion in Suomussalmi, Eastern Finland. *Bulletin of the Geological Society of Finland*, V.79, pp. 117-125.

Hitzman, M., and Valenta, R., 2005. Uranium in iron oxide-copper-gold (IOCG) systems. *Economic Geology*, v. 100, pp. 1657-1661.

Rubin, J., Henry, C., and Price, J., 1993. The mobility of zirconium and other "immobile" elements during hydrothermal alteration. *Chemical Geology*, v. 110, pp. 29-47.

The Proterozoic, albitite-hosted, Valhalla uranium deposit, Queensland, Australia: a description of the alteration assemblage associated with uranium mineralisation in diamond drill hole V39

Paul A. Polito · T. Kurt Kyser · Cliff Stanley

Received: 3 April 2006 / Accepted: 20 July 2007 / Published online: 19 September 2007
© Springer-Verlag 2007

Abstract The Valhalla uranium deposit, located 40 km north of Mount Isa, Queensland, Australia, is an albitite-hosted, Mesoproterozoic U deposit similar to albitite-hosted uranium deposits in the Ukraine, Sweden, Brazil and Guyana. Uranium mineralisation is hosted by a thick package of interbedded fine-grained sandstones, arkoses and gritty siltstones that are bound by metabasalts belonging to the ca. 1,780 Ma Eastern Creek Volcanics in the Western Succession of the Mount Isa basin. Alteration associated with U mineralisation can be divided into an early, main and late stage. The early stage is dominated by laminated and intensely altered rock comprising albitite, reibeckite, calcite, (titano)magnetite ± brannerite. The main stage of mineralisation is dominated by brecciated and intensely altered rocks that comprise laminated and intensely altered rock cemented by brannerite, apatite, (uranoan)-zircon, uraninite, anatase, albitite, reibeckite, calcite and hematite. The late stage of mineralisation comprises uraninite, red hematite, dolomite, calcite, chlorite, quartz and Pb-, Fe-, Cu-sulfides. Brannerite has U–Pb and Pb–Pb ages that indicate formation between

1,555 and 1,510 Ma, with significant Pb loss evident at ca. 1,200 Ma, coincident with the assemblage of Rodinia. The oldest ages of the brannerite overlap with $^{40}\text{Ar}/^{39}\text{Ar}$ ages of $1,533 \pm 9$ Ma and $1,551 \pm 7$ Ma from early and main-stage reibeckite and are interpreted to represent the timing of formation of the deposit. These ages coincide with the timing of peak metamorphism in the Mount Isa area during the Isan Orogeny. Lithochemical assessment of whole rock data that includes mineralised and unmineralised samples from the greater Mount Isa district reveals that mineralisation involved the removal of K, Ba and Si and the addition of Na, Ca, U, V, Zr, P, Sr, F and Y. U/Th ratios indicate that the ore-forming fluid was oxidised, whereas the crystal chemistry of apatite and reibeckite within the ore zone suggests that F^- and PO_4^{3-} were important ore-transporting complexes. $\delta^{18}\text{O}$ values of co-existing calcite and reibeckite indicate that mineralisation occurred between 340 and 380°C and involved a fluid having $\delta^{18}\text{O}_{\text{fluid}}$ values between 6.5 and 8.6‰. Reibeckite δD values reveal that the ore fluid had a $\delta\text{D}_{\text{fluid}}$ value between –98 and –54‰. The mineral assemblages associated with early and main stages of alteration, plus $\delta^{18}\text{O}_{\text{fluid}}$ and $\delta\text{D}_{\text{fluid}}$ values, and timing of the U mineralisation are all very similar to those associated with Na–Ca alteration in the Eastern Succession of the Mount Isa basin, where a magmatic fluid is favoured for this style of alteration. However, isotopic data from Valhalla is also consistent with that from the nearby Mount Isa Cu deposit where a basinal brine is proposed for the transport of metals to the deposit. Based on the evidence to hand, the source fluids could have been derived from either or both the metasediments that underlie the Eastern Creek Volcanics or magmatism that is manifest in the Mount Isa area as small pegmatite dykes that intruded during the Isan Orogeny.

Editorial handling: V. Bouchet

P. A. Polito · T. K. Kyser
Department of Geological Sciences and Geological Engineering,
Queen's University,
Kingston, Ontario, Canada, K7L 3N6

C. Stanley
Department of Geology, Acadia University,
Wolfville, Nova Scotia, Canada, B4P 2R6

P. A. Polito (✉)
Suite 1/ 16 Brodie Hall Drive,
Bentley, Western Australia 6102, Australia,
e-mail: paulpolito@angloamerican.com.au

Keywords Proterozoic · Uranium · Brannerite · Zircon · Albitite · Sodic · Isotope geochemistry · Mount Isa

Introduction

The Valhalla U deposit is located 40 km north of the Mount Isa township/mine in the Western Succession of the Mount Isa basin, north-west Queensland, Australia (Fig. 1). It is one of 107 known uranium occurrences that have been recorded in Palaeoproterozoic metasediments and mafic volcanic rocks belonging to the Leichhardt River Fault Trough (McKay and Mieztis 2001). Valhalla was discovered by prospectors in 1954 and has since been mapped and drilled by government geologists and at least four different companies seeking to define a minable U reserve in the Mount Isa district. As of August 2006, Valhalla had a drilled indicated and inferred resource of 33.3 Mt at 0.077% U_3O_8 for an in ground total of 29,900 t U_3O_8 (Summit Resources media release: <http://www.miningnews.net>). Vanadium resources have not been estimated, but grades of approximately 0.13% V_2O_5 are associated with the U mineralisation (Eggers 1999).

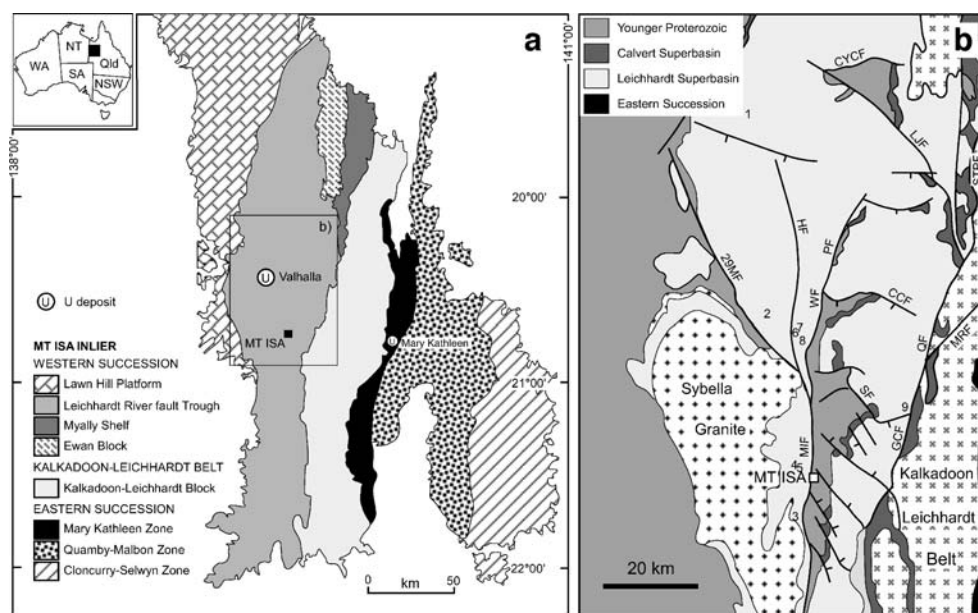
Despite the large number of U prospects and over 50 years of U exploration in the Western Succession (Fig. 1), there is relatively little information regarding any of the deposits in this part of the basin. In fact, apart from papers on the skarn-related Mary Kathleen deposit, 80 km SE of Valhalla in the Wonga Belt of the Eastern Succession (Fig. 1; Page 1983; Maas et al. 1987; Oliver 1995, 1999; Oliver et al. 1993), only papers by Brooks (1960, 1972, 1975), Eggers (1998, 1999) and Gregory et al. (2005) offer any insight into this emerging U province. In fact, the timing and origin of these deposits remains unknown and there is some debate in

regards to what type of deposit this class of mineralisation belongs.

On one hand, Gregory et al. (2005) conclude that U deposits in the Mount Isa district are metamorphosed equivalents of Proterozoic unconformity-type uranium deposits found elsewhere in northern Australia, where mineralisation involved the transport of uranium by oxidised hydrothermal fluids. These authors suggest that the geologic setting of the Mount Isa district U deposits is similar to that around unconformity-type U deposits, including the presence of a major unconformity between the ore-hosting Eastern Creek Volcanics (ECV) and the overlying Surprise Creek Formation. On the other hand, Hitzman and Valenta (2005) report that Valhalla may be a Cu-poor iron oxide–copper–gold (IOCG) deposit hosted in hematite breccias.

In this paper, we present new petrographic and geochemical data from a single diamond drill hole into the deepest part of the Valhalla deposit. This drill hole was terminated at 360 m in the Eastern Creek Volcanics after intersecting hanging-wall and foot-wall mafic volcanics, weakly to strongly altered metasediments and 93 m of U mineralisation grading 0.195% U_3O_8 from 236.4 m. At the time of writing this paper, this was the thickest and one of the highest grade intersections of U mineralisation recovered from the deposit. Although only the one drill hole was investigated, the samples collected for this study were amongst the first to represent the unweathered portion of the deposit and have permitted the identification of (1) the mineralogy associated with mineralisation, (2) the fluid composition of the mineralising fluids, (3) the timing of mineralisation and (4) potential source rocks for the Valhalla U deposit. These results, in conjunction with

Fig. 1 a Locality of the southern Mount Isa Basin with insert (b) showing the larger uranium deposits in the Mount Isa district. 29MF Twenty-nine Mile Fault; HF Hero Fault; WF Western Fault; MIF Mount Isa Fault; PF Paroo Fault; CCF Conglomerate Creek Fault; GCF Gorge Creek Fault; QFZ Quillalar Fault Zone; MRF Mount Remarkable Fault; SF Spillway Fault; LJF Lake Julius Fault; STPF Saint Paul Fault; CYCF Crystal Creek Fault; 1 Batman; 2 Valhalla; 3 Perseverance; 4 Easter Egg; 5 Mighty Glare; 6 Pile; 7 Bikini; 8 Skal; 9 Anderson's Lode. Geological data adopted and modified from the 1:500,000 geology map presented in Blake (1987)



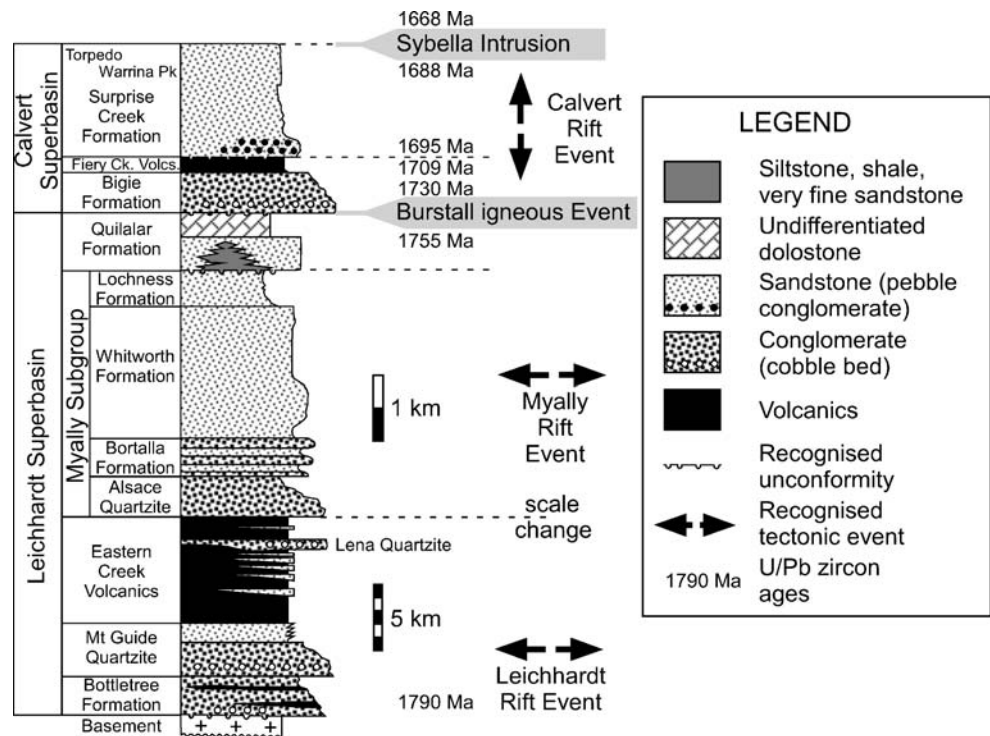
whole-rock geochemical data interpretation and regional tectonic and diagenetic events, have enabled us to propose an alternative model for the formation of this and other U deposits in the Western Succession of the Mount Isa Basin.

Geological considerations

The Mount Isa Basin has historically been subdivided into three cover sequences that sit unconformably on ca. 1,900 Ma basement (Blake 1987), but recent lithostratigraphic mapping, SHRIMP U–Pb zircon geochronology and sequence stratigraphic studies have identified three stratigraphic successions termed the Leichhardt (ca. 1,800 to ca. 1,740 Ma), the Calvert (ca. 1,710 to 1,690 Ma) and the Isa (ca. 1,670 to 1,575 Ma) Superbasins (Page et al. 2000; Southgate et al. 2000; Neumann et al. 2005, 2006). The principal lithologies in these superbasins range from shallow marine and fluvial, coarse to fine grained siliciclastic successions and bimodal igneous rocks in the Calvert and Leichhardt Superbasins, to peritidal and outer ramp carbonate successions which pass laterally and vertically into deeper water and fine grained, turbiditic siliciclastic rocks, organic matter-rich shales and siltstones in the Isa Superbasin, (Jackson et al. 2000; Southgate et al. 2000). The Wonga/Burstall Igneous Event at ~1,740–1,735 Ma separates sediments of the Leichhardt and Calvert Superbasins (Fig. 2), whereas the Sybella Igneous Event at ~1,680–1,670 Ma separates the Calvert and Isa Superbasin successions (Southgate et al. 2000; Neumann et al. 2005, 2006).

Superbasin development in the southern and eastern Mount Isa Basin was terminated at approximately 1,600 Ma by the onset of the Isan Orogeny (Betts et al. 2006). Rb–Sr isotope ages from the Sybella Granite (Fig. 1) were originally attributed to metamorphic events corresponding to D₁ deformation at 1,610±13 Ma, D₂ deformation at 1,544±12 Ma and D₃ deformation at 1,510±13 Ma (Bell 1983; Page and Bell 1986). However, recent U–Pb SHRIMP ages from the Western Succession (Fig. 2) have refined the timing of these events and it is now proposed that an early period of thin-skinned metamorphism beginning as early as 1,600 Ma (Giles and Nutman 2002) but affecting the entire Mount Isa Inlier around 1,585 to 1,565 Ma (Connors and Page 1995; Hand and Rubatto 2002) was overprinted by a later thick-skinned tectonic event between 1,550 and 1,500 Ma (Page and Sun 1998; Oliver et al. 2004; Betts et al. 2006) which included D₂ and D₃. In the Western Succession, this second event appears to be focused in an area around Mount Isa and is constrained to a period between 1,550 and 1,530 Ma (Betts et al. 2006; Hand and Rubatto 2002; Connors and Page 1995). At this time, the 1,540 Ma Mount Isa and Mount Gordon Cu deposits formed (Carr et al. 2001) and the 1,532±7 Ma Mica Creek syn-orogenic pegmatites were emplaced into the Leichhardt River Fault Trough of the Western Succession (Connors and Page 1995). One outcrop of these pegmatites occurs approximately 6 km south of Mount Isa, whereas another occurs approximately 17 km south of Valhalla. Rocks north of Mount Isa, between the Quilalar Fault Zone and the Mount Isa Fault (Fig. 1), experienced peak metamorphism to sub-greenschist facies

Fig. 2 Generalised stratigraphic column for the lower lithologies in the Western Succession of the Mount Isa Basin, subdivided into the Leichhardt and Calvert Superbasins (modified after Jackson et al. 2000; Polito et al. 2006)

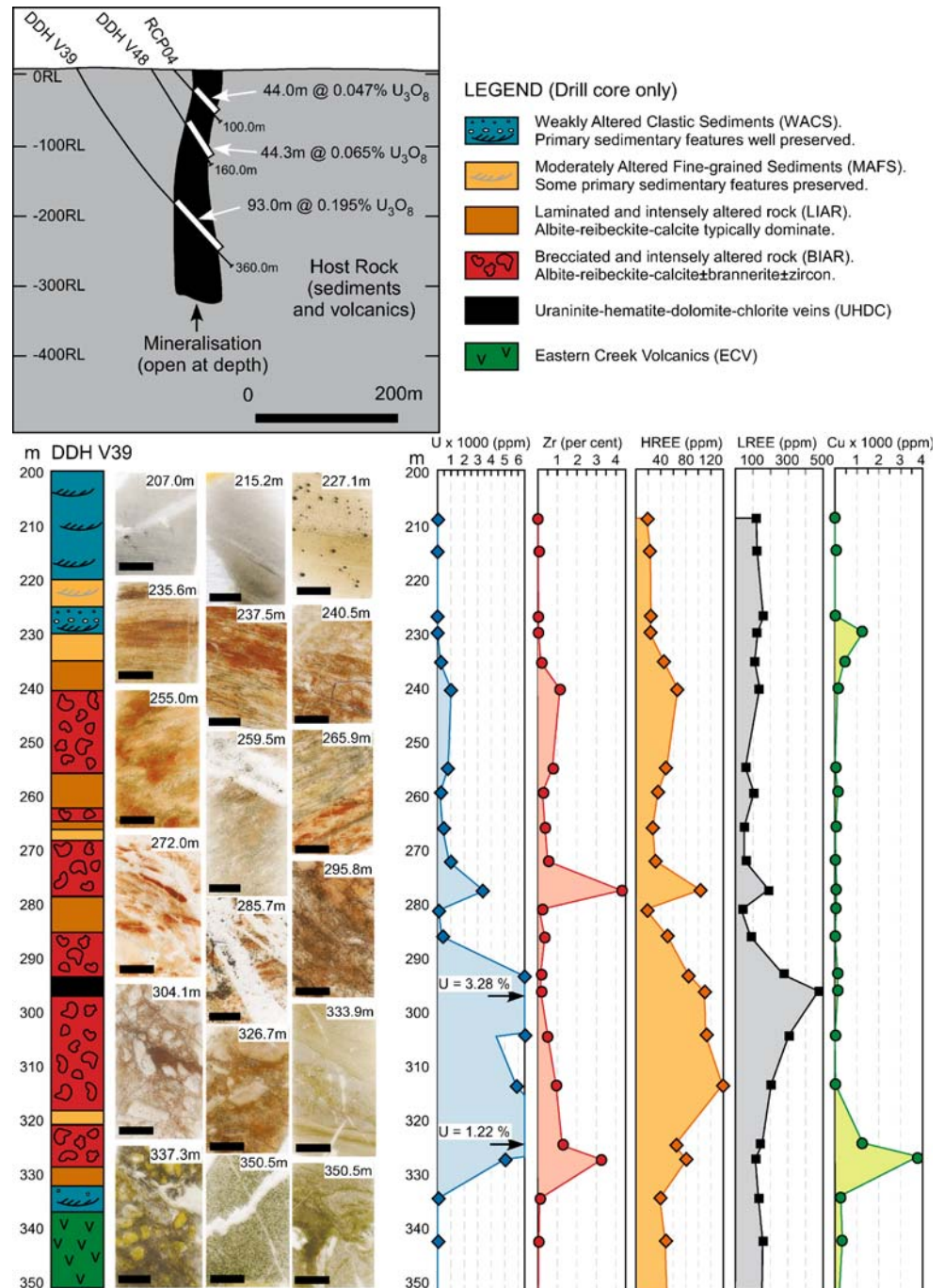


during the second phase of deformation (peak metamorphic temperatures calculated between 300 and 350°C; Foster and Rubenach 2006), whereas rocks south and east of the Mount Isa township and also west of the Mount Isa Fault reached amphibolite facies at this time (Rubenach 1992). U–Pb ages that would support a third deformation event in the Western Succession are lacking, but several samples of hornblende, biotite and illite extracted from rocks near the Mount Isa, Gorge Creek, Quilalar and Mount Remarkable Faults record $^{40}\text{Ar}/^{39}\text{Ar}$ total fusion ages (equivalent to K/Ar ages) between 1,500 and 1,410 Ma and are probably recording

an event that was coincident with the intrusion of post-orogenic pegmatites into the Leichhardt River Fault Trough at $1,480 \pm 14$ Ma (Connors and Page 1995) as well as post-Isan crustal exhumation through to ca. 1,400 Ma (Perkins et al. 1999; Spikings et al. 2001; Polito et al. 2006).

The U occurrences in the Western Succession are hosted in either clastic metasediments or mafic volcanics that belong to the Eastern Creek Volcanics (Fig. 1). The Eastern Creek Volcanics are known to be in excess of 6 km thick. They were deposited around $1,779 \pm 4$ Ma (Neumann et al. 2006) and are part of the Leichhardt Superbasin (Fig. 2).

Fig. 3 A cross section, modified from Eggers (1999), through the Valhalla deposit showing the orientation of the steeply dipping ore body and the location of DDH V39 relative to other drill holes and where it intersected mineralization. A simplified log for DDH V39 is shown on the left side of the diagram with photographs of thin sections demonstrating the different types of rocks that were sampled for this study (see text for details), note that the double refractive nature of calcite in some samples gives the impression that some slides are out of focus. Down-hole geochemical plots for key elements are shown here for comparison to the geological log and photographic examples



Proximal fluvial facies composed of coarse- to fine-grained sandstone, pebbly sandstone and conglomerate and near-shore marine facies comprising medium to fine grained, better sorted and locally more mature sandstones underlie the Eastern Creek Volcanics. The Eastern Creek Volcanics are divided into the lower Cromwell Metabasalt Member and the upper Pickwick Formation. The Cromwell Metabasalt and the Pickwick Formation are formally separated by the Lena Quartzite, but several other metasedimentary packages comprising feldspathic quartzite, orthoquartzite, laminated siltstone, shale, arkose and mafic tuff occur as tens to hundreds of metre thick packages throughout the Cromwell Metabasalt Member and the Pickwick Formation (Hutton and Wilson 1985). Valhalla mineralisation is hosted in one of these metasedimentary packages (Fig. 2).

The majority of the 107 known uranium occurrences in the Leichhardt River Fault Trough (McKay and Miezitis 2001) occur in an area bound to the east by the Gorge Creek Fault and the Quilalar Fault Zone, to the north by the Crystal Creek Fault, to the west by the eastern margin of the Sybella Granite and the Twenty-nine Mile Fault and to the south by a zone coincident with the Mount Isa township (Fig. 1). The Valhalla deposit lies approximately 800 m east of the steeply dipping Mount Isa/Twenty-nine Mile Fault Zone and 6 km west of the NNW striking Hero Fault (Fig. 1).

Materials and methods

Thirty, 10–30 cm long pieces of NQ quarter core were collected from diamond drill hole (DDH) V39, between 209 and 355 m. Ninety-three metres of this intersection is mineralised, containing 0.195% U_3O_8 (Fig. 3; Eggers 1999). Polished thin sections were prepared for all samples that underwent geochemical analysis. The thin sections were examined using transmitted and reflected light to determine a mineral paragenesis. Electron microprobe analyses were performed on polished thin sections using a Cambax MBX electron microprobe equipped with 4 WDX X-ray spectrometers at Carleton University, Ottawa, Canada. A suite of well-characterised natural and synthetic minerals and compounds were used as calibration standards. The Cameca PAP matrix correction program was used to convert the raw X-ray data into elemental weight percent. The detection limit for the majority of the elements is approximately 0.05%. The accuracy of the measurements is 1–2% relative for major elements and 3–5% relative for minor elements (<1 wt%).

Twenty-two samples were submitted to ACME Analytical Laboratories, Vancouver, for whole rock geochemical analysis. Major elements were determined from a 0.2 g, $-75 \mu\text{m}$ pulp sample split that was fused at 1,000°C with $LiBO_2$ flux. The molten bead was digested in 5% HNO_3 and analysed by

inductively coupled plasma (ICP) optical emission spectroscopy. Most of the trace elements and all of the REE were measured by ICP mass spectrometer (ICP-MS) from this solution. Loss on Ignition was determined on a 1 g split ignited at 1,000°C. Total C and S was determined by the LECO method. Silver, As, Bi, Cd, Cu, Mo, Ni, Pb, Sb, Tl and Zn were determined from a 0.25-g sample, digested in a $HF-H_2O-HClO_4-HNO_3$ solution at fuming temperature and taken to dryness. This residue was then taken up in 50% HCl and analysed by ICP-MS.

Oxygen and hydrogen isotopic values were obtained from amphibole using the methods of Clayton and Mayeda (1963) and Kyser and O'Neil (1984), respectively. Five milligram pure separates of amphibole were collected for oxygen isotope analysis from two samples that were crushed, washed in deionised water, sieved for the 63–180- μm fraction and picked using surgical tweezers and a binocular microscope. Fifty-milligram separates comprising primarily amphibole \pm albite \pm quartz \pm hematite were hand picked for hydrogen isotope analysis from four samples, including the two that were selected for oxygen isotope analysis after being crushed, washed and sieved for the 250–500 μm . Neither albite, quartz nor hematite contain hydrogen that could contribute to the δD value. Calcite and dolomite were extracted by micro-drilling and analysed by X-ray diffraction before stable isotope analysis. Carbon and oxygen isotopic values were measured using the method of McCrea (1950). Stable isotopic measurements were made using a Finnigan MAT 252 mass spectrometer and are reported in the δ notation in units of per mil relative to the standard V-SMOW and V-PDB. Oxygen isotope fractionation factors used are those suggested by O'Neil et al. (1969) for water–calcite and Zheng (1993) for water–reibeckite. Hydrogen isotope fractionation factors used are those suggested by Graham (1981) for water–amphibole. Carbon isotope fractionation factors for calcite are those suggested by Bottinga (1969).

Amphibole ages were determined using the $^{40}\text{Ar}/^{39}\text{Ar}$ laser-heating technique of Lee et al. (1990). U–Pb and Pb–Pb analyses were performed on uraninite and brannerite samples using a frequency quintupled (213 nm) Nd-YAG laser (LUV 213, New Wave-Merchanteck, Fremont, CA) to ablate solid sample and introduce it into a Finnigan MAT ELEMENT[®] high-resolution ICP-MS (LA-HR-ICPMS; Finnigan MAT, Bremen, Germany). The ELEMENT is a single collector, sector field, double-focusing mass spectrometer with reverse Nier-Johnson geometry (Gießmann and Greb 1994). The analyses were performed on polished thin sections in spot mode (spot sizes = 15–50 μm) using the technique of Kyser et al. (2003). Before measurement of U and Pb isotope ratios, some instrument parameters were calibrated using solutions. An instrument check is done using a calibrated standard zircon (no. 91500) and davidite from the

Mount Isa area. The standard zircon has been well characterised by TIMS and has a $^{207}\text{Pb}/^{206}\text{Pb}$ age of 1,065 Ma (Wiedenbeck et al. 1995). The Mount Isa davidite was sourced from the Mary Kathleen Fold Belt and consistently gives a $^{207}\text{Pb}/^{206}\text{Pb}$ age of $1,551 \pm 35$ Ma, identical to uraninite from the Mary Kathleen mine (Page 1983). $^{207}\text{Pb}/^{206}\text{Pb}$ age determinations for the standard zircon can be made with about 1% error, whereas errors for the Mount Isa davidite are about 2%. U–Pb ages for both minerals are slightly less precise but typically around 3%. The isotopes measured were ^{201}Hg ^{202}Hg (used for correction of interferences by ^{204}Hg on ^{204}Pb) ^{204}Pb (used for common Pb correction) ^{206}Pb ^{207}Pb ^{208}Pb , ^{235}U , and ^{238}U .

Host rocks and mineralisation

Valhalla mineralisation is hosted within strongly altered clastic sediments that are bound on the lower and upper contacts by the Eastern Creek Volcanics. Two vertically dipping bodies of mineralisation are known (Eggers 1998, 1999). Only the larger, northern-most body of mineralisation is considered here. This body has a NNW strike, sub-vertical dip and a plunge of approximately 50 degrees to the south (Eggers 1999; Fig. 3). Based on texture, composition, mineralogy and fabric, six rock types that include unaltered and altered foot wall and hanging wall host rocks as well as mineralised rocks have been identified in DDH V39.

The Eastern Creek Volcanics

The Eastern Creek Volcanics are a thick sequence of metabasalts that comprise varying amounts of epidote, actinolite, albite, calcite, sphene, chlorite and magnetite (Wyborn 1987; Heinrich et al. 1995). Samples of Eastern Creek Volcanics were collected from the deepest part of DDH-V39, below mineralisation at Valhalla. At 341.2 and 355.6 m, the Eastern Creek Volcanics are a fine-grained mass of calcite, albite and (titano)magnetite that is cut by abundant, fine anastomosing veins of pale green chlorite and larger (3–5 mm wide) veins of quartz \pm calcite (Fig. 3). This rock likely corresponds to the “calcite-magnetite type” described by Wyborn (1987). At 350.5 m, the basalt has a medium-grained equigranular texture comprising albite-chlorite-(titano)magnetite \pm biotite. This sample has retained its primary basalt texture and is cut by early quartz veins and later calcite veins (Fig. 3). This rock likely corresponds to the “chlorite-albite type” described by Wyborn (1987). At 337.3 m, the basalt preserves epidote-filled amygdales in a fine-grained purple-black ground mass comprising hematite, quartz, sphene and elongate grains of albite (Fig. 3). This rock likely corresponds to the “epidote-sphene type” described by Wyborn (1987).

Weakly altered clastic sediments

Weakly altered clastic sediments (WACS) were intersected intermittently within the ECVs between 120.3 and 226.5 m, and then again between 329.7 and 334.5 m in DDH-V39. These fine-grained sandstones and gritty siltstones are bound by the Eastern Creek Volcanics and comprise detrital grains of feldspar, quartz, biotite, muscovite and variable amounts of Fe-, Mg-silicates, hematite and (titano)magnetite. The abundance of Fe oxides and presence of just trace amounts of Fe-, Mg-silicates in some samples indicates that these sandstones were sourced from the Eastern Creek Volcanics, but most samples are dominated by quartz, feldspar and muscovite, suggesting a distal, more felsic source such as rocks from the Kalkadoon–Leichhardt Block. Chlorite exists between detrital grains, but its relationship to mineralisation is ambiguous; it is likely to be a diagenetic phase based on the fact that chlorite is not part of the alteration assemblage at Valhalla. Illite formed after the chlorite and occupies anastomosing veinlets that cut across some samples. The illite formed at $1,467 \pm 4$ Ma (Polito et al. 2006). These sediments are termed WACS because most detrital phases are only weakly altered or unaltered and sedimentary structures such as cross-bedding, graded-bedding and scour and fill surfaces are preserved. These sediments occur in both the foot wall and hanging wall of the mineralisation (e.g. 215.2 and 333.9 m; Fig. 3). In one sample at 227.1 m (Fig. 3), large, cubic, randomly distributed Fe oxide grains co-exist with randomly distributed fine grained Fe oxide grains in a sandstone displaying graded bedding. The large, cubic, Fe oxide grains contrast the texture and grain size of Fe oxides in other samples (e.g. 207.0 and 215.9 m; Fig. 3) and may have originally been diagenetic pyrite.

Moderately altered fine-grained sediment

Moderately altered fine-grained sediment (MAFS) is located at the margins to mineralisation. This rock type usually retains the primary sedimentary structures observed in the WACS (e.g. 235.6 m; Fig. 3), but the majority of the detrital grains are partly or completely replaced by albite, calcite, minor amphibole and trace amounts of red hematite. Most samples still contain relict detrital quartz and well-preserved hematite/(titano)magnetite.

Laminated and intensely altered rock

Laminated and intensely altered rock (LIAR) comprising elongate grains of albite, amphibole and calcite with disseminated (titano)magnetite, minor amounts of red hematite and trace amounts of brannerite, uraninite and dolomite (e.g. 237.5, 259.5 and 265.9 m; Fig. 3) occur sporadically throughout the mineralised zone. Most lami-

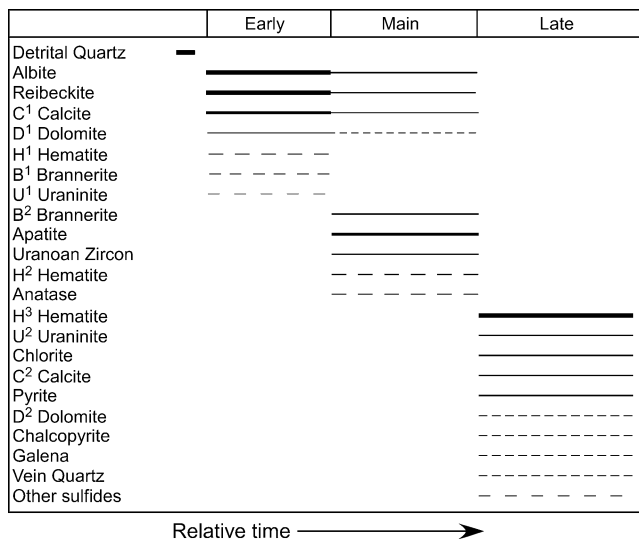


Fig. 4 Paragenetic diagram summarising the relative timing of alteration assemblages in the Valhalla U deposit

nated and intensely altered rocks are green to brown in colour owing to the presence of amphibole. The brown laminated and intensely altered rocks contain trace amounts of red hematite.

Brecciated and intensely altered rock

Brecciated and intensely altered rock (BIAR) displays evidence for a period of brittle deformation (240.5, 255.0, 272.0, 304.1 and 326.7 m; Fig. 3). The rocks comprise fragments of

laminated and intensely altered rocks, cemented by brannerite, apatite, zircon, calcite and minor hematite. This assemblage represents the main stage of U mineralisation. The brecciated fragments are typically sub-angular to angular and range in size from a few millimetres to 2 cm (Fig. 3). The nature of the brecciation suggests a brittle strain environment prevailed during mineralisation. The apatite and zircons are red-brown to purple-brown in colour (Fig. 4) and together with trace amounts of hematite give the core a red-brown colour.

Uraninite, hematite, dolomite, chlorite rock

Uraninite, hematite, dolomite and chlorite (UHDC) veins cut laminated and brecciated intensely altered rocks but occupy less than 5% of the mineralised section intersected in DDH-V39. The best example occurs between 292.8 and 295.9 m (Fig. 3). In this section, anastomosing veinlets of uraninite, hematite, dolomite and chlorite are common. Individual veins range in width from a few microns to 2 cm. The hematite may be steel-grey or ochre red and gives the core a maroon to red-brown colour.

Unmineralised carbonate (calcite or dolomite) veins are common throughout the entire mineralised zone (e.g. 259.5 and 285.7 m; Fig. 3). These veins occasionally contain disseminated, steely hematite with a diffuse hematite selvage (e.g. 285.7 m; Fig. 3). Quartz ± carbonate veins are common at the margin of the deposit (e.g. 207.0 and 333.9 m, Fig. 3). In some samples, the veins occur almost parallel to the core axis and dominate sections of core. In all

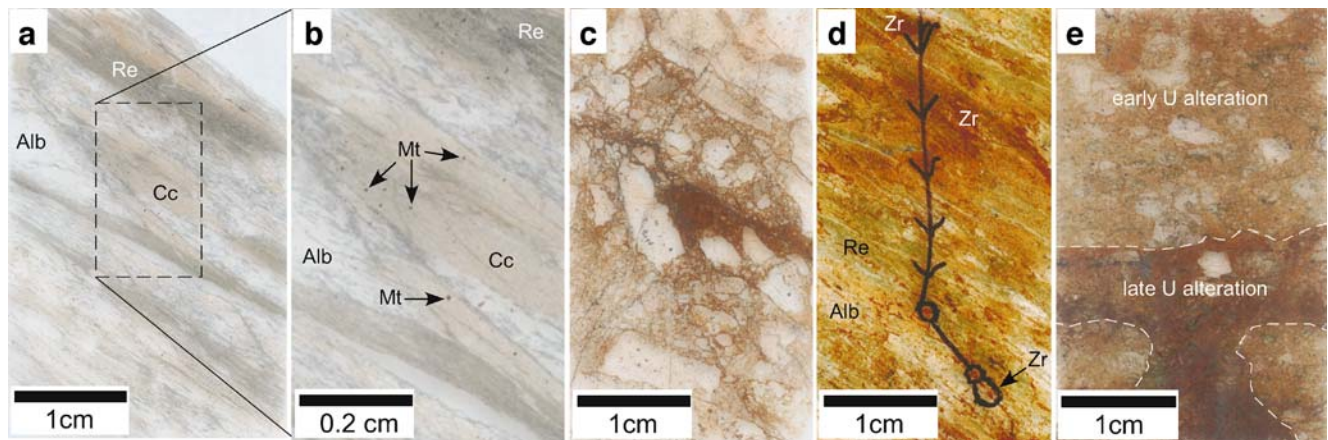


Fig. 5 Photomicrographs of thin sections representing various stages and dominating types of U mineralisation at Valhalla. **a** Laminated and intensely altered rock, the earliest preserved assemblage at Valhalla comprising albite-amphibole-(titano)magnetite-brannerite-uraninite-calcite. *Alb* albite; *Cc* calcite; *Re* reibeckite. Sample DDHV39 281.0 m; **b** A close up of Fig. 4 a showing disseminated (titano) magnetite occurring throughout the assemblage. *Alb* albite; *Cc* calcite; *Re* reibeckite; *Mt* magnetite. Sample DDHV39 281.0 m; **c** An example of brecciated and intensely altered rock comprising albite-(titano) magnetite-calcite ± amphibole cemented by albite-amphibole-calcite-*B*² brannerite-apatite-zircon ± hematite. See Fig. 6 for details. Sample DDHV39 304.1 m; **d** An example of zircon-rich alteration at Valhalla.

The zircon is the red-brown mineral occurring in numerous forms including clusters and veinlets. The *marker pen* identifies three areas that were analysed by electron microprobe. The area identified by the *black arrow* is presented in Fig. 6g as it appears when viewed using a scanning electron microprobe. Sample DDHV39 324.8 m; **(e)** An example of advanced brecciation where the early albite-amphibole-calcite-*B*² brannerite-apatite-zircon ± hematite cement dominates but is cross cut by the late assemblage comprising *U*² uraninite-red hematite-chlorite-dolomite. Note the red-brown colour of the main-stage alteration versus the red colour of the late alteration. Sample DDHV39 321.6 m. See Fig. 6 for petrographic details

Table 1 Electron microprobe analyses of representative reibeckite from Valhalla

Sample oxide wt%	324.1 m ^a	324.1 m ^a	324.1 m ^a	326.1 m ^a	281.0 m ^a	324.1 m ^b	324.1 m ^b	272.0 m ^b	281.0 m ^b	304.1 m ^b
SiO ₂	56.33	56.02	56.77	55.31	56.10	55.11	55.06	55.91	55.33	55.81
Al ₂ O ₃	0.50	0.55	0.58	0.64	0.60	0.60	0.65	0.39	0.50	0.73
FeO	12.88	15.92	16.64	18.02	19.74	20.05	20.30	21.57	22.05	21.49
MnO	0.18	0.14	0.11	0.11	0.16	0.06	0.06	0.07	0.07	0.08
MgO	15.69	14.43	13.72	12.69	11.50	11.32	11.16	10.35	9.88	10.81
CaO	4.93	3.61	2.92	1.37	0.88	0.63	0.76	0.29	0.18	0.65
Na ₂ O	4.92	5.22	5.64	6.50	7.07	7.25	7.17	7.01	7.10	6.81
K ₂ O	0.080	0.082	0.043	0.060	0.053	0.040	0.082	0.034	0.030	0.146
TiO ₂	0.04	0.04	0.05	0.55	0.04	0.06	0.08	0.01	0.01	0.09
F	0.36	0.36	0.27	0.11	0.22	0.18	0.11	0.16	0.21	0.17
V ₂ O ₃	–	0.144	0.125	–	–	–	–	–	–	–
Total	95.91	96.52	96.86	95.36	96.35	95.30	95.43	95.79	95.36	96.77

^a Dark amphibole rim;^b light amphibole core

cases, the carbonate hematite and quartz-carbonate veins cut mineralisation associated with brecciated and intensely altered rock. However, it is unclear if they are related to the uraninite, hematite, dolomite and chlorite veins or some other, possibly later event.

Details of alteration and chemical composition of key minerals

Mineralisation and alteration at Valhalla can be divided into early, main and late stages.

Early mineralisation stage

The early stage of mineralisation corresponds to laminated and intensely altered rocks that comprise albite, amphibole, (titanom)agnetite, calcite, minor amounts of red hematite and trace amounts of brannerite, uraninite and dolomite (Figs. 4, 5a and 6a). The laminated nature of the minerals likely corresponds to their formation during peak metamor-

phism. Albite, amphibole and calcite collectively comprise 98% of this assemblage. Aegerine pyroxene is reported as being part of the alteration assemblage by Eggers (1998, 1999), but it was not observed during this study.

The brannerite (B¹) in this assemblage is rare and typically <3 μm in diameter (Fig. 6b). Early uraninite (U¹) is uncommon, having been identified in only one sample, where it occurred as fine-grained disseminations amongst B¹ brannerite. Euhedral and anhedral magnetite grains are disseminated throughout this assemblage but comprise <2% of the rocks investigated (Fig. 5b). Backscatter electron images show the magnetite grains to be homogeneous with thin alteration rims comprising H¹ hematite or anatase (Fig. 6c). Quantitative EDAX analyses reveal that the magnetite grains can be either pure magnetite or contain significant amounts of Ti and elevated V concentrations indicative of titanomagnetite.

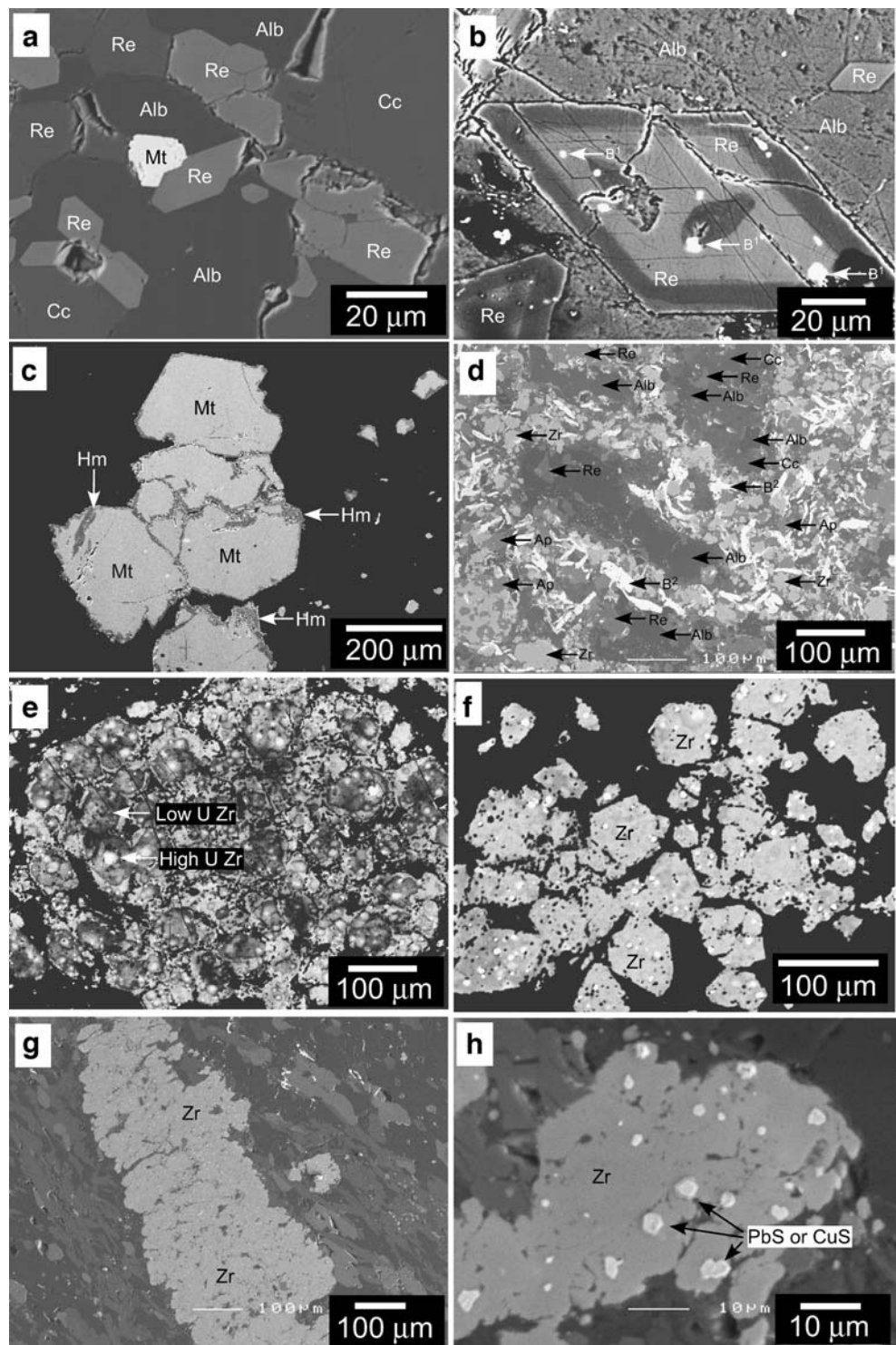
Backscatter electron images show that the amphibole is commonly zoned with pale cores and darker rims (Fig. 6b). Electron microprobe analyses (Table 1) demonstrate that the amphiboles are magnesio-reibeckite with an approxi-

Table 2 Electron microprobe analyses of hydrothermal zircon from Valhalla

Description	SiO ₂	ZrO ₂	UO ₂	FeO	Al ₂ O ₃	PbO ₂	TiO ₂	MnO	P ₂ O ₅	ThO ₂	CaO	V ₂ O ₃	Y ₂ O ₃	HfO ₂	Total
V39 324.8-A	27.6	48.5	2.9	1.7	1.7	0.1	0.6	0.2	0.0	0.0	3.3	0.3	0.1	1.2	88.2
V39 324.8-B	28.2	48.2	2.9	1.7	1.5	0.2	0.6	0.2	0.0	–	3.2	0.2	0.1	1.2	88.2
V39 324.8-C	28.7	49.0	2.8	2.2	1.6	0.3	0.7	0.2	0.7	–	3.1	0.1	0.0	0.9	90.2
V39 324.8-D	29.2	40.0	9.7	1.2	1.9	0.1	0.4	0.2	0.6	0.1	3.3	0.3	0.0	0.6	87.7
V39 324.8-E	30.1	46.2	2.4	5.5	1.4	0.1	0.4	0.1	0.6	–	2.9	0.0	0.2	1.0	91.0
V39 324.8-F	27.5	41.6	9.2	0.7	1.6	0.9	0.4	0.1	0.6	–	3.3	0.2	0.1	0.2	86.6
V39 324.1A	26.7	36.5	15.3	1.2	1.7	0.6	0.6	0.2	0.5	0.1	2.6	0.1	0.0	0.1	86.2
V39 324.1B	28.5	36.4	14.9	1.1	1.9	0.4	0.4	0.1	0.5	0.1	2.7	0.1	0.0	0.6	87.9
V39 324.1C	27.0	34.9	20.4	1.0	1.7	0.6	0.4	0.1	0.6	–	2.6	0.1	0.1	0.8	90.4

En dash (–) Not detected

Fig. 6 **a** Backscatter electron image of the earliest recorded alteration assemblage at Valhalla comprising albite (*Alb*), reibeckite amphibole (*Re*), calcite (*Cc*) and titanomagnetite (*Mt*). Sample DDHV39 272.0 m; **b** Backscatter electron image of disseminated B¹ brannerite in zoned Mg-reibeckite and albite. *Alb* Albite; *Re* reibeckite; B¹ B¹ brannerite. Sample DDHV39 324.1 m; **c** Backscatter electron image of homogeneous magnetite with thin alteration rims comprising hematite and anatase. *Mt* magnetite, *Hm* hematite. Sample DDHV39 285.0 m; **d** Backscatter electron image of B² brannerite laths ranging from 10 to 200 μ m occurring with albite (*Alb*), reibeckite (*Re*), apatite (*Ap*), uranoan zircon (*Zr*) and calcite (*Cc*). Note the abundance of sub-rounded zircons and apatite, which may be responsible for giving the drill core its characteristic red-brown color. Sample DDHV39 304.1 m; **e** High-contrast backscatter electron image of sub-rounded zircons clustering to form an aggregate. Note the variation in brightness within each zircon grain corresponding to high or low U concentration. Sample DDHV39 324.1 m; **f** High-contrast backscatter electron image of sub-hedral zircon grains with areas enriched in U in a matrix of B² brannerite, reibeckite, albite and calcite. Sample DDHV39 324.8 m; **g** A scanning electron micrograph image of a 300- μ m wide veinlet of zircon that cuts the Mg-reibeckite-albite-apatite-calcite-brannerite matrix. The finely disseminated bright spots scattered throughout the vein are PbS and CuS. Sample DDHV39 324.8 m; **h** Scanning electron micrograph close up of a zircon veinlet hosting 1–3- μ m inclusions of PbS and CuS. Sample DDHV39 324.8 m



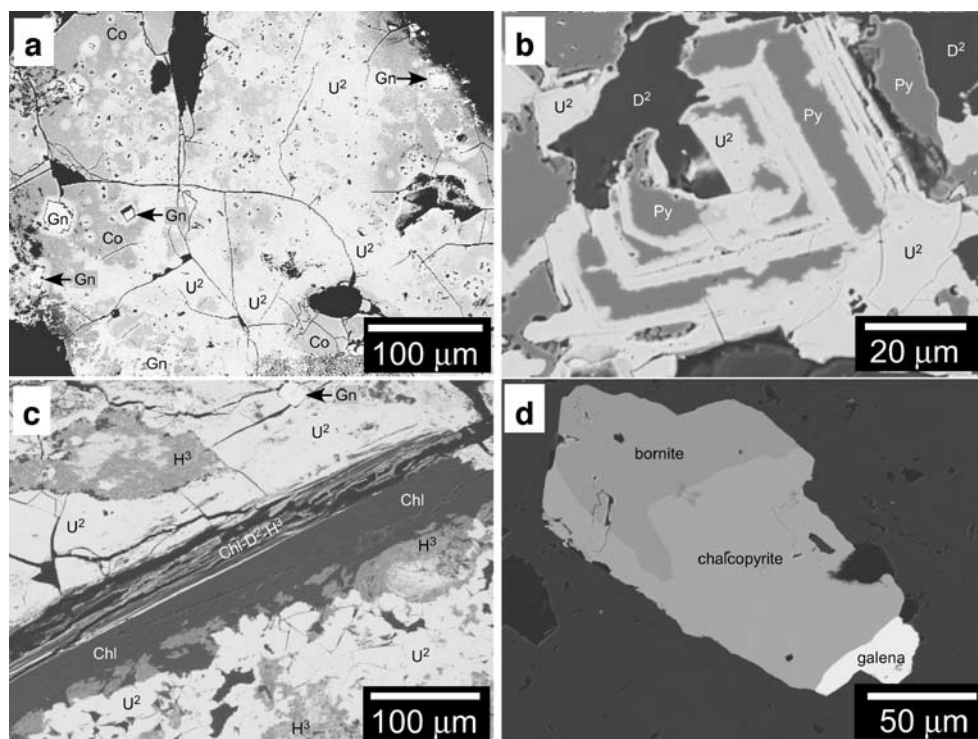
mate chemical formula of $\text{Na}_{1.9}\text{Ca}_{0.2}\text{Fe}_{0.8}\text{Mg}_{2.5}\text{Al}_{0.1}\text{Fe}^{+3}_{1.6}\text{Si}_8\text{O}_{22}(\text{OH}_{1.9}\text{F}_{0.1})$. Fluorine concentrations in the Mg-reibeckite range from 900 to 3,600 ppm (Table 1). V_2O_3 concentrations in the Mg-reibeckite range from 1,300 to 2,600 ppm. Potassium (K_2O), which is not normally associated with reibeckite, is present and exhibits concentrations ranging from 300 to 1,500 ppm (Table 1). The

darker rims on the Mg-reibeckite correspond to higher CaO and MgO and lower FeO and Na_2O concentrations.

Main mineralisation stage

The early stage of low grade U mineralisation (LIAR) was interrupted by multiple episodes of brecciation associated

Fig. 7 **a** Backscatter electron image of heterogeneous U^2 uraninite with highly reflective uraninite being replaced by less reflective uraninite and dull uranyl-silicates (Co). *Gn* Galena. Sample DDHV39 294.0 m; **b** U^2 uraninite replacing pyrite (*Py*), revealing its cubic nature. D^2 D^2 dolomite. Sample DDHV39 294.0 m; **c** U^2 uraninite containing intergrowths of uraniferous red, translucent H^3 hematite, cross-cut by a D^2 dolomite, chlorite (*Chl*) and H^3 hematite vein. Sample DDHV39 294.0 m; **d** A rare grain of co-existing chalcocopyrite, bornite and galena in a dolomite matrix. Sample DDHV39 294.0 m



with the main stage of U mineralisation (BIAR). Brecciated clasts of laminated and intensely altered rocks were cemented by B^2 brannerite, apatite, zircon, albite, reibeckite, calcite \pm H^2 hematite (Figs. 5c and 4). Approximately 95% of the U mineralisation at Valhalla is represented by some variation of this assemblage. B^2 brannerite occurs as randomly orientated elongate laths ranging from 10 to 200 μ m long (Fig. 6d). Apatite and zircon aggregations coincide with the highest U concentrations. Calcite and subordinate dolomite (C^1 calcite; D^1 dolomite) formed during this stage of U mineralisation (Fig. 4). These were cogenetic with the reibeckite and albite (Fig. 6a and d).

Zircon is associated with the main stage of mineralisation and occurs in three forms within the deposit: (1) Subrounded grains of small zircons in aggregates in the Mg–reibeckite–albite–apatite–brannerite matrix (Fig. 6e); (2) Subhedral grains in Mg–reibeckite–albite–calcite dominated lithologies (Figs. 6f and 3) 100–500 μ m wide veinlets that cut the laminated and intensely altered rocks (Figs. 5d and 6g). High-contrast backscatter electron images reveal that most of the zircon is heterogeneous, with coalescing bright and dull areas (Fig. 6e and f). Electron microprobe analyses reveal that the brightest zircon areas contain up to 20.4 wt% UO_2 , whereas the dull areas contain as little as 2.9 wt% UO_2 (Table 2). This mineral is considered uranoan-zircon. We interpret the electron microprobe data to suggest that U, Ca, Fe, Mn, Ti and P substitute for Zr in the zircon. Other chemical peculiarities in the uranoan-zircon include the presence of up to 1.9 wt% Al_2O_3 , 1.9 wt% HfO_2 and 0.31 wt% V_2O_5 . Total analysed oxide contents are typically

below 100 wt%, suggesting the presence of OH^- groups or hydration of the zircon associated with metamictisation. The zircon veinlets are further characterised by 1–3 μ m inclusions of PbS and CuS (Fig. 6g and h). Quantitative EDAX analyses reveal that these grains have highly variable Pb, Cu and S concentrations that rarely conform to compositions that could be construed as being galena, chalcocite or covellite. Finely disseminated H^2 hematite is associated with U mineralisation at Valhalla, but it occurs in trace amounts and is not a major part of the assemblage. No detailed study was undertaken on the apatite, but Gregory et al. (2005) identified fluoroapatite at the Anderson's Lode U prospect that occurs 41 km south east of Valhalla.

Late stage mineralisation

Late stage mineralisation is characterised by disseminated and vein-style U^2 uraninite in a red hematite, dolomite, calcite, chlorite, quartz, Pb-, Fe-, Cu-sulfide assemblage (UHDC; Figs. 5d, 4 and 7). Backscatter electron images demonstrate that U^2 uraninite is heterogeneous, with highly reflective areas of relatively pure uraninite being replaced by less reflective uraninite, which is in turn replaced by dull uranyl-silicates (Fig. 7a). The less-reflective uraninite commonly contains intergrowths of uraniferous red, translucent H^3 hematite. Red, finely disseminated H^3 hematite is a common part of the late-stage alteration assemblage. Some U^2 uraninite replaces pyrite, which has the effect of revealing the cubic structure of the pyrite crystals (Fig. 7b). Elsewhere, the uraninite and pyrite appear to be coeval. A late

Table 3 Chemical compositions from electron microprobe analyses of brannerite at Valhalla

Description	SiO ₂	PbO ₂	UO ₂	FeO	CaO	TiO ₂	Al ₂ O ₃	MnO	P ₂ O ₅	V ₂ O ₃	Total
V39 304.1-1A	5.3	2.6	40.7	2.0	2.3	36.0	–	–	–	–	89.0
V39 304.1-1B	4.7	2.6	40.2	2.1	2.4	37.6	–	–	–	–	89.6
V39 304.1-1C	5.6	3.1	39.0	2.2	2.5	36.6	–	–	–	–	89.0
V39 304.1-2A	6.5	2.9	39.8	1.9	2.6	34.4	–	–	–	–	88.0
V39 304.1-2B	4.6	2.7	41.9	2.4	2.5	36.7	–	–	–	–	90.8
V39 304.1-3A	4.3	2.6	41.0	2.5	2.0	38.9	–	–	–	–	91.2
V39 304.1-3B	4.9	2.7	39.9	2.3	2.2	37.5	–	–	–	–	89.4
V39 304.1-3C	4.2	2.5	41.8	2.2	2.4	37.4	–	–	–	–	90.5
V39 304.1-3D	4.5	2.3	41.0	2.4	2.4	37.0	–	–	–	–	89.5
V39 304.1-4A	3.8	2.2	39.9	2.6	2.1	41.8	–	–	–	–	92.4
V39 304.1-4B	3.9	2.6	41.3	2.2	2.3	38.7	–	–	–	–	91.0
V39 304.1-4C	3.8	2.3	42.6	2.2	2.8	38.9	–	–	–	–	92.7
V39 304.1-4D	5.5	2.8	40.3	2.2	2.2	37.6	–	–	–	–	90.7
V39 304.1-5A	5.3	3.0	40.9	1.9	2.1	35.9	–	–	–	–	89.1
V39 304.1-5B	7.6	2.4	44.5	1.8	2.0	27.5	–	–	–	–	85.8
V39 304.1-5C	5.9	2.8	39.3	1.8	2.4	36.2	–	–	–	–	88.5
V39 324.1D	8.1	4.0	35.6	1.8	4.3	35.2	0.47	0.44	0.14	0.32	90.4

En dash (–) Not measured

stage of dolomite and minor calcite (C² calcite; D² dolomite) forms veins with chlorite and minor quartz (Fig. 7c). Chlorite mostly occurs as late veins that cut U² uraninite (Figs. 4 and 7c). Sulfides, other than pyrite and galena are rare, late in relation to most other alteration minerals (Fig. 5), but include chalcopyrite, bornite and sphalerite (Fig. 7d). The late stage U² uraninite–hematite–dolomite–calcite–chlorite–quartz–(Pb–Fe–Cu) sulfide assemblage occupies <5% of the 93 m of drill core examined, but it can be associated with high U grades. One 0.3 m interval from 295.8 m contains 3.28% U, but other 0.2 to 0.5 m samples that comprise late stage U mineralisation have <0.2% U.

Mineral chemistry of brannerite and uraninite

The chemical composition of brannerite is nominally UTi₂O₆. However, it is commonly reported as (U,Ca,Th,Y,REE)(Ti,Si,Fe,Al)₂O_{6–8}(OH)_x because U may be replaced

by Ca, Th, Y and REE and Si, Al and Fe can replace Ti as a result of oxidation and partial hydration (Smith 1984). All natural brannerites are metamict (Smith 1984) and commonly are amorphous due to alpha-radiation decay of the mineral's structure (Lumpkin et al. 2000). The presence of Pb in its structure is mainly due to the decay of U. Electron microprobe analyses (Table 3) reveal that Valhalla brannerites contain several percent of Ca, Pb, Si and Fe and highly anomalous levels of Al, V, Mn and P in the U and Ti sites. Rare earth element concentrations were not measured, but brannerite at the nearby Anderson's Lode is enriched in yttrium (Gregory et al. 2005). Total analyzed contents range from 88.0 to 92.7%. These low totals are likely to reflect a combination of metamict brannerite, partially hydrated brannerite or slightly amorphous brannerite as described by Lumpkin et al (2000).

Electron microprobe data and backscattered electron images reveal that Valhalla U² uraninite has been variably

Table 4 Chemical compositions from electron microprobe analyses of uraninite at Valhalla

Sample	SiO ₂	PbO ₂	UO ₂	FeO	CaO	TiO ₂	Total	Chemical age (Ma)
V39 294M C1 no. 1	8.0	0.3	75.9	0.6	3.3	0.4	88.6	28
V39 294M C1 no. 2	18.8	0.6	66.3	0.6	2.5	0.0	88.8	54
V39 294M C1 no. 3	16.3	0.5	68.4	1.0	2.0	0.2	88.4	46
V39 294M C3 no. 1	4.2	0.3	80.7	1.0	3.7	0.1	90.0	25
V39 294M C3 no. 2	4.9	0.5	80.6	0.7	3.1	0.1	90.0	41
V39 294M C3 no. 3	2.8	1.1	81.4	1.5	4.5	0.1	91.5	87
V39 294M C3 no. 4	2.5	2.2	83.0	1.2	4.2	0.1	93.2	165
V39 294M C5 no. 1	4.7	0.4	77.4	0.7	5.0	0.1	88.1	29
V39 294M C5 no. 2	4.9	0.1	80.0	0.7	5.4	0.1	91.2	9

Chemical ages calculated using the equation reported by Bowles (1990)

Table 5 Whole rock geochemical analyses of samples from DDH V39

Sample	209.4	215.2	227.1	230.1	235.6	240.5	255.0	259.5	265.9	272.0	277.4	281.0	285.7	292.9	295.8	304.1	313.2	324.1	326.7	333.9	341.9	355.6
rock type	WACS	WACS	WACS	MAFS	MAFS	MAFS	BIAR	BIAR	LIAR	LIAR	BIAR	LIAR	LIAR	UHDC	UHDC	BIAR	BIAR	BIAR	BIAR	WACS	WACS	ECV
Percent																						
SiO ₂	47.9	53.7	54.7	60.0	43.2	48.2	50.1	49.7	50.1	40.9	37.3	52.3	13.6	39.8	38.9	28.9	49.4	39.6	46.3	48.8	47.4	42.2
TiO ₂	0.8	0.9	1.0	0.8	2.0	2.1	0.7	2.1	1.1	0.6	2.0	0.6	0.8	2.1	2.6	1.5	1.6	2.4	1.8	2.2	2.4	3.1
Al ₂ O ₃	12.1	17.3	13.8	11.7	10.1	9.0	11.8	9.2	10.9	10.6	3.5	9.0	3.3	9.2	7.8	6.3	13.4	6.5	7.6	13.0	11.6	14.7
Fe ₂ O ₃	6.3	9.0	7.4	10.0	15.9	12.9	8.9	12.7	14.6	11.3	16.1	12.9	18.4	17.3	18.0	14.4	6.2	13.6	10.6	13.1	14.2	20.2
MnO	0.2	0.1	0.1	0.1	0.2	0.1	0.1	0.2	0.1	0.2	0.1	0.1	0.9	0.2	0.2	0.3	0.2	0.2	0.1	0.1	0.2	0.2
MgO	7.4	4.3	3.0	4.0	5.2	3.1	3.7	3.4	4.5	5.2	3.4	5.0	9.5	6.2	2.8	5.8	3.4	4.5	4.2	3.9	3.2	5.3
CaO	7.2	2.9	6.6	3.9	7.1	7.7	7.8	8.5	3.9	9.2	11.7	5.7	21.1	7.0	11.8	15.5	7.2	12.2	9.2	6.6	12.8	5.3
Na ₂ O	1.4	1.2	2.6	3.3	5.1	6.1	6.8	6.5	6.8	5.9	4.7	7.5	1.8	3.6	4.2	3.3	7.6	4.8	4.4	4.1	1.0	2.5
K ₂ O	3.0	4.8	3.4	0.1	0.3	0.2	1.1	0.1	0.3	0.3	0.1	0.0	0.1	1.0	0.3	0.5	0.1	0.6	0.3	1.5	0.5	1.4
P ₂ O ₅	0.2	0.2	0.2	0.1	0.3	0.6	0.0	0.7	0.0	0.0	3.3	0.4	0.4	0.6	3.1	1.9	0.0	2.4	2.0	0.3	0.4	0.4
Total C	2.8	0.6	1.3	0.8	2.4	1.7	1.7	1.6	1.5	3.7	1.5	1.5	7.9	2.3	2.0	5.0	3.0	2.0	1.4	1.3	1.4	0.4
Total S	0.0	0.0	0.0	0.2	0.2	0.0	0.0	0.0	0.0	0.0	0.0	0.0	0.0	0.1	0.0	0.0	0.1	0.1	0.1	0.1	0.1	0.0
LOI	13.3	5.4	6.9	5.6	10.0	7.6	7.4	6.1	6.4	14.5	10.3	6.2	29.3	11.5	8.2	18.9	10.3	9.0	7.6	6.0	6.2	4.4
TOTAL	99.8	99.8	99.8	99.8	99.6	99.2	99.6	99.6	99.5	99.7	98.8	99.8	99.7	98.9	98.9	98.8	99.9	97.4	98.5	99.8	99.8	99.7
ppm																						
As	4	3	4	4	4	3	2	1	2	1	7	1	3	3	97	3	4	8	6	3	5	4
Ba	346	588	408	9	27	128	207	155	37	46	150	6	15	918	36	109	122	145	118	402	97	369
Be	1	3	2	1	6	25	12	23	9	6	121	12	7	13	15	39	10	54	51	2	1	1
Bi	0.5	0.3	0.3	0.3	0.4	0.3	0.1	0.1	0.1	0.1	0.5	0.1	0.1	0.4	5.1	1.1	0.9	2.8	3.9	0.1	0.1	0.1
Ce	64	64	83	65	56	68	35	53	28	29	87	16	42	139	195	144	99	75	54	66	77	75
Co	21	36	22	27	54	52	31	44	54	49	66	46	20	37	33	40	47	60	62	42	44	60
Cs	4.4	6.8	6.0	0.2	0.4	0.1	1.4	0.1	0.5	0.1	1.7	0.1	0.1	0.3	0.3	0.1	0.2	0.3	0.4	3.5	0.5	2.6
Cu	6	3	7	1291	463	121	3	35	26	42	72	4	43	29	64	3	10	1272	3806	316	322	223
Ga	17	25	19	18	18	16	16	13	17	15	8	16	5	13	6	14	10	11	12	22	21	25
Hf	5	5	7	4	43	309	134	42	61	32	1106	19	57	30	29	161	162	278	976	8	7	7
La	29	31	39	30	21	25	9	22	10	11	44	8	20	49	141	60	37	34	30	28	34	32
Mo	0.2	0.4	0.1	0.7	2.1	1.1	0.5	0.3	0.8	1.6	1.1	0.4	0.4	0.5	1.2	1.4	5.8	0.6	1.5	1.4	1.0	0.5
Nb	12	15	13	9	13	16	7	14	12	8	12	6	6	12	2	14	14	17	18	15	16	17
Nd	23	25	30	26	32	37	17	27	14	13	48	8	23	73	111	85	56	35	26	32	38	37
Ni	36	60	42	43	47	41	31	42	44	32	49	51	10	42	38	59	26	45	43	49	50	57

Pb	6	8	8	8	8	51	153	170	88	52	102	1150	115	85	612	1986	1279	1265	1049	441	5	9	7
Pr	7	7	9	7	7	7	8	4	6	3	3	11	2	5	17	31	19	13	9	6	7	9	9
Rb	135	244	179	3	4	4	3	26	1	9	4	9	0	1	11	2	4	7	9	6	68	13	60
Sc	17	25	20	19	35	39	39	24	40	27	12	28	13	16	32	34	29	16	25	26	34	36	47
Sn	3	4	2	3	2	2	2	2	1	3	1	2	1	2	1	2	2	2	1	1	2	2	2
Sr	49	90	131	142	59	374	556	693	693	133	455	817	195	402	114	111	455	641	707	499	122	239	126
Th	15	18	15	11	9	13	11	9	9	9	10	44	5	8	65	17	75	70	32	29	10	8	7
U	4	4	4	4	210	1009	783	176	379	858	858	3464	99	306	6317	32845	4390	5901	12213	4997	13	5	3
V	106	143	169	178	886	1399	638	1172	796	212	2187	656	1112	1112	712	653	1268	584	821	857	299	360	453
Y	23	30	32	22	64	97	79	49	49	42	49	157	13	85	92	128	117	190	93	124	46	60	61
Zn	92	122	74	92	33	47	55	84	84	59	47	266	87	37	78	58	57	33	53	67	110	133	203
Zr	215	180	249	161	1636	12378	8155	2335	4050	5729	47692	606	47692	3813	1496	1552	5580	10346	13786	36423	282	248	256

WACS Weakly altered clastic sediment; *MAFS* moderately altered fine-grained sediment; *L/LAR* laminated and intensely altered rock; *B/LAR* brecciated intensely altered rock; *U/HDC* (late) Uraninite, Hematite, Dolomite, Chlorite veining; *ECV* Eastern Creek Volcanics

altered to different forms of uranyl-silicate (Table 4; Fig. 7a). Chemical compositions of well-preserved uraninite in sample V39 294.0 m range from 77.4 to 83.0 wt% UO₂, 0.1 to 2.2 wt% PbO₂, 3.1 to 5.4 wt% CaO, 0.7 to 1.5 wt% FeO and 2.5 to 4.9 wt% SiO₂. Naturally occurring, newly formed uraninite has a chemical composition that ranges from UO_{2.07} to UO_{2.25} (Smith 1984; Burns 1999) with <0.1 wt% Pb, CaO, FeO and SiO₂ (Bowles 1990). Therefore, the presence of these elements and oxides at percent concentrations in uraninite is attributed to the gain of Ca, Si and Fe through a process of post-precipitation alteration to various uranium oxide hydrates and uranyl-silicates. The introduction of Pb into the uraninite structure other than by in situ decay is unlikely, but the unusually low Pb concentrations recorded here indicate that the uraninite either formed around 165 Ma (Table 4) or that there has been a significant amount of Pb loss since original formation. The relatively high CaO, FeO and SiO₂ concentrations, combined with the low Pb concentrations in the uraninite at Valhalla (Table 4), indicate that all of the uraninite analyzed in this study experienced post-precipitation alteration.

Whole rock geochemical analysis

Whole rock geochemical data compiled from samples collected during this study (Table 5) plus data downloaded from Geoscience Australia’s OZCHEM database (<http://www.ga.gov.au/meta/ANZCW0703002769.html>) was litho-geochemically assessed using Pearce Element Ratio (PER) analysis (Pearce 1968; Stanley and Russell 1989; Russell and Stanley 1990; Pearce and Stanley 1991; Madeisky and Stanley 1993) and General Element Ratio (GER) analysis (Stanley and Madeisky 1994). The inclusion of data from the OZCHEM database allows comparisons to be made between Valhalla and other uranium prospects such as Skall, Bikini, Pile, Perseverance, Mighty Glare, Easter Egg and Batman in the Western Succession (Fig. 1).

PER/GER analysis was employed here in an attempt to quantify material transfer of elements between the host rocks and the fluids that passed through them (Stanley and Madeisky 1994; Stanley 1998). PER/GER analysis allows comparisons between unaltered and altered samples by dealing with the addition or loss of material without being affected by errors created by closure. Closure arises in geochemical data when the sum total of all components is scaled to equal 100%. Summing all components to 100% effectively masks compositional variation when the size of the rock changes during material transfer. The addition of one or more elements during alteration associated with faulting, shearing or brecciation can lower the concentration of other elements in the rock although there has been no material loss. Closure is avoided by converting the data to molar

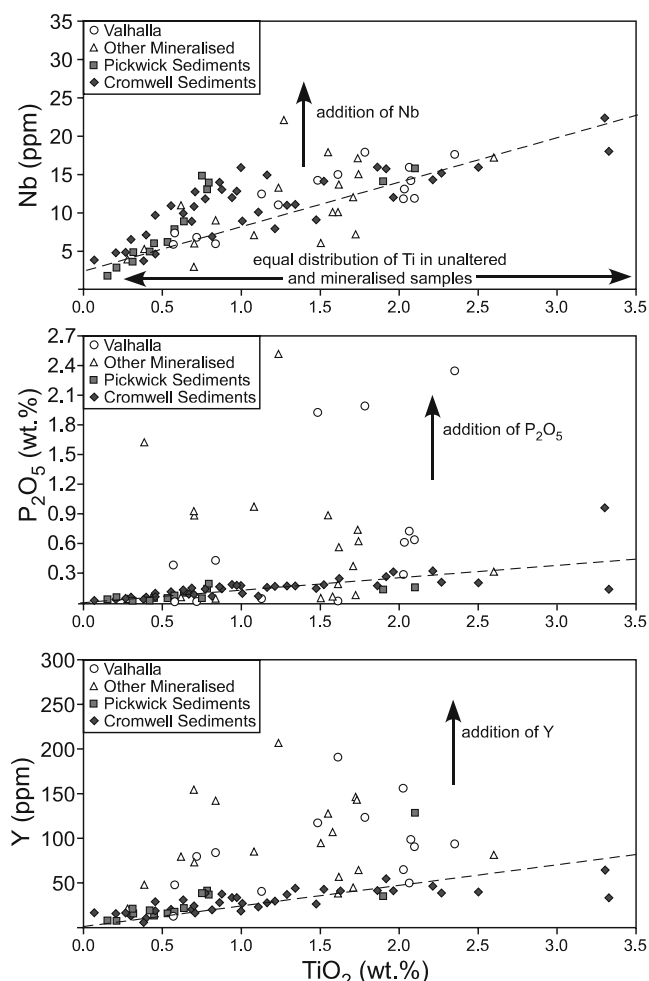


Fig. 8 Scatterplots of TiO_2 versus Nb, P_2O_5 and Y showing that Ti was the least mobile and therefore the most conserved element during metamorphism and hydrothermal alteration. Note that despite the wide concentration range for TiO_2 , this element oxide is no more abundant in the mineralised samples than it is in the unmineralised samples. **a** A scatterplot of TiO_2 versus Nb showing that Nb is slightly less conserved than TiO_2 as indicated by the dashed line that passes through the y-axis above the origin = zero. **b** A scatterplot of TiO_2 versus P_2O_5 showing that both elements are conserved in the unaltered metasedimentary rocks, as indicated by the dashed line that passes through most samples and the origin, but that P was gained or redistributed during mineralisation. P_2O_5 concentrations have been limited to those below 2.7 wt%. **c** A scatterplot of TiO_2 versus Y showing that both elements are conserved in the unaltered metasedimentary rocks as demonstrated by the number of samples that plot close to or just above the dashed line that passes through the origin, but that Y was gained during mineralization

element ratios. This requires the use of an element that did not participate in the material transfer (i.e. a conserved element that was neither gained nor lost, typically a high field strength or immobile element). In this way, the relative material transfers that took place to change the rock composition can be understood (Pearce 1968; Russell and Stanley 1990; Stanley and Madeisky 1994).

Although PERs were initially developed to demonstrate fractionation in igneous rocks (Pearce 1968), Stanley

(1996, 1997) expanded its use and introduced GERs to identify major element variations that are associated with the formation of new minerals in a range of host rocks, including sediment hosted deposits. Some workers in the Mount Isa Basin (Heinrich et al. 1995; Oliver et al. 2004; Mark et al. 2006a) favour the use of isocon analysis (Grant 1986) to deal with closure effects and identify elemental gains and losses. However, this method was not employed here because it assumes that the unaltered rocks were homogeneous before any subsequent alteration (i.e. that there is a single parent rock composition). This assumption indicates that isocon analysis may be compromised when mineralogical sorting or mineral fractionation during rock formation has resulted in the unaltered rock suite having different geochemical starting compositions. Accurately identifying gains and losses due to metasomatism is further complicated in cases when it is difficult to identify cryptic alteration in apparently unaltered rocks, as any conclusions will be undermined if the wrong parent rock is selected during interpretation. Isocon analysis also limits the user to making comparisons between individual samples; large datasets are tedious and time consuming to process. In contrast, PER/GER analysis is undertaken using molar amounts, so interpretation of any material transfers in terms of chemical reactions and mineral formulae is straightforward. PER/GER analysis is also capable of dealing with the material transfer effects created by competing geochemical processes unrelated to alteration and ore formation (e.g. metasomatism during metamorphism, mineral fractionation amongst igneous rocks from a common magmatic chamber and mineral sorting of detritals during sedimentation). This can be achieved through the formation of linear combinations of molar ratios to create geometric projections of geochemical space from material transfer processes. In this way, competing geochemical effects caused by processes that occurred before mineralisation can be removed from consideration and the metasomatism associated with ore formation can be isolated and interpreted without interference.

PERs are formed by dividing the molar concentration of a major element by that of a conserved element (Stanley 1993). Common candidates for conserved elements in sediments are Ti (typically as TiO_2), P (typically as P_2O_5), Nb, Zr, Y, Ce, La and Al (typically as Al_2O_3). The alteration assemblage at Valhalla challenges the principles of conserved element ratios and few elements appear to have been immobile during alteration and metamorphism. Aluminium as Al_2O_3 does not correlate with any of the other high field strength elements, suggesting that Al concentrations in the mineralised and unaltered samples are controlled by mineralogical sorting of detrital grains such as feldspar and phyllosilicates during sedimentation. However, TiO_2 is conserved, as demonstrated by the fact that most unaltered samples have TiO_2 , Nb, P_2O_5 and Y co-variation trends that pass through the origin (Fig. 8),

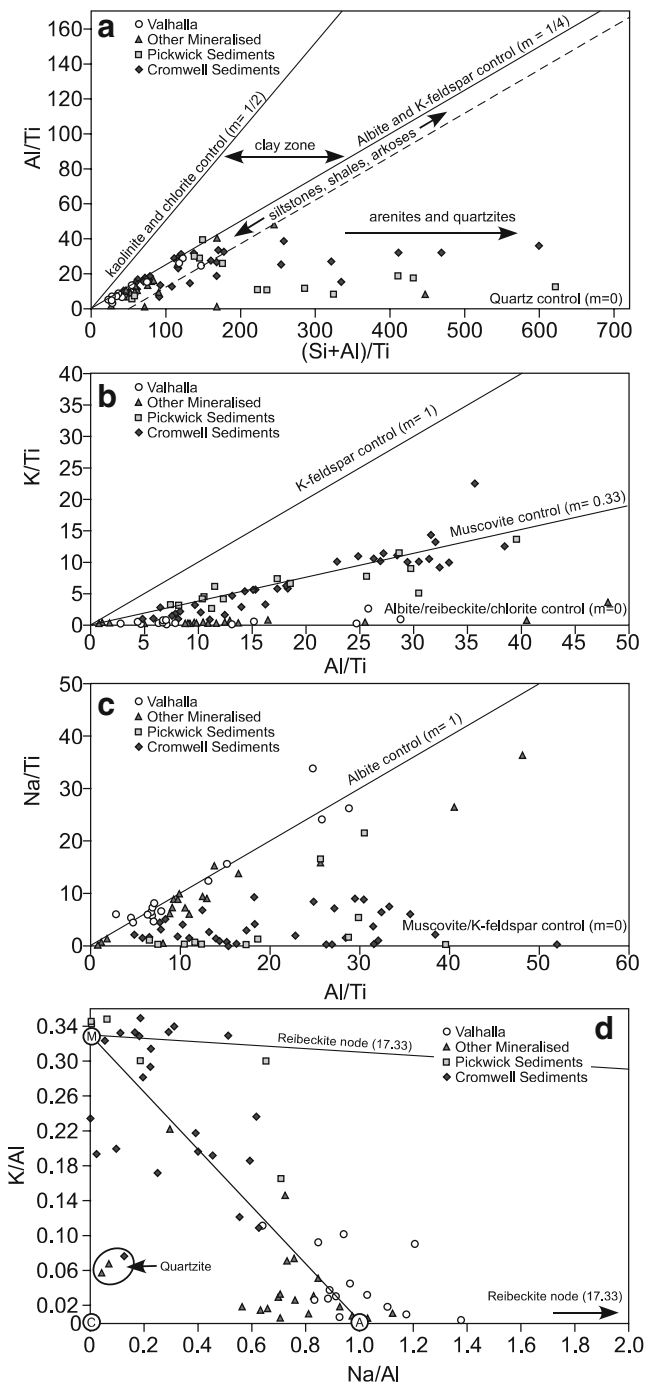


Fig. 9 Pearce Element Ratio diagrams of **a** Al/Ti versus (Si + Al)/Ti modelling alkali feldspar and quartz in sediments. Note that all of the Valhalla samples and most of the other mineralised samples plot within the field of siltstones, shales and arkoses whereas the non-mineralised Pickwick and Cromwell sediments plot in an area that represents arenite and quartzites as well as siltstones, shales and arkoses. Note the lack of clays in the “clay zone,” which suggests that the rocks were not deposited with significant amounts of clay (*m* the molar ratio of the elements plotted on the *x*- and *y*-axis required to form the minerals indicated, e.g. kaolinite, feldspar, chlorite etc.); **b** K/Ti versus Al/Ti demonstrating that K-feldspar is largely absent, whereas muscovite (in the form sericite) is common but only in the unaltered metasediments. K is largely absent from U mineralised samples, implying that it was removed during mineralisation; **c** Na/Ti versus Al/Ti, demonstrating that mineralised samples contain elevated Na, primarily in the form of albite and rebeckite given that they plot close to or above the albite control line, relative to their unmineralised counterparts; **d** A General Element Ratio diagram of K/Al versus Na/Al illustrating the location of all samples in muscovite (*M*), albite (*A*), rebeckite and chlorite (*C*) space. Note that the mineralised samples plot around the albite node with trends toward the chlorite and rebeckite nodes, whereas the unmineralised samples plot around the muscovite node, but trend toward the albite and rebeckite nodes, implying partial alteration, possibly associated with nearby U mineralisation

Mount Isa district (Fig. 9a–c). The (Si + Al)/Ti versus Al/Ti plot (Fig. 9a) models alkali feldspar and quartz sorting in sediments. It demonstrates that all of the Valhalla samples plot within a field that characterises shale, siltstone and arkoses, consistent with thin section investigations that suggest that the host rocks are coarse siltstones and fine-grained dirty arkoses (Fig. 3, 215.2 and 227.1 m). On the other hand, many of the unmineralised samples belonging to the Pickwick and Cromwell sediments plot parallel to the *x*-axis, indicating higher volumes of quartz in these samples, hence most of these unmineralised samples can be characterised as arenites or quartzites. It is noteworthy that clay minerals such as kaolinite, sericite and chlorite, common detrital grains in siltstones and shales, do not plot above the albite and K-feldspar control line as may be expected in this figure. This indicates that clay minerals were not present in significant amounts relative to quartz and feldspar during deposition, despite thin section observations that show these minerals are now locally abundant. The PER diagram therefore demonstrates that the clays in the unaltered samples must be a result of in situ breakdown of feldspar and other detrital grains to clay minerals plus quartz during diagenesis that followed deposition.

The K/Ti versus Al/Ti plot (Fig. 9b) models dominant K-bearing minerals. It demonstrates that K-feldspar is only a trace component in the metasediments. On the other hand, muscovite (as sericite) is the dominant K-bearing phase but primarily in unaltered metasediments. Figure 9b indicates that sericite was the primary clay mineral formed during authogenic/diagenetic alteration of the host rocks, as discussed above. However, there is an absence of sericite in the mineralised samples, indicating that K was com-

plus the fact that TiO₂ is no more abundant in the mineralised samples than it is in the unmineralised samples. This indicates no mass gain or loss of this element and suggests that TiO₂ was neither added nor removed during hydrothermal activity despite the fact that Ti-bearing brannerite is the primary U-bearing mineral at Valhalla.

PER diagrams of (Si + Al)/Ti versus Al/Ti, K/Ti versus Al/Ti and Na/Ti versus Al/Ti highlight the main mineralogical controls that affect all of the metasediments interbedded within the Eastern Creek Volcanics in the

pletely removed from the metasediments during U mineralisation. The thesis that K was removed during U mineralisation correlates with the finding that Na was added during mineralisation as demonstrated by the Na/Ti versus Al/Ti relationship (Fig. 9c). This diagram (Fig. 9c) shows that mineralised samples contain elevated Na, primarily in the form of albite, relative to their unmineralised counterparts. Therefore, it can be concluded that Fig. 9a–c model two major processes: (1) Sericite is the major K-bearing mineral in unaltered sediments. Detrital feldspar is rare or absent indicating non-deposition or more likely, alteration to sericite during diagenesis before mineralisation; and (2) K (\pm Ba \pm Rb) was removed and Na was added during alteration associated with U mineralisation. The excess Na beyond that assigned to albite alone (Fig. 9c) is attributed to the other Na-bearing mineral in the deposit, Mg-reibeckite (Fig. 6a).

GER diagrams allow multiple minerals of different compositions to be plotted as nodes on a single diagram. In these diagrams, samples ‘trend’ towards or away from mineral nodes depending on the abundance of that mineral in the sample. In this study, the GER diagram is used to confirm PER and petrographic observations and to model element addition or loss associated with a specific alteration type. Figure 9d models K/Al versus Na/Al and supports hand specimen observations that unaltered and weakly altered samples contain sericite as the primary K-bearing mineral, with most unaltered samples clustering around this node. Altered and mineralised samples cluster around the albite node with numerous samples from Valhalla trending toward the reibeckite node. Some mineralised samples from deposits other than Valhalla, trend toward the chlorite node from the albite node, indicating the presence of this mineral instead of reibeckite in these samples. Pure quartzite samples also plot near the chlorite node but only because they contain negligible amounts of K and Na. GER versus element concentration diagrams (Figs. 10 and 11) that model K-feldspar and muscovite destruction and albite plus reibeckite formation along the *x*-axis demonstrate that Na, U, V, Zr, P, Sr, Y and Ca addition, and K, Si, Rb and Ba loss, occurred during mineralisation.

In addition to the GER element plots, a down-hole element plot was constructed to compare the relationship between the host rocks and U, Zr, HREE (Ca/La/Nd), LREE (Sm/Eu/Gd/Tb/Dy/Ho) and Cu (Fig. 3). These plots reveal that the WACS contain trace concentrations of U, Zr and Cu but minor to moderate concentrations of both HREE and LREE. This suggests an inheritance of these elements from the detrital grains. The laminated and intensely altered rocks contain anomalous concentrations of U and Zr (generally around 0.1% U and 0.2% Zr), supporting thin section observations of trace amounts of brannerite and zircon in these samples. Only a minor to modest increase in HREE is observed. On the other hand,

Fig. 10 GER (K/Al and Na/Al) versus element concentration diagrams demonstrating that U, V, Zr, Sr and Y addition occurred with alteration that involved the destruction of K-feldspar and muscovite and the formation of albite and reibeckite. *m* Muscovite; *a* albite; *k* K-feldspar

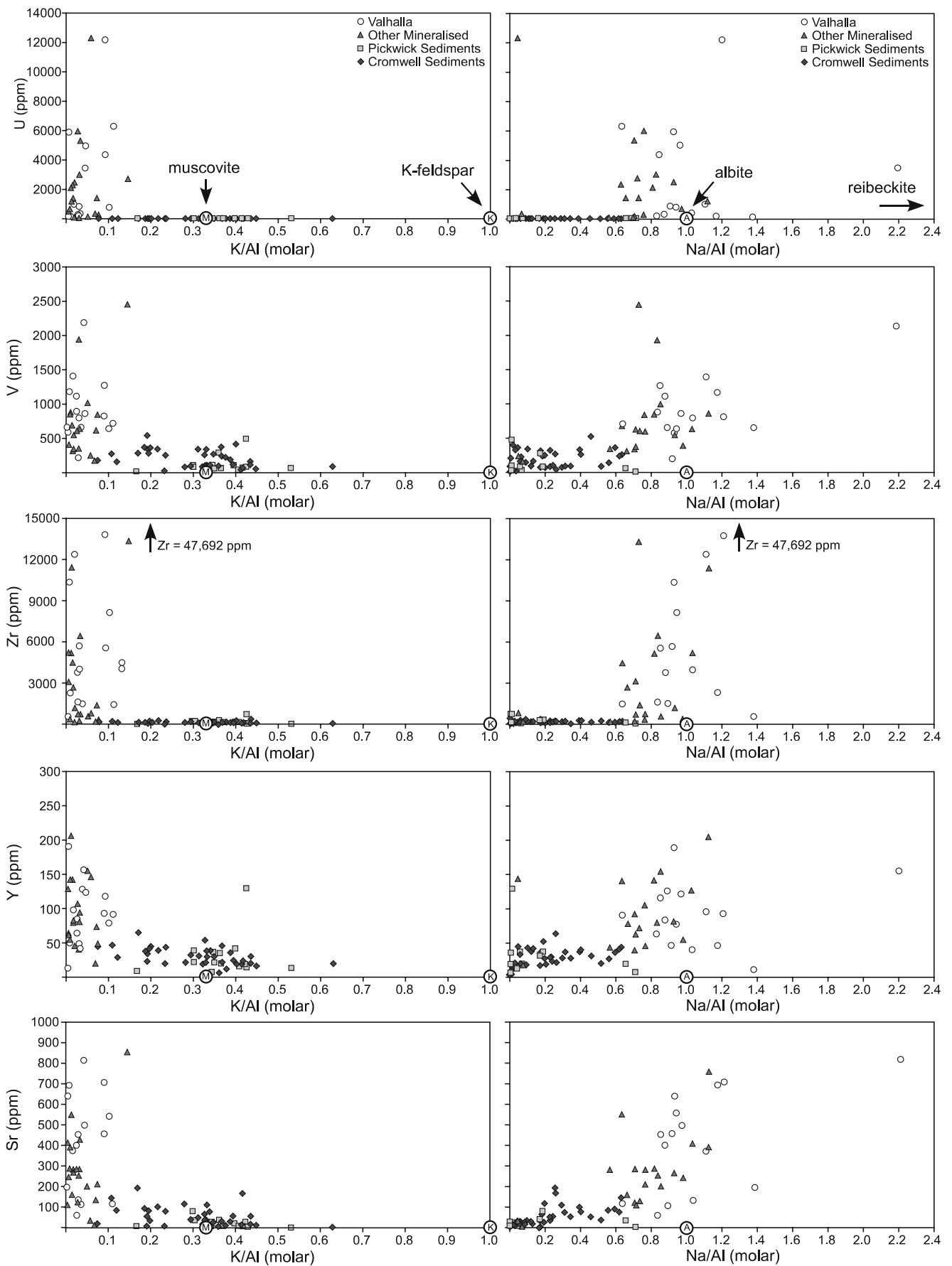
the brecciated and intensely altered rocks that comprise the most brannerite, zircon and apatite consistently contain some of the highest concentrations of U (>0.2% U), Zr (up to 4.8%) and highly anomalous concentrations of HREE. Similar to the brecciated and intensely altered rocks, the late uranium, hematite, dolomite, chlorite rocks correlate to the highest U concentrations, but the major difference between the two contrasting styles of mineralisation is that the late uranium, hematite, dolomite, chlorite rocks correlate to anomalous concentrations of LREE but not necessarily HREE. This supports the view that these two styles of mineralisation formed from two different fluids at different times. Only two samples in the data set contain anomalous concentrations of Cu and both of these occur in samples collected at the margins to mineralisation. There is no correlation between U and Cu.

Geochronology

U–Pb and Pb–Pb ages

Fourteen B² brannerite laths (Fig. 12) analysed by LA-HR-ICPMS have ²⁰⁷Pb/²⁰⁶Pb ages that range from 584±6 to 1,543±15 Ma (Table 6). In contrast, mottled U² uraninite veins analysed by LA-HR-ICPMS have ²⁰⁷Pb/²⁰⁶Pb ages that range from 344±3 to 1,220±12 Ma (Table 6). Sixty percent of the ²⁰⁷Pb/²⁰⁶Pb ages from both minerals are between 800 and 1,150 Ma (Fig. 12), which broadly corresponds to the timing of the amalgamation of Australia and Laurentia during the Grenville Orogeny at ca. 1,140 Ma (Wingate et al. 2002) and the breakup of the proposed super continent, Rodinia, between 1,000 Ma (Tack et al. 2001) and 750 Ma (Wingate and Giddings 2000). The oldest ²⁰⁷Pb/²⁰⁶Pb ages of 1,543±15 and 1,510±15 Ma overlap the time of peak metamorphism, Cu deposition at Mount Isa and Mount Gordon (Carr et al. 2001) and pegmatite intrusion in the Mount Isa area (Page and Bell 1986; Connors and Page 1995; Betts et al. 2006).

Eleven of the 14 B² brannerite laths analysed by LA-HR-ICPMS define a U–Pb discordia line with an upper intercept age of 1,564±27 Ma and lower intercept age of 175±13 Ma (Fig. 12). The mean square of weighted deviates (MSWD) value of 9.3 is high in relation to U–Pb systematics in zircon, but similar to MSWD values are obtained from uraninite in most U deposits (Page 1983; Fayek and Kyser 1997; Fayek et al. 2000; Polito et al. 2005). Most of the analyses are highly discordant and plot



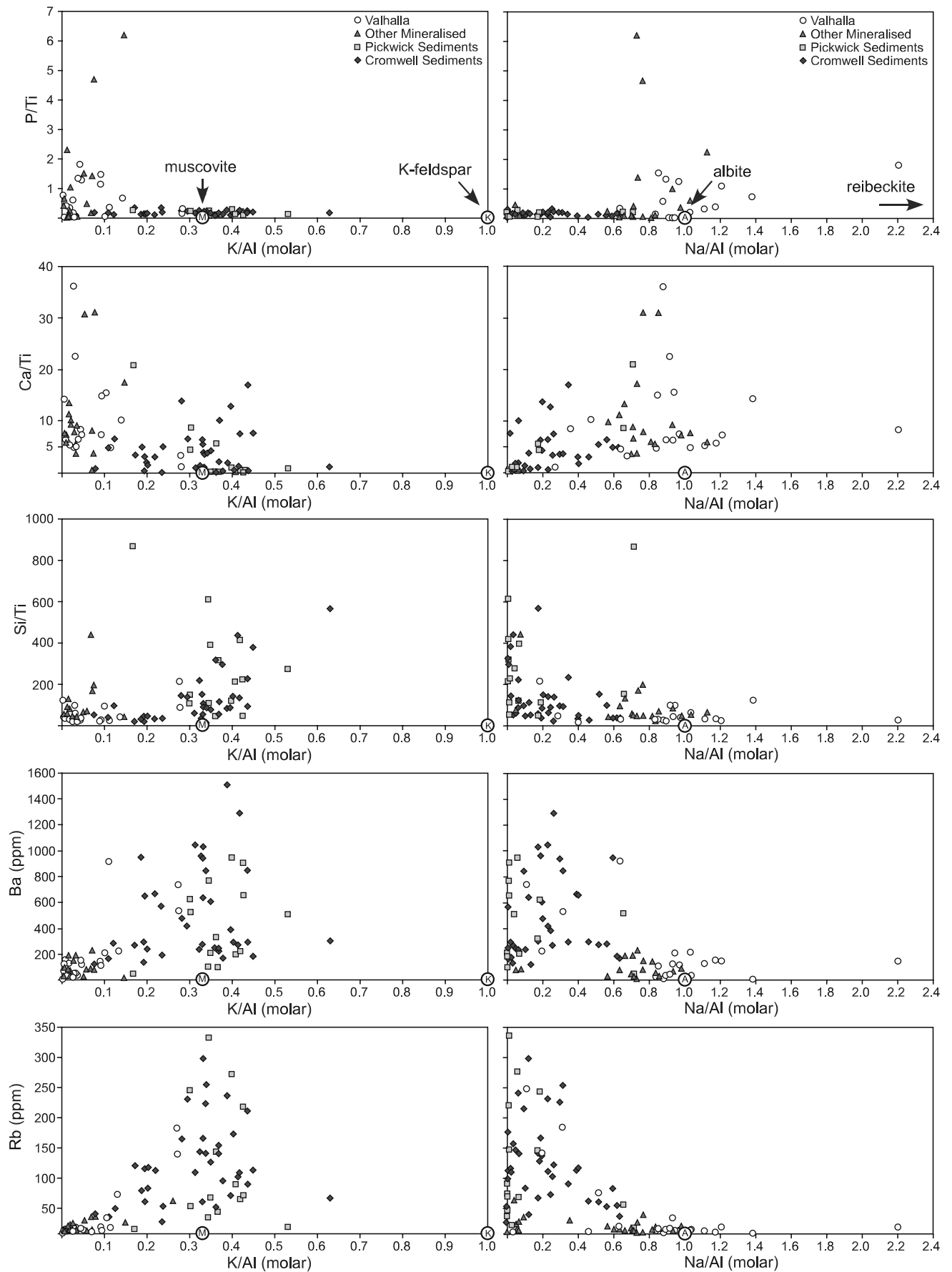


Fig. 11 GER (K/Al and Na/Al) versus PER (element/Ti) diagrams demonstrating that P and Ca addition and Si, Ba and Rb loss is associated with alteration that involved the destruction of K-feldspar and muscovite and the formation of albite and reibeckite. Some samples do not appear on all diagrams because they occur at concentrations below the detection limit. *m* Muscovite; *a* albite; *k* K-feldspar

close to the lower intercept on the Concordia curve. The lower intercept age of 175 ± 13 Ma is indistinguishable from the majority of U–Pb chemical ages determined for U^2 uraninite, suggesting that a major resetting event occurred at this time. High discordance, high error margins and high MSWD values are primarily due to the refractive nature of uraniferous minerals (Romberger 1984) and variable Pb loss from uraninite/brannerite after formation. Therefore, although the $1,564 \pm 27$ Ma U–Pb age is within error of the $1,543 \pm 15$ Ma $^{207}\text{Pb}/^{206}\text{Pb}$ age (Table 6), it is likely to be less accurate than the two oldest $^{207}\text{Pb}/^{206}\text{Pb}$ ages because $^{207}\text{Pb}/^{206}\text{Pb}$ ages in uranium minerals are more reliable than U–Pb ages (Kotzer and Kyser 1993; Burns 1999; Kyser et al. 2003).

Six of 14 LA-HR-ICPMS uraninite analyses define a U–Pb isocron with an upper intercept age of $1,222 \pm 26$ Ma and lower intercept age of 107 ± 11 Ma (Fig. 12). The upper intercept age is indistinguishable from the oldest $^{207}\text{Pb}/^{206}\text{Pb}$ age of $1,220 \pm 12$ Ma from uraninite and may represent structurally controlled fluid flow related to the assemblage of the proposed supercontinent, Rodinia. The lower intercept age is similar to that obtained from brannerite, suggesting that both minerals were subject to Pb-loss between 100 and 200 Ma. The other eight uraninite analyses do not define a meaningful isocron but suggest that a more recent event has caused further Pb loss from the uraninite (Fig. 12).

$^{40}\text{Ar}/^{39}\text{Ar}$ ages

Three reibeckite separates were extracted from DDH-V39 and analysed using the $^{40}\text{Ar}/^{39}\text{Ar}$ laser-heating technique of Lee et al. (1990). The reibeckite grains were handpicked under binocular microscope to ensure sample purity. Several milligrams of sample was irradiated and analysed to compensate for the small K content in this mineral (Table 1). The data and spectra for these samples are presented in Fig. 13 and Table 7.

One of the reibeckite separates (V39 281.0 m) has a disturbed spectra with an initial apparent age of $1,051 \pm 129$ Ma followed by individual step ages between $1,326 \pm 56$ and $1,566 \pm 11$ Ma (Table 7). No plateau age is evident, but an integrated age of $1,479 \pm 10$ Ma is within error of a total fusion Ar age of 1,460 Ma from amphibole in a splay related to the Mount Isa Fault Zone near Mica Creek, south of Mount Isa (Perkins et al. 1999). Numerous $^{40}\text{Ar}/^{39}\text{Ar}$ ages between 1,410 and 1,500 Ma come from biotite and amphibole from the Eastern Mount Isa Fold Belt, where peak metamorphism

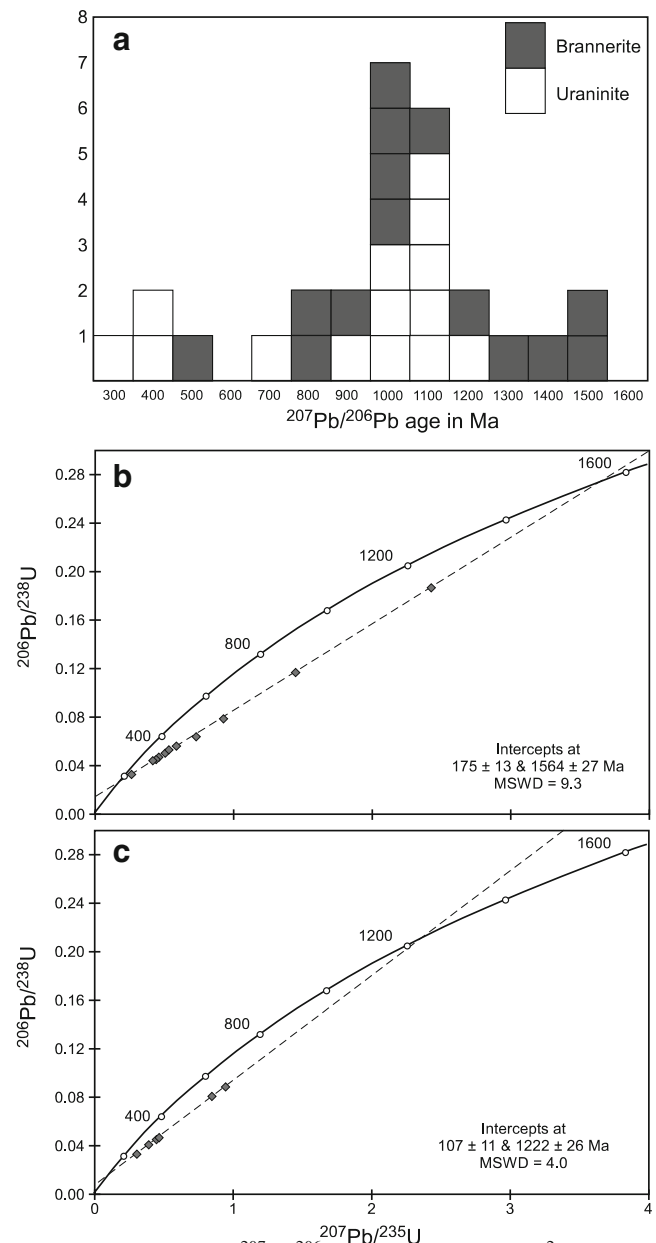


Fig. 12 a Histogram of $^{207}\text{Pb}/^{206}\text{Pb}$ ages obtained from B^2 brannerite and late alteration U^2 uraninite grains by LA-HR-ICPMS (Table 6). b U–Pb concordia diagrams from in situ isotopic analysis by LA-HR-ICPMS of B^2 brannerite from Valhalla. Data presented in Table 8. c U–Pb concordia diagrams from in situ isotopic analysis by LA-HR-ICPMS of U^2 uraninite from Valhalla. Plots were constructed using ISOPLOT (Ludwig 1993) from the isotope ratios presented in Table 6

reached upper amphibolite facies (Spikings et al. 2001). These ages have been attributed to reactivation of major fault zones during post-Isan exhumation.

A second reibeckite separate (V39 267.4 m), also with a disturbed spectra, has an initial apparent age of $1,099 \pm 85$ Ma and a final step age of $1,985 \pm 15$ Ma. Three consecutive individual steps representing 57.3% of ^{39}Ar released from the sample form a pseudo-plateau age of $1,533 \pm 9$ Ma which is within error of the oldest $^{207}\text{Pb}/^{206}\text{Pb}$ age of $1,543 \pm 15$ Ma

Table 6 LA-HR-ICPMS acquired U–Pb and isotopic data from uraninite and brannerite from Valhalla with calculated $^{235}\text{U}/^{207}\text{Pb}$, $^{238}\text{U}/^{206}\text{Pb}$ and $^{207}\text{Pb}/^{206}\text{Pb}$ ages

Sample no.	Mineral	Isotopic ratios			Calculated ages (Ma ^a)		
		$^{207}\text{Pb}/^{235}\text{U}$	$^{206}\text{Pb}/^{238}\text{U}$	$^{207}\text{Pb}/^{206}\text{Pb}$	$^{207}\text{Pb}/^{235}\text{U}$	$^{206}\text{Pb}/^{238}\text{U}$	$^{207}\text{Pb}/^{206}\text{Pb}$
DDH V39 294.1 m	Uraninite	0.02698	0.20577	0.05336	172	190	344
DDH V39 294.1 m	Uraninite	0.00862	0.06287	0.05609	55	62	456
DDH V39 294.1 m	Uraninite	0.00472	0.03672	0.05629	30	37	463
DDH V39 294.1 m	Uraninite	0.03281	0.29382	0.06284	208	262	703
DDH V39 294.1 m	Uraninite	0.00244	0.02287	0.06916	16	23	903
DDH V39 294.1 m	Uraninite	0.04063	0.38637	0.07288	244	332	1011
DDH V39 294.1 m	Uraninite	0.04599	0.45486	0.07407	281	381	1043
DDH V39 294.1 m	Uraninite	0.00141	0.01415	0.07447	9	14	1054
DDH V39 294.1 m	Uraninite	0.04500	0.44010	0.07651	284	370	1109
DDH V39 294.1 m	Uraninite	0.08016	0.84282	0.07653	497	621	1109
DDH V39 294.1 m	Uraninite	0.00106	0.01115	0.07656	7	11	1110
DDH V39 294.1 m	Uraninite	0.08812	0.93754	0.07746	544	672	1133
DDH V39 294.1 m	Uraninite	0.00117	0.01276	0.07774	8	13	1140
DDH V39 294.1 m	Uraninite	0.00234	0.02175	0.08093	15	22	1220
DDH V39 304.1 m	Brannerite	0.03319	0.26336	0.05947	212	237	584
DDH V39 304.1 m	Brannerite	0.05039	0.46095	0.06644	317	385	820
DDH V39 304.1 m	Brannerite	0.04443	0.41655	0.06829	280	354	877
DDH V39 304.1 m	Brannerite	0.04691	0.45994	0.07120	296	384	963
DDH V39 304.1 m	Brannerite	0.05050	0.50782	0.07294	318	417	1012
DDH V39 304.1 m	Brannerite	0.05317	0.53434	0.07299	334	435	1014
DDH V39 304.1 m	Brannerite	0.05649	0.58547	0.07417	354	468	1046
DDH V39 304.1 m	Brannerite	0.04532	0.44629	0.07579	286	375	1090
DDH V39 304.1 m	Brannerite	0.04850	0.51885	0.07774	305	424	1140
DDH V39 304.1 m	Brannerite	0.06388	0.73258	0.08327	399	558	1275
DDH V39 304.1 m	Brannerite	0.07891	0.92856	0.08542	490	667	1325
DDH V39 304.1 m	Brannerite	0.06302	0.78971	0.09095	394	591	1446
DDH V39 304.1 m	Brannerite	0.11737	1.44958	0.09409	715	910	1510
DDH V39 304.1 m	Brannerite	0.18692	2.42669	0.09575	1105	1251	1543

^a $^{206}\text{Pb}/^{238}\text{U}$, $^{207}\text{Pb}/^{235}\text{U}$ and $^{207}\text{Pb}/^{206}\text{Pb}$ ages calculated using equations reported by Ludwig (1993).

obtained from brannerite. The third rebeckite separate (V39 255.0 m) forms a six-step plateau age of $1,551 \pm 7$ Ma (84.0% of ^{39}Ar released; Fig. 13; Table 7). The two $^{40}\text{Ar}/^{39}\text{Ar}$ ages of $1,551 \pm 7$ and $1,533 \pm 9$ Ma are indistinguishable from the oldest $^{207}\text{Pb}/^{206}\text{Pb}$ ages from Valhalla brannerite and overlap the timing of peak metamorphism in the Mount Isa area (Page and Bell 1986; Connors and Page 1995; Betts et al. 2006).

Stable isotopic compositions of calcite, dolomite and rebeckite

Two samples of pure rebeckite have $\delta^{18}\text{O}$ values of 7.1 and 8.9 per mil (Table 8; Fig. 14). Ten C^1 calcite samples have $\delta^{18}\text{O}$ values between 10.6 and 12.8 per mil (Table 9; Fig. 15). The calcite and rebeckite are cogenetic and can therefore be used as geothermometers using the isotopic fractionation factors of Zheng (1993, 1999). These equations reveal that the calcite and rebeckite formed between 340 and 380°C, in

agreement with temperature calculations from peak metamorphic, sub-greenschist facies assemblages in the area (Rubenach 1992). At this temperature, the rebeckite and calcite formed in equilibrium with a fluid having $\delta^{18}\text{O}_{\text{fluid}}$ values between 6.5 and 9.1 per mil (Tables 8 and 9).

Four rebeckite samples have δD values between -147 and -103 per mil and structural H_2O contents of 1.6 and 2.1 wt% (Table 8), the latter within the ideal range for pure amphibole. Assuming a formation temperature of $360 \pm 20^\circ\text{C}$, the rebeckite formed in equilibrium with fluids having a $\delta\text{D}_{\text{fluid}}$ value between -98 and -54 per mil (Fig. 14). The ten C^1 calcite samples have $\delta^{13}\text{C}$ values between -2.8 and -0.7 per mil (Fig. 14; Table 9). Carbonate in albitite-hosted U deposits is thought to source C from CO_2 (Tugarinov 1980; Belevtsev 1980). At $360 \pm 20^\circ\text{C}$, the calcite most likely precipitated from a CO_2 -bearing fluid having a $\delta^{13}\text{C}_{\text{fluid}}$ value between -0.3 and 1.7‰ (Table 9; Fig. 15).

Seven D^2 dolomite samples have $\delta^{18}\text{O}$ values between 16.0 and 23.6 per mil and $\delta^{13}\text{C}$ values between -2.4 and -1.3 per mil (Fig. 15; Table 9). The relatively high $\delta^{18}\text{O}$

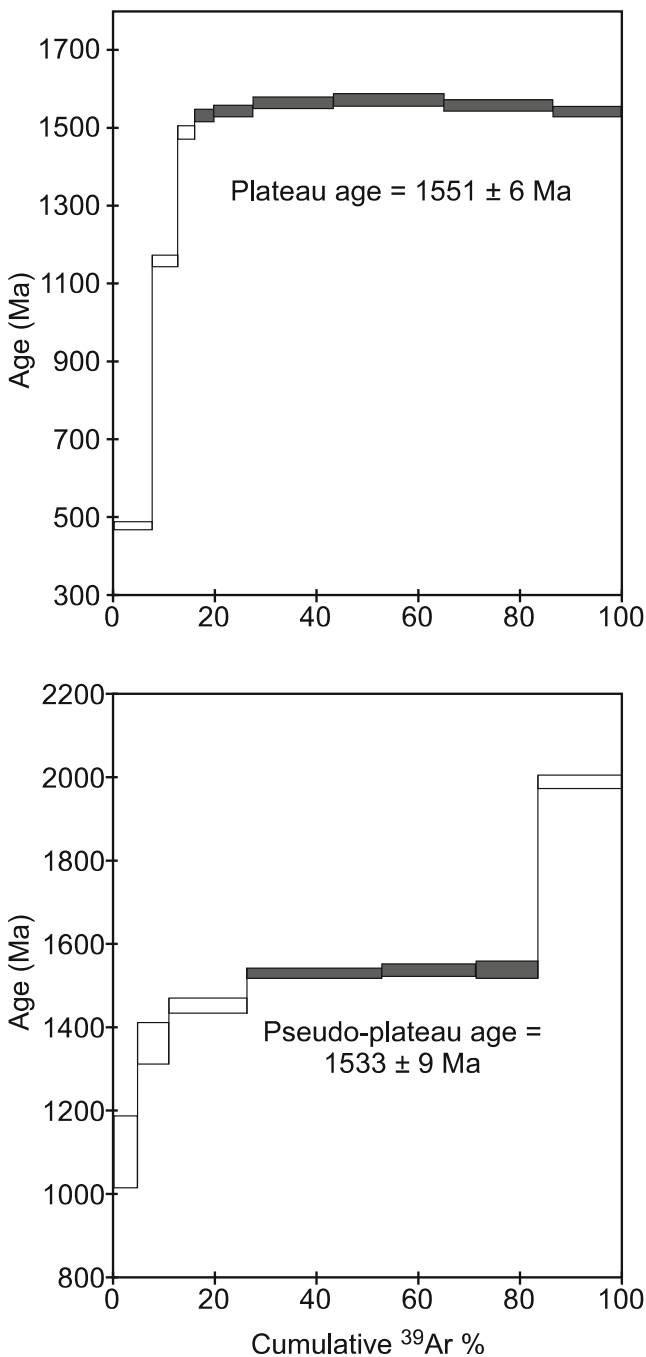


Fig. 13 $^{40}\text{Ar}/^{39}\text{Ar}$ age spectra for two samples of reibeckite from Valhalla. **a** DDH V39 255.0 m. **b** DDH V39 267.0 m. Data from Table 7

values suggest formation at temperatures much lower than $360 \pm 20^\circ\text{C}$. Dolomite veins with $\delta^{18}\text{O}$ values between 16 and 28 per mil are common in calcareous sediments and Zn–Pb deposits throughout the Mount Isa Basin and are known to have formed between 50 and 200°C (McGoldrick et al. 1998; Lindsay and Brasier 2000; Polito et al. 2006). Formation of the late D^2 dolomite between 50 and 200°C would be in agreement with temperature estimates between

70 and 160°C which have been calculated for a mineral assemblage comprising uraninite, chlorite, hematite and dolomite in many Ukrainian albitite-hosted U deposits (Kalyaev 1980; Belevtsev 1980).

Comparison with unconformity-style uranium and IOCG deposits

Previous workers have likened the Mount Isa U deposits to (1) unconformity-style U deposits (Gregory et al. 2005) and (2) Cu-poor IOCG deposits (Hitzman and Valenta 2005), but neither of these deposit styles is supported by the findings reported here. Gregory et al. (2005) proposed that the Anderson’s Lode, Eldorado and Lucky Break prospects formed when uranium in an oxidised fluid interacted with a reduced mineral assemblage near the unconformity above the Eastern Creek Volcanics at the base of the Surprise Creek Formation. These authors went on to conclude that these uranium deposits are therefore metamorphosed equivalents of Proterozoic unconformity-type uranium deposits found elsewhere in northern Australia. In their argument, Gregory et al. (2005) report that uranium mineralisation formed before peak metamorphism in the Western Succession of the Mount Isa Basin. However, neither Valhalla nor any of the other eight U deposits lithochemically investigated in this study have an alteration assemblage comprising syn-ore hematite, sericite (\pm phengite), chlorite or uraninite like that found in unconformity-type U deposits in either Australia or Canada (Wilde and Wall 1987; Kotzer and Kyser 1991; Fayek and Kyser 1997; Polito et al. 2005), and geochronological evidence shows that Valhalla formed during metamorphism, not before.

In a genetic sense, it is mere happenstance that the Myally Subgroup and the Surprise Creek Formation unconformably overlay the Eastern Creek Volcanics, and in any case, it has not been demonstrated that any of the Western Succession uranium deposits formed at the boundary between the Eastern Creek Volcanics and overlying clastic sediments. Further, neither the Myally Subgroup nor the Surprise Creek Formation have the diagenetic and geochemical complexities that are features in the sandstones and conglomerates that overlie the Australian and Canadian unconformity-type U deposits (Kotzer and Kyser 1991; Fayek and Kyser 1997; Alexandre et al. 2005; Polito et al. 2006). These complexities include (1) the presence of diagenetic illite, chlorite and dickite in the clastic sediments that occur regionally, directly above and immediately surrounding unconformity-type U deposits. These diagenetic phyllosilicates are uncommon in the Myally Subgroup and the Surprise Creek Formation due to the occurrence of early-formed porosity occluding quartz overgrowths (Polito et al. 2006). (2) The diagenetic phyllosilicates that occur basin-wide in the sediments

Table 7 Individual spot fusion ages, argon isotope ratios, per cent ^{40}Ar atmospheric contents and per cent ^{39}Ar released from reibeckite from Valhalla

$^{36}\text{Ar}/^{40}\text{Ar}$	$^{39}\text{Ar}_k/^{40}\text{Ar}$	Ca/K	^{40}Ar atm, %	^{39}Ar , %	$^{40}\text{Ar}/^{39}\text{Ar}$	Age (Ma)
DDH V39-281.0, reibeckite; Integrated age = 1,479±0 Ma						
0.00249	0.00975	67.3	73.57	4.47	27.10	1051±129
0.00062	0.02199	146.3	18.24	7.91	37.17	1325.6±56
0.00023	0.02164	11.0	6.81	39.21	43.06	1468±10
0.00005	0.02081	7.9	1.48	32.63	47.35	1566±11
0.00038	0.02217	5.9	11.23	4.78	40.04	1397±77
0.00017	0.02171	5.0	4.94	1.70	43.78	1485±212
0.00038	0.01912	5.4	11.18	9.30	46.45	1546±40
DDH V39-267.0, reibeckite; pseudo-plateau age = 1,533±9 Ma						
0.00226	0.01162	6.5	66.58	4.79	28.74	1099±85
0.00066	0.02090	17.5	19.60	5.97	38.47	1358±49
0.00017	0.02253	11.7	4.96	15.56	42.19	1448±17
0.00005	0.02163	13.3	1.51	26.47	45.53	1525±11
0.00002	0.02164	12.5	0.70	18.49	45.88	1533±14
0.00009	0.02119	4.9	2.68	12.34	45.92	1534±19
0.00007	0.01424	7.1	2.18	16.38	68.68	1985±15
DDH V39-255.0, reibeckite; plateau age = 1,551±7 Ma						
0.00094	0.06946	0.6	27.60	7.59	10.41	479±4
0.00020	0.03052	18.4	5.83	5.05	30.86	1159±6
0.00018	0.02155	30.5	5.42	3.35	43.89	1488±7
0.00012	0.02108	9.9	3.49	3.80	45.79	1532±6
0.00006	0.02117	1.7	1.89	7.63	46.34	1544±6
0.00003	0.02097	1.1	0.85	15.87	47.28	1565±6
0.00001	0.02093	0.5	0.41	21.76	47.59	1572±6
0.00002	0.02120	0.2	0.49	21.37	46.94	1558±6
0.00001	0.02156	0.2	0.44	13.58	46.19	1541±5

overlying the unconformity-type U deposits have isotopic values that are identical to those obtained from syn-ore minerals in the U deposits, suggesting a genetic link exists between the two (Kotzer and Kyser 1991; Kyser et al. 2000; Polito et al. 2005; Alexandre et al. 2005). Illite and chlorite extracted from the Myally Subgroup and the Surprise Creek Formation have $\delta^{18}\text{O}_{\text{fluid}}$ and $\delta\text{D}_{\text{fluid}}$ values that are distinct from syn-ore minerals in the Valhalla deposit (Polito et al. 2006). (3) Illite from the clastic sediments that occur regionally in the basins hosting unconformity-type U deposits records a range of $^{40}\text{Ar}/^{39}\text{Ar}$ ages, but most correspond to the timing of U precipitation

in the deposits (Kyser et al. 2000; Polito et al. 2005). $^{40}\text{Ar}/^{39}\text{Ar}$ ages from diagenetic illite extracted from the Surprise Creek Formation in the southern Mount Isa basin range between 1,672±9 and 1,680±23 Ma, older than U precipitation at Valhalla but coincident with intrusion by the Sybella Granite (1,671±8 Ma), extrusion of the regionally occurring Carters Bore Rhyolite (1,678±2 Ma) and uplift and erosion that marks the unconformity between the Calvert and Isa Superbasins (Polito et al. 2006). Younger $^{40}\text{Ar}/^{39}\text{Ar}$ ages around 1,450 Ma are recorded by illite extracted from fractures in the Myally Subgroup and the Surprise Creek Formation, but these have been

Table 8 Oxygen and hydrogen stable isotopic values for Mg–reibeckite and co-genetic calcite with calculated formation temperatures and fluid values from Valhalla

Sample	Mineral	$\delta^{18}\text{O}$	$\delta^{18}\text{O}_{\text{fluid}}$	Temp	δD	$\delta\text{D}_{\text{fluid}}$	Yield H_2O
V39 281.0	Reibeckite	8.9	9.1	380°C	−103	−54	1.6
	Calcite	12.3					
V39 255.0	Reibeckite	7.1	6.8	340°C	−109	−60	1.9
	Calcite	11.3					
V39 321.6	Reibeckite				−127	−78	2.1
V39 267.4	Reibeckite				−147	−98	1.7

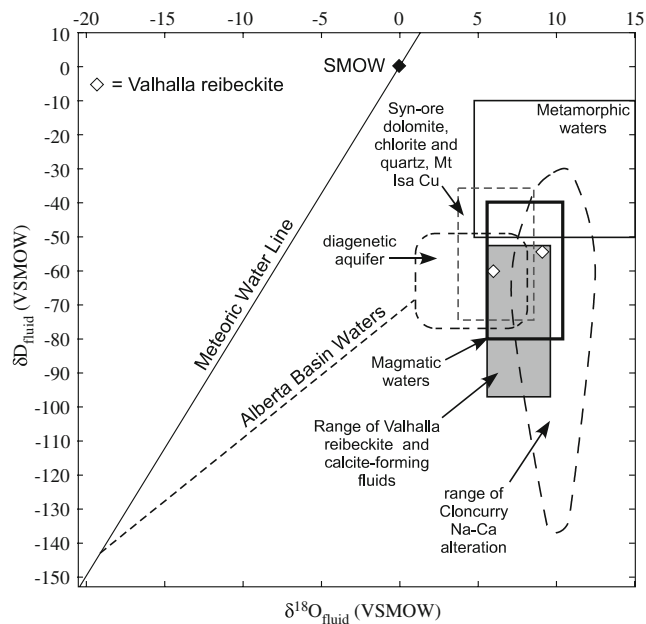


Fig. 14 Calculated $\delta^{18}\text{O}_{\text{fluid}}$ and $\delta\text{D}_{\text{fluid}}$ values for reibeckite from Valhalla. The values and calculations for each mineral are presented in Table 8. The grey polygon represents the range of $\delta\text{D}_{\text{fluid}}$ values determined for reibeckite and the $\delta^{18}\text{O}_{\text{fluid}}$ determined for reibeckite and syn-ore calcite in this study. For comparison, the diagenetic aquifer field was determined by Polito et al. (2006) from illite and chlorite extracted from the Mount Guide Quartzite diagenetic aquifer; the Na–Ca alteration range was determined by Mark et al. (2004b) from minerals in the Cloncurry district, the Mount Isa Cu syn-ore range was determined by Heinrich et al. (1989, 1995) from dolomite, chlorite and quartz and the metamorphic and magmatic waters fields are those presented by Rollinson (1993) and Taylor (1974). See Fig. 2 for stratigraphy of the Mount Isa basin

Table 9 Carbon and oxygen stable isotope data for syn-mineralisation C¹ calcite and late alteration D² dolomite from Valhalla

Sample	$\delta^{18}\text{O}$	$\delta^{13}\text{C}$	$\delta^{18}\text{O}_{\text{fluid}}$	$\delta^{13}\text{C}_{\text{fluid}}$
C¹ calcite				
V39 226.6	11.3	−0.7	6.9	1.7
V39 255.0	11.3	−2.8	6.9	−0.4
V39 272.0	12.8	−0.9	8.4	1.4
V39 281.0	12.3	−1.1	7.9	1.3
V39 295.8	12.8	−2.3	8.4	0.1
V39 304.1	11.4	−0.9	7.0	1.5
V39 320.2	11.5	−1.6	7.1	0.8
V39 333.9	10.6	−1.3	6.2	1.0
V39 259.5	11.6	−1.9	7.2	0.5
V39 285.7	12.7	−2.1	8.3	0.2
D² dolomite				
V39 207.0	20.8	−1.3	–	–
V39 230.9	20.9	−1.4	–	–
V39 235.6	21.1	−1.9	–	–
V39 245.7	16.0	−2.4	–	–
V39-267.4	23.6	−1.7	–	–
V39 292.9	20.1	−2.4	–	–
V39 294.1	19.9	−2.0	–	–

C¹ calcite fluid values calculated for 340 and 380°C
En dash (–) Value not calculated for this study

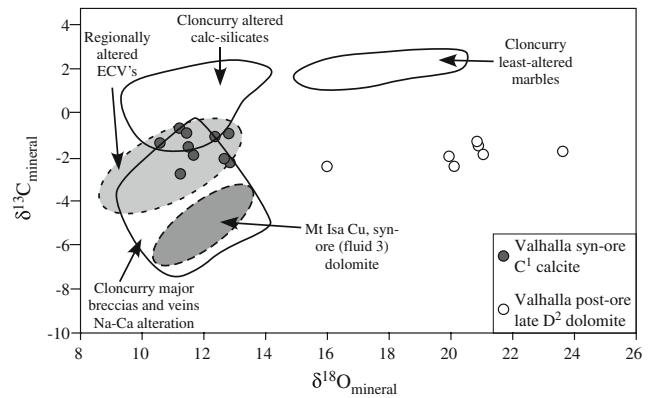


Fig. 15 $\delta^{13}\text{C}$ versus $\delta^{18}\text{O}$ diagram for syn-mineralisation C¹ calcite and late alteration D² dolomite from the Valhalla U deposit. The values are presented in Table 9. Fields of $\delta^{13}\text{C}$ and $\delta^{18}\text{O}$ values that represent various stages of 1,550–1,510 Ma alteration in the Cloncurry and Mount Isa district are shown for comparison with Valhalla C¹ calcite (Heinrich et al. 1989, 1995; Oliver et al. 1993, 2004; Marshall et al. 2006). The D² dolomite formed after the main stage of uranium mineralisation and cannot be compared with these fields

attributed to the end of the Isan Orogeny and reactivation of major fault zones related to post-Isan exhumation (Spikings et al. 2001; Polito et al. 2006), not any mineralisation event.

In regard to Cu-poor IOCG deposits, Valhalla shares some similarities with specific IOCG deposits, but further work will be needed to demonstrate any firm link to this class of mineralisation. Valhalla and IOCG's in the Eastern Succession both have a pre-mineralisation Na–Ca alteration assemblage (Mark et al. 2000, 2006a b; Pollard 2001; Oliver et al. 2004; Williams et al. 2005), and numerous IOCG deposits have anomalous P concentrations associated with the formation of apatite (Williams et al. 2005). However, Valhalla lacks the Fe-oxide-rich breccias that are typical of true IOCG deposits (Roberts and Hudson 1983; Hitzman et al. 1992; Reynolds 2000; Williams et al. 2005; Mark et al. 2006a, b). This study has demonstrated that most of Valhalla's modest Fe concentration (i.e. between 1.2 and 15.3% Fe) occurs in the form of reibeckite. In contrast, IOCG deposits such as Olympic Dam and Earnest Henry have Fe concentrations between 10 and 60 wt% in the form of hematite and magnetite (Roberts and Hudson 1983; Hitzman et al. 1992; Reynolds 2000; Mark et al. 2006a, b).

Comparison to Na–Ca alteration in the Eastern and Western Successions

Geochemical and geological assessment reveals that Valhalla is hosted by fine-grained sandstones, arkoses and gritty siltstones that are bound by the Eastern Creek Volcanics. The majority of the U-related alteration is

Table 10 A comparison between Valhalla and other albitite-hosted uranium deposits reported in the literature

Deposit (country)	Host rocks	Alteration assemblage	Deposit geochemistry (if reported)	Formation temperature	References
Valhalla (Australia)	siltstone and fine-grained sandstone derived from mafic volcanics	Early alteration: albite, riebeckite, calcite, brannerite. Syn-U alteration: brannerite, apatite, zircon, albite, riebeckite, calcite. Late alteration: uraninite, hematite, dolomite, chlorite, coffinite, quartz, galena, pyrite, Cu sulfides	Si (?), K, Ba, Rb loss; Na, Ca, U, Zr, P, V, Y and Sr enrichment. Th/U = 0.05.	340–380°C (isotope geothermometry)	This study
Several examples of unnamed albitite-hosted U deposits (Ukraine)	quartz-mica schist, quartz-carbonate gneiss, amphibolite, siltstone, mafic volcanics	Stage 1 alteration: albite, riebeckite or arfvedsonite, carbonate, magnetite, stilpnomelane, trace apatite, sphene and brannerite. Stage 2 U alteration: Albite, apatite, carbonate, zircon, hematite, pyrite, uraninite, uranium-titanate and brannerite. Late (barren) alteration: Aegirine, calcite, hematite, martite, talc. Late U alteration: uraninite, coffinite, calcite, dolomite, biotite, Fe oxides, epidote, chlorite, Fe–Cu–Pb sulphides	Si loss; Na, Ca, U, Zr, P, V, Y and Sr enrichment.	Stage 1 and 2 alteration 300–500°C. Late alteration 150–200°C	Kalyaev (1980); Tugarinov (1980); Zhukova (1980); Belevtsev (1980); Dahlkamp (1993)
Lagoa Real (Brazil)	Subalkaline granites and orthogneisses	Albite, pyroxene, garnet, uraninite, zircon, allanite, carbonate	Si, K, Rb loss; Na, Ca, Sr enrichment.	not speculated	Lobarto et al. (1983); Turpin et al. (1988)
Espinharas (Brazil)	Leucocratic granites and orthogneisses plus mesocratic biotite–amphibole paragneisses	Albite, riebeckite, chlorite, calcite, coffinite, apatite, Ti-silicates, xenotime	Si, K, Rb, Sr loss; Na, Ca, Fe, U, Th, Nb, Y and Pb enrichment. Th/U = 0.45.	not speculated	Porto da Silveira et al. (1991)
Skuppesavon (Sweden)	Metavolcanics of rhyolitic to trachytic composition	Early alteration: Albite, Ca-pyroxene, garnet, magnetite, epidote, amphibole. Syn-U alteration: uraninite, sphene, uranotitanites, hydroxy-Fe-oxides, calcite. Late alteration: Calcite, epidote, hematite, quartz, chlorite, galena	Si, K loss; Na, Ca, Al and U enrichment.	not speculated	Smellie and Laurikko (1984); Adamek and Wilson (1979)
Kurupung Batholith (Guyana)	monzogranite, syenite, episyenite	Albite, carbonate, chlorite, hydrothermal zircon, uraninite, Ti-U oxides.		250–350°C (fluid inclusions); 210–280°C (chlorite geochemistry)	Cinelua and Cuney (2006)

characterised by an early assemblage dominated by albite, Mg-riebeckite and calcite ± dolomite (albitite) and a syn-ore assemblage comprising brannerite, apatite, (uranoan) zircon and calcite ± albite ± riebeckite ± dolomite. The timing and nature of the early Na–Ca alteration that characterises the Valhalla U deposit is similar to that associated with the Na–Ca alteration that is widespread throughout the Eastern Succession of the Mount Isa Basin

(Fig. 1; de Jong and Williams 1995; Mark 1998, 2004a; Mark and Foster 2000; Oliver et al. 2004; Mark et al. 2006a; Marshall et al. 2006) and a comparison is warranted.

Most cases of Na–Ca alteration in the Eastern Succession is associated with shear zones, veins and breccias, similar to those identified at Valhalla. Na–Ca alteration in the Cloncurry region is also characterised by albite, amphibole and calcite ± titanate ± apatite ± quartz ±

pyroxene. U mineralisation associated with Na–Ca alteration in the Cloncurry region is locally anomalous but never reaches ore grades. U–Pb ages from titanite extracted from albitites in the Cloncurry region (1,555±9 to 1,521±5 Ma; Mark et al. 2006a; Oliver et al. 2004b) are identical to the $^{40}\text{Ar}/^{39}\text{Ar}$ and $^{207}\text{Pb}/^{206}\text{Pb}$ ages between 1,551±7 and 1,510±15 Ma obtained from Valhalla syn-ore minerals. All of these ages overlap the time when several phases of the Williams Suite intruded into the Eastern Succession (1,545–1,500 Ma; Page and Sun 1998; Pollard et al. 1998) and pegmatites intruded the southern portion of the Western Succession (1,532±7 Ma; Connors and Page 1995).

Before the advent of the U–Pb ages in the Eastern Succession, the source fluid responsible for the regional Na–Ca alteration was openly debated. The majority of the dialogue was based on (1) stable isotope evidence, (2) the need to mobilise large volumes of NaCl-rich fluids and (3) spatial relationships between granites and albitites. Oliver et al. (1993) first proposed that to form intense albitisation in the Mary Kathleen belt (Fig. 1), a highly saline fluid was required. They subsequently appealed to selective dissolution of pure halite layers from buried meta-evaporites to explain the salinities required. At the same time, however, these authors noted that calcite from the most altered albitites had $\delta^{18}\text{O}$ and $\delta^{13}\text{C}$ values (Fig. 15) that were in disequilibrium with a metacarbonate-evaporite source and in agreement with magmatic values, although an obvious igneous source was not apparent in the Mary Kathleen belt. Recent geochronological data (Oliver et al. 2004; Mark et al. 2006a) now indicates that metamorphism associated with the onset of the Isan Orogeny in the Eastern Succession at 1,600 Ma could have produced highly saline fluids from evaporates, resulting in the formation of albitite, but only at the ca. 1,600 Ma Osborne deposit. Saline fluids could not have been derived from meta-evaporites between 1,550 and 1,500 Ma because the evaporite salt should have been sequestered into scapolite in amphiboles by the 1,600–1,665 Ma thermal event (Oliver et al. 2004). New stable isotope data and the spatial association between Na–Ca alteration and intrusions of the same age has now been cited as evidence that albitisation in the Eastern Succession formed in response to fluids released during magma crystallisation (Figs. 14 and 15; Mark and Foster 2000; Perring et al. 2000; Pollard 2001; Mark et al. 2004b, 2006a; Oliver et al. 2004; Marshall et al. 2006).

Na–Ca alteration at Valhalla is not spatially associated with intrusions of the same age; syn-orogenic magmatism in the Western Succession is limited to a few pegmatite veins approximately 17 and 44 km to the south of Valhalla (Connors and Page 1995). However, stable isotopic fingerprinting of the early Na–Ca alteration (LIAR) and the later syn-ore U-related alteration (BIAR) at Valhalla reveals that these alteration assemblages formed from fluids having

$\delta^{18}\text{O}_{\text{fluid}}$ values of $7.2\pm 1.9\%$, $\delta\text{D}_{\text{fluid}}$ values of $-76\pm 22\%$ and $\delta^{13}\text{C}_{\text{fluid}}$ values of $1.1\pm 0.7\%$ (Tables 6 and 7; Figs. 14 and 15), similar to values obtained from Na–Ca metasomatised rocks in the Eastern Succession (Mark et al. 2004b; Oliver et al. 1993, 2004; Marshall et al. 2006). This suggests that mineralisation at Valhalla may be related to an unknown intrusive at depth. However, a magmatic origin for 1,550–1,500 Ma fluids in the Western Succession is at odds with the conclusions drawn by Hannan et al. (1993) and Heinrich et al. (1989, 1995), who report stable isotope data from the 1,540 Ma Mount Isa Cu ore body that is indistinguishable from that recorded at Valhalla (Fig. 1).

Syn-ore dolomite, chlorite and quartz (NaCl-dominated, fluid 3; Heinrich et al. 1989, 1995) from the Mount Isa Cu deposit and regional carbonate alteration in the Eastern Creek Volcanics record isotopic fluid values that are indistinguishable if not identical to those obtained from Valhalla (Figs. 14 and 15). Heinrich et al. (1995) proposed that the fluid that altered the metabasalts was identical to that which formed the Mount Isa Cu deposit, with the difference in $\delta^{13}\text{C}$ values attributed to equilibration between the introduced fluid and the host rocks. These authors dismiss a magmatic origin for the fluids, and in consideration of high Br/Cl ratios that were obtained from syn-ore fluid inclusions, appealed to fluids derived during metamorphic dehydration from an evaporite-bearing sedimentary sequence, and highly evolved basin brines of meteoric origin, as the most likely source for the ore forming fluids. Such fluids could have originated in the underlying Bottletree Formation and the lower Mount Guide Quartzite (Fig. 2; Polito et al. 2006), both proximal fluvial packages that had the potential to release large volumes of fluid during dehydration reactions associated with metamorphism.

The Bottletree Formation and the lower Mount Guide Quartzite contain variable but commonly anomalous concentrations of U (up to 22 and 9.5 ppm, respectively), Zr (1100 and 396 ppm), V (30 and 322 ppm), Y (78 and 98 ppm), P_2O_5 (0.53 and 0.18%) and Sr (500 and 207 ppm), all of which are anomalous at Valhalla. Before the Isan Orogeny, the Bottletree Formation and the lower Mount Guide Quartzite contained large volumes of diagenetic illite and chlorite (Polito et al. 2006). Assuming this illite and chlorite initially contained ca. 8 and 16 wt% structural water, respectively, and comprised up to 20% of the total rock mass, metamorphism to greenschist and amphibolite facies south and east of the Mount Isa township during the Isan Orogeny could have resulted in muscovite (4 wt% structural water), crystalline chlorite (10–12 wt% structural water) and the release of large volumes of fluid. Evidence for a fluid originating in the Bottletree Formation and Mount Guide Quartzite may come from muscovite in the lower Mount Guide Quartzite that has a δD value of -78 ± 12 per mil (Polito et al. 2006).

Water derived from this illite would have generated metamorphic fluids with δD_{fluid} values within range of those obtained from the syn-ore amphibole at Valhalla. However, the $\delta^{18}\text{O}_{\text{fluid}}$ values generated from this illite were probably higher than that indicated by the reibeckite and calcite from Valhalla, suggesting that another fluid, such as a magmatic fluid, was probably involved. Based on these results, it is proposed that the U-bearing fluids that formed Valhalla and other Mount Isa basin U deposits originated from the Bottletree Formation and the lower Mount Guide Quartzite during metamorphism, but a second fluid needed to be involved and this may have been of magmatic origin.

Comparison to other albitite-hosted uranium deposits

Despite the convincing likeness between alteration at Valhalla with that in the Eastern Succession, the characteristics that define Valhalla are indistinguishable from those that characterise albitite-hosted uranium deposits in the Ukraine, Sweden, Brazil and Guyana (Table 10; Adamek and Wilson 1979; Kalyaev 1980; Tugarinov 1980; Zhukova 1980; Belevtsev 1980; Lobato et al. 1983; Smellie and Laurikko 1984; Turpin et al. 1988; Porto da Silveira et al. 1991; Cinelua and Cuney 2006). Where detailed paragenetic studies are documented, the main stage of uranium mineralisation is always preceded by a Na–Ca metasomatic stage and typically followed by a late, weaker, uranium stage dominated by hematite, carbonate, quartz, chlorite, Fe–Cu–Pb–sulfides \pm uraninite or coffinite similar to that described at Valhalla (Table 10; Anonymous 1980; Tugarinov 1980; Smellie and Laurikko 1984; this study). In all cases, the main stage of uranium mineralisation is characterised by the precipitation of brannerite or uraninite plus uranium-titanites, apatite, zircon or xenotime and carbonate, commonly as calcite.

The host rocks for these albitite-hosted deposits vary widely. In some cases, the original host rocks before Na–Ca alteration are unrecognisable due to post-mineralisation deformation (e.g. Lagoa Real and Espinharas), but elsewhere, quartz-mica schists, quartz-dolomite gneisses, felsic tuffs, amphibolites, siltstones, fine-grained sandstones, (epi-) syenites and mafic volcanics are all documented hosts (Table 10). Geothermometric studies show that the early Na–Ca alteration and the main-stage of uranium mineralisation consistently forms between 250 and 500°C, with most temperatures clustering between 300 and 400°C (Anonymous 1980; Tugarinov 1980; Belevtsev 1980; Cinelua and Cuney 2006; this study). When whole rock geochemistry is reported, albitite-hosted uranium deposits show depletion in Si, K, Ba and Rb relative to the host rocks and enrichment in Na, Ca, U, Zr, P, V, Y and Sr (Table 10). The introduction of Ti with the mineralising

fluid is not supported by any of the petrological observations or geochemical modelling. At Valhalla, Ti was likely introduced as part of a detrital phase, primarily titanomagnetite, that originated in the Eastern Creek Volcanics before mineralisation.

The nature and origin of the fluids that formed the deposits other than Valhalla is rarely documented and, in most cases, speculative. However, based on consistent Th/U ratios $\ll 1$ (Tugarinov 1980; Smellie and Laurikko 1984; Porto da Silveira et al. 1991; this study), it appears that the ore transporting fluid was relatively oxidised (Romberger 1984). Further, the occurrence of hydrothermal zircon and xenotime suggests that the ore transporting fluid comprised B, F^- or PO_4^{3-} complexes (Giere 1990; Rubin et al. 1993), the later specifically required to transport Zr to the site of deposition. The occurrence of apatite and high fluorine reibeckite at Valhalla supports a fluid containing F^- and PO_4^{3-} complexes (Table 1).

An outline origin for the mineralisation at Valhalla

Despite similarities with Na–Ca alteration in Eastern Succession and comparisons to unconformity-type U deposits and iron oxide copper–gold deposits, the Valhalla uranium deposit compares best with albitite-hosted uranium deposits in the Ukraine, Sweden, Brazil and Guyana and is therefore classified as such. Our favoured model for Valhalla, and subsequently for most deposits in the Western Succession, involves the transportation of U, Zr, P, F, V, HREE \pm LREE in a Na–Ca-dominated fluid that has basinal and magmatic fluid characteristics. Mixing between two fluids during peak metamorphism appears to have occurred. Geochronological evidence and a detailed paragenetic study places the timing of the main stage of mineralisation between 1,555 and 1,510 Ma, coincident with the timing of the Isan Orogeny. Subsequent mineralisation dominated by uraninite instead of brannerite formed from a fluid that was able to mobilise LREE and U at relatively low temperatures. This style of mineralisation formed much later in the regions history, probably coincident with the assemblage and break-up of Rodinia.

This study has demonstrated that albitite-hosted deposits:

1. Exist in the Western Succession of the Mount Isa basin in Australia
2. Form at relatively high temperatures, apparently during peak metamorphism
3. Are likely to contain high grades of mineralisation in zones of brecciation
4. Have a distinct paragenesis that involves the formation of an early, syn and late stage of alteration

5. Have a distinct mineralogy that can be modelled geochemically in PER/GER space
6. Are characterised by Na, U, V, Zr, P, Sr, Y and Ca addition, and K, Si, Rb and Ba loss.

Acknowledgements This paper was jointly funded by Cameco Corporation, and an NSERC Collaborative Research Development grant to TKK. We are indebted to Alan Eggers of Summit Resources who permitted collection of drill core from the core storage facility in Mount Isa. The authors would like to thank Kurt Barnett for field assistance. Peter Jones and Lew Ling kindly assisted with the electron microprobe analyses at Carleton University, Ottawa. Kerry Klassen, April Vulletich, Don Chipley and Paul Alexander are thanked for help with stable and radiogenic isotope analyses at the Queen's University Facility for Isotope Research. The authors would like to thank Nick Oliver, Michel Cuney and Gary Davidson for their constructive comments that helped to improve the clarity and focus of this paper.

References

- Adamek PM, Wilson MR (1979) The evolution of a uranium province in northern Sweden. *Proc R Soc Lond* 291:355–368
- Alexandre P, Kyser K, Polito P, Thomas D (2005) Alteration mineralogy and stable isotope geochemistry of paleoproterozoic basement-hosted unconformity-type uranium deposits in the Athabasca Basin, Canada. *Econ Geol* 100:1547–1563
- Anonymous (1980) Hydrothermal uranium deposits of ancient shields. In: Abou-Zied S, Kerns G (eds) *Albitized uranium deposits: six articles translated from Russian literature*. United States Department of Energy, Grand Junction Office, Colorado, pp 15–34
- Belevtsev YN (1980) Endogenic uranium deposits of Precambrian shields: Environment of formation. In: Abou-Zied S, Kerns G (eds) *Albitized uranium deposits: six articles translated from Russian literature*. United States Department of Energy, Grand Junction Office, Colorado, pp 55–80
- Bell T (1983) Thrusting and duplex formation at Mount Isa, Queensland, Australia. *Nature* 304:493–497
- Betts PG, Giles D, Mark G, Lister GS, Goleby BR, Ailleres L (2006) Synthesis of the Proterozoic evolution of the Mt Isa Inlier. *Australian Journal of Earth Sciences* 53:187–211
- Blake DH (1987) Geology of the Mount Isa Inlier and environs, Queensland and Northern Territory. *BMR Bulletin* 225, pp 83
- Bottinga Y (1969) Calculated fractionation factors for carbon and hydrogen isotope exchange in the system calcite-carbon dioxide-graphite-methane-hydrogen-water vapour. *Geochim Cosmochim Acta* 33:49–64
- Bowles JFW (1990) Age dating of individual grains of uraninite in rocks from electron microprobe analyses. *Chem Geol* 83:47–53
- Brooks JH (1960) Uranium deposits of north western Queensland. Geological Survey of Queensland, Publication 297
- Brooks JH (1972) Uranium exploration in Queensland 1967/71. Geological Survey of Queensland, Report 69
- Brooks JH (1975) Uranium in the Mount Isa/Cloncurry District. In Knight CL (ed) *Economic Geology of Australia and Papua New Guinea: 1. Metals*. AIMM Monogr 5, pp 396–398
- Burns PC (1999) The crystal chemistry of uranium. In Burns PC, Finch R (eds) *Uranium: mineralogy, geochemistry and the environment*. *Rev Miner* 38:23–90
- Carr GR, Denton GJ, Korsch MJ, Gardner BL, Parr JM, Andrew AS, Whitford DJ, Wybom LAI, Sun S-S (2001) User friendly isotope technologies in mineral exploration: pb isotope applications, Northern Australian Proterozoic Basins. CSIRO Report No. 713C, p 127
- Cinélu S, Cuney M (2006) Sodic metasomatism and U–Zr mineralization: a model based on the Kurupung batholith (Guyana). *Geochim Cosmochim Acta* 70(Suppl 1):A103 (abstract)
- Clayton R, Mayeda TK (1963) The use of bromine pentafluoride in the extraction of oxygen from oxides and silicates for isotopic analysis. *Geochim Cosmochim Acta* 27:43–52
- Connors KA, Page RW (1995) Relationships between magmatism, metamorphism and deformation in the western Mount Isa inlier, Australia. *Precambrian Res* 71:131–153
- Dahlkamp FJ (1993) Uranium Ore Deposits. Springer-Verlag, Berlin Heidelberg, p 460
- De Jong G, Williams PJ (1995) Giant metasomatic system formed during exhumation of mid-crustal Proterozoic rocks in the vicinity of the Cloncurry Fault, northwest Queensland. *Aust J Earth Sci* 42:281–290
- Eggers AJ (1998) Exploration and assessment of the Valhalla uranium deposit Northwest Queensland. Australian Uranium Summit, extended abstracts, February 11–13 1998, Hyatt Hotel, Adelaide, South Australia, Australia, p 18
- Eggers AJ (1999) The Valhalla Uranium Project Northwest Queensland, an update. Australian Uranium Summit, extended abstracts, March 29–30 1999, Rydges Plaza Hotel, Darwin, Northern Territory, Australia, p 22
- Fayek M, Kyser TK (1997) Characterization of multiple fluid flow events and rare-earth-element mobility associated with formation of unconformity-type uranium deposits in the Athabasca Basin, Saskatchewan. *Can Mineral* 35:627–658
- Fayek M, Harrison TM, Grove M, Coath CD (2000) A rapid in situ method for determining the ages of uranium oxide minerals. *Int Geol Rev* 42:163–171
- Foster DRW, Rubenach MJ (2006) Isograd pattern and regional low-pressure, high-temperature metamorphism of pelitic, mafic and calc-silicate rocks along an east–west section through the Mt Isa Inlier. *Aust J Earth Sci* 53:167–186
- Giebmann U, Greb U (1994) High resolution ICP-MS—a new concept for elemental mass spectrometry. *Fresenius J Anal Chem* 350:186–193
- Giere R (1990) Hydrothermal mobility of Ti, Zr and REE: examples from the Bergell and Adamello contact aureoles (Italy). *Terra Nova* 2:60–67
- Giles D, Nutman AP (2002) SHRIMP U-Pb monazite dating of 1600–1580 Ma amphibolite facies metamorphism in the southeastern Mount Isa block, Australia. *Aust J Earth Sci* 49:455–466
- Graham CM (1981) Experimental hydrogen isotope studies, III: Diffusion of hydrogen in hydrous minerals and stable isotope exchange in metamorphic rocks. *Contrib Mineral Petrol* 76: 216–228
- Grant JA (1986) The isocon diagram— a simple solution to Gresen's equation for metasomatic alteration. *Econ Geol* 81:1976–1982
- Gregory MJ, Wilde AR, Jones PR (2005) Uranium Deposits of the Mount Isa Region and Their Relationship to Deformation, Metamorphism, and Copper Deposition. *Econ Geol* 100:537–546
- Hand M, Rubatto D (2002) The scale of the thermal problem in the Mount Isa Inlier. *Geoscience 2002: Expanding Horizons: Geological Society of Australia, Abstracts, 67, July 1–5 2002, Adelaide Convention Centre, Adelaide, South Australia, p 173*
- Hannan KW, Golding SD, Herbert HK, Krouse HR (1993) Contrasting alteration assemblages in metabasites from Mount Isa, Queensland; implications for copper ore genesis. *Econ Geol* 88:1135–1175
- Heinrich CA, Andrew AS, Wilkins RWT, Patterson DJ (1989) A fluid inclusion and stable isotope study of synmetamorphic copper ore formation at Mount Isa, Australia. *Econ Geol* 84:529–550
- Heinrich CA, Bain JH, Mernagh TP, Wybom LAI, Andrew AS, Waring CL (1995) Fluid and mass transfer during metabasalt alteration and copper mineralization at Mount Isa, Australia. *Econ Geol* 90:705–730

- Hitzman MW, Valenta R (2005) Uranium in iron oxide–copper–gold (IOCG) systems. *Econ Geol* 100:1657–1661
- Hitzman MW, Oreskes N, Einaudi MT (1992) Geological characteristics and tectonic setting of Proterozoic iron oxide (Cu–U–Au–REE) deposits. *Precambrian Res* 58:241–287
- Hutton LJ, Wilson IH (1985) 1:100,000 geological map commentary, Mammoth Mines region, Queensland. Bureau of Mineral Resources Geology and Geophysics, Australian Government, Canberra, p 26
- Jackson MJ, Scott DL, Rawlings DJ (2000) Stratigraphic framework for the Leichhardt and Calvert Superbasins: review and correlations of the pre-1700 Ma successions between Mt Isa and McArthur River. *Aust J Earth Sci* 47:381–403
- Kalyaev GI (1980) Mode of albitite distribution in zones of the Ukrainian Shield. In: Abou-Zied S, Kerns G (eds) Albitized uranium deposits: Six articles translated from Russian literature. United States Department of Energy, Grand Junction Office, Colorado, pp 1–14
- Kotzer TG, Kyser TK (1991) Retrograde alteration of clay minerals in uranium deposits: Radiation catalysed or simply low-temperature exchange? *Chem Geol* 86:307–321
- Kotzer TG, Kyser TK (1993) O, U and Pb isotopic and chemical variations in uraninite: Implications for determining the temporal and fluid history of ancient terrains. *Am Mineral* 78:1262–1274
- Kyser TK, O’Neil J (1984) Hydrogen isotope systematics of submarine basalts. *Geochim Cosmochim Acta* 48:48–53
- Kyser TK, Chipley D, Bukata A, Polito P, Fitzpatrick A, Alexandre P (2003) Application of laser ablation to high resolution ICPMS. *Can J Anal Sci Spectrosc* 48:258–268
- Kyser TK, Hiatt E, Renac C, Durocher K, Holk G, Deckart K (2000) Diagenetic fluids in Paleo- and Meso-Proterozoic sedimentary basins and their implications for long protracted fluid histories. In: Kyser TK (ed) Fluid and Basin Evolution: Mineralogical Association of Canada Short Course 28:255–262
- Lee JKW, Onstott TC, Hanes JA (1990) An $^{40}\text{Ar}/^{39}\text{Ar}$ investigation of the contact effects of dyke intrusion, Kapuskasing structural zone, Ontario: A comparison of laser microprobe and furnace extraction techniques. *Contrib Mineral Petrol* 105:87–105
- Lindsay JF, Braiser MD (2000) A carbon isotope reference curve for ca. 1700–1575 Ma, McArthur and Mount Isa Basins, Northern Australia. *Precambrian Res* 99:271–308
- Lobato LM, Forman JMA, Fyfe WS, Kerrich R, Barnett RL (1983) Uranium enrichment in Archean crustal basement associated with overthrusting. *Nature* 303:235–237
- Ludwig KR (1993) ISOPLOT: A plotting and regression program for radiogenic-isotope data: United States Geological Survey, Open File Report 91-445, pp 1–42
- Lumpkin GR, Leung SHF, Colella M (2000) Composition, geochemical alteration, and alpha-decay damage effects of natural brannerite. *Scientific Basis for Nuclear Waste Management XXIII, Symposium (Materials Research Society Symposium Proceedings)* 608:359–365
- Maas R, McCulloch MT, Campbell IH (1987) Sm–Nd isotope systematics in uranium-rare earth element mineralization at the Mary Kathleen uranium mine, Queensland. *Econ Geol* 82:1805–1826
- Madeisky HE, Stanley CR (1993) Litho-geochemical Exploration for Metasomatic Zones Associated with Volcanic-Hosted Massive Sulphide Deposits Using Pearce Element Ratio Analysis. *Int Geol Rev* 35:1121–1148
- Marshall LJ, Oliver NHS, Davidson GJ (2006) Carbon and oxygen isotope constraints on fluid sources and fluid wall rock interaction in regional alteration and iron-oxide-copper-gold mineralization, eastern Mt Isa Block, Australia. *Miner Depos* 40:429–452
- Mark G (1998) Albitite formation by selective pervasive sodic alteration of tonalite plutons in the Cloncurry district, NW Queensland. *Aust J Earth Sci* 45:765–774
- Mark G, Foster DRW (2000) Magmatic albite-actinolite-apatite rich rocks from the Cloncurry district, Northwest Queensland, Australia. *Lithos* 51:223–245
- Mark G, Oliver NHS, Williams PJ, Valenta RK, Crookes RA (2000) The evolution of the Ernest Henry hydrothermal system. In: Porter TM (ed) Hydrothermal iron oxide copper-gold and related deposits: A global perspective, Adelaide, Australian Mineral Foundation, pp 132–136
- Mark G, Williams PJ, Boyce AJ (2004a) Low-latitude meteoric fluid flow along the Cloncurry Fault, Cloncurry District, NW Queensland, Australia: geodynamic and metallogenic implications. *Chem Geol* 207:133–148
- Mark G, Foster DRW, Pollard PJ, Williams PJ, Tolman J, Darvall M, Blake KL (2004b) Stable isotope evidence for magmatic fluid input during large-scale Na–Ca alteration in the Cloncurry Fe oxide Cu–Au district, NW Queensland, Australia. *Terra Nova* 16: 54–61
- Mark G, Oliver, NHS, Williams PJ (2006a) Mineralogical and chemical evolution of the Ernest Henry Fe oxide-Cu-Au ore system, Cloncurry district, northwest Queensland, Australia. *Miner Depos* 40:769–801
- Mark G, Oliver, NHS, Carew MJ (2006a) Insights into the genesis and diversity of epigenetic Cu–Au mineralisation in the Cloncurry district, Mt Isa Inlier, northwest Queensland. *Aust J Earth Sci* 53:109–124
- McCrea T (1950) The isotopic chemistry of carbonates and a paleotemperature scale. *J Chem Phys* 18:849–857
- McGoldrick PJ, Kitto RA, Large RR (1998) Variation of carbon and oxygen isotopes in the alteration halo to the Lady Loretta deposit - implications for exploration and ore genesis. In: Arehart GB, Hulston JR (eds) Water rock interaction WRI-9, A. A. Balkema, pp 561–564
- McKay AD, Miezitis Y (2001) Australia’s uranium resources, geology and development of deposits. Australian Geological Survey Organisation, Geoscience Australia, Canberra, Mineral Resource Report 1, p 171
- Neumann N, Southgate PN, McIntyre A, Gibson G (2005) New Geochronology in the Mt Isa Inlier - constraining the evolution of Proterozoic sedimentary basins. Central Australian Basins Symposium Petroleum and Minerals Potential: Extended abstracts, Northern Territory Geological Survey, Alice Springs Convention Centre, August 16–18 2005, p 34
- Neumann N, Southgate PN, McIntyre A, Gibson G (2006) New SHRIMP geochronology for the Western Fold Belt of the Mount Isa Inlier: Developing a 1800–1650 Ma Event Framework. *Aust J Earth Sci* 53:1023–1039
- Oliver NHS (1995) The hydrothermal history of the Mary Kathleen fold belt, Mount Isa block, Queensland, Australia. *Aust J Earth Sci* 42:267–280
- Oliver NHS (1999) Mary Kathleen metamorphic-hydrothermal uranium-rare-earth element deposit: ore genesis and numerical model of coupled deformation and fluid flow. *Aust J Earth Sci* 46:467–484
- Oliver NHS, Cartwright I, Wall VJ, and Golding SD (1993) The stable isotopic signature of large-scale fracture-hosted metamorphic fluid pathways, Mary Kathleen, Australia. *J Metamorph Geol* 11:705–720
- Oliver NHS, Cleverley JS, Mark G, Pollard PJ, Fu B, Marshall LJ, Rubenach MJ, Williams PJ, Baker T (2004) The role of sodic alteration in the genesis of iron oxide-copper-gold deposits, eastern Mt Isa Block, Australia. *Econ Geol* 99:1145–1176
- O’Neil JR, Clayton RN, Mayeda TK (1969) Oxygen isotope fractionation in divalent metal carbonates. *J Chem Phys* 51:5547–5558
- Page RW (1983) Chronology of magmatism, skarn formation, and uranium mineralization, Mary Kathleen, Queensland, Australia. *Econ Geol* 78:838–853
- Page RW, Bell TH (1986) Isotopic and structural responses of granite to successive deformation and metamorphism. *J Geol* 94:365–379

- Page RW, Sun S-S (1998) Aspects of geochronology and crustal evolution in the Eastern fold belt, Mount Isa inlier. *Aust J Earth Sci* 45:343–362
- Page RW, Jackson MJ, Krassay AA (2000) Constraining sequence stratigraphy in the north Australian Basins: SHRIMP U-Pb zircon geochronology between Mt Isa and McArthur River. *Aust J Earth Sci* 47:431–459
- Pearce TH (1968) A Contribution to the Theory of Variation Diagrams. *Contrib Mineral Petrol* 19:142–157
- Pearce TH, Stanley CR (1991) The validity of Pearce Element Ratio analysis in petrology; An example from the Uwekahuna Laccolith, Hawaii. *Contrib Mineral Petrol* 108:212–218
- Perkins C, Heinrich CA, Wyborn LAI (1999) $^{40}\text{Ar}/^{39}\text{Ar}$ geochronology of copper mineralisation and regional alteration, Mt Isa, Australia. *Econ Geol* 94:23–36
- Perring CS, Pollard PJ, Dong G, Nunn AJ, Blake KL (2000) The Lightning Creek sill complex, Cloncurry district, northwest Queensland: A source of fluids for Fe oxide Cu-Au mineralization and sodic-calcic alteration. *Econ Geol* 95:1067–1089
- Polito PA, Kyser TK, Thomas D, Marlatt J, Drever G (2005) Re-evaluation of the petrogenesis of the Proterozoic Jabiluka unconformity-related uranium deposit, Northern Territory, Australia. *Miner Depos* 40:257–288
- Polito PA, Kyser TK, Southgate PN, Jackson MJ (2006) Sandstone Diagenesis in the Mount Isa Basin: An isotopic and fluid inclusion perspective in relation to district-wide Zn, Pb, and Cu mineralization. *Econ Geol* 101:1159–1188
- Pollard PJ (2001) Sodic(-calcic) alteration associated with Fe-oxide-Cu-Au deposits: An origin via unmixing of magmatic-derived H_2O - CO_2 -salt fluids. *Miner Depos* 36:93–100
- Pollard PJ, Mark G, Mitchell LC (1998) Geochemistry of post-1540 granites spatially associated within regional sodic-calcic alteration and Cu-Au-Co mineralisation, Cloncurry district, northwest Queensland. *Econ Geol* 93:1330–1344
- Porto da Silveira CL, Schorscher HD, Miekeley N (1991) The geochemistry of albitization and related uranium mineralization, Espinharas, Paraiba (PB), Brazil. *J Geochem Explor* 40:329–347
- Reynolds LJ (2000) Geology of the Olympic Dam Cu-U-Au-Ag-REE deposit. In: Porter TM (ed) *Hydrothermal iron oxide copper-gold and related deposits: A global perspective*: Adelaide, Australian Mineral Foundation, p 93–104
- Roberts DE, Hudson GRT (1983) The Olympic Dam copper-uranium-gold-silver deposit, Roxby Downs, South Australia. *Econ Geol* 78:799–822
- Romerger SB (1984) Transport and deposition of uranium in hydrothermal systems at temperatures up to 300°C: geological implications. In: De Vivo B, Ippolito F, Capaldi G, Simpson PR (eds) *Uranium geochemistry, mineralogy, geology, exploration and resources*. The Institute of Mining and Metallurgy, London, pp 12–17
- Rollinson HR (1993) Using geochemical data: evaluation, presentation, interpretation. Longman Group, UK, p 352
- Rubenach MJ (1992) Proterozoic low-pressure/high-temperature metamorphism and an anticlockwise P-T-t path for the Hazeldene area, Mount Isa inlier, Queensland, Australia. *J Metamorph Geol* 10:333–346
- Rubin JN, Henry CD, Price JG (1993) Hydrothermal zircon and zircon overgrowths, Sierra Blanca Peaks, Texas. *Am Mineral* 74:865–869
- Russell JK, Stanley CR (1990) A theoretical basis for the development and use of chemical variation diagrams. *Geochim Cosmochim Acta* 54:2419–2431
- Smellie JAT, Laurikko J (1984) Skuppesavo, Northern Sweden: a uranium mineralisation associated with alkali metasomatism. *Miner Depos* 19:183–192
- Smith DK (1984) Uranium mineralogy. In: De Vivo B, Ippolito F, Capaldi G, Simpson PR (eds) *Uranium geochemistry, mineralogy, geology, exploration and resources*. The Institution of Mining and Metallurgy, London, England, pp 43–88
- Southgate PN, Bradshaw BE, Domagala J, Jackson MJ, Idnum M, Krassay AA, Page RW, Sami TT, Scott DL, Lindsay JF, Mcconachie BA, Tarlowski C (2000) Chronostratigraphic framework for Palaeoproterozoic rocks (1730–1575 Ma) in Northern Australia and implications for base-metal mineralization. *Aust J Earth Sci* 47:461–483
- Spikings RA, Foster DA, Kohn BP, Lister GS (2001) Post-orogenic (<1500 Ma) thermal history of the Proterozoic Eastern Fold Belt, Mt Isa Inlier, Australia. *Precambrian Res* 109:103–144
- Stanley CR (1993) Effects of nonconserved denominators on Pearce element ratio diagrams. *Math Geol* 25:1049–1070
- Stanley CR (1996) A Lithochemical Analysis of Host Rock Compositional Variability at the Citronen Fjord Zn-Pb Sediment Hosted Massive Sulphide Deposit, Peary Land, Greenland. Geological Association of Canada Annual Meeting, Winnipeg, May, Abstracts with Program, pp. A89
- Stanley CR (1997) Petrologic controls on the compositional variation of turbidites in the Miocene Whakataki Formation, Castlepoint, New Zealand: Insights from Pearce Element Ratio Analysis. Abstracts with Program, Geological Association of Canada Annual Meeting, Ottawa, May, pp A-141
- Stanley CR (1998) Lithochemical exploration for metasomatic zones associated with hydrothermal mineral deposits using Molar Element Ratio Analysis. Mineral Deposit Research Unit, Lithochemical Exploration Research Project, Short Course Notes, p 120
- Stanley CR, Madeisky HE (1994) Lithochemical Exploration for Hydrothermal Ore Deposits Using Pearce Element Ratio Analysis. In: Lentz D (ed) *Alteration and Alteration Processes Associated With Ore Forming Systems*, Geological Association of Canada Short Course Notes, No. 11 193–211
- Stanley CR, Russell JK (1989) Petrologic hypothesis testing with Pearce Element Ratio diagrams; derivation of diagram axes. *Contrib Mineral Petrol* 103:78–89
- Tack L, Wingate MTD, Liegeois JP, Fernandez-Alonso M, Deblond A (2001) Early Neoproterozoic magmatism (1000 - 910 Ma) of the Zadinian and Mayumbian Groups (Bas Congo): onset of Rodinia rifting at the western edge of the Congo Craton. *Precambrian Res* 110:277–306
- Taylor HP (1974) The application of oxygen and hydrogen isotope studies to problems of hydrothermal alteration and ore deposition. *Econ Geol* 69:843–883
- Tugarinov AI, (1980) Complex metasomatic uranium deposits. In: Abou-Zied S, Kerns G (eds) *Albitized uranium deposits: six articles translated from Russian literature*. United States Department of Energy, Grand Junction Office, Colorado, pp 35–54
- Turpin L, Maruejo P, Cuney M (1988) U-Pb, Rb-Sr and Sm-Nd chronology of granitic basement, hydrothermal albitites and uranium mineralization (Lagoa Real, South-Bahia, Brazil). *Contrib Mineral Petrol* 98:139–147
- Wiedenbeck M, Alle P, Corfu F, Griffin WL, Meier M, Oberli F, von Quadt A, Roddick JC, Spiegel W (1995) Three natural zircon standards for U-Th-Pb, Lu-Hf, trace element and REE analyses. *Geostand Newsl* 19:1–23
- Wilde AR, Wall VJ (1987) Geology of the Nabarlek Uranium Deposit, Northern Territory, Australia. *Econ Geol* 82:1152–1168
- Williams PJ, Barton MD, Johnson DA, Fontbote L, de Haller A, Mark G, Oliver NHS, Marschik R (2005) Iron-oxide Copper-Gold Deposits: Geology, space-time distribution, and possible modes of origin. In: Hendenquist JW, Thompson JFH, Goldfarb RJ, Richards JP (eds) *Economic Geology 100th Anniversary Volume*. Society of Economic Geologists, Colorado, pp 371–405

- Wingate MTD, Giddings JW (2000) Age and paleomagnetism of the Mundine Well dyke swarm, Western Australia: implications for an Australia - Laurentia connection at 755 Ma. *Precambrian Res* 100:335–357
- Wingate MTD, Pisarevsky SA, Evans DAD (2002) Rodinia connections between Australia and Laurentia: no SWEAT, no AUSWUS. *Terra Nova* 14:121–128
- Wyborn LA (1987) The petrology and geochemistry of alteration assemblages in the Eastern Creek Volcanics, as a guide to copper and uranium mobility associated with regional metamorphism and deformation, Mount Isa, Queensland. In: Pharaoh TC, Beckinsale RD, Rickard D (eds) *Geochemistry and Mineralization of Proterozoic Volcanic Suites*. Geological Society Special Publication no. 33, pp 425–434
- Zheng YF (1993) Calculation of oxygen isotope fractionation in hydroxyl-bearing silicates. *Earth Planet Sci Lett* 120:247–263
- Zheng YF (1999) Oxygen isotope fractionation in carbonate and sulfate minerals. *Geochem J* 33:109–126
- Zhukova (1980). In Abou-Zied S, Kerns G (eds) *Albitized uranium deposits: Six articles translated from Russian literature*. United States Department of Energy, Grand Junction Office, Colorado, pp 91–114

Precambrian dome-and-keel structure in the Penokean orogenic belt of northern Michigan, USA

Douglas K. Tinkham*

Department of Geology and Geophysics, University of Calgary, Calgary Alberta T2N 1N4, Canada

Stephen Marshak

Department of Geology, University of Illinois, Urbana, Illinois 61801, USA

ABSTRACT

The Penokean orogen of Michigan's Upper Peninsula includes a belt of dome-and-keel structure presently defined by deep troughs, or "keels," of Paleoproterozoic Marquette Range Supergroup strata between gneiss domes composed of Archean basement rock. Structural, metamorphic, and geochronological data from the Southern Complex indicates that dome-and-keel structure developed in two stages. The first stage involved rise (intrusion, possibly diapirically) of the 2.6 Ga Bell Creek Assemblage (a gneissic megacrystic granite) into the Twin Lake Assemblage (migmatitic mafic to felsic gneiss). Flow folding in gneisses and migmatites indicate that this Archean event involved plastic flow of basement. The second stage occurred after the ca. 1.8 Ga Penokean orogeny, subsequent to the formation of a fold-thrust belt involving Paleoproterozoic Marquette Range Supergroup strata. During this stage, deep, narrow troughs developed in the region that had been the fold-thrust belt. Analysis of structures bordering the Republic Trough indicates that Paleoproterozoic keel borders are shear zones; keel rocks moved down relative to dome rocks. In effect, the Paleoproterozoic keels are steep- to vertical-sided grabens, suggesting that the dome-and-keel architecture is a consequence of extensional faulting. Amphibolite facies metamorphism occurred in Paleoproterozoic keel strata along dome-keel borders. Peak-metamorphism developed adjacent to dome borders at the time keel-bounding shear zones were active. The relative timing of Paleoproterozoic keel formation supports the model that this stage reflects collapse of the Penokean orogen. Our results show that the present dome-and-keel structure of the Southern Complex region represents superposition of Paleoproterozoic collapse structures on preexisting Archean gneiss domes.

Keywords: dome-and-keel, gneiss dome, Penokean orogen, Southern Complex, Republic Trough, granite-greenstone belt.

INTRODUCTION

In many Precambrian provinces of the world, deformed supracrustal (sedimentary and/or volcanic) rock sequences surround dome-shaped bodies consisting of basement gneissic and

plutonic rock. Typically, the supracrustal rocks occupy narrow troughs between domes, so that the overall distribution of basement and supracrustal rocks defines "dome-and-keel structure" (e.g., Anhaeusser et al., 1969). Dome-and-keel structure is typical of Archean granite-greenstone terranes throughout the world,

*Corresponding author: tinkham@ucalgary.ca.

but in a few localities, the structure also involves Paleoproterozoic strata (Marshak, 1999; Marshak et al., 1992; Holm and Lux, 1996). The formation of dome-and-keel structure remains a subject of debate—domes have been called diapirs, core complexes, and interference structures (Marshak et al., 1997).

Dome-and-keel structure has developed in a 300-km-long east-west-trending belt that traverses the Upper Peninsula of Michigan and continues into adjacent Wisconsin and Minnesota. This belt lies in the Penokean orogen, a Paleoproterozoic deformation belt fringing the south edge of the Archean Superior Province of the Canadian Shield (Fig. 1A). Key elements of this dome-and-keel structure are displayed at the eastern end of this belt in the Southern Complex region (Fig. 1B). Basement rocks of the Archean-age "Southern Complex" are exposed in gneiss domes that are separated from each other by deep troughs, or "keels," containing Paleoproterozoic Marquette Range Supergroup.

How and when did dome-and-keel structure involving the Southern Complex region develop? To address this question, we conducted a structural, petrologic, and geochronologic analysis of both the keels and domes in the Republic (Michigan) area. Based on our results, we argue that there have been two very distinct phases of gneiss dome formation. The first phase was Archean and involved plastic flow and possibly diapiric rise of silicic and intermediate metamorphic and intrusive rocks of the Southern Complex up into a supracrustal assemblage of Archean greenstone and associated sedimentary rocks. The second phase is Paleoproterozoic in age and formed by displacement on discrete shear zones dropping Paleoproterozoic strata (including banded iron formations) into steep- to vertical-sided grabens (keels or troughs) between basement domes. Amphibolite facies metamorphism associated with Paleoproterozoic dome formation may reflect the high thermal productivity of the basement rocks, which are rich in radioactive elements (Attoh, 2000; Hoffman, 1987).

GEOLOGIC SETTING

Lithotectonic Assemblages

The portion of the Canadian Shield that lies in the Upper Peninsula of Michigan and in northern Wisconsin contains five distinct Precambrian lithotectonic assemblages (Fig. 1A): (1) Archean high-grade tonalite-trondhjemite-granodiorite (TTG) gneiss, intrusives, and migmatite; (2) Archean granite-greenstone belts; (3) Paleoproterozoic continental-margin metasedimentary strata (the Marquette Range Supergroup of the Animikie basin); (4) a Paleoproterozoic volcano-plutonic complex (the Wisconsin magmatic terrane); and (5) Mesoproterozoic rift volcanics and sediments (the Keweenaw Midcontinent Rift). Our study area lies near the east end of an east-west-trending belt of dome-and-keel structure south of Lake Superior. This belt, the Penokean dome-and-keel belt, is part of the generally east-west-trending 1.8–1.9 Ga Penokean

orogen. Gneiss domes in the Penokean dome-and-keel belt are composed of Archean felsic gneisses with locally abundant migmatites, amphibolites, granites, and Archean supracrustal rocks (Sims et al., 1993). Rocks comprising these domes range in age from 3.56 Ga to 2.5 Ga (Sims et al., 1984, 1993; Peterman et al., 1980).

Outcrops in our study area, the Republic region, expose a variety of Archean high-grade TTG gneiss, intrusives, migmatite, and high-grade Archean supracrustals, which together comprise a package of Archean rocks called the Southern Complex (Fig. 2). The northern limit of the Southern Complex outcrop belt is the Great Lakes tectonic zone (Fig. 1B), a major Archean shear zone (Sims, 1991) that developed during suturing of the Southern Complex to the Northern Complex. To the north of the Great Lakes tectonic zone, basement comprises the Northern Complex, a 2.6–2.7 Ga granite-greenstone belt of the Superior Province containing TTG basement rocks, mafic and ultramafic volcanics (including pillow basalts) and intrusives, dacitic volcanics, and metasediments.

The Republic area also contains strata of the Marquette Range Supergroup, which were deposited in the Animikie Basin on basement of the Southern Complex and Northern Complex in Paleoproterozoic time. During the Paleoproterozoic-age Penokean orogeny (1870–1820 Ma), volcanic arcs (Wisconsin magmatic terrane) collided with the southern edge of the Superior province. In the process, strata of the Animikie basin were incorporated in a north-verging fold-thrust belt. Holm and Lux (1996) and Marshak et al. (1997) argue that development of the present geometry of dome-and-keel structure, involving strata of the Marquette Range Supergroup, occurred at a late stage of the Penokean orogeny in association with extensional collapse of this orogen.

The Twin Lake and Grant Lake domes in the Republic area at the western end of the Southern Complex are separated from each other by the steep-sided northwest-trending Republic Trough containing Marquette Range Supergroup strata (Fig. 2). The distribution of lithotectonic assemblages in this area defines dome-and-keel structure, and in this context, the Republic Trough is a keel because it resembles the keel of a sailboat in shape. Marquette Range Supergroup rocks also border the western, northwestern, and northern margins of the domes. The northern margin of the Twin Lake Dome borders the west end of the Marquette Trough, a 40-km-long by 5-km-wide east-west-trending synclinal keel that continues eastward to the shore of Lake Superior.

Figures 3A and 3B provide a map and cross section, respectively, of the northwest portion of the Southern Complex based on our local mapping and on previously published maps by Cannon and Simmons (1973), Hoffman (1987), and Cannon and Klasner (1976). Archean lithologies are divided into two main units, the Bell Creek Assemblage and the Twin Lake Assemblage. The Southern Complex also includes exposures of the 1806 Ma. (Holm et al., 2001) Humboldt Granite, the Palmer Gneiss (to the east near Palmer), and mafic dikes.

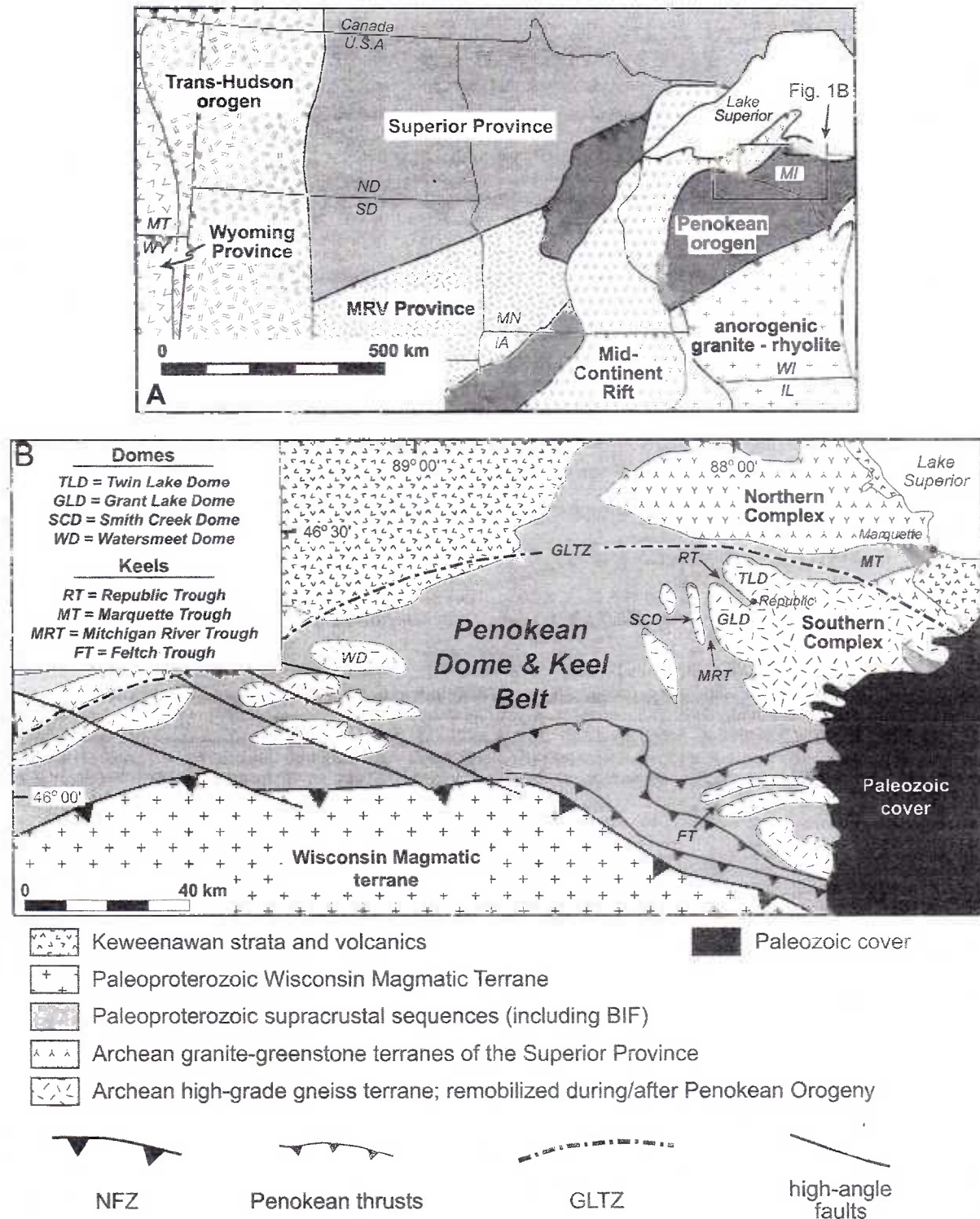
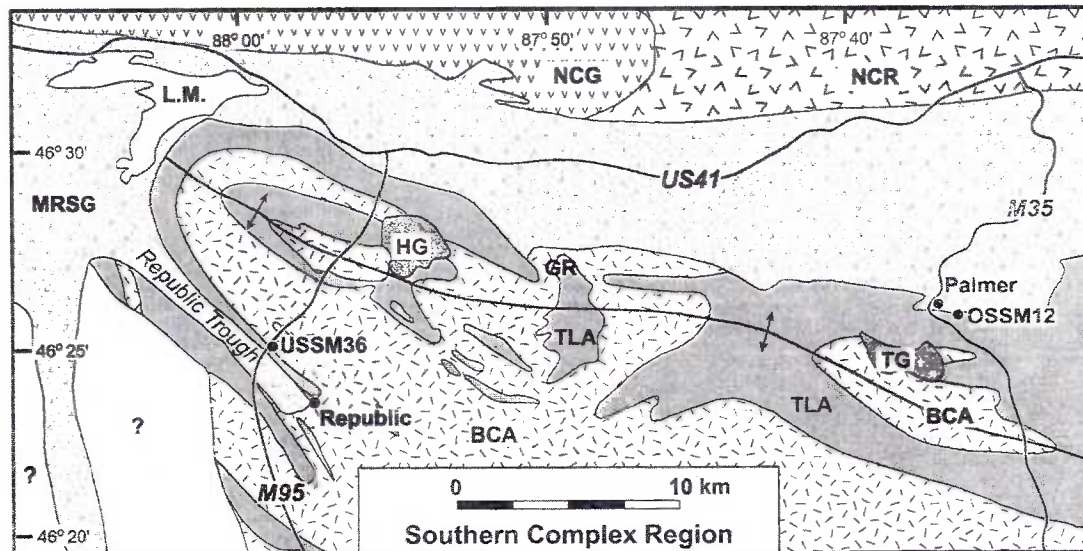


Figure 1. Regional geologic setting. (A) Tectonic province map of the north-central United States and adjacent Canada. Archean provinces include the Superior province, Minnesota River Valley province (MRV), and the Wyoming province. Paleoproterozoic orogenic belts include the Trans-Hudson orogen, Central-Plains orogen, and the Penokean orogen. Proterozoic igneous provinces include the anorogenic granite-rhyolite province and Midcontinent rift (MCR). IA—Iowa; IL—Illinois; MI—Michigan; MN—Minnesota; MT—Montana; ND—North Dakota; SD—South Dakota; WI—Wisconsin. (Modified from Sims, 1996). (B) Geologic map of the southern Lake Superior Region, midwestern United States (location shown by rectangle in A). MRSG—Marquette Range Supergroup; SC—Southern Complex; NC—Northern Complex; WD—Watersmeet Dome; MD—McGrath Dome; LM—Lake Michigan; NFZ—Niagra fault zone; GLTZ—Great Lakes tectonic zone. (Modified from Sims, 1992.)



modified from Hoffman (1987)



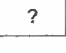





Paleoproterozoic rocks		Northern Complex Archean gneiss		Southern Complex Archean gneiss	
	Tilden Granite		Northern Complex granite and gneiss		Undivided gneiss (not exposed)
	Humboldt Granite		Northern Complex greenstone		Bell Creek Assemblage
	Marquette Range Supergroup				Twin Lake Assemblage (Migmatite Complex of Hoffman, 1987)

Figure 2. Geological map of the Southern Complex. LM—Lake Michigamme; R—town of Republic; LMT—Lake Michigamme Traverse. The M95 traverse is along Route M95. The Twin Lake Assemblage is broadly equivalent to the Migmatite Complex mapped by Hoffman (1987). The location of Palmer Gneiss sample OSSM-12 and Bell Creek Assemblage sample USSM-36 are indicated. GR—Greenwood Reservoir locality displaying F_{3-4} interference folds, discussed in text. (Modified from Hoffman, 1987.)

The Twin Lake Assemblage outcrop belt nearly parallels the border of the Twin Lake Dome at its western end (Figs. 4A and 4B), but the dome boundary truncates the Twin Lake Assemblage outcrop belt at the northern termination of the dome along the southern edge of the Marquette Trough. Twin Lake Assemblage lithologies on the north side of the Republic Trough correlate across the trough with Twin Lake Assemblage lithologies along the northern margin of Grant Lake Dome, suggesting that the Republic Trough is underlain by the Twin Lake Assemblage. Due to lack of exposure, a large portion of Grant Lake Dome is mapped as undivided gneiss; presumably, this region is composed of the Twin Lake and Bell Creek Assemblages.

Paleoproterozoic Metamorphism

Rocks of the Penokean dome-and-keel belt have been metamorphosed to varying degrees up to the amphibolite facies. In his now classic study, James (1955) mapped several regional metamorphic nodes resembling bull's-eyes. These nodes are typified by high-temperature-low-pressure metamorphism, with a general margin-to-center progression through the

chlorite, biotite, garnet, staurolite, and andalusite-sillimanite zones. Notably, to the west in the Watersmeet District (Fig. 1B), kyanite occurs as the stable aluminosilicate polymorph, suggesting that the western end of the dome-and-keel belt exposes deeper crustal levels than the eastern end (see Schneider et al., this volume).

The timing of Paleoproterozoic metamorphism in the Penokean dome-and-keel belt has recently been constrained by U-Th-Pb ion microprobe dating of metamorphic monazite (Rose et al., 2003). Monazites from the Peavy node yield ages of 1828 and 1832 Ma, with a secondary event detected at ca. 1795 Ma. Kyanite schist monazite from the Watersmeet node yielded an age of 1822 Ma, also with a secondary event at ca. 1795 Ma. However, monazite in a staurolite-bearing schist from the Republic node yielded a significantly younger age of 1760 Ma, indicating metamorphism is post-Penokean in age.

There have been numerous efforts to explain the metamorphic patterns of the Penokean dome-and-keel belt. For example, James (1955) argued for subsurface plutons, Attoh and van der Muelen (1984) suggested that it was a consequence of crustal thickening and plutonism, Gregg (1993) suggested

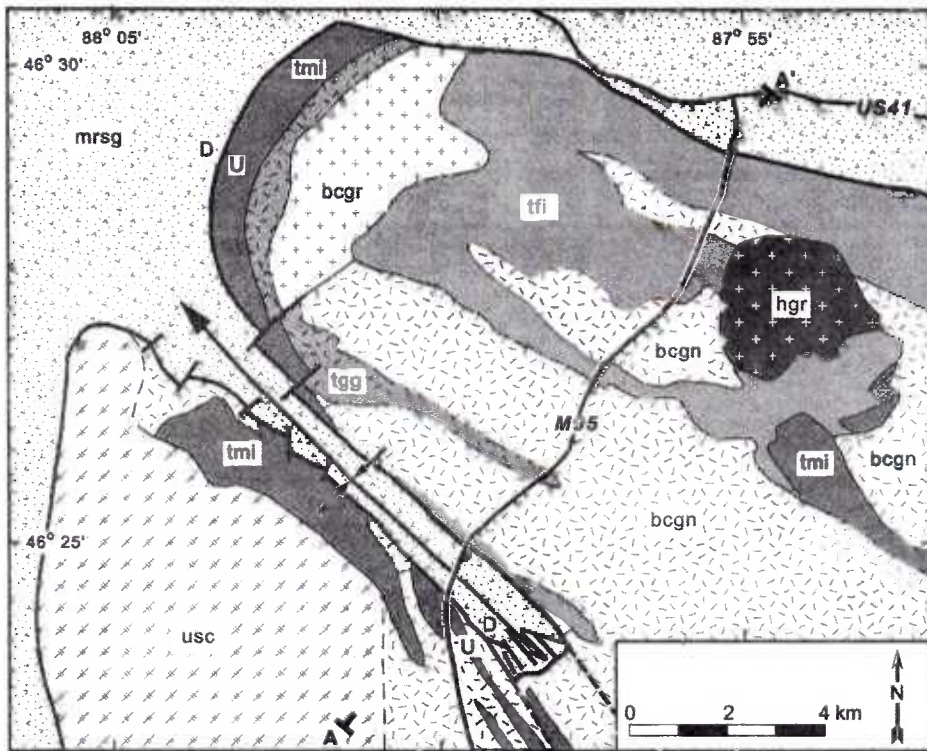
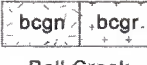



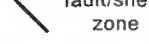
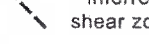
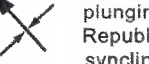


Figure 3. (A) Geologic map of the western part of the Southern Complex and surrounding supracrustals, showing the distribution of basement lithologies in Twin Lake Dome and Grant Lake Dome. bcgr—Bell Creek Granite, bcgn—Bell Creek Gneiss, tgg—granite of Twin Lake Assemblage, tmi—mafic to intermediate gneiss of Twin Lake Assemblage, tfi—felsic to intermediate gneiss of Twin Lake Assemblage, usc—undifferentiated Southern Complex. (Modified from Cannon, 1975; Cannon and Klasner, 1976; and Hoffman, 1987). (B) Geological cross section along the M95 traverse (A-A'). RT—Republic Trough, MT—Marquette Trough. Lines within the Bell Creek Gneiss represent shear-zone fabric, and dipmeters across top of cross section represent attitude of compositional layering in the Bell Creek Gneiss. Lines within Twin Lake Assemblage represent compositional layering. Lines within Marquette Range Supergroup represent bedding.

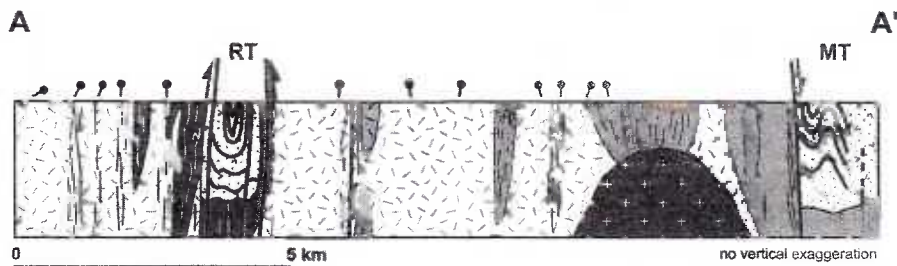
Paleoproterozoic Rocks

-  Humboldt Granite
-  Marquette Supergroup

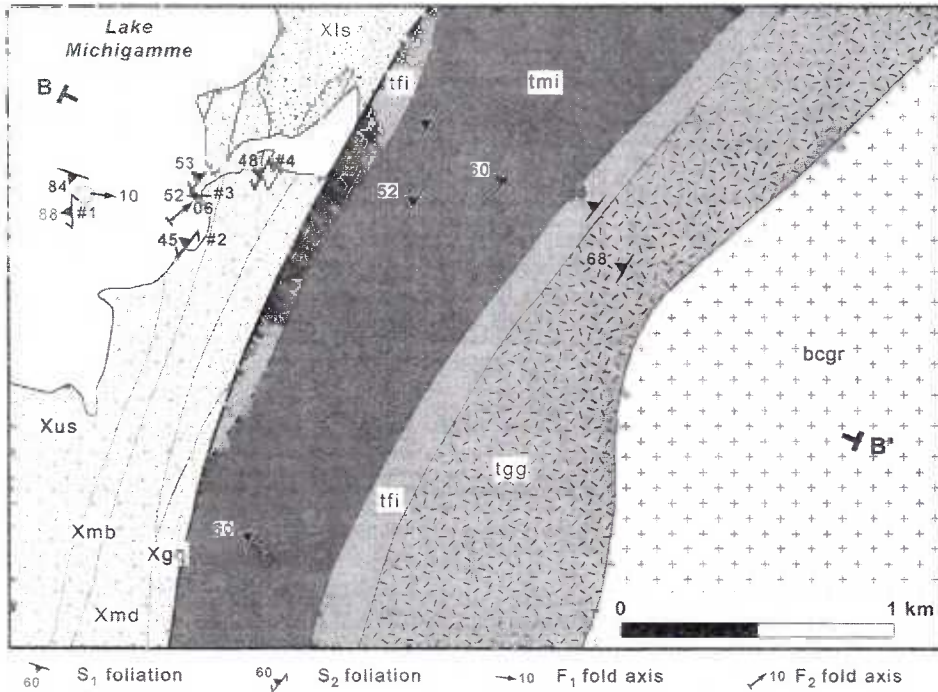
Southern Complex Basement

-  Bell Creek Assemblage
-  Twin Lake Assemblage
-  granite
-  undifferentiated gneiss
-  fault/shear zone
-  inferred shear zone
-  plunging Republic syncline

A



-  Humboldt Granite
-  Marquette Range Supergroup
-  Bell Creek Assemblage
-  granite
-  felsic-intermediate gneiss
-  mafic-intermediate gneiss
- RT = Republic Trough
- MT = Marquette Trough
-  attitude of compositional layering in Bell Creek Assemblage
-  bedding in Marquette Range Supergroup strata
-  shear foliation in Bell Creek Ass.;
-  compositional layering in Twin Lake Ass.



Marquette Range Supergroup

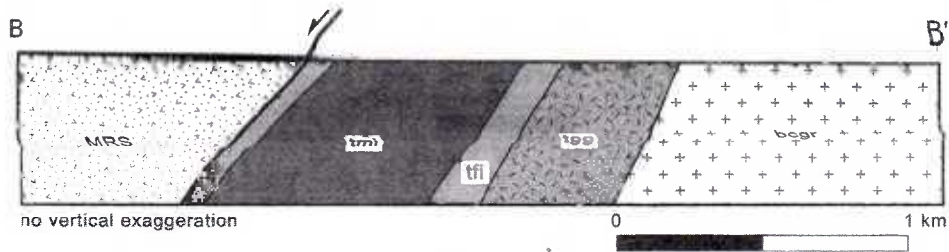
Xus	Upper Slate Member
Xmb	Bijiki Iron-Formation
Xmd	metadiabase
Xls	Lower Slate Member
Xgq	Goodrich Quartzite

Southern Complex Basement

Bell Creek Assemblage	
bcgr	Bell Creek Granite
Twin Lake Assemblage	
tgg	granite
tfi	felsic-intermediate gneiss
tmi	mafic-intermediate gneiss

A

Figure 4. (A) Geologic map of the Lake Michigamme traverse region. Numbers refer to locations discussed in text. Xus—Upper Slate Member of Marquette Range Supergroup (MRSG); Xmb—Bijiki Iron Formation Member of MRSG; Xls—Lower Slate Member of MRSG; Xgq—Goodrich Quartzite of MRSG; Xmd—metadiabase dike; tfi—felsic to intermediate gneiss of the Twin Lake Assemblage; tmi—mafic to intermediate gneiss of the Twin Lake Assemblage; tgg—granite to granitic gneiss of the Twin Lake Assemblage; bcgr—granite of the Bell Creek Assemblage. Modified from Cannon and Klasner (1976). (B) Cross section along the Lake Michigamme traverse (B–B’).



Marquette Range Supergroup

MRS	undivided
-----	-----------

Bell Creek Assemblage

bcgr	Bell Creek Granite
------	--------------------

Twin Lake Assemblage

tgg	granite
tfi	felsic-intermediate gneiss
tmi	mafic-intermediate gneiss

fault/shear zone



lithologic contact



B

the pattern reflected folding, and Sims and Peterman (1976) related the metamorphism to heat transfer during diapiric rise of the domes. Schneider et al. (1996) suggest instead that the pattern of metamorphic nodes is due to "folding" of preexisting isograds during uplift of the domes in some places, or due to post-tectonic heating associated with post-tectonic plutons in other places. Attoh (2000) suggests that the Republic metamorphic node (Fig. 5A) represents radiogenic heating by basement, because he finds a correlation between radiogenic heat production rates from basement and the grade of metamorphism.

We point out that James' (1955) isograd map was based primarily on his examination of pelitic to sub-pelitic rocks of the Marquette Range Supergroup, but he extended isograds based on pelitic- to sub-pelitic lithologies into basement domes using mineral assemblages in metamorphosed basic dikes. The number of samples within the basement domes is quite small (Fig. 5A), so the position of isograd lines within domes (and continuity with isograds in the Marquette Range Supergroup) is not well constrained. Notably, metamorphic nodes are spatially related to exposures of Archean gneiss domes, but James' (1955) map suggests that the sillimanite isograd cross-cuts the Twin Lake Dome and Grant Lake Dome basement-supracrustal contact. We note that, considering the location of James' sample locations, the sillimanite isograd within supracrustals could just as well be positioned parallel to the Grant Lake Dome boundary, or could surround several basement domes. This interpretation (Fig. 5B) still fits James' data, but shows the sillimanite and staurolite isograds roughly following the borders of the domes.

Assemblages suitable for detailed thermobarometry are rare in the highest-grade portion of the Republic node. Limited thermometry results from the Republic node indicate metamorphism in supracrustals reached temperatures of 552–617 °C at 200–300 MPa (Attoh and Klasner, 1989; Tinkham, 1997). Thermobarometry from a garnet-muscovite-biotite-plagioclase-epidote-quartz schist in Grant Lake Dome yielded 575 °C and 400 MPa (Tinkham, 1997) based on the garnet-biotite calibration of Hodges and Spear (1982) and the garnet-biotite-plagioclase-quartz calibration of Hoisch (1990).

FIELD DESCRIPTIONS OF ROCK UNITS

Following are summary descriptions of the individual rock units that occur within our study area. We begin with units of the Southern Complex (the Twin Lake Assemblage, Bell Creek Assemblage, Humboldt Granite, cross-cutting dikes, and the Palmer Gneiss), then discuss metasedimentary rocks of the Marquette Range Supergroup.

Twin Lake Assemblage

The Twin Lake Assemblage contains a wide variety of lithologies divided into three main units: (1) granite and granitic gneiss; (2) felsic to intermediate gneiss; and (3) mafic to intermediate gneiss. These three units grade into one another, and

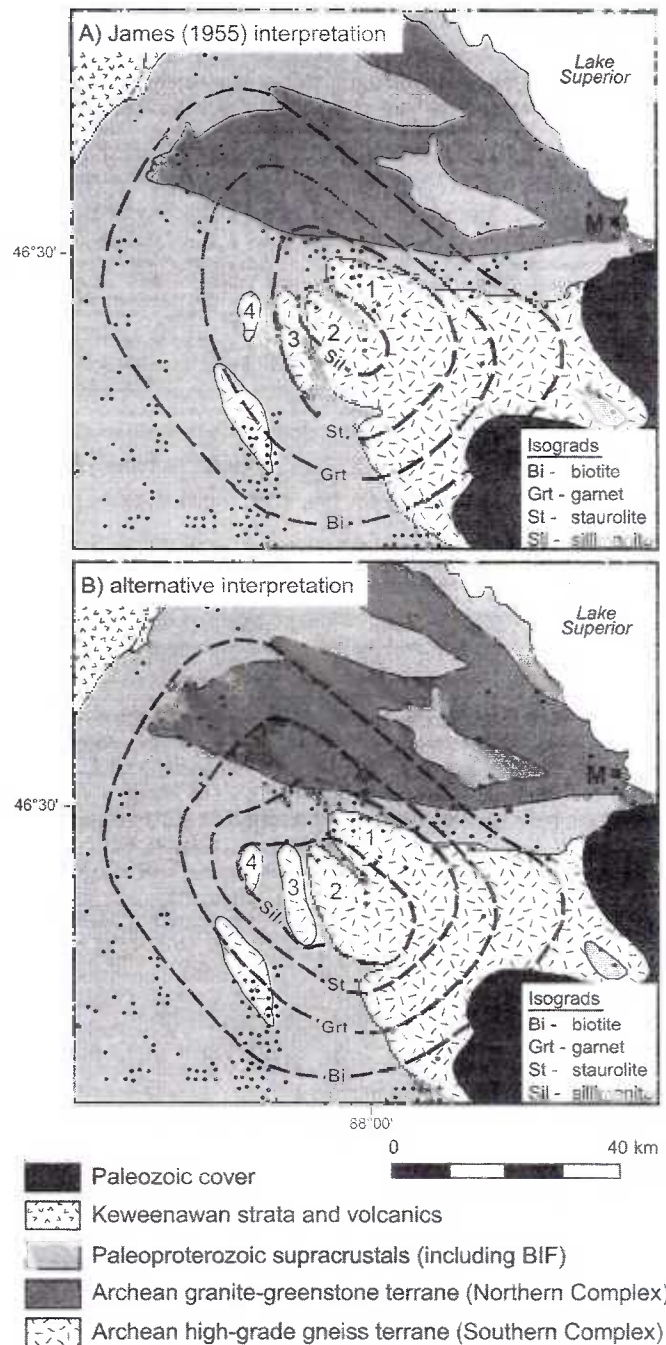


Figure 5. The Republic metamorphic node. (A) The node as mapped by James (1955). Black dots indicate the sample localities upon which James based his isograds. (B) A reinterpretation of the location of isograds based on the original data collection locality sites of James (1955). The sillimanite isograd follows the boundaries of Grant Lake Dome (2), Smith Creek Dome (3), and Wilson Creek Dome (4). Bi—biotite isograd; Grt—garnet isograd; St—staurolite isograd; Sil—sillimanite isograd; 1—Twin Lake Dome; 2—Grant Lake Dome; 3—Smith Creek Dome; M—Marquette. (Modified from James, 1955.)

lithologies of the units are locally mixed with one another at the outcrop scale. The Twin Lake Assemblage is locally migmatitic where in contact with granitoids of the Bell Creek Assemblage (described below). Some lithologies of the granite and granitic gneiss unit are similar to lithologies of the Bell Creek Gneiss, but because of their proximity and relationship to other units of the Twin Lake Assemblage, they have been included with the Twin Lake Assemblage.

The various rock types of the Twin Lake Assemblage are best exposed in the western portion of Twin Lake Dome (Fig. 4A). In sequence, starting at the dome-keel contact, a west-to-east traverse exposes: (1) felsic to intermediate gneiss, (2) mafic to intermediate gneiss, (3) a second zone of felsic to intermediate gneiss, and finally, (4) granite to granitic gneiss. The felsic to intermediate gneiss adjacent to the dome-keel contact consists of locally sheared quartzo-feldspathic gneiss, and amphibole ± epidote-bearing quartzo-feldspathic biotite gneiss. These rocks host localized occurrences of concordant and discordant massive granitoid that locally possess a strong solid-state foliation. The mafic to intermediate gneiss of this region, which consists of amphibolitic gneiss and quartzo-feldspathic biotite gneiss-schist, hosts concordant and locally discordant bodies of massive granitoid. The second zone of felsic-intermediate gneiss is similar to the first one, but does not contain sheared granitoid. This zone grades into a granitic gneiss that contains xenoliths of intermediate, mafic, and granitic gneiss. Rocks within the Twin Lake Assemblage commonly exhibit stromatic migmatitic textures in that host gneiss is interlayered with concordant layers of massive and locally pegmatitic granitic leucosomes.

The Twin Lake Assemblage contains rare lenses of iron formation, and Hoffman (1987) noted the possibility that some compositional banding in the Twin Lake Assemblage may also represent original volcanogenic layering. Cannon and Simmons (1973) noted that some amphibolite lenses in the Twin Lake assemblage resemble pillows, suggesting that portions of the Twin Lake Assemblage represent a remnant Archean greenstone belt.

Bell Creek Assemblage

The Bell Creek Assemblage consists primarily of Bell Creek Gneiss; at the west end of Twin Lake Dome, the Assemblage locally contains Bell Creek Granite. The Bell Creek Gneiss is a predominantly light pink to gray, medium to mostly coarse-grained, and megacrystic gneissic granite- to granodiorite- to quartz monzonite. Granite is its most abundant component. Local compositional banding (5 cm to several meters thick), aligned feldspar megacrysts, and local shear fabrics define gneissosity. Variations in the amount of matrix biotite and megacryst abundance define the compositional banding. Feldspar megacrysts are weakly to well aligned, range in size from 1 to 5 cm in length, and are typically tabular or linear in shape, defining a foliation or lineation. Where intensely sheared, the Bell Creek Gneiss grades into a biotite- and muscovite-rich schistose augen gneiss.

In addition to megacrystic gneiss, the Bell Creek Gneiss includes granitic pegmatites and lenses of mafic gneiss. Mafic gneiss lenses range from <3 cm to several meters thick. These lenses, consisting of banded amphibolites, biotite schists, and biotite-amphibole gneiss are steeply dipping and typically concordant with foliation in surrounding gneissic granite. Granite locally crosscuts foliation in the mafic gneiss, and elongate rafts of mafic gneiss are incorporated into the granite, indicating the granite is younger than the mafic gneiss.

Grant Lake Dome also contains thin layers of foliated amphibolites that are younger than the megacrystic granitoids of the Bell Creek Gneiss based on cross-cutting relationships. Locally, thin layers (3–8 cm thick) of amphibolite cut across thick compositional banding of megacrystic Bell Creek Gneiss. These amphibolites likely represent metamorphosed mafic dikes; however, they are strongly foliated and rather thin, distinguishing them from the majority of metamorphosed mafic dikes seen elsewhere in the domes (as discussed below). These amphibolite layers are found in zones of slightly sheared Bell Creek Gneiss, where they are concordant to shear fabric, but discordant to compositional layering in the Bell Creek Gneiss.

Humboldt Granite

The Humboldt Granite is a light red, medium grained, albite granite within the Twin Lake Dome (Figs. 2 and 3A). It is massive and relatively undeformed, but contains thin, planar bands (<2 cm wide) of biotite and chlorite schist. Unlike all other Southern Complex lithologies, which are thought to be Archean in age, radiometric dating indicates the Humboldt Granite is Paleoproterozoic in age. Schulz et al. (1988) obtained a whole-rock Rb/Sr age of 1733 ± 25 Ma, but more recent zircon U-Pb dating yielded an older age of 1806 ± 21 Ma (Holm et al., 2001).

Mafic Dikes

The Southern Complex contains a large number of relatively undeformed mafic dikes. There are two sets, distinguished by their degree of metamorphism. The set of metamorphosed dikes is considered pre-Penokean in age, whereas the set of unmetamorphosed dikes is considered Keweenawan (ca. 1.1 Ga) in age, related to the Midcontinent rifting event (Sims et al., 1993). Metamorphosed mafic dikes commonly contain a shear fabric along their margins.

Palmer Gneiss

The Palmer Gneiss is limited in extent to the eastern portion of the Southern Complex near Palmer and is exposed between the outcrop belt of the Twin Lake Assemblage and the Marquette Trough. Discrete contacts between the Palmer Gneiss and surrounding units are not exposed. Rock types within the Palmer Gneiss include granitic-gneiss, quartzite, slate-phyllite, quartz-sericite schist, and dolomite. Granitic lenses ranging from 2 cm

to 25 cm locally intrude schists parallel to subparallel to schistosity. These granitic lenses locally contain a mylonitic foliation and are cut by planar tension gashes filled with quartz and carbonate. Evidently, brittle fracturing and tension-gash formation occurred within the more competent granitic lenses while the less-competent schistose units were undergoing shearing.

Marquette Range Supergroup

Strata of the Marquette Range Supergroup in the Republic region are divided into the Chocoday, Menominee, and the Baraga Groups. The Marquette Trough contains the older Chocoday Group in the eastern region and the younger Menominee and Baraga Groups in the central and western regions. The Chocoday Group contains conglomerates, quartzites, slates, and stromatolitic dolomites (Sims et al., 1993). The Menominee Group contains the Negaunee Iron Formation, Siamo Slate, and the Ajibic Quartzite. The Baraga Group contains the Goodrich Quartzite and the Michigamme Formation. The Michigamme Formation includes slates, quartzites, several intervals of banded iron formation, and basaltic to andesitic pyroclastics of the Clarksburg volcanics, all of which have been metamorphosed to varying degrees.

Unlike the Marquette Trough, the Republic Trough only contains the Ajibic Quartzite of the Menominee Group and the Goodrich Quartzite and Michigamme Formation of the Baraga Group. West and south of Grant Lake Dome, the Marquette Range Supergroup also includes bimodal volcanics, including continental flood basalts, such as the Badwater Greenstone and Hemlock Formation, which are locally as much as 5–10 km thick each (Beck and Rama Murthy, 1991).

STRUCTURAL FEATURES

To understand the internal structure of basement domes and nature of the basement-supracrustal contact where domes border keels, we describe structural observations and measurements along two traverses. The first traverse follows the NNE-SSW trending Route M95 (Fig. 3A). This traverse illustrates the architecture of the northern part of Grant Lake Dome, the Republic Trough, Twin Lake Dome, and the dome border contact between the Twin Lake Dome and the Marquette Trough. The second traverse, called the Lake Michigamme traverse, crosses the western margin of Twin Lake Dome (Figs. 3A and 4A), and illustrates the basement-supracrustal contact and geometry of rock units within the dome (Fig. 4A).

Structures in Basement Gneiss Domes and Dome-Keel Contacts

Folds

Primary layering in the Twin Lake Assemblage cannot be readily identified in the Southern Complex. However, Hoffman (1987) identified primary layering (S_0) in rare lenses of banded

iron formation included within the Twin Lake Assemblage. The first generation of folding observed in the Southern Complex is defined by isoclinal folds of S_0 within these banded-iron-formation lenses (Hoffman, 1987). The rare iron-formation lenses within the Twin Lake Assemblage are commonly aligned parallel to compositional banding in surrounding gneiss. Banded-iron-formation lenses contain isoclinal folds (F_1) defined by the trace of S_0 . The dominant compositional banding of Twin Lake Assemblage gneiss is axial planar to these folds, and thus we consider it to be S_1 . In this context, any S_0 that existed has been transposed into S_1 .

F_2 folds are local, tight-to-isoclinal folds defined by the trace of S_1 . They can be recognized at the thin-section to outcrop scale. S_2 foliation, defined by alignment of biotite, is axial planar to F_2 . F_2 folds at the mesoscopic scale have wavelengths ranging from <1 cm to 2 m, much less than their amplitude. Some of the smaller examples of F_2 folds are rootless, intrafolial folds. Along the M95 traverse, most F_2 folds have northwest-striking, near-vertical axial planes, whereas along the Lake Michigamme traverse, intrafolial isoclinal folds within the mafic to intermediate gneiss unit have north-to-northeast-striking axial planes that dip moderately to the west-northwest, parallel to compositional banding.

F_3 and F_4 can be recognized only locally, and are defined by open-close folding of F_2 folds. These folds are best expressed at one outcrop near Greenwood Reservoir (GR, Fig. 2), where F_3 and F_4 axes are nearly perpendicular to one another, producing a dome-and-basin interference folding of F_2 axial planes. It is unresolved as to which set of open folds formed first, so examples of both F_3 and F_4 are designated $F_{3,4}$. Along the M95 traverse, only one generation of open folding ($F_{3,4}$) was observed; here, F_2 and $F_{3,4}$ axes are nearly parallel. $F_{3,4}$ was not observed at the outcrop scale along the Lake Michigamme traverse.

A stereoplot of foliation attitudes within the Twin Lake Assemblage for the western portion of the Twin Lake and Grant Lake domes (Figs. 6A and 6B) suggests that the Twin Lake Assemblage has been folded around an axis oriented $62^\circ/331^\circ$. The Lake Michigamme traverse passes through the closure of this fold, the Twin Lake antiform. Because of its orientation and style, we tentatively correlate this large structure with mesoscopic $F_{3,4}$ folds. Foliation (compositional layering and schistosity) within gneiss of the Twin Lake Assemblage along the Lake Michigamme traverse consistently dips moderately to the west (Fig. 6C). Mineral lineations are not common within rocks of the Twin Lake Assemblage along this traverse, but where observed (defined by amphiboles in mafic gneiss), they are moderately plunging to the north (Fig. 6D).

Where observed along the M95 traverse, the Bell Creek Assemblage contains compositional banding that is not isoclinally folded, suggesting F_1 of the Twin Lake Assemblage is pre-Bell Creek intrusion in age. In the Twin Lake Dome, fabric within the Bell Creek Gneiss is almost invariably northwest-striking and steeply dipping to vertical (Figs. 6E and 6F). In Grant Lake Dome, the fabric is also predominantly northwest-

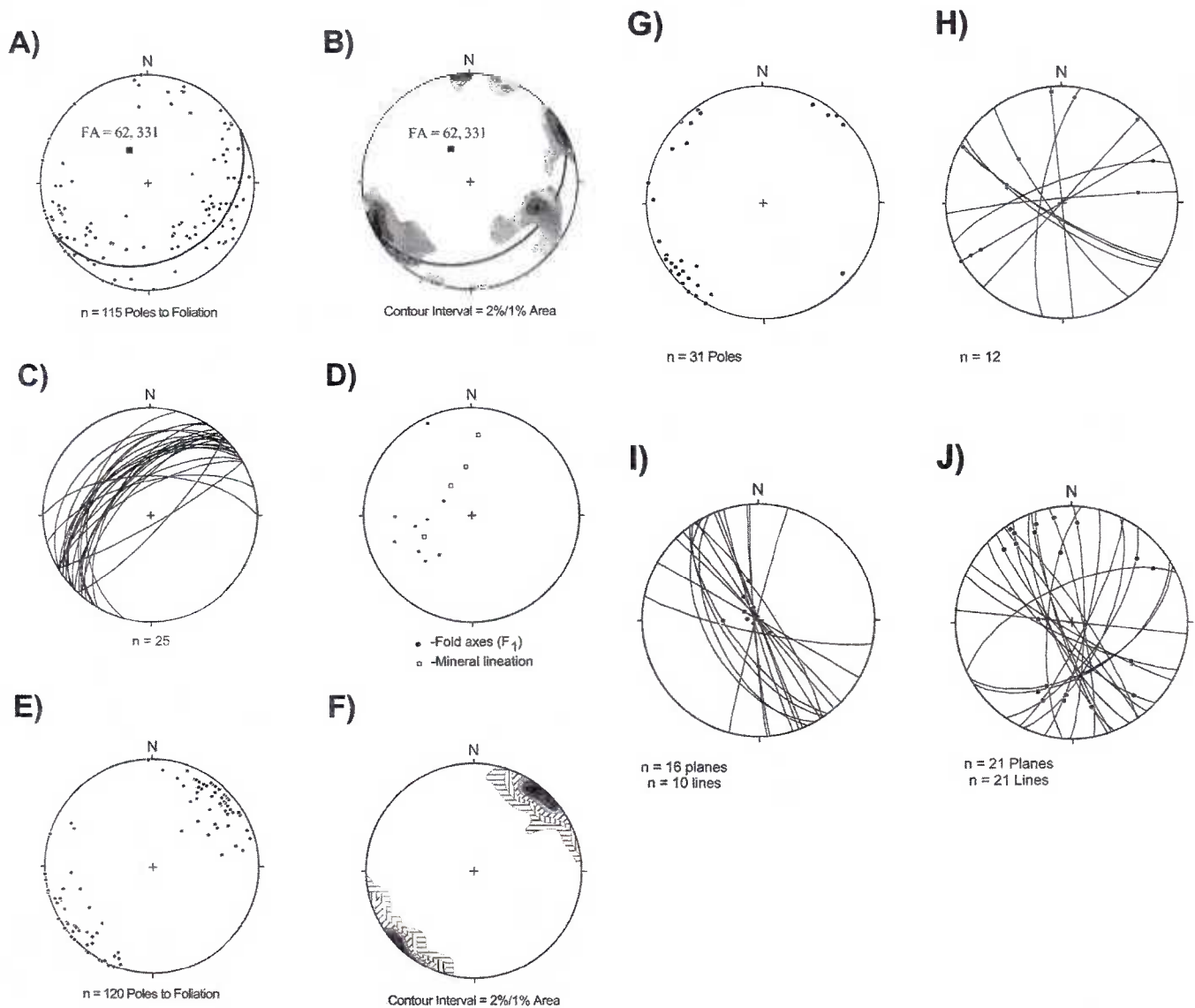


Figure 6. Stereoplots of structural features. All plots are equal-area lower hemispheric projections. (A) Poles to Twin Lake Assemblage foliation in Twin Lake Dome and Grant Lake Dome. (B) Contour plot of foliation in A with pole to best-fit great circle indicated. (C) Twin Lake Assemblage foliation in Twin Lake Dome along the Lake Michigamme traverse. (D) Mineral lineations and fold axes in Twin Lake Dome along the Lake Michigamme traverse. (E) Poles to Bell Creek Gneiss foliation in Twin Lake Dome and Grant Lake Dome. (F) Contour plot of foliation in E. (G) Poles to metamorphosed mafic dike orientations along the M95 traverse. (H) Foliation and crenulation fold axes of thin (<10 cm wide) biotite schist layers between basement granitoid blocks. Fold axes are moderately plunging to subhorizontal and schist layers are steeply dipping. (I) Basement shear zone orientations and stretching lineations within shear zones along M95 traverse. (J) Orientation of chlorite-coated slip surfaces (planes) and groove lineations (points) along those surfaces.

striking with nearly vertical dips. However, three consecutive outcrops along the M95 traverse in the Grant Lake Dome shows northwest-striking compositional layering gradually changing orientation from vertical to a dip of only 17°S while traversing southwards toward the center of the dome. This suggests that compositional layering of the Bell Creek Granite may be folded in this region, but the generation of folding is uncertain. The change in orientation could represent magmatic foliation related

to emplacement of magma, but the fold style is consistent with the F_{3-4} folding event.

Several generations of steeply dipping to vertical mafic dikes intrude rocks of the Southern Complex along the M95 traverse. Of those that are metamorphosed, two dominant sets of dikes can be identified based on orientation: one set strikes NNW, while the other set strikes NNE (Fig. 6G). Generally, these dikes are not folded at the outcrop scale, and locally crosscut F_2 and F_{3-4}

folds. Many of the metamorphosed mafic dikes have developed schistosity defined by alignment of biotite along their margins.

Thin, distinct, near-vertical layers of biotite schist occur in the Bell Creek Gneiss and Twin Lake Assemblages in the central and northern portions of Twin Lake Dome along the M95 traverse. The schist layers possess a strong vertical schistosity that, in most localities, is crenulated. Axes of these crenulations are typically moderately plunging to horizontal (Fig. 6H). These schist layers locally cut across compositional banding in surrounding gneiss and may represent sheared and hydrated dikes. In cases where the schist layers cut compositional banding in the gneiss, the contact between the two is very sharp. In cases where the schist layers are parallel to foliation in the surrounding gneiss, the contact is gradational over 2–3 cm, and the surrounding gneiss in the contact zone resembles an augen gneiss, suggesting the surrounding gneiss has been sheared along with the schist layer. The crenulation folds (F_5) in the biotite-schist layers are interpreted to have developed during shearing as blocks of gneiss-granitoid moved relative to one another, and not by folding of the whole schist layer, because the contact between the schist and gneiss is itself not folded. F_5 fabric along the M95 traverse is, therefore, restricted to the thin schist layers, and does not represent folding of foliation in surrounding gneisses. The moderately plunging to horizontal crenulation axes (F_5) suggest the gneissic-granitoid blocks were moving in a dip-slip to moderately oblique-slip manner.

Shear Zones

Ductile to brittle-ductile shear zones are abundant within basement rocks along the M95 traverse. Most of these shear zones are relatively thin (<2 cm wide), but several reach widths of several meters. The majority of the shear zones strike northwest and are steeply dipping to vertical (Fig. 6I). The shear zones are defined by a decrease in grain size, an increase in mica content, and development of strong foliation. In typical shear zones cutting the Bell Creek Gneiss, feldspar megacrysts are rounded and are surrounded by micas, leading to an augen-gneiss texture. An apparent increase in shearing leads to progressive decrease in size of the relict feldspar megacrysts, and an increase in mica, yielding a quartz-feldspar porphyroclastic biotite (\pm muscovite) schist with good S/C fabric development. Quartz and feldspar crystals are stretched in these shear zones, and the alignment of stretched crystals define a steeply plunging stretching lineation, indicating dip-slip movement along the shear zones. Shear zones locally truncate metamorphosed mafic dikes, indicating that shear zones were active after emplacement of the dikes. Several poorly developed (incipient) shear zones exhibit a very weak stretching lineation that is moderately plunging to horizontal, suggesting there were multiple shearing events within the basement. Unfortunately, many shear zones can only be observed on a glacially polished, near-horizontal surface, making the determination of shear-zone kinematics impossible.

Some well-developed schistose shear zones are cut by a later set of thin shear zones. The late shear zones are <0.5 cm wide and

anastomose at the outcrop scale. The rock is preferentially broken along these anastomosing surfaces to form lozenge-shaped blocks oriented to define an apparent mega-S/C structure. The late shear surfaces are chlorite coated and exhibit a phyllitic sheen, suggesting they formed at a lower metamorphic grade than the earlier shear zones in which they are found. Groove lineations in these shear zones typically display a shallow plunge (Fig. 6J).

In thin section, basement shear-zone rocks exhibit a weak to well-developed S/C fabric. The S/C fabric is defined by mica fish and by mica-wrapped asymmetric porphyroclasts of quartz and feldspar. Most samples show evidence of dynamic recrystallization defined by subgrain formation (locally displaying core-mantle textures) around strained grains that exhibit deformation bands, undulose extinction, and patchy extinction. Some samples contain quartz and feldspar subgrains with jagged boundaries, indicating the effects of dynamic recrystallization, not static recrystallization. Aligned muscovite typically recrystallized in feldspar porphyroclast tails. These micas wrap around feldspar and quartz grains that were undergoing dynamic recrystallization, suggesting that metamorphism was synchronous with shearing. However, several samples contain quartz grains with straight or curved boundaries, approaching an equilibrium texture, suggesting static recrystallization occurred locally, and thus that metamorphism outlasted movement in these shear zones.

A particularly notable shear zone developed in the Twin Lake Assemblage ~20 m south of the southwestern edge of the Republic Trough along the M95 traverse. This shear zone strikes parallel to the Republic Trough, is ~5 m wide, and contains a variety of schists. One biotite schist layer within the zone contains abundant garnets that show clear evidence of rotation during growth. The shear zone contains lineations that are steeply plunging to the northwest (average of 75°NW). Stretched ribbon quartz grains forming quartz rods, aligned mineral grains, and elongated aggregates of mica define the lineations. The shear zone also contains isoclinal folds that are intrafolial and rootless. S/C fabric is locally developed and all shear-sense indicators show basement-side-up relative to the Republic Trough along a steeply plunging displacement path. Although we have not observed sillimanite in this shear zone, Mahlburg (1969) observed sillimanite in a thin schist horizon, indicating high-temperature metamorphism. She also found several schist horizons similar to this one along the southern border of the Republic Trough.

The actual contact between basement and supracrustals in the Republic Trough is not exposed along M95, but is exposed in the open pit of the Republic Mine (which has subsequently filled with water), and at a location ~3 km to the northwest of the mine, along the southern edge of the trough. At both locations, the contact is a shear zone with lineations and S/C fabric indicating basement-side up relative to the supracrustals. Foliation increases in intensity within the basement rocks as the contact is approached, forming locally well-developed S/C fabric.

The contact is somewhat gradational over an interval of 0.3–1 m wide, especially where adjacent to the Ajibic Quartzite. The Ajibic Quartzite becomes a muscovite-rich vitreous quartzite close to the contact. In the shear-zone itself, rock consists of a feldspar porphyroclast bearing, vitreous, muscovite-rich quartzite.

Structures in the Marquette Range Supergroup

In outcrops of Marquette Range Supergroup in the Marquette Trough and in regions to the west of the Twin Lake Dome, strata of the Supergroup have been metamorphosed only to greenschist grade, and contain spaced to slaty cleavage (S_1). This cleavage is axial planar to generally east-west-trending upright folds, and generally cuts across bedding (S_0) of the Supergroup. Close to the dome boundaries, the S_1 cleavage is overprinted by an S_2 fabric that parallels the dome boundaries and becomes stronger closer to the dome borders. We describe this geometry below, first as it appears along the Lake Michigamme traverse, and then as it appears along the M95 traverse.

Lake Michigamme Traverse

We examined structures at the western margin of the Twin Lake Dome along a roughly east-west traverse that extends from small islands in Lake Michigamme to almost the contact between supracrustal rocks (the Marquette Range Supergroup) and basement rocks (the Twin Lake Assemblage) on the dome surface. Low-grade metasedimentary rocks of the Marquette Range Supergroup crop out at the western edge of the traverse on the islands (location #1; Fig. 4A) in Lake Michigamme. These rocks contain two generations of foliation and fold development. The first is a penetrative schistosity (S_1), and the second is an asymmetric crenulation cleavage (S_2). S_1 cleavage cuts across relict bedding (S_0). At this locality, bedding, as well as quartz veins and pods, have been folded into tight to open folds (F_1) with subhorizontal fold axes that trend approximately east-west; the S_1 foliation is axial planar to these folds. The S_2 cleavage strikes roughly north-south with a very steep dip to the west; and thus it strikes at a high angle to the S_1 cleavage. The S_2 cleavage is axial planar to F_2 folds.

Approaching the basement-supracrustal contact (locations #2 and #3; Fig. 4A), S_2 crenulation spacing decreases, F_2 folds become more abundant, and the sense of asymmetry between S_1 and S_2 indicating top-down becomes more apparent. Their axes trend parallel to the basement-supracrustal contact and their axial planes dip moderately to the northwest. Rare F_1 folds were observed at locality #3 (Fig. 4A); axes of these folds trend east-west and moderately plunge to the west. Locally, the enveloping surface of F_1 folds strikes parallel to S_2 , suggesting progressive rotation of F_1 axes into parallelism with F_2 during formation of F_2 and S_2 . Within 250 m of the basement-supracrustal contact, S_2 becomes the only visible foliation, for S_1 has been completely overprinted, and close to the basement-supracrustal contact, S_2 parallels the contact.

The actual contact between the supracrustals and dome rocks is not exposed along the Lake Michigamme traverse, but its location can be identified to within 50 m. In the contact region, dome-rock and supracrustal foliation and compositional layering are concordant to one another and dip moderately to the northwest (Fig. 4B), suggesting that the contact itself is moderately dipping to the northwest at the northwest end of the Twin Lake Dome.

Republic Trough

Deformational features in the Republic Trough could be observed in the Republic Pit (an inactive iron-ore mine) and in roadcuts along M95. The Republic Pit, located at the southeast termination of the Republic Trough (Fig. 3A), provided a nearly complete cross section of the Republic Trough prior to its flooding, and shows that Marquette Range Supergroup metasediments within the trough have been folded into a tight-isoclinal synclinorium whose limbs have near-vertical dips (Fig. 3B). The axis of this fold plunges at $\sim 5^\circ$ – 15° to the northwest. A strong vertical schistosity has developed in the metasediments, and this schistosity is axial planar to the synclinorium. On the northeast limb of the trough, relict S_0 (as defined by lithologic contrasts) is vertical and parallel to the basement-supracrustal contact (i.e., parallel to the dome-keel contact). S_0 on the southwest limb of the trough is slightly discordant to the contact in the Republic Pit. However, the basement-supracrustal contact is defined by a steep shear zone several meters wide in which fabrics have locally been transposed into parallelism with the contact. The basement-supracrustal contact on the northeast limb of the synclinorium is not exposed. Within the trough, metasediments are complexly deformed by both mesoscopic folding and shear zones. Most shear zones within the trough are nearly vertical and strike nearly parallel to the Republic Trough trend. Shear zones near the southeast termination of the trough, however, are spaced and fan outwards to the southeast (Fig. 3A), resembling those produced in the models of interdiapir synclines by Dixon and Summers (1983).

The Republic Trough contains abundant amphibolite sills that are folded along with the supracrustals. They are generally relatively homogenous and appear internally undeformed, but contain quartz veins which are locally isoclinally folded with an axial plane approximately parallel to the Republic Trough, indicating the sills are, in fact, intensely internally deformed.

Outcrop-scale fold structure in the Michigamme Formation is beautifully displayed in roadcuts along the M95 traverse. Metamorphism has transformed the strata into thin layers (<1 cm to several cm thick) of alternating quartz-grunerite-garnet biotite schist and psammitic layers of biotitic quartzite which representing primary layering. Bedding (S_0) has been isoclinally folded and is nearly parallel to foliation that is well developed within schistose layers. Axial planes to these isoclinal folds parallel the Republic Trough trend, and fold axes range from moderately to steeply plunging to the northwest, to near horizontal and slightly plunging to the southeast. The

prominent foliation in the schistose layers occasionally transects isoclinal fold axes of primary layering at a slight angle. Folds locally display asymmetry that reverses at the outcrop scale. This change in asymmetry at the outcrop scale and lack of continuous exposure across the trough of appropriate lithologies makes the use of fold asymmetry for constraining map-scale shear sense across the trough essentially impossible.

Microstructures within garnet-biotite-quartz \pm grunerite \pm muscovite \pm chlorite schists of the Michigamme and Negaunee Formations provide evidence for the relative timing of deformation and Paleoproterozoic metamorphism in the Republic Trough. Foliation is defined by compositional layering, by alignment of biotite, and, locally, by quartz with a shape-preferred orientation (elongated quartz grains). Compositional layering at the thin section scale is defined by <1–3 mm thick layers with variable biotite and/or grunerite content. Generally, garnet porphyroblasts possess biotite-rich strain caps and associated strain shadows. The predominant biotite foliation is locally deflected around the garnets, indicating garnet growth is at least partially pre- to syntectonic relative to the main biotite foliation. However, garnet has locally partially overgrown its strain cap, truncating aligned biotite where euhedral edges of garnet are growing within the cap. This indicates the latest stages of garnet growth occurred during or after the predominant biotite foliation-forming event. Locally, an early biotite foliation preserved within garnet pressure shadows is oblique to the predominant foliation. Furthermore, garnet locally contains an internal foliation defined by aligned quartz inclusions that are oblique to the predominant foliation. This preserved foliation within garnet and garnet pressure shadows is interpreted as S_1 , and the predominant foliation as S_2 . Grunerite occurs as elongated prisms and locally defines a very steep down-dip lineation within S_2 foliation. Garnet cores in grunerite-bearing rocks contain randomly oriented grunerite inclusions, while garnet rims locally overgrow aligned grunerite. These garnet-grunerite relationships indicate initial garnet growth was pre- S_2 and syn- S_2 in grunerite-bearing rocks, and that the steep grunerite lineations formed during the S_2 event. Muscovite locally occurs as porphyroblasts crosscutting S_2 biotite foliation, and chlorite locally partially replaces biotite. These late muscovite and chlorite occurrences are attributed to a late retrograde event.

Summary of Structural Features

In summary, rocks within the Republic Trough and along the western edge of Twin Lake Dome are poly-deformed and strongly foliated. The first foliation (S_1), an east-west-striking slaty cleavage to schistosity, formed during regional metamorphism (biotite-grade and lower). This foliation is axial-planar to F_1 , a set of east-west-trending, open-to-tight folds, and can be observed in the region to the northwest of the Republic Trough. The second foliation (S_2) formed during higher-grade metamorphism and is found only near the contact between domes and keels. Because of the narrowness of the Republic Trough, S_2 development in the Republic Trough has almost

completely transposed S_1 , which is only locally observed. At a distance from the dome-keel contact west of Twin Lake Dome, S_2 is an asymmetric crenulation cleavage, but closer to the contact, it evolves into a strong schistosity that parallels the dome-keel contact; where this happens, S_1 can no longer be identified in outcrops. Thus, the dome-keel contacts are shear zones, and kinematic indicators require keel-side down sense of shear. Grunerite + garnet was stable during S_2 development. These minerals continued through to the latter stages of the second foliation-forming event. Muscovite and chlorite growth occurred either during the cooling portion of the P-T path or during a later retrograde event. Available data does not allow us to decipher whether there was one prolonged metamorphic event, or if there were several metamorphic events. Our results concur with those of Klasner (1978), who stated that peak metamorphism in the Lake Michigamme area was contemporaneous with the development of S_2 structural fabric. He found rotation of staurolite porphyroblasts and synkinematic garnet growth during S_2 development.

Approaching the western margin of the Twin Lake Dome contact, F_1 fold axes and bedding rotate away from their regional orientations, and tight-to-isoclinal folds develop. Axes of these folds have a shallow plunge and trend nearly parallel to the dome-keel contact trace, and the axial planes of these folds strike nearly parallel to the dome-keel contact trace and dip moderately to the west. Adjacent to the dome-keel contact, we can only identify one set of folds, which we interpret to be F_2 folds, because S_2 is axial planar to them.

It is important to note that S_1 fabric is the dominant regional fabric in the Lake Michigamme area. Here, S_2 is localized to the vicinity of the domes. But in the Republic Trough area, S_1 fabric has been almost completely destroyed by S_2 fabric. Because S_2 structures are strongly developed adjacent to domes, we conclude, as did Klasner (1978), that D_2 structures are related to dome emplacement.

U-Pb CHRONOLOGY

Previous Studies, Purpose, and Procedure

Previous geochronologic work by Van Schmus and Woolsey (1975) indicates that the majority of rocks within the Southern Complex are Late Archean in age (2500–2800 Ma.). Their dates are based on Rb/Sr whole rock ages that show a wide range of ages for the same unit (the Bell Creek Gneiss).

Schneider et al. (1996) have used $^{40}\text{Ar}/^{39}\text{Ar}$ dating methods to constrain cooling ages and uplift in the region. They obtained dates in the range of 1720–1680 Ma, considerably younger than the main phase of the Penokean orogeny.

We have dated two granitoid samples using U-Pb zircon geochronology. The first sample that we dated comes from the Bell Creek Gneiss–Bell Creek Granite, and the second date is on granite within the Palmer Gneiss. Our purpose in determining these ages was to determine if both rocks are Archean, or if

they could possibly represent Penokean magmatism. See Table 1 for analytical data and Figure 7 for concordia plots.

USSM-36 (Granite from the Bell Creek Assemblage)

Sample USSM-36 is coarse-grained granite from the Bell Creek Assemblage with moderately aligned feldspar phenocrysts ranging from 1 cm to 2 cm in length. The sample was collected at a roadcut just north of the Michigamme River bridge along M95 (5140401N, 423897E, UTM Zone 16 NAD27; #12, Fig. 2). Although the megacrysts in this sample are slightly smaller than those of the average Bell Creek Gneiss, it is a good representative of the Bell Creek Gneiss as a whole. The Bell Creek Gneiss at this location exhibits an obscure but gradational contact with migmatites of the Twin Lake Assemblage.

This sample yielded brown zircons of which three fractions were processed for dating. Two fractions consisted of single grains of zircons and the third fraction consisted of two zircon grains. All three fractions are discordant and collinear defining a single discordia (Fig. 7A). The discordia has an upper intercept age of 2613.6 \pm 4.1–3.7 Ma and lower intercept age of 1187

Ma. The upper intercept age is interpreted to represent the age of granite emplacement, and the lower intercept may represent some average age of Pb-loss.

OSSM-12 (Granitoid in the Palmer Gneiss)

Sample OSSM-12 was taken from the Palmer Gneiss near Palmer (5142015N, 456906E, UTM Zone 16 NAD27; OSSM-12, Fig. 2). It is a medium-grained, foliated, pink weathering, sheared granite which contains elongated quartz streaks defining a weak lineation within the foliation. We analyzed the Palmer Gneiss because it occurs along the basement-supracrustal contact on the border of the Marquette trough. Thus, it was possible that the Palmer Gneiss could be either a portion of the Twin Lake Assemblage or a portion of the Marquette Range Supergroup intruded by granitoids. If it were the latter, its age could help constrain the timing of dome formation.

This sample yielded a population of brown zircon prisms high in uranium. Three fractions were processed for this sample, but one fraction was not completely dissolved and was not used in the regression of data. Of the two fractions used, one was a

TABLE 1. ZIRCON U-Pb ISOTOPE DILUTION ANALYSES FOR SAMPLES FROM THE SOUTHERN COMPLEX

FRACTIONS		CONCENTRATIONS					ATOMIC RATIOS					AGE [Ma]			
No.	Properties	Wt. [μ g]	Pb rad [ppm]	U [ppm]	Pb com [pg]	Th/U	$\frac{^{206}\text{Pb}}{^{204}\text{Pb}}$	$\frac{^{207}\text{Pb}}{^{206}\text{Pb}}$	\pm	$\frac{^{207}\text{Pb}}{^{235}\text{U}}$	\pm	$\frac{^{206}\text{Pb}}{^{238}\text{U}}$	\pm	$\frac{^{207}\text{Pb}}{^{206}\text{Pb}}$	\pm
	(1)	(2)	(2)	(2)	(3)	(4)	(5)	(6)		(6)		(6)		(6)	
PALMER GNEISS															
OSSM-12															
1	2gr, cl,c,r	1	612	940	2.4	0.618	6,702	0.19962	27	15.1532	240	0.55057	110	2823.1	2.2
2	1 gr, br,st-f,pr, i	2	663	1011	4.2	0.667	12,533	0.19900	38	15.07/84	371	0.54955	170	2818.0	3.1
BELL CREEK GRANITE															
USSM-36															
3	2 gr,cl,br,r,st- pr,A	2	388	712	3.2	0.476	12,807	0.17353	10	11.5958	179	0.48465	77	2592.0	0.9
4	1 gr, cl,br,st-pr,A	1	635	1193	2.5	0.383	10,239	0.17359	8	11.5527	135	0.48267	55	2592.6	0.8
5	1 gr,cl,br,st-pr,A	1	628	1292	6.0	0.294	3,109	0.16867	10	10.4841	146	0.45080	62	2544.5	1.0

Notes:

- (1) All analyses are of zircon. Cardinal number indicates the number of zircon grains analyzed (e.g., 2 grains); all zircon grains were selected from non-paramagnetic separates at 0° tilt at full magnetic field in Frantz magnetic separator; br = brown; c = colorless; cl = clear; i = inclusions; st-pr = stubby prismatic. All grains air-abraded following Krogh (1982).
- (2) Concentrations are known to \pm 30% for sample weights of about 30 μ g and \pm 50% for samples < 3 μ g.
- (3) Corrected for 0.0125 mole fraction common-Pb in the $^{206}\text{Pb} - ^{235}\text{U}$ spike.
- (4) Calculated Th/U ratio assuming that all ^{206}Pb in excess of blank, common-Pb, and spike is radiogenic ($\lambda \text{ } ^{232}\text{Th} = 4.9475 \times 10^{-11} \text{ y}^{-1}$)
- (5) Measured, uncorrected ratio.
- (6) Ratio corrected for fractionation, spike, blank, and initial common-Pb (at the determined age from Stacey and Kramers, 1975). Pb fractionation correction = 0.094% / amu (\pm 0.025%, 1 σ); U fractionation correction = 0.111% / amu (\pm 0.02% 1 σ). U blank = 0.2 pg; Pb blank \leq 10 pg. Absolute uncertainties (1 σ) in the Pb/U and $^{207}\text{Pb}/^{206}\text{Pb}$ ratios calculated following Ludwig (1980). U and Pb half-lives and isotopic abundance ratios from Jaffey et al (1971).

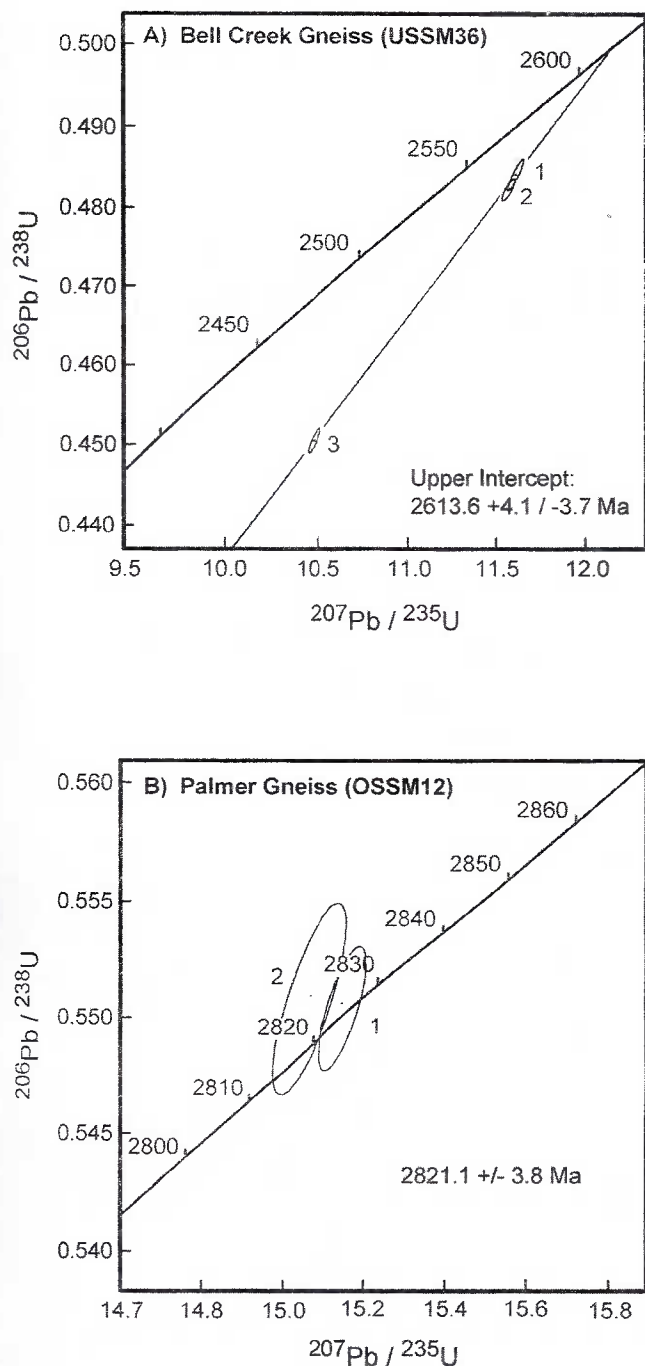


Figure 7. (A) Zircon U/Pb concordia plot for sample USSM-36. (B) Zircon U/Pb concordia plot for sample OSSM-12.

single zircon grain and the other was a two-grain fraction. The two fractions are overlapping concordia (Fig. 7B) with a mean $^{207}\text{Pb}/^{206}\text{Pb}$ age of 2821.1 ± 3.8 Ma, and are interpreted to be the granite's crystallization age.

Discussion of Geochronological Results

The two ages described above help clarify the tectonic history of the Southern Complex. The Bell Creek Gneiss was interpreted by Hoffman (1987), based on geochemistry, to represent a syntectonic granite, associated with collision of the Southern Complex with the Northern Complex along the Great Lakes tectonic zone at ca. 2.69 Ga. Field observations are compatible with this interpretation, for xenoliths in the assemblage have been folded, and rocks of the assemblage contain shear fabrics. Our date indicates that the tectonothermal event during which Bell Creek Assemblage granites were emplaced continued to 2614 Ma.

The 2821 Ma age of granitoids in the Palmer Gneiss region indicates the presence of gneiss in the Southern Complex region that predates the previously proposed timing of collision along the Great Lakes tectonic zone at 2.69 Ga. The location of the Palmer Gneiss and its age indicates the Palmer Gneiss should be classified as a unit within the Twin Lake Assemblage. Further, its age indicates that it does not represent the cooling of a Penokean magma, and thus that Penokean magma bodies have not been identified adjacent to the dome-keel contacts.

TECTONIC SYNTHESIS

The Republic region of the Penokean dome-and-keel province records a poly-orogenic history spanning a time interval of over 1.1 billion years. A granite-greenstone terrane that forms the basement of the region dates to at least 2821 Ma based on the age of granite in the Palmer Gneiss. At 2614 Ma, the Bell Creek Gneiss–Bell Creek Granite intruded into the overlying Twin Lake Assemblage. In the process, the Twin Lake Assemblage was intensely metamorphosed and penetratively deformed, and was arched into a dome shape. In effect, the Twin Lake Assemblage became a discontinuous carapace surrounding the Bell Creek Assemblage. We suggest that this geometry indicates that a phase of Archean gneiss dome formation (i.e., Archean dome-and-keel formation) affected the region. Although the exact mechanism leading to Archean dome formation is not fully constrained, emplacement of magma (Bell Creek Gneiss–Bell Creek Granite) in a domal geometry and development of poly-phase plastic flow folding in crystallized magma and its host rocks (Twin Lake Assemblage) indicates a hot environment and high rock mobility. If the Twin Lake assemblage has been correctly identified as the remnants of an Archean supracrustal terrane containing mafic-ultramafic volcanics and banded iron formation, the formation of this dome-and-keel structure could be viewed as a diapiric process driven by a density inversion. This early history led to the formation of dome-and-keel structure defined by the presence of granitoid domes surrounded by a carapace of overlying and intervening gneiss and migmatite. The regional-scale Twin Lake antiform is a consequence of this doming, so if our interpretation that the antiform developed during emplacement of the Bell Creek Gneiss–Bell Creek Granite

is correct, then this first "diapiric doming event" occurred at ca. 2614 Ma. Similar mechanisms may apply to the entire Penokean dome-and-keel belt and have been documented in numerous Archean dome-and-keel provinces throughout the world (Anhaeusser, 1984; Bouhallier et al., 1993).

In Paleoproterozoic time, the region was affected by the Penokean orogeny. This event resulted in the formation of a roughly east-west-trending fold-thrust belt involving Paleoproterozoic supracrustal rocks (the Marquette Range Supergroup). Formation of these structures was accompanied by development of a regional east-west-striking cleavage (S_1) that cuts across relict bedding (S_0). Near the domes, S_1 schistosity has been overprinted by a second foliation (S_2) that strikes roughly parallel to the dome borders. Immediately adjacent to the dome borders, shear zones have developed in which all previous fabrics are completely transposed into S_2 . The dome-parallel shear zones associated with (S_2) development generally trend parallel to the Twin Lake Assemblage-Bell Creek Assemblage contact in the Republic Trough and Lake Michigamme area. S_2 parallels the borders of the Republic Trough, suggesting the borders of the trough are shear zones. Discrete shear zones of similar orientation also occur within the interior of gneiss domes.

Petrographic analysis of rocks from the dome-border shear zones and basement shear zones paralleling the dome border indicates that the shear sense is uniformly supracrustal-side down, and S-C fabrics and lineations in the shear zones indicate that movement in the shear zones is dip slip. In this sense, the keels resemble steep-sided grabens or troughs with near-vertical borders. The relationship between foliation associated with keel formation and metamorphic mineral growth in Paleoproterozoic strata indicates that keel formation overlapped with peak metamorphism in the supracrustal rocks. This relationship implies that the formation of keels containing Marquette Range Supergroup strata occurred during the peak of metamorphism in the Republic node, after development of regional Penokean fold-thrust belt structures.

The majority of displacement between basement domes and overlying supracrustals occurred along discrete shear zones at or adjacent to the dome-keel contact itself. The deformation style experienced within the domes and within the keels during this event was quite different. Basement domes acted as rigid blocks with internal deformation occurring predominantly within discrete shear zones oriented parallel to subparallel to the dome-keel contacts and did not experience homogenous plastic flow folding, explaining why many pre-Penokean dikes within domes are not significantly deformed. However, within the Republic Trough, supracrustals experienced both displacement along shear zones oriented parallel to subparallel to the dome-keel contact, and complex homogenous plastic flow-folding during which tight to predominantly isoclinal folds developed.

The exact timing of movement along keel-parallel shear zones within the basement domes is uncertain, but it is unlikely the shear zones predate the Paleoproterozoic peak thermal event because rocks in shear zones still retain strained and dynamically

recrystallized quartz and feldspar grains. We suggest that if the dome-interior shear zones had formed before the regional peak thermal event reaching the sillimanite zone, quartz and feldspar grains within these zones would have been annealed. Because the shear zones along the borders of keels containing Paleoproterozoic strata generally follow the trace of the Archean dome boundaries (as defined by the outcrop distribution of the Twin Lake Assemblage and the foliation within it), Paleoproterozoic dome-and-keel formation was apparently controlled, in part, by the geometry of Archean dome-and-keel structure.

The formation of the Paleoproterozoic keels is a manifestation of regional extensional strain (their borders are younger-side-down shear zones), and because it occurred after the main stage of the Penokean orogeny, we concur with earlier proposals (Holm and Lux, 1996; Marshak et al., 1997; Rose et al., 2003) that the formation of keels containing Paleoproterozoic strata (e.g., the Republic Trough) could be a manifestation of Penokean orogenic collapse. We emphasize that Paleoproterozoic dome-and-keel structure near Republic, though a consequence of regional extension, does not resemble metamorphic core complex structure such as that which formed during Cenozoic extension in the southern Basin and Range. Unlike core-complex structure, the dome-and-keel structure of the Republic area does not display regionally uniform shear sense, there is not an abrupt contrast in metamorphic grade across the basement-supracrustal contact, and the supracrustal terrane away from domes is not diced up by major normal faults. The steepness of the keel-bounding shear zones gives the impression that extension in the Republic area represents crustal-scale boudinage (Marshak, 1999). A crustal-scale boudinage process explains the difference in deformation style exhibited by basement domes and overlying-intervening supracrustals discussed above. The domes acted as competent bodies while the supracrustals flowed downward between domes, resulting in complex tight-to-isoclinal folding in the supracrustals.

CONCLUSIONS

The Southern Complex region underwent two distinct periods of dome-and-keel formation. The first period occurred during the Archean and likely involved diapiric rise of basement into overlying supracrustals, producing plastically deformed domes of silicic-intermediate gneiss, migmatite, and granitoid (Fig. 8A). The second stage of dome-and-keel formation occurred in the Paleoproterozoic and was a consequence of displacement on steep, dip-slip shear zones (Fig. 8B). This structure is possibly a manifestation of Penokean orogenic collapse (Marshak et al., 1997). Paleoproterozoic dome-and-keel formation occurred during the peak of metamorphism associated with the Republic metamorphic node. The rough parallelism of Archean domal structures and lithologies with Paleoproterozoic dome-cover contacts suggest preexisting structures controlled the reactivation and emplacement of domes during the Paleoproterozoic. The existence of clearly post-Penokean hornblende cooling

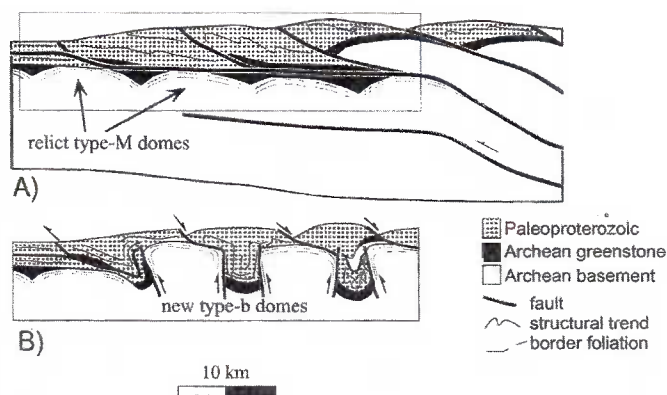


Figure 8. Tectonic model showing the development of solid-state domes during a postorogenic collapse event. (A) Preexisting domal architecture in basement overlain by a fold-thrust belt during a compressional orogenic event. (B) Reactivation of preexisting basement domes during a postorogenic collapse event and development of dome-and-keel architecture in previous fold-thrust belt. From Marshak et al., 1997.

ages (Holm and Lux, 1996; Holm et al., 1998) is most compatible with dome emplacement after the compressional phase of the Penokean orogeny. The recent finding of post-compressional extension structures in supracrustals of the Penokean orogenic belt (Gregg and Saja, 1998) is further evidence for a post-Penokean extensional event.

The regionally developed Republic metamorphic node outlined by James (1955) clearly indicates a spatial relationship between Paleoproterozoic metamorphism and basement domes. Our study indicates that peak metamorphism in the Paleoproterozoic occurred during development of dome-and-keel structure. Attoh (2000) presented thermal modeling results from northern Michigan and attributed Republic metamorphic node metamorphism in the Marquette Range Supergroup sequence to heating by adjacent Archean gneiss enriched in radiogenic elements. We therefore conclude that the formation of the Republic metamorphic node is a direct consequence of rise and emplacement of hot Archean gneiss domes into the overlying banded iron formation-rich Marquette Range Supergroup.

ACKNOWLEDGMENTS

Funding for this research was provided by the Morris M. and Ada B. Leighton Award and the Department of Geology at the University of Illinois, and by a University of Illinois Research Board grant to S. Marshak. We thank R.D. Tucker for performing the isotope analysis and providing the zircon U-Pb ages. Ted Bornhorst provided valuable discussions and field maps of Southern Complex geology. Ian Steele generously assisted with electron microprobe analyses at the University of Chicago. We thank Dan Holm and Sven Morgan for providing

valuable reviews of this manuscript, and Fernando Alkmim for helpful discussions.

REFERENCES CITED

- Anhaeusser, C.R., 1984, Structural elements of Archaean granite-greenstone terranes as exemplified by the Barberton Mountain Land, southern Africa, in Kroener, A., and Greiling, R., eds., *Precambrian tectonics illustrated*: Stuttgart, Federal Republic of Germany (Naeglele u. Obermiller), p. 57–78.
- Anhaeusser, C.R., Mason, R., Viljoen, M.J., and Viljoen, R.P., 1969, Reappraisal of some aspects of Precambrian shield geology: *Geological Society of America Bulletin*, v. 80, p. 2175–2220.
- Attoh, K., 2000, Contrasting metamorphic record of heat production anomalies in the Penokean Orogen of northern Michigan: *Journal of Geology*, v. 108, p. 353–361, doi: 10.1086/314406.
- Attoh, K., and Klasner, J.S., 1989, Tectonic implications of metamorphism and gravity field in the Penokean orogen of northern Michigan: *Tectonics*, v. 8, p. 911–933.
- Attoh, K., and van der Muelen, M.J., 1984, Metamorphic temperatures in the Michigamme Formation compared with the thermal effect of an intrusion, northern Michigan: *Journal of Geology*, v. 92, no. 4, p. 417–432.
- Beck, W., and Rama Murthy, V., 1991, Evidence for continental crustal assimilation in the Hemlock Formation flood basalts of the Early Proterozoic Penokean orogen, Lake Superior region: *U.S. Geological Survey Bulletin* 1904-I, p. 11–124.
- Bouhallier, H., Choukroune, P., and Balleve, M., 1993, Diapirism, bulk homogeneous shortening and transcurrent shearing in the Archaean Dharwar Craton; the Holenarsipur area, southern India: *Precambrian Research*, v. 63, no. 1–2, p. 43–58, doi: 10.1016/0301-9268(93)90004-L.
- Cannon, W.F., 1975, Geologic map of the Republic quadrangle, Marquette County, Michigan: U.S. Geological Survey, Miscellaneous Investigation Series, Map I-862.
- Cannon, W.F., and Klasner, J.S., 1976, Geologic map and geophysical interpretation of the Witch Lake quadrangle, Marquette, Iron, and Baraga Counties, Michigan: U.S. Geological Survey, Miscellaneous Investigation Series, Map I-987.
- Cannon, W.F., and Simmons, G.C., 1973, Geology of part of the Southern Complex, Marquette district, Michigan: *Journal of Research, U.S. Geological Survey*, v. 1, p. 165–172.
- Dixon, J.M., and Summers, J.M., 1983, Patterns of total and incremental strain in subsiding troughs: experimental centrifuged models of inter-diapir synclines: *Canadian Journal of Earth Sciences*, v. 20, p. 1843–1861.
- Gregg, W.J., 1993, Structural geology of parautochthonous and allochthonous terranes of the Penokean orogeny in Upper Michigan—Comparisons with Northern Appalachian tectonics: *U.S. Geological Survey Bulletin* 1904-Q, p. Q1–Q28.
- Gregg, W.J., and Saja, D.B., 1998, Field evidence for orogenic collapse, examples from the Penokean Orogeny of Upper Michigan [abs.]: *Geological Society of America Abstracts with Programs*, v. 30, no. 7, p. A-95.
- Hodges, K.V., and Spear, F.S., 1982, Geothermometry, geobarometry and the Al_2SiO_5 triple point at Mt. Moosilauke, New Hampshire: *American Mineralogist*, v. 67, p. 1118–1134.
- Hoffman, M.A., 1987, *The Southern Complex: Geology, geochemistry, mineralogy and mineral chemistry of selected uranium- and thorium-rich granites* [Ph.D. thesis]: Houghton, Michigan, Michigan Technological University, 382 p.
- Hoisch, T.D., 1990, Empirical calibration of six geobarometers for the mineral assemblage quartz+muscovite+biotite+plagioclase+garnet: *Contributions to Mineralogy and Petrology*, v. 104, p. 225–234.
- Holm, D.K., and Lux, D.R., 1996, Core complex model proposed for gneiss dome development during collapse of the Paleoproterozoic Penokean orogen, Minnesota: *Geology*, v. 24, p. 343–346, doi: 10.1130/0091-7613(1996)0242.3.CO;2.
- Holm, D.K., Darrach, K.S., and Lux, D.R., 1998, Evidence for widespread ≈1760 Ma metamorphism and rapid crustal stabilization of the Early Proterozoic (1870–1820 Ma) Penokean Orogen, Minnesota: *American Journal of Science*, v. 298, p. 60–81.
- Holm, D.K., Van Schmus, W.R., and MacNeill, L.C., 2001, Age of the Humboldt Granite, northern Michigan; implications for the origin of the Republic metamorphic node, in Mudrey, M.G., Jr., ed., 47th Annual

- Meeting, Institute on Lake Superior Geology, Proceedings, Program, and Abstracts: Institute on Lake Superior Geology, v. 47, p. 31–32.
- Jaffey, A.H., Flynn, K.F., Glendenin, L.E., Bentley, W.C., and Essling, A.M., 1971, Precision measurement of half-lives and specific activities of ^{235}U and ^{238}U : *Physical Review*, v. 4, p. 1889–1906, doi: 10.1103/PHYSREVC.4.1889.
- James, H.L., 1955, Zones of regional metamorphism in the Precambrian of northern Michigan: *Geological Society of America Bulletin*, v. 66, p. 1455–1488.
- Klasner, J.S., 1978, Penokean deformation and associated metamorphism in the western Marquette Range, northern Michigan: *Geological Society of America Bulletin*, v. 89, p. 711–722.
- Krogh, T.E., 1982, Improved accuracy of U-Pb zircon dating by the creation of more concordant systems using an air abrasion technique: *Geochimica et Cosmochimica Acta*, v. 46, p. 637–649, doi: 10.1016/0016-7037(82)90165-X.
- Ludwig, K.R., 1980, Calculation of uncertainties of U-Pb isotope data: *Earth and Planetary Science Letters*, v. 46, p. 212–220, doi: 10.1016/0012-821X(80)90007-2.
- Mahlburg, S.E., 1969, Precambrian geology of the Republic Trough, Marquette County, Michigan [M.S. thesis]: University of Illinois, 152 p.
- Marshak, S., 1999, Deformation style way back when: Thoughts on the contrasts between Archean/Paleoproterozoic and contemporary orogens: *Journal of Structural Geology*, v. 21, p. 1175–1182, doi: 10.1016/S0191-8141(99)00057-7.
- Marshak, S., Alkmim, F.F., and Jordt-Evangelista, H., 1992, Proterozoic crustal extension and the generation of dome-and-keel structure in an Archean granite-greenstone terrane: *Nature*, v. 357, p. 491–493, doi: 10.1038/357491A0.
- Marshak, S., Tinkham, D., Alkmim, F., Brueckner, H., and Bornhorst, T., 1997, Dome-and-keel provinces formed during Paleoproterozoic orogenic collapse–core complexes, diapirs, or neither?: Examples from the Quadrilatero Ferrifero and the Penokean orogen: *Geology*, v. 25, no. 5, p. 415–418, doi: 10.1130/0091-7613(1997)0252.3.CO;2.
- Peterman, Z.E., Zartman, R.E., and Sims, P.K., 1980, Tonalitic gneiss of Early Archean age from northern Michigan, in Morey, G.B., and Hanson, G.N., eds., *Selected studies of Archean gneisses and Lower Proterozoic rocks, southern Canadian Shield (S.S. Goldich Volume)*: Geological Society of America Special Paper 182, p. 125–134.
- Rose, S., Schneider, D.A., Loofboro, J., and Holm, D.K., (2003), Results and implications of monazite geochronology from the central Penokean orogen, WI & MI [abs.]: *Geological Society of America Abstracts with Programs*, v. 35, no. 6, p. 505 (abstract 206-8).
- Schneider, D., Holm, D., and Lux, D., 1996, On the origin of Early Proterozoic gneiss domes and metamorphic nodes, northern Michigan: *Canadian Journal of Earth Sciences*, v. 33, p. 1053–1063.
- Schulz, K.J., Sims, P.K., and Peterman, Z.E., 1988, A post-tectonic rare-metal-rich granite in the Southern Complex, Upper Peninsula, Michigan, in Klasner, J.S., ed., *34th Annual Meeting, Institute on Lake Superior Geology, Proceedings, Program, and Abstracts: Institute on Lake Superior Geology, Abstracts*, v. 34, p. A95–A96.
- Sims, P.K., 1991, Great Lakes Tectonic Zone in Marquette area, Michigan—Implications for Archean Tectonics in North-Central United States: *U.S. Geological Survey Bulletin 1904-E*, p. E1–E17.
- Sims, P.K., 1992, Geologic map of Precambrian rocks, southern Lake Superior region, Wisconsin and northern Michigan: U.S. Geological Survey, Miscellaneous Investigations Series, Map I-2185.
- Sims, P.K., 1996, Regional tectonic elements, in Sims, P. K., and Carter, L.M.H., eds., *Archean and Proterozoic geology of the Lake Superior region, U.S.A., 1993*: U.S. Geological Survey Professional Paper: Reston, Virginia, U.S. Geological Survey, p. 95–99.
- Sims, P.K., and Peterman, Z.E., 1976, Geology and Rb/Sr ages of reactivated Precambrian gneisses and granite in the Marenisco-Watersmeet area, northern Michigan: *Journal of Research of the U.S. Geological Survey*, v. 4, p. 405–414.
- Sims, P.K., Peterman, Z.E., Prinz, W.C., and Benedict, F.C., 1984, Geology, Geochemistry, and Age of Archean and Early Proterozoic Rocks in the Marenisco-Watersmeet Area, Northern Michigan: *Geological Survey Professional Paper 1292-A*, A1–A25.
- Sims, P.K., Anderson, J.L., Bauer, R.L., Chandler, V.W., Hanson, G.N., Kalliokoski, J., Morey, G.B., Mudrey, M.G., Jr., Ojakangas, R.W., Peterman, Z.E., Schulz, K.J., Shirey, S.B., Smith, E.I., Southwick, D.L., and Weiblen, P.W., 1993, The Lake Superior region and Trans-Hudson orogen, in Reed, J.C., Jr., Bickford, M.E., Houston, R.S., Link, P.K., Randin, D.W., Sims, P.K., and Van Schmus, W.R., eds., *Precambrian: Conterminous U.S.: Boulder, Colorado, Geological Society of America, Geology of North America*, v. C-2, p. 11–120.
- Stacey, J.S., and Kramers, J.D., 1975, Approximation of terrestrial lead isotope evolution by a two-stage model: *Earth and Planetary Science Letters*, v. 26, p. 207–221, doi: 10.1016/0012-821X(75)90088-6.
- Tinkham, D.K., 1997, Tectonic evolution of the Southern Complex region of the Penokean orogenic belt, Upper Peninsula, Michigan: The formation of Precambrian dome-and-keel architecture [M.S. thesis]: University of Illinois at Urbana-Champaign, 151 p.
- Van Schmus, W.R., and Woolsey, L.L., 1975, Rb-Sr geochronology of the Republic area, Marquette County, Michigan: *Canadian Journal of Earth Sciences*, v. 12, p. 1723–1733.

MANUSCRIPT ACCEPTED BY THE SOCIETY APRIL 8, 2004

Age and petrology of the Kaapinsalmi sanukitoid intrusion in Suomussalmi, Eastern Finland



ESA HEILIMO^{1)*}, PERTTU MIKKOLA²⁾ AND JAANA HALLA³⁾

¹⁾ Department of Geology, P.O. Box 64, FI-00014, University of Helsinki, Finland

²⁾ Geological Survey of Finland, P.O. Box 1237, FI-70211, Kuopio, Finland

³⁾ Geological Museum, Finnish Museum of Natural History, P.O. Box 11, FI-00014, University of Helsinki, Finland

Short Communication

Key words: intrusions, sanukitoids, geochemistry, absolute age, U/Pb, zircon, Neoproterozoic, Kaapinsalmi, Suomussalmi, Finland

*Corresponding author email: esa.heilimo@helsinki.fi

1. Introduction

Sanukitoids (high Mg-granitoids) are a group of distinctive Neoproterozoic granitoids, which differ in chemical composition from the voluminous tonalite-trondhjemite-granodiorite (TTG) suite. Shirey and Hanson (1984) first introduced the term sanukitoid to refer to mantle-derived rocks, which resemble high-Mg andesites, known as sanukites in the Miocene Setouchi belt of Japan. Stern et al. (1989) defined sanukitoid geochemistry as $\text{SiO}_2 = 55 - 60 \%$, $\text{MgO} > 6 \%$, $\text{Mg\#} > 60$, $\text{Sr} > 600 - 1800 \text{ ppm}$, $\text{Ba} > 600 - 1800 \text{ ppm}$, $\text{Cr} > 100 \text{ ppm}$, $\text{Ni} > 100 \text{ ppm}$ and LREE enriched compared to HREE. The term sanukitoid series has been introduced for granitoids with relatively high Mg#, MgO, Sr, Ba, Cr and Ni at any given silica level (Lobach-Zhuchenko et al., 2005). Sanukitoids composition shows some similarities to adakites (Martin, 1999) and to recently described Neoproterozoic Closepet-granites (Moyen et al., 2001).

Interpretation of the geochemistry of sanukitoids is controversial. High Mg#, MgO, Ni and Cr implies

that sanukitoids are mantle-derived rocks, but high Sr, Ba and LREE suggest crustal origin (Stern & Hanson, 1991). These aspects of sanukitoid geochemistry have been explained with a two-stage process, which includes Archean subduction. In the first stage, melts and/or fluids derived from a subducting basaltic slab enriched the overlying mantle wedge with Sr, Ba and LREE. Later melting of the enriched mantle generated sanukitoid magmas (Stern & Hanson, 1991; Kovalenko et al., 2005). Pb isotopic studies indicate that subducted sediments may also have played an important role in the sanukitoid petrogenesis (Halla, 2005). Sanukitoids might thus be the first sign of existence of an enriched mantle wedge and the beginning of the modern style of plate tectonics (Martin & Moyen, 2005).

Sanukitoids have been found in many Archean cratons and most of them are ~2.7 Ga in age (Rollinson & Martin, 2005). The ~3.0 Ga sanukitoids from the Ukrainian Shield (Artemenko et al., 2003), the

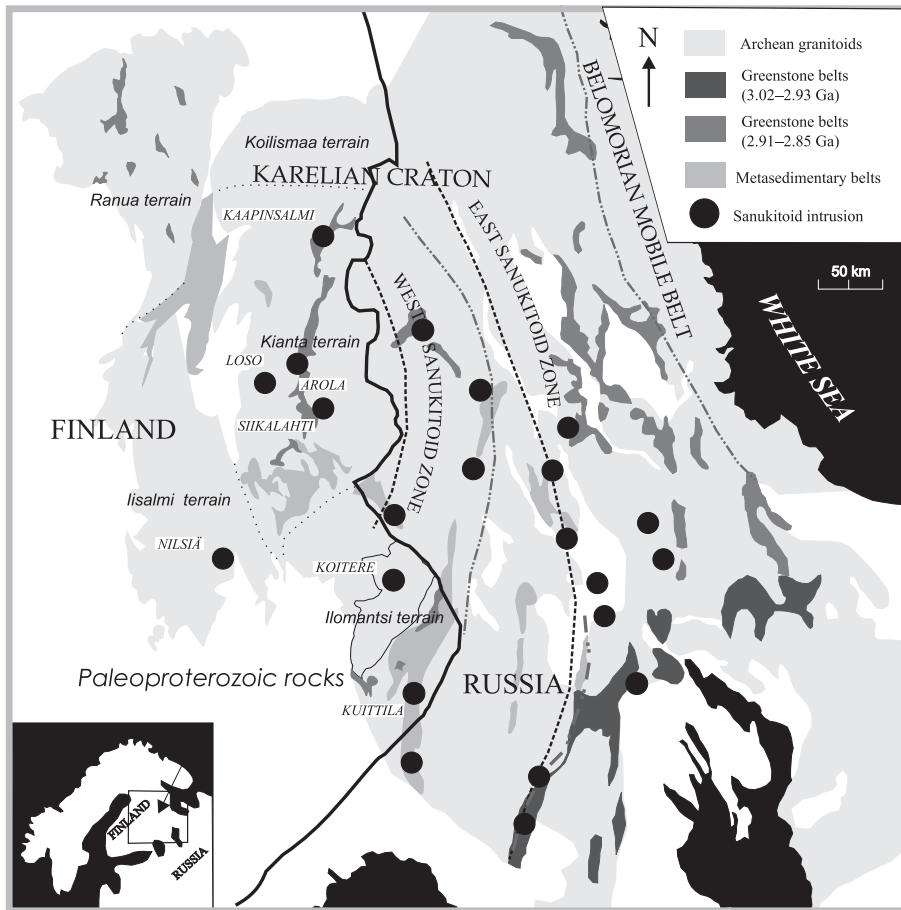


Fig. 1. Geological map of the Karelian craton and sanukitoid intrusions. Sanukitoid zones and Russian sanukitoids are from Lobach-Zhuchenko et al. (2005); Loso, Arola and Siikalahti sanukitoids are from Käpyaho et al. (2006); and Koitere and Nilsia sanukitoids are from Halla (2005). General features of the map according to Koistinen et al. (2001) and Sorjonen-Ward & Luukkonen (2005).

~2.9 Ga sanukitoids from the Pilbara craton (Smithies & Champion, 2000), and the ~2.89 Ga sanukitoids from the Amazonian craton (Oliveira et al., 2006) are the only sanukitoid intrusions known to be older than ~2.7 Ga.

More than 20 sanukitoid intrusions have been found in the Karelian craton. Sanukitoid intrusions in the Russian part of the Karelian craton are divided into Eastern and Western sanukitoid zones, which differ in composition and age (Lobach-Zhuchenko et al., 2005; Bibikova et al., 2005). Seven sanukitoid intrusions located in Finland have been described:

Kuittila (O'Brien et al., 1993), Nilsia, Koitere (Halla, 2005), Arola, Loso, Siikalahti (Käpyaho et al., 2006; Käpyaho 2006) and the recently recognised Kaapinsalmi sanukitoid intrusion (Heilimo, 2006a; 2006b) (Fig. 1). This paper describes in more detail the petrology of the Kaapinsalmi sanukitoid intrusion.

2. Geological setting

The Kaapinsalmi sanukitoid intrusion is located in Suomussalmi, in the Kianta terrain on the western margin of the Archean Karelian craton (Fig. 1). The

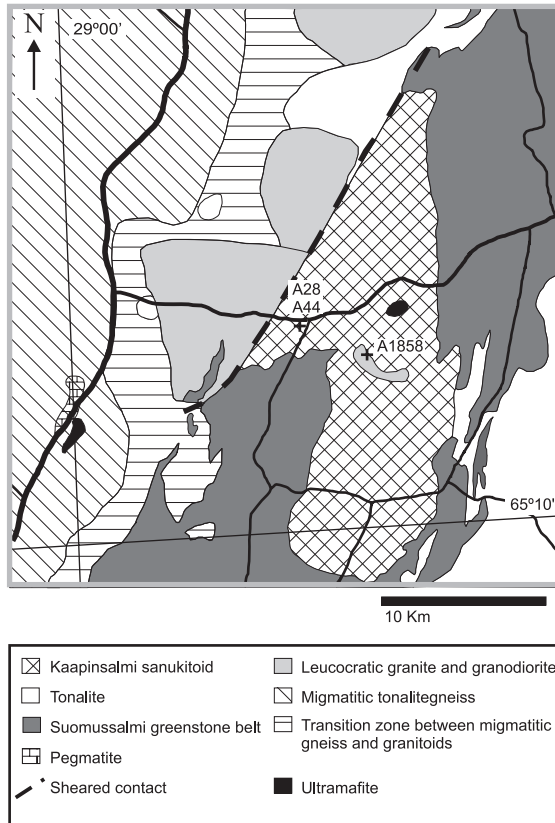


Fig. 2. Geological map of the Kaapinsalmi area, showing the locations of the dated samples. The greenstone belt is modified from Sorjonen-Ward & Luukkonen (2005).

Kianta terrain is a granite-greenstone terrain consisting mostly of migmatitic gneisses, greenstone belts, paragneisses and granitoids (Sorjonen-Ward & Luukkonen, 2005). Migmatitic Päivärinta gneiss in the vicinity of Kaapinsalmi has mesosome aged 2.83 – 2.84 Ga and leucosome aged between 2.70 – 2.67 Ga (Käpyaho et al., 2007). Greenstone belts in the Kianta terrain have been tectonically segregated into Tipasjärvi, Kuhmo, and Suomussalmi greenstone belts. The ages of the greenstone belts are between ~2.80 – 2.83 Ga (Luukkonen, 1992). Nurmes-type paragneisses in the Kianta terrain evidently have protolith ages as young as ~2.71 – 2.69 Ga (Kontinen et al., 2007). Granitoids of the Kianta terrain are metamorphosed, but they have preserved their magmatic texture. Käpyaho et al. (2006) and Käpyaho (2006) have divided the Kianta granitoids into three magmatic

episodes: 1) TTG-granitoids 2.83 – 2.74 Ga, 2) sanukitoids 2.74 – 2.70 Ga and 3) leucocratic granites and granodiorites 2.70 – 2.68 Ga.

The Kaapinsalmi sanukitoid lies adjacent to the western margin of the Suomussalmi greenstone belt (Fig. 2). It has intrusive contacts with the greenstone belt and contains greenstone xenoliths, contacts with granitoids are sheared and no contact has been observed with migmatitic gneisses. Within the Kaapinsalmi sanukitoid there is a small, brecciating intrusion of leucogranodiorite called Kivilahti. The Kaapinsalmi sanukitoid is mineralogically tonalite and also contains melatonalite inclusions. The texture of the Kaapinsalmi sanukitoid is granular and mortar. The major minerals are plagioclase, quartz, hornblende and biotite, while accessory minerals include microcline, sphene, allanite, apatite, zircon and opaque minerals. The secondary minerals are biotite, epidote, sericite, saussurite, chlorite and carbonate.

3. Geochemistry

The Kaapinsalmi sanukitoid and melatonalite inclusions display distinct sanukitoid characteristics: low SiO_2 and high $\text{Mg}\#$, MgO , Ni , Cr (Fig. 3). The Kaapinsalmi sanukitoid is intermediate (SiO_2 56.0 – 66.8 %) and has high $\text{Mg}\#$ (51.3 – 64.2). There is a 2.8 – 7.4 % variation in MgO , while Ni and Cr abundances are greater compared to eastern Finland TTGs. The K_2O content of the Kaapinsalmi sanukitoid is 0.8 – 2.7 %, while Sr varies between 206 ppm and 643 ppm and Ba from 316 ppm to 1366 ppm. Melatonalite inclusions of the Kaapinsalmi sanukitoid have slightly higher $\text{Mg}\#$ and higher contents of MgO , Ni and Cr than the Kaapinsalmi sanukitoid, with Cr abundances of up to 626 ppm and Ni abundances of up to 221 ppm; respective numbers for the Kaapinsalmi sanukitoid are 408 ppm and 207 ppm. The Kaapinsalmi sanukitoid and inclusions both have fractionated REE patterns with higher HREE than average eastern Finland TTG. Average $(\text{La}/\text{Lu})_n$ for the Kaapinsalmi sanukitoid is 21.2 and for the melatonalite inclusions 12.2 (Fig. 4).

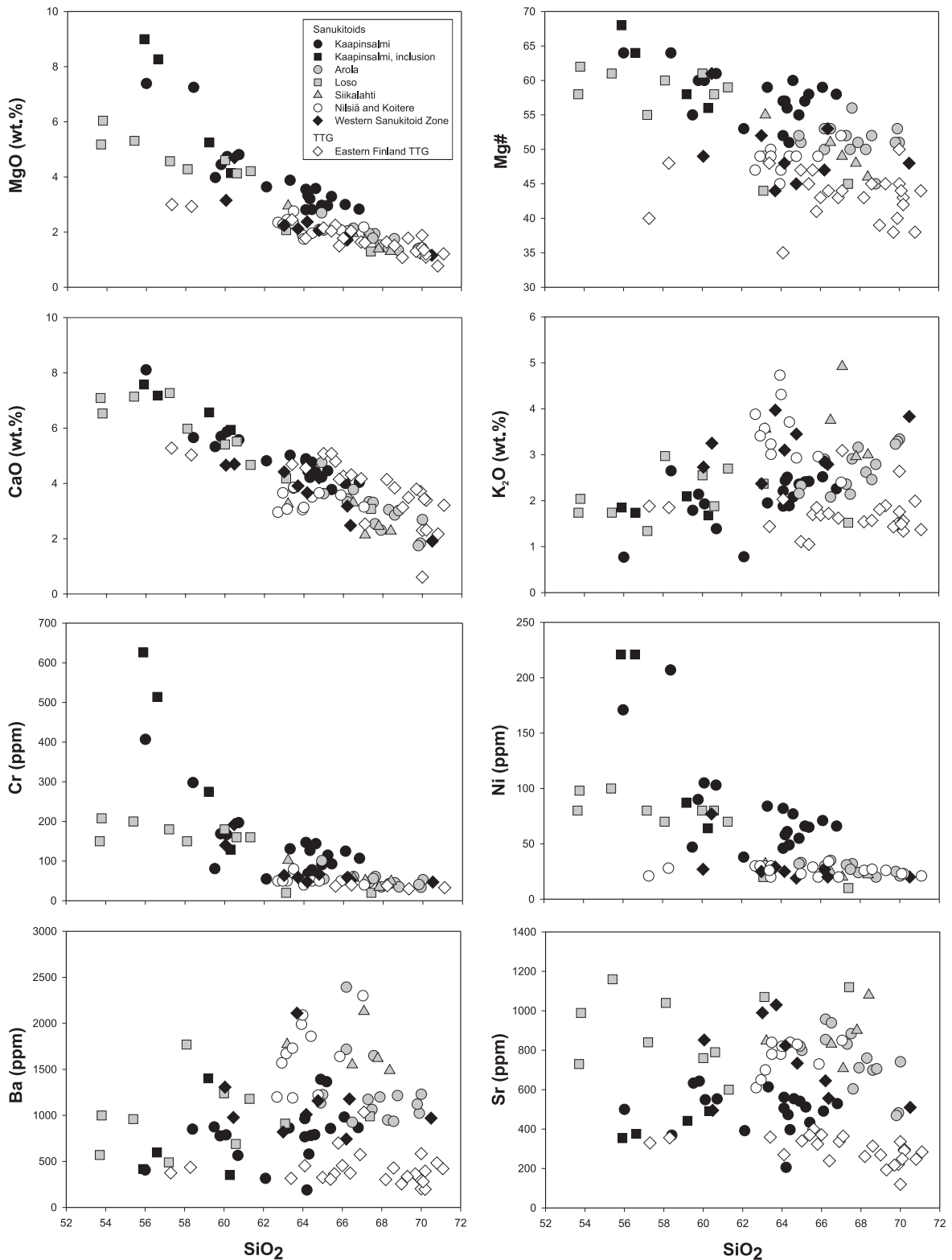


Fig. 3. Selected Harker diagrams illustrating geochemistry of West Karelian craton sanukitoids and TTGs. Data for Kaapinsalmi sanukitoid is from Heilimo (2006b); Arola, Loso, Siikalahti sanukitoids and Eastern Finland TTG data from Käpyaho (2006); data for Nilsia and Koitere sanukitoids from Halla (2005) and that for Western sanukitoid zone is from Lobach-Zhuchenko et al. (2005).

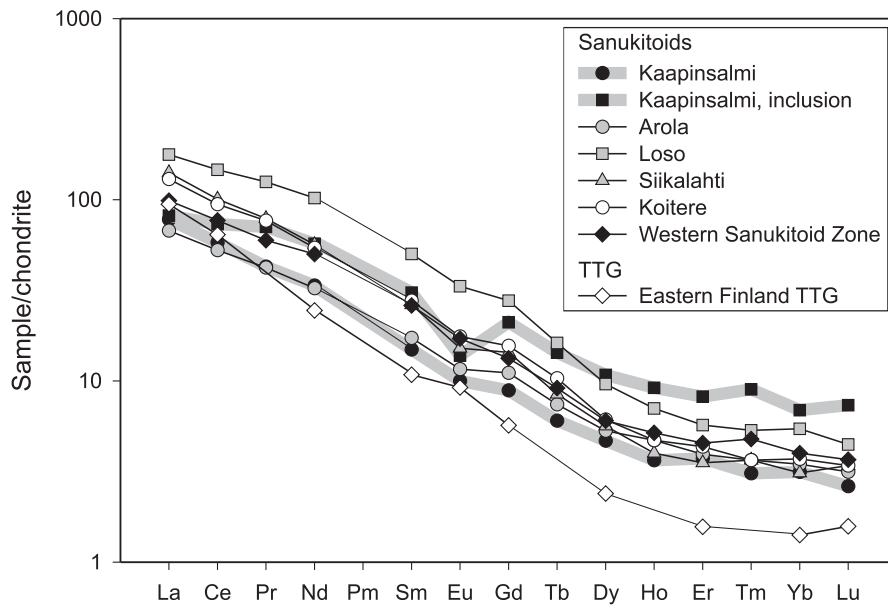


Fig. 4. Representative chondrite normalised REE-patterns of West Karelian craton sanukitoids and Eastern Finland TTG (normalisation values from Taylor & McLennan, 1985). Kaapinsalmi sanukitoid data from Heilimo (2006b); Arola, Loso, Siikalahti sanukitoids analyses after Käpyaho (2006); Nilsä and Koitere data from Halla (2005); Western sanukitoid zone data from Lobach-Zhuchenko et al. (2005) and Eastern Finland TTG patterns after Martin (1987).

4. U-Pb dating methods

Two samples from the Kaapinsalmi sanukitoid were collected for U-Pb dating (A28 by Eero Pehkonen and A44 by Erkki Luukkonen, see Fig. 2). U-Pb samples were treated with methods described by Vaasjoki (2001) in 1978 and 1981 by Olavi Kouvo and staff of the isotopic laboratory of Geological Survey of Finland. Samples were washed, crushed and sorted on a wet shaking table and then treated with heavy liquids (bromofrom and Clerici™) and a Frantz magnetic separator. Zircon and sphene grains were selected for analysis by handpicking. U and Pb multigrain analyses were done using Krogh's method (1973). ^{235}U - ^{208}Pb -spiked and unspiked isotopic ratios were measured using thermal ionisation single collector mass spectrometer (TIMS) at the isotopic laboratory of Geological Survey of Finland, Espoo. U-Pb calculations were done with PbDat (Ludwig, 1991) and IsoPlot/Ex (Ludwig, 2003) programs.

5. U-Pb dating results

Zircons from the Kaapinsalmi sanukitoid were light brown and translucent in the heavy fraction. Crystal shapes were pyramidal and prismatic from subhedral to euhedral. Sample A28A was originally analysed by Kouvo & Tilton (1966) using old borax method and the resulting $^{207}\text{Pb}/^{206}\text{Pb}$ age was 2681 Ma. Afterwards, three discordant zircon fractions from sample A28 were analysed producing an upper intersect at 2718 ± 6 Ma. Additional sample A44 gave an upper intersect at 2719 ± 4 Ma, with two discordant zircon fractions and an almost concordant sphene fraction. Both ages are same within the error limits. A combined age of 2716 ± 9 Ma from both samples (A28 & A44) is thus a relatively good estimate of the Kaapinsalmi sanukitoid intrusion age (Fig. 5, Table 1).

Kivilahti leucogranodiorite located inside the Kaapinsalmi sanukitoid was also sampled (A1858) (see Fig. 2) for U-Pb dating. However, separation did not produce enough zircon or monazite for TIMS analysis.

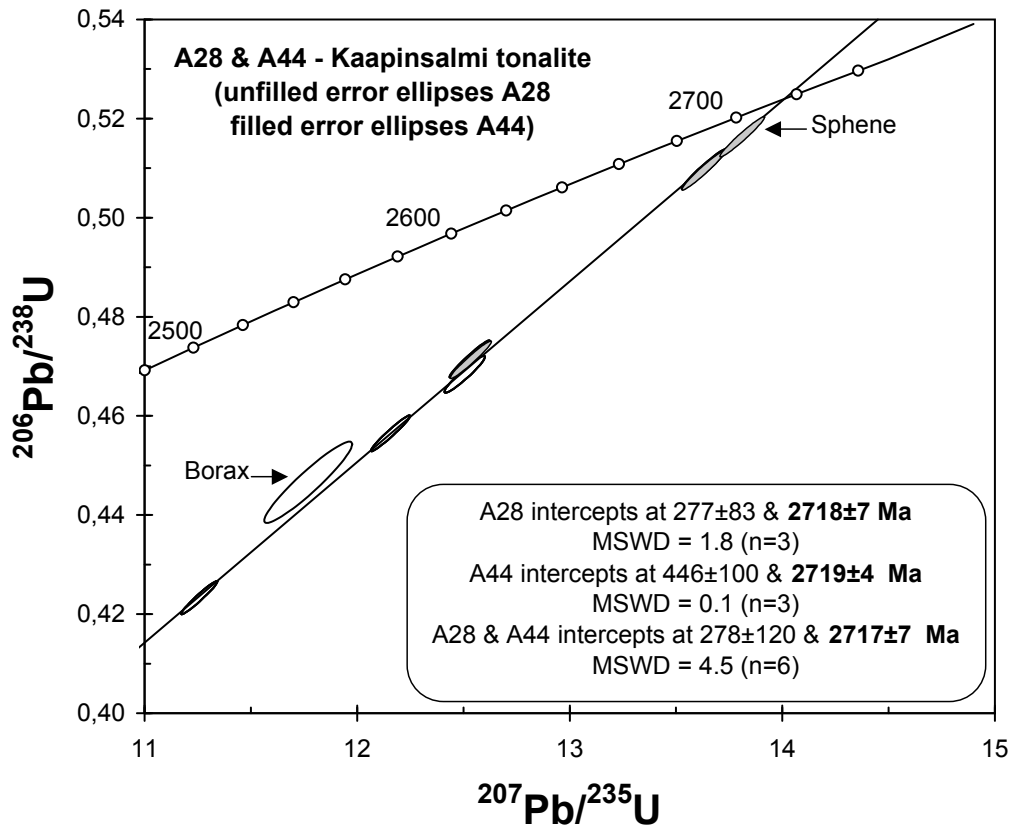


Fig. 5. Concordia diagram showing U-Pb isotopic data for the Kaapinsalmi sanukitoid. A28 fractions are unfilled error ellipses and A44 fractions are filled error ellipses. A44C sphene U-Pb isotopic data is included and A28A borax U-Pb isotopic data is excluded from the geochron (Kouvo and Tilton, 1966).

6. Discussion

In the Karelian craton, sanukitoids are younger than the surrounding TTG, implying that sanukitoids are not directly linked to the subduction processes that might have produced TTGs (Bibikova et al., 2005). The sanukitoid intrusions of the Russian part of the Karelian craton are divided into Eastern and Western sanukitoid zones (Lobach-Zhuchenko et al., 2005; Bibikova et al., 2005). The sanukitoid intrusions in the Eastern sanukitoid zone were formed 2.730 – 2.745 Ga ago. They are more mafic in composition, with higher MgO, Ni, Cr and lower Ba, Sr compared to the Western sanukitoid zone intrusions. The Eastern sanukitoid zone also shows more heteroge-

neity and a larger mantle-derived component than the Western sanukitoid zone. The Western sanukitoid zone is younger, with intrusions in the age range 2.700 – 2.720 Ga.

Location, age (~2.72 Ga) and composition of the Kaapinsalmi sanukitoid all show certain similarities to the Western sanukitoid zone (Figs. 1, 3 & 4), although the Mg#, MgO, Ni and Cr contents of the Kaapinsalmi sanukitoid are higher at their respective SiO_2 level than in the other west Karelian sanukitoids (Fig. 4). The Kaapinsalmi sanukitoid also has relatively low Ba and Sr contents when compared to those of the Western sanukitoid zone and other Finnish sanukitoids. Comparatively low K_2O , Ba, Sr and

Table 1. TIMS U-Pb data from the Kaapinsalmi tonalite (A28 & A44).

Sample information density	Sample weight/mg	U	Pb ppm	$^{206}\text{Pb}/$ ^{204}Pb	$^{208}\text{Pb}/^{206}\text{Pb}$	Isotopic ratios*				Rho**			Apparent ages / Ma		
						measured	radiogenic	$^{206}\text{Pb}/^{238}\text{U}$	2 σ %	$^{207}\text{Pb}/$ ^{235}U	2 σ %	$^{207}\text{Pb}/$ ^{206}Pb	2 σ %	$^{206}\text{Pb}/$ ^{238}U	$^{207}\text{Pb}/$ ^{235}U
A28-Kaapinsalmi tonalite															
A28A. Total (borax)	611.6	345	184	1588	0.168	0.4466	1.3	11.270	1.5	0.1831	0.5	0.94	2380	2546	2681
A28B. +4.6	23.6	270	153	2322	0.194	0.4684	0.7	12.006	0.7	0.1859	0.2	0.96	2476	2604	2706
A28C. 4.2-4.6	21.8	411	220	2158	0.147	0.4565	0.7	11.657	0.7	0.1852	0.2	0.97	2424	2577	2700
A28D. 3.8-4.0	5.9	638	307	2265	0.113	0.4233	0.7	10.757	0.7	0.1843	0.2	0.97	2275	2502	2692
A44-Kaapinsalmi tonalite															
A44A. +4.6/+200	24.2	170	106	12411	0.234	0.5098	0.7	13.131	0.7	0.1868	0.2	0.97	2655	2689	2714
A44B. 4.2-4.6	20.8	240	137	5746	0.210	0.4715	0.7	12.029	0.7	0.1850	0.2	0.97	2490	2606	2698
A44C. Sphene	31.2	57	40	499	0.257	0.5166	0.7	13.318	0.7	0.1870	0.3	0.91	2684	2702	2716

*) Isotopic ratios corrected for fractionation, blank and age related common lead (Stacey and Kramers, 1975).

**) Error correlation for $^{207}\text{Pb}/^{235}\text{U}$ vs. $^{206}\text{Pb}/^{238}\text{U}$ ratios.

A28A from Kouvo and Tilton (1966)

high MgO, Ni, Cr contents make the Kaapinsalmi sanukitoid a distinct sanukitoid in western part of the Karelian craton. The Rio Maria sanukitoid, located in the Amazonian craton in Brazil (Oliveira et al., 2006), is similar in composition to the Kaapinsalmi sanukitoid.

Current models for the petrogenesis of sanukitoids propose that fluids and/or melts from subducted basaltic slab and possible sediments enriched the overlying mantle wedge. Subsequent melting of the enriched mantle wedge then formed the sanukitoid magmas. Sanukitoids thus might contain material from three different sources: basaltic slab, sediments and mantle wedge (Stern & Hanson, 1991; Kovalenko et al., 2005; Halla, 2005). A probable source of MgO, Ni and Cr is the mantle wedge; and of K_2O , Ba and Sr the slab melts and/or fluids from a crustal component, possibly subducted sediments.

There are two possible explanations for the distinct composition of the Kaapinsalmi type sanukitoid: 1) Less involvement of recycled crust in the petrogenesis of the Kaapinsalmi type sanukitoid. This could explain the lower K_2O , Sr and Ba contents and higher MgO, Ni and Cr content. 2) Heterogeneity in the enrichment of the mantle wedge could also explain the composition of Kaapinsalmi type sanukitoid. If fluids and/or melts from the basaltic slab and possible sediments infiltrated the mantle wedge in an irregular manner, then partial melting of the less enriched parts of the wedge would have caused Kaapinsalmi type sanukitoid magmas. These two explanations are not mutually exclusive and could occur simultaneously.

7. Conclusions

The newly-recognised Kaapinsalmi intrusion has chemical composition similar to sanukitoid. Its age, location and certain compositional similarities indicate that it forms the northern extension of the Western sanukitoid zone of the Karelian craton. However, there are two important geochemical differences between the Kaapinsalmi sanukitoid and with other West Karelian sanukitoids:

1. The Kaapinsalmi sanukitoid has lower SiO₂ and higher MgO, Ni, and Cr contents compared to those of the other west Karelian sanukitoids, indicating that the primary source of the Kaapinsalmi sanukitoid was mantle peridotite.

2. The Kaapinsalmi sanukitoid has relatively low K₂O, Ba, and Sr concentrations. This might indicate smaller recycled crustal sediment component in the source of the Kaapinsalmi sanukitoid than in more felsic sanukitoids and/or mantle heterogeneity.

Acknowledgements

We would like to thank journal referee Svetlana Lobach-Zhuchenko for thoughtful review of the manuscript. Olavi Kouvo and staff of the isotopic laboratory of Geological Survey of Finland are acknowledged for isotopic determinations. Peter Sorjonen-Ward is thanked for comments and reviewing the language and Mikko Pitkänen for reviewing the language. This work was done as part of the GSF's regional bedrock mapping in the Suomussalmi area.

References

- Artemenko, G.V., Lobach-Zhuchenko, S.B., Krylov, I.N. & Orsa, V.I., 2003. Archean high-Mg granitoids (sanukitoids) in the Ukrainian Shield and its comparison with rocks of TTG suite. *Geophysical Research Abstracts* 5. Abstracts of the Contributions of the EGS-AGU-EUG Joint Assembly, Nice, France, 06–11 April, 2003. European Geophysical Society (CD-ROM).
- Bibikova, E.V., Petrova, A. & Claesson, S., 2005. The temporal evolution of sanukitoids in the Karelian craton, Baltic Shield: an ion microprobe U–Th–Pb isotopic study of zircons. *Lithos* 79, 129–145.
- Halla, J., 2005. Late Archean high-Mg granitoids (sanukitoids) in the Southern Karelian domain, Eastern Finland. *Lithos* 79, 161–178.
- Heilimo, E., 2006a. *Petrography and geochemistry of the Kaapinsalmi 2.72 Ga Sanukitoid intrusion*, Eastern Finland. *Bulletin of the Geological Society of Finland*, Special Issue 1, p. 47.
- Heilimo, E., 2006b. Kaapinsalmen sanukitoidin ja sitä ympäröivien granitoidien petrologia ja geokemia. Unpublished M.Sc. Thesis (available at request from the author), University of Helsinki, Finland, 62 p.
- Koistinen, T., Stephens, M.B., Bogatchev, V., Nordgulen, Ø., Wennerström, M. & Korhonen, J., (eds.), 2001. Geological map of the Fennoscandian Shield, scale 1:2 000 000. Geological Surveys of Finland, Norway, Sweden and the North-West department of Natural Resources of Russia.
- Kontinen, A., Käpyaho, A., Huhma, H., Karhu, J., Matukov, D.I., Larionov, A. & Sergeev, S.A., 2007. Nurmes paragneisses in Eastern Finland, Karelian craton: Provenance, tectonic setting and implications for Neoproterozoic craton correlation. *Precambrian Research* 152, 119–148.
- Kouvo, O. & Tilton, G., 1966. Mineral ages from the Finnish Precambrian. *Journal of Geology* 74, 421–442.
- Kovalenko, A., Clemens, J.D. & Savatkov, V., 2005. Petrogenetic constraints for the genesis of Archean sanukitoid suites: geochemistry and isotopic evidence from Karelia, Baltic Shield. *Lithos* 79, 147–160.
- Krogh, T.E., 1973. A low-contamination method for hydrothermal decomposition of zircon and extraction of U and Pb for isotopic age determinations. *Geochimica et Cosmochimica Acta* 37, 485–494.
- Käpyaho, A., 2006. Whole-rock geochemistry of some tonalite and high Mg/Fe gabbro, diorite, and granodiorite plutons (sanukitoid suite) in the Kuhmo district, Eastern Finland. *Bulletin of the Geological Society of Finland* 78, 121–141.
- Käpyaho, A., Mänttari, I. & Huhma, H., 2006. Growth of Archean crust in the Kuhmo district, Eastern Finland: U–Pb and Sm–Nd isotope constraints on plutonic rocks. *Precambrian Research* 146, 95–119.
- Käpyaho, A., Hölttä, P. & Whitehouse J.W. 2007. U–Pb zircon geochronology of selected Neoproterozoic migmatites in eastern Finland. *Bulletin of the Geological Society of Finland* 79, 95–115.
- Lobach-Zhuchenko, S.B., Rollinson, H.R., Cherkulaev, V.P., Arestova, N.A., Kovalenko, A.V., Ivanikov, V.V., Guseva, N.S., Sergeev, S.A., Matukov, D.I. & Jarvis, K.E., 2005. The Archean sanukitoid series of the Baltic Shield: geological setting, geochemical characteristics and implication for their origin. *Lithos* 79, 107–128.
- Ludwig, K.R., 1991. PbDat 1.21 for MS-dos: A computer program for processing Pb–U–Th isotope data. Version 1.08. U.S. Geological Survey Open-File Report 88–542, 35 p.
- Ludwig, K.R., 2003. Isoplot/Ex 3. A Geochronological Toolkit for Microsoft Excel. Berkeley Geochronology Center, Special Publication No. 4.
- Luukkonen, E.J., 1992. Late Archean and early Proterozoic structural evolution in the Kuhmo-Suomussalmi terrain, Eastern Finland. *Annales Universitatis Turkuensis. Sarja Ser. A.II. Biologica-Geographica-Geologica* 78, 113 p.
- Martin, H., 1987. Petrogenesis of of Archean trondhjemites, tonalites, and granodiorites from Eastern Finland: Major and trace elements geochemistry. *Journal of Petrology*, 28, 921–953.
- Martin, H., 1999. Adakitic magmas: modern analogues of Archean granitoids. *Lithos* 46, 411–429.

- Martin, H. & Moyen, J.-F., 2005. The Archaean-Proterozoic transition: Sanukitoid and Closepet type magmatism. *Mineralogical Society of Poland - Special papers Volume 26*, 57–68.
- Moyen, J.-F., Martin, H. & Jayananda, M., 2001. **Multi-element geochemical modeling of crust-mantle interactions during late-Archaean crustal growth: the Closepet granite (South Indian).** *Precambrian Research* 112, 87–105.
- O'Brien, H., Huhma, H. & Sorjonen-Ward, P., 1993. **Petrogenesis of the late Archaean Hattu Shist belt, Ilomantsi, Eastern Finland: geochemistry and Sr, Nd isotopic composition.** Geological Survey of Finland, Special Paper 17, 147–184.
- Oliveira, M.A., Dall'Agnol, R. & Althoff, F.J., 2006. Petrography and geochemistry of the Archaean sanukitoid Rio Maria granodiorite and mafic rocks associated, Rio Maria granite-greenstone terrane, Amazon craton. In: Dall'Agnol, R., Rosa-Costa, L.T. & Klein, E.L. (eds.) *Symposium on magmatism, crustal evolution, and metallogenesis of the Amazonian craton. Abstracts volume and field trips guide.* Belém, PRONEX-UFPA/SBG-NO, p. 29.
- Rollinson, H. & Martin, H., 2005. Geodynamic controls on adakite, TTG and sanukitoid genesis: implications for models of crust formation Introduction to the Special Issue. *Lithos* 79, ix–xii.
- Shirey, S.B. & Hanson, G.N., 1984. Mantle-derived Archaean monzodiorites and trachyandesites. *Nature* 310, 222–224.
- Sorjonen-Ward, P. & Luukkonen, E.J., 2005. Archaean rocks. In: Lehtinen M., Nurmi, P.A. & Rämö, O.T. (eds.) *Precambrian Geology of Finland – Key to the evolution of the Fennoscandian shield.* *Developments in Precambrian Geology* 14, Elsevier, Amsterdam, pp. 19–100.
- Smithies, R.H. & Champion, D.C., 2000. The Archaean high-Mg diorite suite: links to tonalite-trondhjemite-granodiorite magmatism and implications for early Archaean crustal growth. *Journal of Petrology* 41, 1653–1671.
- Taylor, S.R. & McLennan, S.M., 1985. **The continental crust: its composition and evolution.** Blackwell, Oxford, 312 p.
- Stacey, J.S. & Kramers, J.D., 1975. Approximation of terrestrial lead isotope evolution by two-stage model. *Earth and Planetary Science Letters* 26, 207–221.
- Stern, R.A., Hanson, G.N. & Shirey, S.B., 1989. Petrogenesis of mantle-derived, LILE-enriched Archaean monzodiorites and trachyandesites (sanukitoids) in southwestern Superior Province. *Canadian Journal of Earth Science* 26, 1688–1712.
- Stern, R.A. & Hanson, G.N., 1991. **Archaean high-Mg granodiorite: a derivative of light rare earth element-enriched monzodiorite of mantle origin.** *Journal of Petrology* 32, 201–238.
- Vaasjoki, M., 2001. Three decades of U–Pb mineral analyses at the Geological Survey of Finland. In: Vaasjoki, M. (ed.) **Radiometric age determinations from Finnish Lapland and their bearing on the timing of Precambrian volcano-sedimentary sequences.** Geological Survey of Finland, Special Paper 33, 9–13.

EXPRESS LETTER

URANIUM IN IRON OXIDE-COPPER-GOLD (IOCG) SYSTEMS

MURRAY W. HITZMAN[†]

Department of Geology and Geological Engineering, Colorado School of Mines, Golden, Colorado 80401

AND RICK K. VALENTA

Frontier Development Group Inc., 1066 West Hastings Street, Suite 1640, Vancouver, British Columbia, Canada V6E 3X1

Abstract

The Olympic Dam iron oxide-copper-gold (IOCG) deposit is currently the world's largest producer of uranium. Other IOCG deposits generally have anomalous, though uneconomic, uranium grades. The fluids that generate IOCG deposits are thought to be saline and highly oxidized and would be capable of leaching and transporting significant uranium. The reasons for uranium enrichment in certain IOCG deposits remain speculative but could include the composition of mineralization-related magmas, of the wall rocks altered by hydrothermal fluids or of the fluids mixing at the site of mineralization. There is sparse data available on uranium abundance in IOCG ores; there is even less reliable data on the uranium content of unaltered wall rocks for the deposits. However, the data that is available suggest that the uranium grade of IOCG deposits may be primarily related to the uranium content of their unaltered host rocks. Many IOCG deposits appear to have approximately 10 to 40 times enrichment in the ore compared to unaltered host rocks. This suggests that exploration for uranium-rich IOCG deposits should focus on areas with anomalously high uranium contents in host-rock sequences.

Introduction

The Olympic Dam deposit in Australia contains a measured resource of 650 million tons (Mt) of 500 g/t U₃O₈ (425 ppm U), 1.5 percent Cu, and 0.5 g/t Au (A. Michelmore, unpub. report for Citigroup Global Markets, 2004). The total resource in the deposit is estimated to be approximately 3.8 billion tons of 400 g/t U₃O₈ (339 ppm U), 1.1 percent Cu, and 0.5 g/t Au.

A number of other deposits of this class are in or nearing production (e.g., Ernest Henry, Selwyn, Osborne, Mt. Elliot, Eloise, and Prominent Hill, Australia; Candelaria and Manto Verde, Chile; Sossego, Cristalino, and Alemão/Igarapé Bahia, Brazil; Khetri, India; Guelb Moghrein, Mauritania; Dahongshan, China; Sin Quyen, Vietnam), but Olympic Dam is the only member of the class to produce uranium. Given the current interest in uranium exploration, IOCG deposits are being examined as possible targets.

IOCG deposits are a relatively recently recognized class of deposits (Hitzman et al., 1992; Williams et al., 2005). They range in age from Late Archean to the Pliocene and are found in a number of different tectonic settings (e.g., rift, subduction zone, basin collapse; Hitzman, 2000). They display a variety of morphologies but generally show a spatial relationship to major, crustal-scale fault zones. The metal content of the deposits is highly variable. Iron oxides are the dominant mineral gangue. The deposits are sought for copper and gold but may contain a host of trace metals, including light rare earth elements (predominantly Ce and La), silver, molybdenum, zinc, cobalt, lead, tungsten, bismuth, and uranium, as well as significant fluorine, boron, and chlorine.

IOCG deposits occur in mafic to felsic igneous, metamorphic, or sedimentary rocks. They are generally spatially and temporally associated with batholithic complexes of intermediate to felsic composition, although there is continuing debate about whether the deposits are genetically directly related to these magmas (Pollard, 2000) or whether these intrusive bodies simply provided the thermal energy to drive large-scale hydrothermal systems which resulted in metal scavenging from surrounding host rocks (Barton and Johnson, 2000). Whatever their origin, IOCG deposits are invariably associated with very large volumes of hydrothermally altered rocks (10 to over 100 km³; Hitzman, 2000).

The deposits share a characteristic suite of alteration types (Hitzman et al., 1992; Haynes, 2000). Magnetite-bearing sodic-calcic alteration, characterized by the development of replacive albite (scapolite) in more felsic host rocks and albite-actinolite-diopside (scapolite) in more mafic rocks, is the dominant alteration type in most IOCG systems. Potassic alteration generally postdates sodic-calcic alteration. This style of alteration is also commonly replacive, unlike the vein-controlled alteration in porphyry systems, and is characterized by the formation of orthoclase-magnetite in more felsic rocks and biotite-magnetite in more mafic rocks. Hematite may replace, or form instead of, magnetite in structurally high-level systems. A number of IOCG deposits contain late and structurally high-level zones of hydrolytic alteration characterized by the replacement of earlier alteration assemblages by martite (hematite after magnetite), sericite, carbonate minerals, and quartz. Copper-gold and other metals may be precipitated during any of the alteration stages, but significant mineralization is most common during potassic alteration,

[†] Corresponding author: e-mail, mhitzman@mines.edu

although the giant Olympic Dam deposit is associated with hydrolytic alteration (Reeve et al., 1990).

Uranium in IOCG Deposits and Their Host Rocks

Most IOCG deposits, including Olympic Dam, have extremely low uranium grades in comparison to other types of uranium deposits (Fig. 1, Table 1). Available data indicates that IOCG deposits have a range of uranium contents from negligible (Chilean deposits) to maximum grades of about 0.1 wt percent U_3O_8 (Olympic Dam and Oak Dam, Australia). Several prospects with higher grades (up to about 0.14% U_3O_8) are known (Michelin, Canada, and Valhalla, Australia) but their classification as IOCG deposits is not yet well established. The highest uranium grades in well established IOCG deposits overlap the field of uranium grades in sandstone-hosted uranium deposits (Dahlkamp, 1993). Based on the available data, IOCG deposits will probably be sources of uranium only where coproducts such as copper and gold are produced.

Uranium in IOCG deposits generally occurs as uraninite, although brannerite and coffinite have also been recognized in some deposits and prospects (Reeve et al., 1990; Hitzman et al., 1992). Uranium minerals are generally associated with copper-iron sulfides and occur within copper-enriched zones, commonly within potassically altered zones. Anomalous uranium is also commonly associated with late hydrolytic alteration in many systems, occurring with copper sulfides or in late quartz veins cutting earlier sulfide assemblages.

In many deposits and prospects, anomalous uranium also occurs outside zones of copper mineralization. Reconnaissance drilling around the Ernest Henry mine indicates that the deposit is surrounded by a broad (several kilometers wide) zone of weak uranium enrichment (R. Valenta, unpub.

data). A similar annulus of uranium enrichment is observed in radiometric surveys around the Sue-Diane deposit (Gandhi et al., 1996). Weak uranium mineralization is also observed from field relationships as a distal fringe in many of the Wernecke breccia bodies in the Yukon (Hitzman et al., 1992). It is suspected that dispersal of minor uranium beyond the core of hydrothermal alteration is common in many IOCG systems. Because alteration associated with many IOCG deposits is generally spatially extensive, it is challenging to determine what the background level of uranium in these systems was prior to alteration and mineralization.

Average continental crustal rocks have uranium contents of approximately 1 (Taylor and McLennan, 1995) to 1.5 ppm (Rudnick and Fountain, 1995). Basalts average 0.5 ppm U, whereas granites average 5 ppm U (Krauskopf, 1979), although there is a wide range of uranium contents in felsic intrusive rocks. Oxidized (magnetite-series) I- or A-type granites are spatially and temporally associated with many IOCG deposits, such as those of the Gawler craton, Australia (Creaser, 1996), Cloncurry, Australia (Pollard et al., 1998; Wyborn, 1998), and Carajás, Brazil (Lindenmayer, 1990; Barros et al., 1997) districts. These granites commonly contain relatively elevated uranium relative to other igneous rocks (Keppler and Wyllie, 1991; Keppler, 1993).

The relatively sparse data for IOCG deposits (Table 1) indicate highly variable uranium contents, although most appear to be anomalous compared to the expected uranium contents of their host rocks.

In addition to Olympic Dam, a number of other deposits in the Gawler craton of South Australia, notably Oak Dam and Prominent Hill, contain significant uranium (Table 1). The uranium contents of the Hiltaba granites, the host rocks for the Olympic Dam deposit, average 14 ppm U (Neumann et al., 2000). Similar rocks occur in the area of the Oak Dam deposit (Davidson and Paterson, 1993). The Prominent Hill deposit, which has somewhat lower uranium concentrations than Olympic Dam and Oak Dam, occurs in a mixed succession of metavolcanic and metasedimentary rocks with isolated Hiltaba suite igneous bodies (PIRSA, 2004).

IOCG deposits in the Cloncurry district of Australia also contain anomalous uranium (Pollard, 2000); copper-bearing hematite breccia bodies in the Valhalla prospect at Cloncurry have enriched values (~1,000 ppm U: Summit Resources, Press Release 8/30/05). The intrusive rocks of the Cloncurry district have a wide range of uranium contents (2–14 ppm: Pollard et al., 1998), and the highly variable uranium content of the host rocks may account for the variability in uranium grades of the deposits.

The IOCG deposits of the Carajás district in Brazil also have a range of uranium contents from approximately 30 to 50 ppm (Salobo and Sossego: Requia and Fontboté, 2000; Grainger et al., 2002; R. Leveille, pers. commun., 2005) to 99 to 170 ppm (Igarapé Bahia: Tazava and de Oliveira, 2000; Talarico et al., 2005). These deposits occur within a mixed metavolcanic-metasedimentary sequence that has been intruded by a variety of felsic to mafic igneous bodies. Several of the deposits are spatially and temporally associated with I- or A-type granites, but data on the uranium contents of these rocks is extremely sparse. Host rocks immediately adjacent to the Igarapé Bahia deposit have uranium contents averaging 5

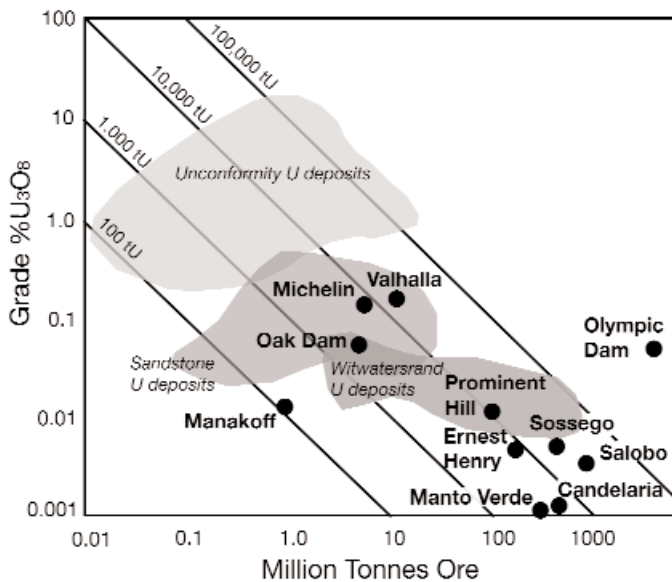


FIG. 1. Grade vs. tonnage plot for uranium in iron oxide-copper-gold (IOCG) deposits and prospects in relationship to the fields for unconformity-related uranium deposits, sandstone-hosted uranium deposits, and Witwatersrand uranium deposits (data from Dahlkamp, 1993). The IOCG deposits have a broad range of uranium contents. Although the giant Olympic Dam deposit has a relatively low uranium grade, it is currently the world's largest uranium producer.

TABLE 1. Uranium in IOCG Deposits

Deposit	Location	Tonnage (Mt)	U (ppm)	Cu %	Au g/t	Reference	Comments
Olympic Dam	Gawler craton, Australia	650	425	1.5	0.5	A. Michelmore (unpub. report for Citigroup Global Markets, 2004)	
Prominent Hill	Gawler craton, Australia	97	103	1.5	0.5	PIRSA (2004), Minotaur Resources Ltd, 2004 Annual Report	
Oak Dam	Gawler craton, Australia	~10	690	0.3		Davidson and Paterson (1993), Skirrow et al. (2002)	Estimated tonnage from data in Skirrow et al. (2002)
Ernest Henry	Cloncurry, Australia	167	50	1.1	0.5	Mark et al. (2000), R. Valenta (unpub. data, 2005)	
Monakoff	Cloncurry, Australia	1	~100	1.5	0.5	Davidson et al. (2002)	
Valhalla	Cloncurry, Australia	11.5	1,224			Uranium Information Center Ltd. www.uic.com.au/pmune.htm#valhalla (2005)	
Sossego	Carajas, Brazil	355	60	1	0.3	Williams et al. (2005), R. Leveille (pers. commun. 2005)	Structurally higher Sossego deposit with ~60 ppm U; structurally lower Sequeirinho deposit with <10 ppm U (Leveille, pers. commun., 2005)
Salobo	Carajas, Brazil	789	32–57	1	0.5	Grainger et al. (2002), Requia and Fontbote (2000)	Requia and Fontbote (2000) report a mean of 32 ppm from 4 samples; Grainger et al. (2002) report one sample with a value of 57 ppm
Igarape Bahia	Carajas, Brazil	219	99–170	1.4	0.9	Tallarico et al. (2005), Tazava and de Oliveira (2000)	Tallarico et al. (2005) report a mean of 170 ppm U from 10 samples of siderite breccia; Tazava and deOliveira (2000) report mean of 99 ppm U from 4 samples of siderite breccia and magnetite breccia
Candelaria	Chile	470	3–5	0.95	0.2	Marschik and Fontbote (2001), Marschik et al. (2000)	
Manto Verde	Chile	230	3	0.6	0.1	J. Benavides (pers. commun. 2005) with permission of Anglo American plc; Williams et al. (2005)	Benavides (pers. commun., 2005) reports magnetite ore ranges from 1.8–6.2 ppm U with a mean of 3.2 ppm U (34 samples) whereas hematite ore has a range of 0.9–5.3 ppm U with a mean of 2.3 ppm U (23 samples)
Sue-Dianne	Great Bear, NWT, Canada	10.6	<10	0.9		Goad et al. (2000)	Local zones of U enrichment to >3,000 ppm U
Michelin	Labrador, Canada	6.4	1,100			www.fronteergroup.com/s/CentralLabrador.asp (2005), R. Valenta (unpublished data, 2005)	

to 6 ppm U from six samples (Tazava and de Oliveira, 2000), but these values may represent a uranium halo to the deposit.

In Canada, the Michelin prospect in the Labrador Central mineral belt, which is being actively explored, is currently classified as an IOCG system based on the occurrence of mineralization in breccias with U, Cu, Au, and REE enrichment and magnetite- and/or hematite-bearing actinolite-albite-calcite alteration assemblages. Although the Michelin prospect contains relatively low copper, it is highly enriched in uranium, with an average of over 1,000 ppm U. Apparently unaltered felsic volcanic rocks of the Aillik sequence in the area of the deposit are also anomalous in uranium with an average of approximately 19 ppm (C. Payette and R. F. Martin, unpub. report for the Geological Survey of Canada project 24ST-23233-6-1281, 1987), whereas the average uranium content of Aillik volcanic sequence rocks, as sampled by Sinclair et al.

(2002) from the Makkovik Bay area 75 km away, is approximately 5 ppm. The high uranium values in the area of the Michelin prospect may represent a uranium-rich halo to the deposit or could be indicative of fertile source rocks for uranium. IOCG-style uranium occurrences in the Great Bear magmatic zone, Northwest Territories, Canada, are also reported to be spatially associated with uranium-enriched intrusive and volcanic rocks (Gandhi, 1994).

The Chilean IOCG deposits have the lowest uranium contents (high of 6 ppm at Manto Verde; Table 1) of all the IOCG deposits for which there are data. Although anomalous uranium is recognized in some Chilean IOCG prospects (Sillitoe, 2003; Productura: Fox, 2000; Minita-Despreciada: Espinoza et al., 1996; Gatico: Boric et al., 1990; Las Animas: Gelchich et al., 1998), the Chilean deposits appear, in general, to contain extremely low levels of uranium. The host rocks for these

deposits are comprised primarily of calc-alkaline basaltic andesites that also would be expected to have very low uranium contents. Analysis of 286 samples of host-rock andesites from the area of the Manto Verde deposit shows a range of uranium values from 0.05 to 6.2 ppm (overlapping the highest grades in the deposit; J. Benavides, pers. commun., 2005). It is suspected that the majority of these samples are from within the alteration system and thus do not represent true background values. Marschik et al. (2003) reported the geochemistry of samples from the Candelaria district and concluded that there is a preferential and homogeneous removal of uranium from these rocks in the broad alteration zone surrounding the deposits. However, the range of data (U contents of <2–11 ppm) suggests that both uranium depletion and enrichment are taking place within the alteration zone.

Discussion

The available evidence indicates that the uranium grade of IOCG deposits is highly variable. Many deposits appear to have a broad halo of weakly anomalous uranium in the alteration zone surrounding the deposit. High uranium values in IOCG deposits could be related to uranium-rich magmatic fluids from causative intrusions, particularly oxidized (magnetite-series) granites. Alternatively, uranium could be contributed by a second fluid mixing with hydrothermal fluids at the site of mineralization (cf. Haynes et al., 1995). However, the highly oxidizing fluids thought to be responsible for the broad-scale alteration in IOCG systems should be capable of leaching and transporting significant amounts of uranium. The available data suggests that the uranium content of some IOCG deposits may be directly related to the amount of uranium in the unaltered host-rock sequence (Fig. 2). This suggestion is not new. Haynes (2000) stated that hydrothermal fluids passing through felsic-dominated wall rocks would be relatively uranium rich, whereas those interacting with dominantly mafic rocks would be uranium poor. However, the source rocks apparently must be pre-enriched in uranium to be able to form uranium-rich IOCG deposits. IOCG deposits in which U may have been leached from host rocks contain approximately 10 to 40 times the average uranium content of

the unaltered source. Additional data are required to determine if the concentrations of copper and gold in IOCG deposits can also be related to the abundance of these elements in their unaltered host-rock sequence.

Exploration Implications

Most IOCG deposits contain insufficient uranium to be economically interesting for this commodity. However, the Olympic Dam deposit demonstrates that IOCG systems can form significant uranium orebodies. It is suggested that the host rocks for the IOCG hydrothermal system need to be enriched in uranium, as is the case with the Hiltaba granite suite in the Gawler craton, in order to form a uranium-rich IOCG deposit. Exploration programs targeted at locating uranium-rich IOCG deposits should concentrate on areas that contain suitable uranium-rich host rocks. Obvious candidates include high heat flow granites—those with anomalous uranium. For example, in the Mount Isa area there is a strong spatial association between uranium occurrences (Gregory et al., 2005) and the uranium-enriched (8–14 ppm U), high radiogenic heat-producing Sybella Granite (McLaren et al., 1999). Conversely, IOCG systems within intermediate to mafic calc-alkaline volcanic sequences, such as the subduction-related deposits of the Peruvian and Chilean coastal belt, would be expected to have low uranium contents. Iron oxide-rich systems with abundant uranium, but relatively low copper and/or gold values (e.g., Valhalla and Michelin), suggest that iron oxide uranium deposits exist and may be important exploration targets.

Acknowledgments

We gratefully acknowledge support from National Science Foundation grant EAR-0207217 to Hitzman for this work. The authors would also like to acknowledge a number of individuals (Jorge Benavides, Chris Carlson, Richard Leveille, and Derek Wilton) who provided unpublished data on uranium contents in IOCG deposits and their associated sequences. Andy Wilde is acknowledged for providing a synthesis of some of the grade-tonnage information for uranium deposits. The manuscript was significantly improved by comments from editor Mark Hannington and associate editor David Burrows.

August 16, December 15, 2005

REFERENCES

- Barros, C.E.M., Dall'Agnol, R., Barbey, P., and Boullier, A., 1997, Geochemistry of the Estrela granite complex, Carajas region, Brazil: An example of an Archean A-type granitoid: *Journal of South American Earth Sciences*, v. 10, p. 321–330.
- Barton, M.D., and Johnson, D.A., 2000, Alternative brine sources for Fe-oxide (-Cu-Au) systems: Implications for hydrothermal alteration and metals, in Porter, T.M. ed., *Hydrothermal iron oxide-copper-gold and related deposits: A global perspective*: Adelaide, Australia, Australian Mineral Foundation, p. 43–60.
- Boric, P.R., Diaz, F.F., and Maksae, J.V., 1990, Geología y yacimientos metalíferos de la Región de Antofagasta: *Servicios Nacional Geología Minera Bolletín*, v. 40, p. 1–246.
- Creaser, R.A., 1996, Petrogenesis of a Mesoproterozoic quartz-lattice-granitoid suite from the Roxby Downs area, South Australia: *Precambrian Research*, v. 79, p. 371–394.
- Dahlkamp, F.J., 1993, *Uranium ore deposits*: Berlin-Heidelberg, Springer-Verlag, 460 p.

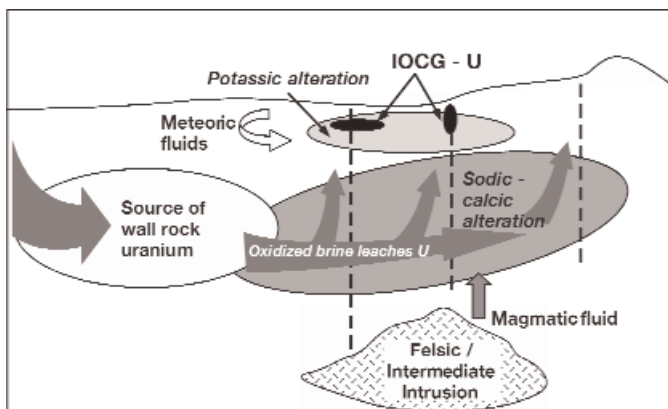


FIG. 2. Schematic model for the formation of uranium-rich IOCG deposits. In this model, uranium-rich IOCG deposits probably require a rich source of wall-rock uranium within the host-rock sequence altered as part of the IOCG system. Additional uranium could also be contributed by magmatic or meteoric fluids.

- Davidson, G.J., and Paterson, H.L., 1993, Oak Dam East: A prodigious uranium-bearing, massive oxide body on the Stuart shelf [abs.]: Geological Society of Australia Abstracts, v. 34, p. 18–19.
- Davidson, G.J., Davis, B.K., and Garner, A., 2002, Structural and geochemical constraints on the emplacement of the Monakoff oxide Cu-Au (-Co-U-REE-Ag-Zn-Pb) deposit, Mt. Isa inlier, Australia, in Porter, T.M., ed., Hydrothermal iron oxide-copper-gold and related deposits: A global perspective: Linden Park, Australia, Porter GeoConsultancy Publishing, v. 2, p. 49–76.
- Espinoza, S.R., Veliz, H.G., Squirrel, J.L., Arias, J.F., and Moraga, A.B., 1996, The cupriferous province of the Coastal Range, northern Chile: Society of Economic Geologists Special Publication 5, p. 19–32.
- Fox, K.A., 2000, Fe-oxide (Cu-U-Au-REE) mineralization and alteration at the Productura prospect: Unpublished M.S. thesis, Golden, CO, Colorado School of Mines, 141 p.
- Gandhi, S.S., 1994, Geological setting and genetic aspects of mineral occurrences in the southern Great Bear magmatic zone, Northwest Territories: Geological Survey of Canada Bulletin 475, p. 63–96.
- Gandhi, S.S., Prasad, N., and Charbonneau, B.W., 1996, Geological and geophysical signatures of a large polymetallic exploration target at Lou Lake, southern Great Bear magmatic zone, Northwest Territories: Geological Survey of Canada Current Research 1996–E, p. 147–158.
- Gelchich, E.S., Espinoza, P.C., and Vivallo, S.W., 1998, Yacimientos metalíferos de las Hojas Chañaral y Diego de Almagro, Región de Atacama: Servicios Nacional Geología Minería Mapa Recursos Mineral Chile 3:17.
- Goad, R.E., Mumin, A.H., Duke, N.A., Neale, K.L., Mulligan, D.L., and Camier, W.J., 2000, The NICO and Sue-Dianne Proterozoic, iron oxide-hosted, polymetallic deposits, Northwest Territories: Application of the Olympic Dam model in exploration: Exploration and Mining Geology, v. 9, p. 123–140.
- Grainger, C.J., Groves, D.I., and Costa, C.H.C., 2002, The epigenetic sediment-hosted Serra Pelada Au-PGE deposit and its potential genetic association with Fe-oxide Cu-Au mineralization within the Carajás mineral province, Amazon craton, Brazil, in Porter, T.M., ed., Hydrothermal iron oxide-copper-gold and related deposits: A global perspective: Linden Park, Australia, Porter GeoConsultancy Publishing, v. 2, p. 227–246.
- Gregory, M.J., Wilde, A.R., and Jones, P.A., 2005, Uranium deposits of the Mount Isa region and their relationship to deformation, metamorphism, and copper deposition: ECONOMIC GEOLOGY, v. 100, p. 537–546.
- Haynes, D.W., 2000, Iron oxide copper (-gold) deposits: Their position in the ore deposit spectrum and modes of origin, in Porter, T.M., ed., Hydrothermal iron oxide-copper-gold and related deposits: A global perspective: Linden Park, Australia, Porter GeoConsultancy Publishing, v. 2, p. 71–90.
- Haynes, D.W., Cross, K.C., Bills, R.T., and Reed, M.H., 1995, Olympic Dam ore genesis: A fluid mixing model: ECONOMIC GEOLOGY, v. 90, p. 281–307.
- Hitzman, M.W., 2000, Iron oxide-Cu-Au deposits: What, where, when, and why, in Porter, T.M., ed., Hydrothermal iron oxide-copper-gold and related deposits: A global perspective: Adelaide, Australia, Australian Mineral Foundation, p. 9–25.
- Hitzman, M.W., Oreskes, N., and Einaudi, M.T., 1992, Geological characteristics and tectonic setting of Proterozoic iron oxide (Cu-U-Au-LREE) deposits: Precambrian Research, v. 58, p. 241–287.
- Keppler, H., 1993, Influence of fluorine on the enrichment of high field strength trace elements in granitic rocks: Contributions to Mineralogy and Petrology, v. 114, p. 479–488.
- Keppler, H., and Wyllie, P.J., 1991, Partitioning of Cu, Sn, Mo, W, U and Th between melt and aqueous fluid in the systems haplogranite-H₂O-HCl and haplogranite-H₂O-HF: Contributions to Mineralogy and Petrology, v. 109, p. 139–150.
- Krauskopf, K.B., 1979, Introduction to geochemistry: New York, McGraw-Hill, 617 p.
- Lindenmayer, Z.G., 1990, Salobo sequence, Carajás, Brazil: Geology, geochemistry and metamorphism: Unpublished Ph.D. thesis, London, ON, University of Western Ontario, 406 p.
- Mark, G., Oliver, N.H.S., Williams, P.J., Valenta, R.K., and Crookes, R.A., 2000, The evolution of the Ernest Henry Fe-oxide-(Cu-Au) hydrothermal system, in Porter, T.M., ed., Hydrothermal iron oxide-copper-gold and related deposits: A global perspective: Adelaide, Australia, Australian Mineral Foundation, p. 123–136.
- Marschik, R., and Fontboté, L., 2001, The Candelaria-Punta del Cobre iron oxide Cu-Au (-Zn-Pb) deposits, Chile: ECONOMIC GEOLOGY, v. 96, p. 1799–1826.
- Marschik, R., Leveille, R.A., and Martin, W., 2000, La Candelaria and the Punta del Cobre district, Chile: Early Cretaceous iron-oxide Cu-Au (-Zn-Pb) mineralization, in Porter, T.M., ed., Hydrothermal iron oxide-copper-gold and related deposits: A global perspective: Adelaide, Australia, Australian Mineral Foundation, p. 163–176.
- Marschik, R., Chiaradia, M., and Fontboté, L., 2003, Implications of Pb isotope signatures of rocks and iron oxide Cu-Au ores in the Candelaria-Punta del Cobre district, Chile: Mineralium Deposita, v. 38, p. 900–912.
- McLaren, S., Sandiford, M., and Hand, M., 1999, High radiogenic heat-producing granites and metamorphism—an example from the western Mount Isa inlier, Australia: Geology, v. 27, p. 679–682.
- Neumann, N., Sandiford, M., and Foden, J., 2000, Regional geochemistry and continental heat flow: Implications for the origin of the South Australian heat flow anomaly: Earth and Planetary Science Letters, v. 183, p. 107–120.
- Pollard, P.J., 2000, Evidence of a magmatic fluid and metal source for Fe-Oxide Cu-Au mineralisation, in Porter, T.M., ed., Hydrothermal iron oxide-copper-gold and related deposits: A global perspective: Adelaide, Australia, Australian Mineral Foundation, p. 27–42.
- Pollard, P.J., Mark, G., and Mitchell, L.C., 1998, Geochemistry of post-1540 Ma granites in the Cloncurry district, northwest Queensland: ECONOMIC GEOLOGY, v. 93, p. 1330–1344.
- Primary Industries and Resources South Australia (PIRSA), 2004, Prominent Hill—resource estimation a major step forward: MESA Journal, v. 35, p. 4–5.
- Reeve, J.S., Cross, K.C., Smith, R.N., and Oreskes, N., 1990, Olympic Dam copper-uranium-gold-silver deposit: Melbourne, Australasian Institute of Mining and Metallurgy Monograph 14, p. 1009–1035.
- Requia, K., and Fontboté, L., 2000, The Salobo iron oxide copper-gold deposit, Carajás, northern Brazil, in Porter, T.M., ed., Hydrothermal iron oxide-copper-gold and related deposits: A global perspective: Adelaide, Australia, Australian Mineral Foundation, p. 225–236.
- Rudnick, R.L., and Fountain, D.M., 1995, Nature and composition of the continental crust: A lower crustal perspective: Reviews of Geophysics, v. 33, p. 267–309.
- Sillitoe, R.H., 2003, Iron oxide-copper-gold deposits: An Andean view: Mineralium Deposita, v. 38, p. 787–812.
- Sinclair, G.S., Barr, S.M., Culshaw, N.G., and Ketchum, J.W.F., 2002, Geochemistry and age of the Aillik Group and associated plutonic rocks, Makkovik Bay area, Labrador: Implications for tectonic development of the Makkovik province: Canadian Journal of Earth Sciences, v. 39, p. 731–748.
- Skirrow, R.G., Bastrakov, E., Davidson, G., Raymond, O.L., and Heathersay, P., 2002, The geological framework, distribution and controls of Fe-oxide Cu-Au mineralization in the Gawler craton, South Australia: Part II. Alteration and mineralization, in Porter, T.M., ed., Hydrothermal iron oxide copper-gold and related deposits: A global perspective: Linden Park, Australia, Porter GeoConsultancy Publishing, v. 2, p. 33–48.
- Tallarico, F.H.B., Figueiredo, B.R., Groves, D.I., Kositcín, N., McNaughton, J., Fletcher, I.R., and Rego, J.L., 2005, Geology and SHRIMP U-Pb geochronology of the Igarapé Bahia deposit, Carajás copper-gold belt, Brazil: An Archean (2.57 Ga) example of iron-oxide Cu-Au mineralization: ECONOMIC GEOLOGY, v. 100, p. 7–28.
- Taylor, S.R., and McLennan, S.M., 1995, The geochemical evolution of the continental crust: Reviews of Geophysics, v. 33, p. 241–265.
- Tazava, E., and de Oliveira, C.G., 2000, The Igarapé Bahia Au-Cu-(REE-U) deposit, Carajás mineral province, northern Brazil, in Porter, T.M., ed., Hydrothermal iron oxide-copper-gold and related deposits: A global perspective: Adelaide, Australia, Australian Mineral Foundation, p. 203–212.
- Williams, P.J., Barton, M.D., Fontboté, L., de Haller, A., Johnson, D.A., Mark, G., Marschik, R., and Oliver, N.H.S., 2005, Iron oxide-copper-gold deposits: Geology, space-time distribution, and possible modes of origin: ECONOMIC GEOLOGY 100TH ANNIVERSARY VOLUME, p. 371–406.
- Wyborn, L., 1998, Younger ca 1500 Ma granites of the Williams and Nakaku batholiths, Cloncurry district, eastern Mt. Isa inlier: Geochemistry, origin, metallogenic significance and exploration indicators: Australian Journal of Earth Sciences, v. 45, p. 397–411.

The mobility of zirconium and other “immobile” elements during hydrothermal alteration

Jeffrey N. Rubin^a, Christopher D. Henry^b and Jonathan G. Price^c

^a*Department of Geological Sciences, University of Texas at Austin, Austin, TX 78712, USA*

^b*Bureau of Economic Geology, University of Texas at Austin, P.O. Box X, Austin, TX 78713-7508, USA*

^c*Nevada Bureau of Mines and Geology, University of Nevada-Reno, Reno, NV 89557-0088, USA*

(Received May 10, 1992; revised and accepted October 26, 1992)

ABSTRACT

Development of zircon and other Zr phases in hydrothermal deposits indicates that Zr can be highly mobile in these systems. Mobility is most common in, but not restricted to, F-rich hydrothermal systems related to alkalic, F-rich igneous suites; these suites can range from peralkaline through metaluminous to peraluminous. A few examples are neither alkalic nor F rich.

Three locations in the Trans-Pecos Magmatic Province, Texas, U.S.A., demonstrate this hydrothermal Zr mobility. All three igneous systems are alkalic and F rich but vary in alkali/Al ratios. Peralkaline rhyolites and trachytes in the Christmas Mountains contain as much as 2100 ppm Zr, mostly in aegirine or arfvedsonite; zircon is rare or absent. Fluorspar replacement deposits in limestone at contacts with the rhyolites contain as much as 38,000 ppm Zr, occurring as small, disseminated zircons. The deposits also are enriched in a variety of incompatible elements, including Be, rare-earth elements (REE), Y, Nb, Mo, Hf, Pb, Th and U. The Sierra Blanca intrusions, a series of mildly peraluminous, F-rich rhyolite laccoliths, contain as much as 1000 ppm Zr, mostly as zircon. Hydrothermal zircon occurs as overgrowths on magmatic grains, as veinlets connected to overgrowths, and in fluorspar replacement bodies in adjacent limestone. The highest Zr concentrations in fluorspar are ~200 ppm. Metaluminous quartz monzonite from the Infiernito caldera contains 400–600 ppm Zr, mostly as zircon. Euhedral zircon in quartz-fluorite veins in the quartz monzonite indicates mobility of Zr. Zirconium concentrations in the veins are unknown, but the paucity of zircon suggests little Zr enrichment relative to the host. Zircon and, more rarely, zirconolite, occur in skarn in the Ertsberg District of Irian Jaya, Indonesia. Unlike in Texas, related igneous rocks are metaluminous, and the hydrothermal system was F poor. Worldwide, hydrothermal zircon, other Zr phases, and Ti- and Al-bearing phases occur in skarn, epithermal precious metal veins, volcanogenic massive-sulfide deposits and mylonites.

We propose that differences in Zr mineralogy of igneous source rocks is an important factor in determining the availability of Zr to hydrothermal fluids. Although Zr concentrations in the Sierra Blanca and Christmas Mountains rhyolites are similar, Zr enrichment in fluorspar was much greater in the Christmas Mountains. We suggest that hydrothermal solutions could easily break down aegirine and arfvedsonite to release Zr, but that zircon was only moderately attacked. Therefore, far more Zr was available for transport and subsequent deposition in the Christmas Mountains than at Sierra Blanca. Availability of other trace elements probably is also governed by their mineral host. Although Zr mobility is most common in F-rich hydrothermal systems related to alkalic and F-rich igneous systems, mobility at Ertsberg may have been promoted by sulfate complexing.

1. Introduction

Zirconium is widely regarded as an immobile element and is used to classify the type and tectonic setting of altered or metamorphosed igneous rocks (J.A. Pearce and Cann, 1973; Floyd and Winchester, 1975). Furthermore,

Finlow-Bates and Stumpfl (1981) suggested that Zr and Ti were also mostly immobile during hydrothermal alteration. The purpose of this study is to demonstrate that Zr (and other immobile elements, such as Ti) can be highly mobile during hydrothermal alteration, mostly as a result of leaching from igneous source

rocks. First, we provide several examples of hydrothermal Zr mobility from our own work in Trans-Pecos Texas, U.S.A., and the Ertsberg District, Irian Jaya, Indonesia, and from the literature. Then we discuss the distribution of Zr in igneous source rocks and how this is influenced by magma composition, particularly alkalis and F. Finally, we conclude that primary, magmatic Zr mineralogy strongly influences subsequent leachability and therefore mobility of Zr.

2. Trans-Pecos Magmatic Province, Texas

Magmatism in Trans-Pecos Texas occurred between 48 and 17 Ma ago (Henry and McDowell, 1986). Most of the activity, including that in all three areas discussed here, occurred between ~48 and ~32 Ma ago as part of a continental volcanic arc related to plate convergence and subduction off the west coast of North America (Henry et al., 1991). As with other magmatic arcs well inboard from a continental margin, Trans-Pecos magmatism is alkalic. Activity in Texas has been divided into a western, alkali-calcic belt and an eastern, alkalic belt (Henry and Price, 1984; Barker, 1987; Price et al., 1987).

Three locations in Trans-Pecos Texas (Fig. 1), representative of the range of igneous activity, show unequivocal evidence of hydrothermal Zr mobility. These are: (1) the Christmas Mountains intrusions, a group of peralkaline to metaluminous rhyolites to trachytes (Henry et al., 1989); (2) the Sierra Blanca intrusions, a group of five peraluminous rhyolite laccoliths (Rubin et al., 1987; Price et al., 1990); and (3) the Infiernito caldera, a metaluminous to mildly peralkaline caldera complex (Henry and Price, 1984; Henry et al., 1992). All three igneous systems are alkalic, with $\text{Na}_2\text{O} + \text{K}_2\text{O}$ in rhyolites of between 9 and 11 wt%, but vary in alkali/Al ratios (Table 1). Magmas in all three locations were also F rich, as shown by the common presence of fluorspar or fluorite-bearing vein

deposits associated with the igneous bodies (McAnulty, 1974; Daugherty, 1982; Henry et al., 1989, 1992; Rubin et al., 1989b, 1990).

2.1. Peralkaline Intrusions of the Christmas Mountains

The Christmas Mountains (Fig. 1) are a cluster of small (1–3-km diameter), shallow stocks and laccoliths emplaced between 44 and 40 Ma in southern Trans-Pecos Texas (Cameron et al., 1986; Henry et al., 1989). Individual intrusions range from peralkaline to metaluminous rhyolites and trachytes. Fluorite deposits are common at the contacts between intrusions and Cretaceous limestone wall-rock. However, Zr-enriched deposits and evidence of hydrothermal Zr mobility are associated only with the peralkaline intrusions.

The peralkaline rocks are composed dominantly of alkali feldspar and quartz, which occur both in the groundmass and as sparse to moderately abundant phenocrysts. Sodic amphibole (arfvedsonite) or pyroxene (aegirine) are the only other common phases. Relative abundance of the sodic minerals correlates crudely with silica content, with arfvedsonite most common in rhyolites and aegirine in quartz trachytes. Accessory phases include magnetite, ilmenite and apatite. Zircon is present in a few samples but in general is rare, as are monazite and possible bastnaesite (CeCO_3F) and euxenite ($(\text{Y,Ca,Ce,U,Th})(\text{Nb,Ta,Ti})_2\text{O}_6$).

Silica content in the peralkaline intrusions ranges from ~64 to ~76 wt% (Table 1). All listed samples are peralkaline, as indicated by their composition or presence of sodic pyroxene or amphibole. The high CaO content, low total and apparent nonperalkalinity of the sample from the Paisano intrusion (H90-74) reflects calcite in the mildly altered rock. Fluorine contents of these rocks have not been determined. They are unlikely to be representative of magmatic compositions in any event, due to fluorine loss during crystallization or

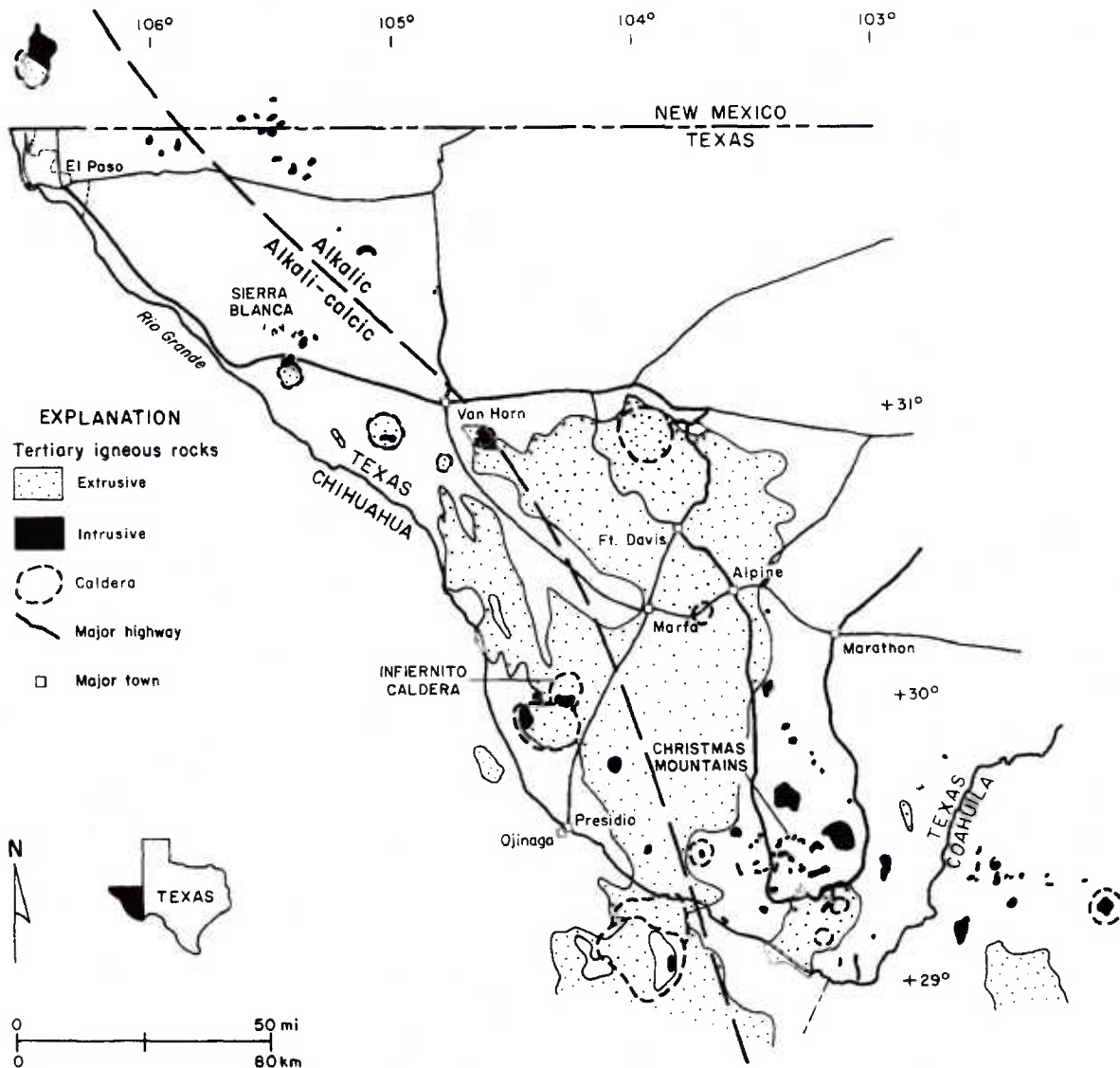


Fig. 1. Index map showing locations of Sierra Blanca Peaks, Christmas Mountains and Infiernito caldera within Trans-Pecos Magmatic Province.

hydrothermal alteration (Noble et al., 1967; Weaver et al., 1990). The common association of fluorite deposits indicates that the magmas were undoubtedly F rich. The intrusions are markedly enriched in Zr, with concentrations ranging from ~1000 to ~2100 ppm (Table 1) and in other incompatible trace elements, including Rb, Y, Nb, REE, Pb, Th and U.

The high concentrations of Zr and paucity of zircon are consistent with the high solubility of zircon in alkalic and F-rich magmas (Wat-

son, 1979; Watson and Harrison, 1983; Kepler, 1991). Microprobe analyses indicate that aegirine and arfvedsonite contain up to 3.2 and 0.95 wt% ZrO_2 , respectively (see Table 3). A whole rock containing 5 wt% each of aegirine and arfvedsonite with these concentrations would have ~1500 ppm Zr. Thus these minerals hold nearly all the Zr in the rocks.

Many small fluorite-replacement deposits developed in Cretaceous limestone at the contacts with intrusions (Daugherty, 1982; Henry

TABLE 1

Analyses of selected igneous rocks from Trans-Pecos Texas, U.S.A., and Irian Jaya, Indonesia

Sample	Intrusions of the Christmas Mountains			Sierra Blanca intrusions			Rocks of the Infiernito caldera				Ertisberg GB-1 ^b intrusion
	H90-74 Paisano	H81-41 Adobe	MGD-788 North Adobe	HE3 ^a Hen Egg	81-60 Sierra Blanca	81-65 Little Blanca	J85-55 Round Top	MGE-783 AFT	MGE-794 resurgent intrusions	MGF-047 intrusions	
SiO ₂	70.59	71.50	71.28	75.64	75.01	75.14	73.60	75.25	66.15	66.78	59.60
TiO ₂	0.23	0.18	0.15	0.10	0.02	0.02	0.02	0.27	0.82	0.72	0.58
Al ₂ O ₃	12.52	13.12	12.68	11.84	14.18	13.92	13.89	12.61	15.67	15.71	16.30
Fe ₂ O ₃	5.25	3.80	4.16	2.26	0.29	1.13	0.73	1.05	2.02	1.98	4.08
FeO	0.11	0.18	0.10	0.05	0.53	0.18	0.70	0.72	1.80	1.94	0.15
MnO	0.00	0.21	0.39	0.26	0.05	0.05	0.08	0.06	0.11	0.15	0.09
MgO	2.05	0.45	0.90	0.14	0.45	0.38	0.08	1.13	1.13	0.72	2.09
CaO	4.41	5.18	4.77	5.67	5.10	5.05	6.58	4.66	2.36	1.96	6.06
Na ₂ O	4.81	4.41	4.37	4.03	4.34	4.11	4.29	4.93	4.96	4.68	3.59
K ₂ O	0.02	0.01	0.01	0.05	0.01	0.01	0.01	0.01	0.28	0.19	3.45
P ₂ O ₅		0.80	0.77	0.05	0.18	0.40	0.13	0.31	0.27	0.50	0.33
H ₂ O ⁺		0.10	0.40		0.15	0.22	0.00	0.30	0.30	0.25	0.40
CO ₂					0.65	0.54	1.30	0.12	0.05	0.07	0.14
F					99.87	100.01	99.34	99.09	99.91	99.72	S ^d
Unnorm- alized total	96.37	97.90	99.99	99.99	99.87	100.01	99.34	99.09	99.91	99.72	99.50

(wt%):

(ppm):		7.3	9.9	170	370	440	5	<2.5	2.5	20.7
Li				4	18	170				
Be		252	413	140	520	610	106	93	176	44
Zn	510			1,090 ^c	1,870 ^c	1,960 ^c	216	127	133	118
Rb	480			9	32	28	12	371	207	842
Sr	32	16	70	200	220	220	85	33	48	18.1
Y	236			135	840	1,040	530	411	612	119
Zr	2,127	1,640	1,530	72	280	340	76	45	58	11
Nb	451			5.6	4	<5	2.3	2	2.4	
Mo		9.4		16	85	<10	58	1,010	1,040	603
Ba	50	28	183							
La	263			20	37.9	23	48.6	65	86	27.4
Ce	610			53.6	100	90	103	128	172	50.2
Pr				7.6	12	11	12.2	15	21	6.4
Nd				25.7	28.6	28	47.9	52	71	22.5
Sm				9.2	9.8	10	12.5	11	14	3.4
Eu				0.5	0.1	0.1	0.8	2.4	2.8	1.3
Gd				11.7	10.4	11	11.2	9.8	13	
Tb				2.4	3.4	3.7	2.2	1.7	2.5	0.6
Dy				17.9	28.5	36	13.7	7.9	11	3.3
Ho				4.2	7	7.8	2.8	2	2.8	0.7
Er				15.7	29.1	33	8.4	4.3	5.8	1.9
Tm				3	5.8	6.7	1.2	0.9	1.3	0.3
Yb				24.4	46.4	55	8	4.2	5.5	1.9
Lu				3.6	6.8	7.2	1.2	0.9	1.5	0.4
Hf				16	22	17	16			3.8
Ta				14	18	35	4.1			<1
Pb	31	12		70	220	320	23.6			8
Th	62	39		60	210	230	20.3			8.2
U				14	27	54	3.8			2.6

AFT = ash-flow tuff. Analyses by X-ray fluorescence spectrometry (XRF) (Washington State University), and inductively coupled plasma-atomic emission spectrometry (ICP-AES), inductively coupled plasma-mass spectrometry (ICP-MS) and ion selective electrode method (ISE) (Bureau of Economic Geology, University of Texas at Austin).
^aXRF from Cameron et al. (1986).
^bXRF, ICP-AES and instrumental neutron activation analysis (INAA) from McMahon and McDowell (1991).
^cXRF by D.S. Barlier, Department of Geological Sciences, University of Texas at Austin.
^dS = sulfur.

et al., 1989). The deposits consist chiefly of fine-grained purple and gray fluorite, generally ≤ 0.1 mm in diameter, plus quartz and minor clay minerals, calcite, siderite and pyrite. Low salinities (0.1–1.5 eq wt% NaCl) and homog-

enization temperatures (165–215°C) of fluid inclusions indicate that the solutions responsible for alteration probably were dominated by meteoric water (Ash and Kyle, 1984), although the F undoubtedly was magmatic.

TABLE 2

Analyses (ppm, unless indicated otherwise) of limestone, and fluoritized rocks from Trans-Pecos Texas

Location	Christmas Mountains						
		Paisano Intrusion			Adobe Walls		North Adobe
Sample No. Rock type ^a	J88-8 Buda Ls ^b	MGD403 Flu	MGD-404 Flu	J81-133A Flu	J81-135 Flu-rhy	MGD-777 Flu	MGD-786 Rhy bx
Li	5	8	9	9	14	15	44
Be	<1	32	10	588	37	83	13
F	300	430,000	370,000	333,000	44,800	333,000	300
Al ₂ O ₃ (%)	0.55	0.91	0.93	5.31	12.29	3.47	6.26
SiO ₂ (%)	3.46	5.38	18.92	16.25	62.79	12.34	76.4
K ₂ O (%)	0.25	0.15	0.15	3.53	4.7	2.15	1.2
TiO ₂ (%)	0.02	0.01	0.03	0.05	0.15	0.13	0.09
V	6	14	7	<5	198	729	175
Mn	231	7	26	7	1,130	141	51
Fe	1,070	1,240	3,110	1,630	25,400	7,710	48,600
Zn	<50	<50	100	<50	210	110	120
As	<2	70	7	7	73	210	940
Rb	4	30		378	260	130	52
Sr	628	925	612	935	214	925	1,200
Y	9	9	754	18	172	330	364
Zr	25	302	116	525	4,000	38,000	22,000
Nb	3	27	<2	17	190	383	540
Mo	<5	47	20	6	91	175	154
Ba	104	12	73	243	143	53	225
La	2	14	5	7	130	75	250
Ce	4		150	13	260	130	760
Pr	0.64						
Nd	2.6		43	8	110		200
Sm	0.4		43	1.7	23	28	88
Eu	0.12	<0.2	1.9	0.3	3.1	1.6	4.8
Gd	0.64						
Tb	0.09	<0.5	56	0.5	5.1	16	32
Dy	0.47						
Ho	0.09						
Er	0.28						
Tm	0.03						
Yb	0.2	0.3	122	0.9	18.5	53.3	92
Lu	0.02	<0.05	13.9	0.13	3.01	7.5	13.5
Hf	<1	2	1	<1	62	850	260
Ta	<1	<1	<1	<1	12	3	14
Pb	<20	<20	<20	<20	70	170	1,240
Th	<0.5	0.8	1,100	6.2	63	59	250
U	0.6	240	12	1.9	330	1,400	1,800

TABLE 2 (continued)

Location	Sierra Blanca							Infiernito caldera		
	Round Top				Little Blanca		Sierra Blanca	J81-71 Qz vein	J81-72 QMP w/stck	J81-83 Qz vein
Sample No.	J87-83	J87-84	J87-96	RT4-258	J81-24	J81-29	J85-50			
Rock type ^a	Flu-rhy	Flu	Flu	Flu	Flu	Flu	Flu			
Li	71	72	17	14	60	1160	16	42	3	29
Be	1,290	1,350	27,900	25,100	4,200	61	3,300	16	5.1	1.1
F	287,000	237,000	230,000	320,000	279,000	263,000	387,000	240	950	360
Al ₂ O ₃ (%)	13.96	5.6	3.72	1.64	7.39	8.76	4.17			
SiO ₂ (%)	12.34	14.94	21.72	9.85	21.11	25.06	13.7			
K ₂ O (%)	0.31	1.33	0.36	0.36	1.53	2.21	0.57			
TiO ₂ (%)	0.01	0.25	0.13	0.07	0.22	0.25	0.12			
V	5	41	33	15	35	31	36	16	36	11
Mn	469	887	178	157	1,080	761	200	280	520	720
Fe	21,700	17,200	14,700	3,900	22,800	16,300		65,000	23,000	3,000
Zn	1,580	49	700	24	970	221	110	160	230	220
As	54	66	260	57	24	406		51	<5	<5
Rb	150	290	80	50						
Sr	1,280	1,150	930	870	2,510	2,860	1,220			
Y	79	12	23	3	53	191	15			
Zr	160	120	54	64	74	187	47			
Nb	45	9	3.6	5.2						
Mo	4.4	1.8	0.4	1.1	<5	28	<5	140	18	46
Ba	18	105	110	67	167	88	96			
La	7.3	16.1	34	4.1	23	31	13.9			
Ce	18.2	31.8	64	6.9	39	66	15.2			
Pr	3.6	3.5	8.4	1	4.9	9.7	3.4			
Nd	9.2	11.3	28	3.1	16.9	28.6	13			
Sm	3.9	2.2	5.4	0.6	4	10.1	2.6			
Eu	0.04	0.4	1.1	0.1	0.6	0.5	0.7			
Gd	4	2.3	5.6	0.7	4	11.2	2.5			
Tb	1.4	0.3	0.8	0.1	0.5	3.4	0.2			
Dy	11.9	1.6	4	0.5	5.2	26.5	1.9			
Ho	2.7	0.3	0.7	0.1	1	6.1	0.3			
Er	10.3	0.8	1.8	0.2	3.9	24.2	1			
Tm	2.2	0.1	0.2	0.01	0.5	5.1	0.1			
Yb	17.9	0.9	1.4	0.2	3.7	41.8	1.2			
Lu	2.4	0.1	0.2	0.02	0.4	6.2	0.1			
Hf	9.1	3.4	1.1	1.7						
Ta	3.1	1.3	1.9	0.8						
Pb	490	19	840	3	750	1,470	<20	40	<10	30
Th	62	7	2.4	1.7	<10	<10	<10	30	20	20
U	115	31	53	6.2	30	137	370	10	<5	<5

Analyses by inductively coupled plasma-atomic emission spectrometry (ICP-AES), inductively coupled plasma-mass spectrometry (ICP-MS) and ion selective electrode method (ISE) (Bureau of Economic Geology, University of Texas at Austin) and instrumental neutron activation analysis (INAA) (Activation Laboratories Ltd.).

^a Ls = Limestone; Flu = fluorspar; Flu-rhy = fluoritized rhyolite; Rhy bx = rhyolite breccia; QMP w/stck = quartz monzonite porphyry with stockwork.

^b Used as unaltered limestone baseline in Figs. 2 and 6.

Tables 1 and 2 and Figs. 2–6 present representative geochemical data from unaltered rhyolite, unaltered limestone and fluorite or fluoritized rhyolite associated with the unaltered rhyolites. A sample of unaltered Buda Limestone (J88-8; Table 2), which is the host for most deposits, is used as a baseline for evaluating trace-element enrichment in fluorite. Fluorite samples MGD-403, MGD-404 and J81-133A (Table 2) are associated with unaltered rhyolite H90-74 (Table 1). Similarly, fluorite sample MGD-777 and fluoritized rhyolite J81-135 are associated with rhyolite H81-41, and rhyolite breccia MGD-786 with rhyolite MGD-788. In evaluating enrichment, we assume fluoritization caused no volume change. The magnitude of enrichment is such that even relatively large volume changes would not negate this assumption.

The fluorite deposits are locally highly en-

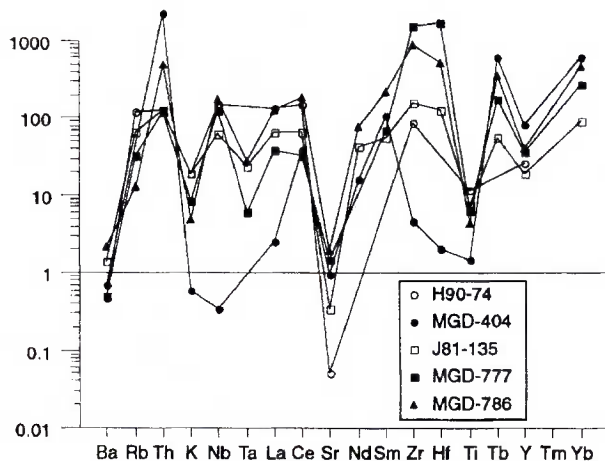


Fig. 2. Spidergram of rhyolite (H90-74, Paisano intrusion), fluoritized limestone (MGD-404, MGD-777), fluoritized rhyolite (J81-135) and altered rhyolite contact breccia (MGD-786), normalized to unaltered Cretaceous limestone (J88-8). All samples are enriched relative to limestone in most elements ($>1000\times$ for Zr) and also relative to rhyolite ($\leq 20\times$ for Zr). Enrichment can be highly variable. For example, sample MGD-777 is greatly enriched in Zr but much less so in Th, whereas sample MGD-404 is greatly enriched in Th but not in Zr. Samples MGD-404 and J81-135 are from fluorite deposits adjacent to the Paisano intrusion. Samples MGD-777 and MGD-786 are adjacent to two other intrusions [rhyolites H81-41 and MGD-783 (Table 1), respectively].

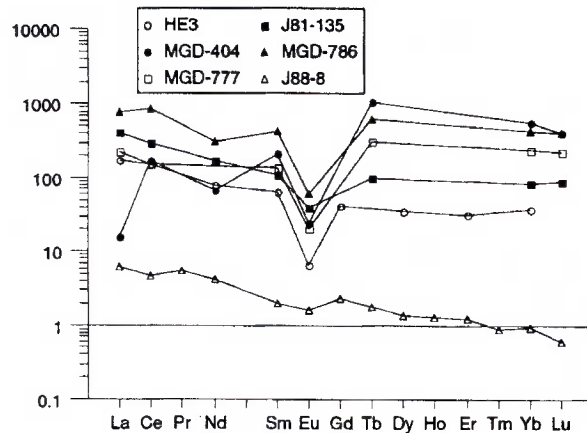


Fig. 3. Chondrite-normalized rare-earth element patterns of Christmas Mountains fluorite, rhyolite and unaltered limestone. Same samples as Fig. 2 except that rhyolite is HE3 (Table 1; data from Cameron et al., 1986). Fluorite samples have rare-earth patterns that mimic the rhyolite pattern and are distinctly unlike the limestone pattern, indicating an igneous source for the rare earths in fluorite. Fluorite is enriched $>100\times$ compared to limestone and $\leq 20\times$ relative to rhyolite, particularly in the heavy rare earths. Chondrite data from Nakamura (1974).

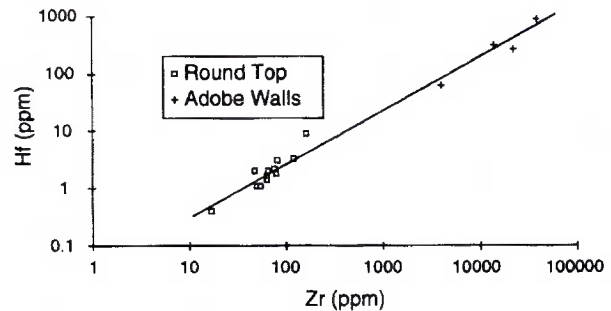


Fig. 4. Hf and Zr concentrations in fluorite from the Christmas Mountains and Sierra Blanca (Round Top intrusion). Zr/Hf ratio of ~ 40 , similar to that found in igneous rocks (Gill, 1981), indicates an igneous source for the elements.

riched in Be, V, As, Rb, Y, Zr, Nb, Mo, REE [particularly heavy REE (HREE)], Hf, Pb, Th and U (Fig. 2; Table 2). Zr concentrations in whole-rock fluorite samples range to 38,000 ppm. Backscattered electron imaging shows that the Zr occurs as minute ($\leq 10\ \mu\text{m}$), subhedral to anhedral zircons disseminated in the fluorite.

Zr enrichment in fluorspar is as much as

1000 times that in unaltered limestone but is not directly proportional to enrichment in the source rhyolite (Table 2; Fig. 2). Enrichment is markedly variable, both between deposits associated with different intrusions and within a single intrusion. Fluorspar deposits adjacent to the Adobe Walls and North intrusions, which have high Zr concentrations (Table 1), are the most highly and consistently enriched in Zr. However, fluorspar adjacent to the Paisano intrusion, which has the highest igneous Zr concentration, is only slightly enriched relative to limestone and has lower concentrations than the rhyolite (compare samples H90-74 and MGD-404 in Fig. 2). Other elements are also variable. Different fluorspar samples from the Paisano deposits, in some cases separated by < 50 m, are enriched in U but not Th, and vice versa (Table 2).

High concentrations of Zr in fluoritized rhyolite can be only partly residual from rhyolite protolith. For example, fluoritized rhyolite or breccia samples J81-135 and MGD-786 contain 4000 and 22,000 ppm Zr, respectively, whereas their associated unaltered rhyolites contain 1640 and 1530 ppm (Table 2; Fig. 2). Thus, enrichment factors relative to rhyolite are as much as 15.

These data demonstrate not only Zr mobility but tremendous enrichment in the fluorspar deposits. The rhyolites were almost certainly the source of Zr and other trace elements in the fluorspar. Evidence for this interpretation includes the general match between elements enriched in the rhyolites and in the deposits and is particularly notable for REE (Fig. 3). REE concentrations in fluorspar and rhyolite show similar patterns of light REE (LREE) and HREE enrichment and Eu depletion, in marked contrast to the low concentrations and negative slope for unaltered limestone. Also, the relatively constant Zr/Hf of ~40 (Fig. 4) in these and the Sierra Blanca deposits discussed below is similar to that found in igneous rocks (Gill, 1981).

2.2. Peraluminous rhyolites at Sierra Blanca

The Sierra Blanca intrusions are a group of five small (1–4-km diameter), shallow laccoliths emplaced into Cretaceous sedimentary rocks ~120 km southeast of El Paso (Fig. 1; Rubin et al., 1987; Price et al., 1990). In geologic setting, geometry of intrusion, type of host rock and common association with fluorspar, they are markedly similar to the intrusions of the Christmas Mountains. However, they differ substantially in being peraluminous, are compositionally similar to topaz rhyolites (Christiansen et al., 1983, 1986), but lack topaz.

The intrusions are mineralogically complex. Two alkali feldspars and quartz make up 90–95 vol% of the rocks, mostly as groundmass and minor phenocrysts (Rubin et al., 1987). The potassium feldspar is probably sanidine with almost no Ca substitution. The other alkali feldspar is nearly pure albite in the most evolved intrusions (e.g., Round Top and Little Blanca) but shows minor Ca substitution in Sierra Blanca proper (Rubin et al., 1987). Quartz commonly contains inclusions of Nb-rich rutile. Trioctahedral mica with variable Fe content and Fe-rich biotite are also present. Relatively abundant accessory phases include magnetite, zircon and cryolite (Na_3AlF_6). Cryolite occurs as a late crystallizing phase associated with rutiled quartz; Rubin et al. (1987) and Price et al. (1990) present chemical and textural evidence that cryolite precipitated from a pegmatitic vapor phase. Finally, the rocks contain a wide range of trace minerals, including, but not limited to, cassiterite, changbaiite (PbNb_2O_6), columbite ((Fe, Mn) Nb_2O_6), thorite, xenotime ((Y, HREE) PO_4), and several Y- and REE-rich fluorides (Rubin et al., 1987; Price et al., 1990).

The Sierra Blanca intrusions are low- to high-silica rhyolites (Table 1). Price et al. (1990) suggested that the range in silica reflects quartz fractionation and that the lower silica rocks are

the most evolved. Despite being peraluminous, the Sierra Blanca intrusions are as alkalic as the Christmas Mountains peralkaline intrusions (Table 1). The Sierra Blanca rocks differ in having distinctly higher Al_2O_3 and lower total Fe at a given SiO_2 content. Normative calculations of some analyses of the Round Top intrusion, including J85-55 (Table 1), are peralkaline but become peraluminous when abundant cryolite (up to 2.5 vol%) is subtracted from the analyses. Subtracting cryolite is appropriate because it is not a magmatic phase. All Sierra Blanca intrusions are remarkably F rich (Table 1), although the degree to which magmatic concentrations have been altered by vapor-phase crystallization or other secondary processes is uncertain (Price et al., 1990).

The Sierra Blanca intrusions also contain high concentrations of the same suite of incompatible trace elements as the Christmas Mountains intrusions (Table 1). Most trace-element concentrations increase with decreasing SiO_2 content, probably reflecting quartz fractionation. For example, Zr concentrations range from 1040 ppm in the Round Top intrusion (73.6 wt% SiO_2) to 135 ppm in Sierra Blanca proper (75.0 wt% SiO_2). REE patterns show distinctive positive slopes (Fig. 5), i.e. HREE enrichment, that is most pronounced in the least silicic rocks. As with F, the extent to which magmatic concentrations have been modified by vapor-phase processes is uncertain (Rubin et al., 1987; Price et al., 1990).

In contrast to the Christmas Mountains rocks, most Zr resides in zircon in the igneous rocks. For example, conventional petrography and backscattered electron imaging indicate ~0.2 vol% zircon in the Round Top intrusion (sample J85-55; Table 1). These zircons contain 60–65 wt% ZrO_2 (Rubin et al., 1989a). The resulting calculated Zr concentration of 900 ppm compares closely with the 1040 ppm analyzed whole-rock concentration (Table 1). Magmatic zircon is commonly amoeboid and corroded with abundant thorite inclusions in

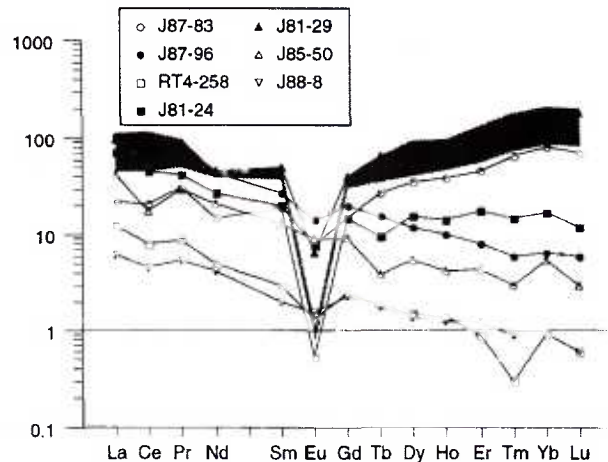


Fig. 5. Chondrite-normalized rare-earth element patterns for fluorite samples from the Round Top, Little Blanca and Sierra Blanca intrusions. Shaded area indicates range of concentrations found in associated rhyolites. Concentrations and patterns for fluorite range from identical to that of rhyolite to nearly identical to that of unaltered limestone (sample J88-8). This suggests that the rare earths in fluorite represent variable mixtures from rhyolite and limestone. Because all samples are fluoritized limestone, the rare earths must have been transported and deposited from hydrothermal solution. Chondrite data from Nakamura (1974).

the more Th-rich samples (Rubin et al., 1989a). Zircon overgrowths on the magmatic zircons and veinlets connected to overgrowths and cutting cryolite are probably hydrothermal. The other enriched, incompatible trace elements probably reside in the unusual trace-mineral assemblage.

Fluorspar deposits commonly developed at contacts with Cretaceous limestone, as in the Christmas Mountains. As in the Christmas Mountains, fluid inclusion data indicate that the hydrothermal solutions are dominated by meteoric water. Homogenization temperatures of aqueous inclusions range from 90°C to almost 250°C, with salinities ranging from 0 to 9 eq wt% NaCl (Rubin et al., 1990). Deposits adjacent to the Round Top intrusion are the most enriched in Be (Table 2) and constitute a high-grade Be resource. Fluorspar adjacent to the Little Blanca and Sierra Blanca intrusions show lesser but still pronounced Be enrichment. Chemical and mineralogical data

indicate mobility of Al, Ti, As, Rb, Y, Zr, Mo, REE, Hf, Pb and U (Fig. 6; Table 2). For example, all fluorite deposits contain euhedral, inclusion-free zircon that is clearly hydrothermal, as probably are the overgrowths and veinlets in the igneous rocks (Rubin et al., 1989a). However, except for Be and to a lesser extent Pb, fluorite deposits are only modestly enriched relative to unaltered limestone (Table 2; Fig. 6). Maximum Zr concentrations in fluorite are ~ 200 ppm, which represents less than $10\times$ enrichment relative to limestone. Zr and Be enrichment is antithetical, possibly due to the large differences in ionic radius and charge.

The other elements are enriched mostly by less than a factor of ten relative to limestone (Fig. 6). Nevertheless, they do suggest transport in and deposition by a hydrothermal fluid that derived the elements from rhyolite. For example, some fluorite samples have REE concentrations and patterns similar to the rhyolites; other samples have low REE concentrations and patterns similar to unaltered limestone (Fig. 5). Mobility of Al and Ti is indicated by the occurrence of Al or Ti phases,

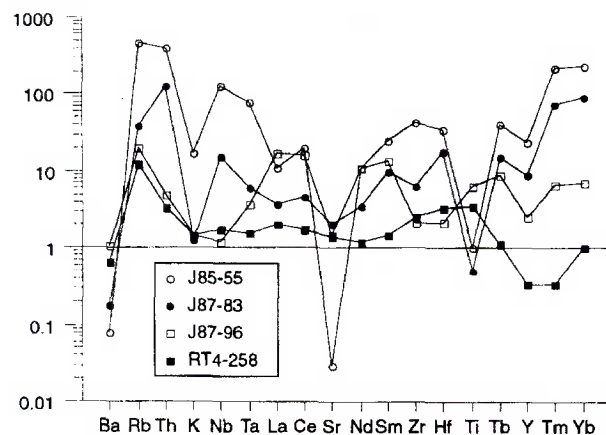


Fig. 6. Spidergram of Round Top rhyolite (J85-55) and associated fluorite (all fluoritized limestone) normalized to unaltered limestone. Fluorite samples range from enriched relative to limestone and with a pattern mimicking rhyolite to similar to limestone. Note that two fluorite samples are enriched in Ti relative to either limestone or rhyolite.

including analcime, grossular, white mica, kaolinite, montmorillonite, prosopite, and at least one form of TiO_2 , in the fluorite (Rubin et al., 1989b).

2.3. Metaluminous quartz monzonite of the Infiernito caldera

The Infiernito caldera underwent a complex sequence of tuff and lava eruption, caldera collapse, intrusion and hydrothermal alteration at ~ 37 Ma ago (Henry et al., 1988, 1992). Although mildly peralkaline rhyolites were present, Zr mobility was restricted to hydrothermal activity related to a metaluminous quartz monzonite intrusion. The quartz monzonite contains complexly zoned alkali and plagioclase feldspar, biotite, calcic amphibole, clinopyroxene and quartz. Magnetite, ilmenite, apatite and zircon are ubiquitous accessory minerals.

The quartz monzonite is alkalic with almost 10 wt% $\text{Na}_2\text{O} + \text{K}_2\text{O}$ in rocks with 66 wt% SiO_2 (Table 1). Its metaluminous character reflects much higher Al_2O_3 and CaO contents than either the Christmas Mountains or Sierra Blanca intrusions. Also, incompatible trace-element concentrations are typical of broadly calc-alkaline plutonic rocks. Zr concentrations increase from < 400 ppm in more mafic samples to a maximum of ~ 600 ppm in the most evolved samples (Table 1). Most of the Zr probably occurs as zircon. F concentrations are also modest, although analyses of coarse-grained intrusive rocks are probably not representative of magmatic concentrations.

Extensive hydrothermal alteration associated with the intrusion includes epithermal veins, skarn, porphyry-type mineralization and propylitic alteration of the intrusion itself. Stockwork quartz-magnetite-pyrite-pyrrhotite-fluorite veins occur at the margins of an apophysis of the intrusion. Euhedral zircon with lensoidal zircon overgrowths occurs in the veins. The zircon is surrounded by vein quartz and therefore was clearly deposited from the

hydrothermal fluid (Rubin et al., 1989a; Henry et al., 1992). Rocks containing stockwork veins are moderately enriched in Ag, Cd, As, Mo and Be (Table 2). Zr concentrations in the veins are unknown, but the low abundance of zircon suggests low concentrations. Thus Zr was mobile in hydrothermal fluids, as in the other systems, but was not significantly enriched in hydrothermal deposits.

3. Other occurrences

3.1. Ertsberg District skarns, Indonesia

The Ertsberg mining district is located near the eastern border of Irian Jaya, Indonesia, in the Central Highlands of New Guinea (Fig. 7). The district occurs within the Papuan fold belt on the northern margin of the Australian Plate,

and currently hosts five mines in varying stages of activity, including the Grasberg Cu–Au porphyry-type deposit, which currently possesses the greatest Au reserves of any single operating mine in the world. The other mines in the district exploit Cu–Au mineralization in skarn-type deposits in folded and faulted Tertiary carbonates. The skarn-hosted mineralization is related to the ~3.1-Ma Ertsberg intrusion, which varies in composition from quartz monzonite to quartz diorite. The intrusion is alkali-rich but metaluminous (Table 1; McMahon and McDowell, 1991). The skarns are magnesian, with prograde mineralogy dominated by forsterite, diopsidic clinopyroxene, grandite garnet and monticellite (Rubin, 1991). Skarn mineralogy, as well as alteration mineralogy within the intrusion, is Al-rich, with phlogopite, clintonite, garnet and other

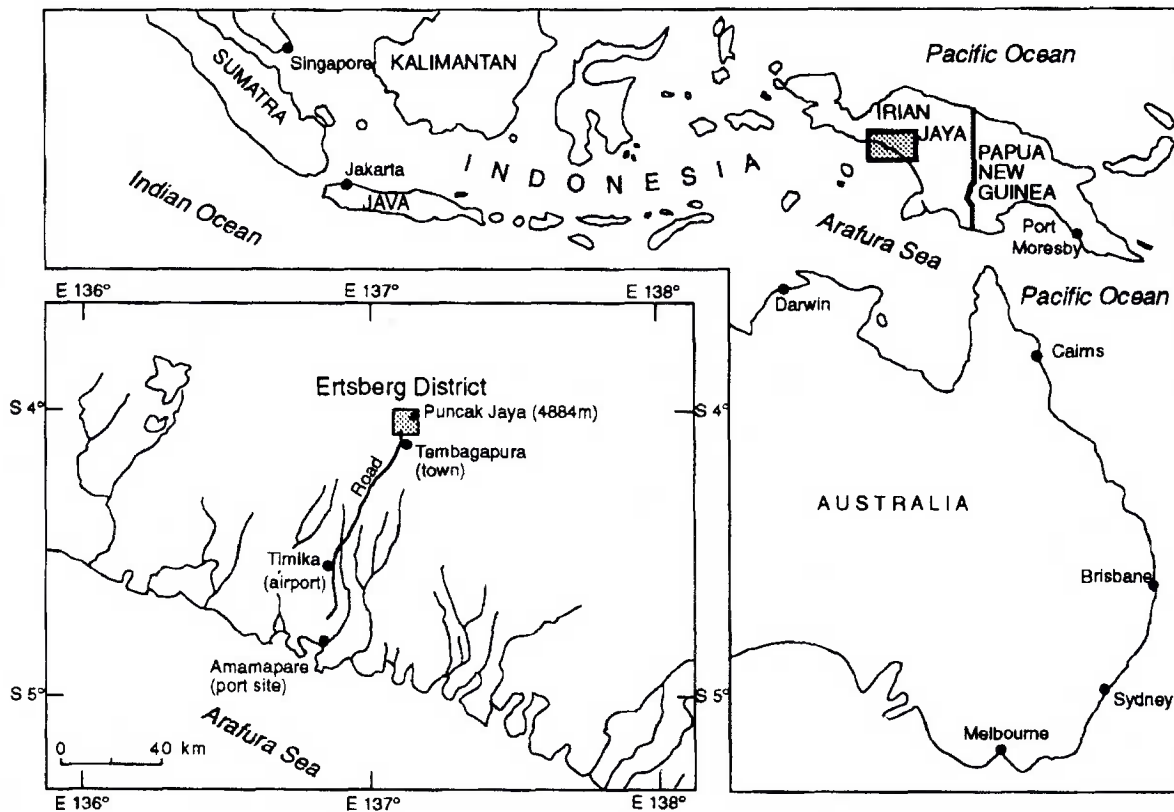


Fig. 7. Index map showing location of Ertsberg District, Irian Jaya, Indonesia.

aluminous phases abundant. Anhydrite is ubiquitous, especially at depth. The district is generally F-poor; fluorite is rare in the skarns and the porphyry. Most F appears to be in phlogopite, which contains from 1 to 4 wt% F (J.N. Rubín, unpublished data, 1992).

Mineralogical and geochemical data indicate mobility of both Zr and Ti. Grandite garnets in the Ertsberg mine (Indonesian: Gunung Bijih, or GB) contain anomalous concentrations of ZrO_2 and TiO_2 , up to 4.2 and 12.5 wt%, respectively (Katchan, 1982). Whole-rock concentrations of Zr are not available for the GB skarn, which is mined out. Although Zr has not been detected in garnets from other skarn-hosted orebodies, zircon is present as inclusions in garnet in one sample from the upper portion of the Ertsberg East (Gunung Bijih Timur, or GBT) complex. Micro-inclusions of zircon could explain Katchan's anomalous Zr levels in garnet, but they would not account for the high Ti concentrations. Zircon is a common trace mineral in the GBT skarn, particularly at depth, generally occurring as inclusions in apatite and phlogopite and in skarn matrix. Zirconolite ($(Ca,Fe)(Zr,U)Ti_2O_7$) occurs as inclusions in phlogopite in one sample from GBT complex skarn (J.N. Rubín, unpublished data, 1992). Zircon is an accessory phase in the associated intrusion, which contains only 120 ppm Zr (Table 1; McMahan and McDowell, 1991). Evidence for Ti mobility in the GBT complex includes the presence, in skarn, of sphene, Ti- and Fe-Ti-oxides, and biotite and garnet containing up to 2 wt% TiO_2 (J.N. Rubín, unpublished data, 1992).

3.2. Reported occurrences

Zircon or other Zr-bearing minerals have been reported in a wide variety of hydrothermal mineral deposits and alteration suites. Many occurrences are associated with highly alkalic or F-rich intrusions, including the alkaline ring complexes of Nigeria (Bowden, 1985; Kinnaird, 1985), several sites in the

Arabian Shield (Jackson et al., 1985), the Elk Massif in NE Poland (Dziedzic, 1984) and Thor Lake, Northwest Territories, Canada (Smith et al., 1991). In most of these examples, Zr mineralization is associated with various combinations of Be, Y, REE, Nb, Ta, U and Th. Skarn associated with the Bergell and Adamello intrusions, Italy, contains REE-bearing zirconolite, which indicates mobility of Ti, REE, U, Th and Y, as well as Zr (Gieré, 1986, 1990). Gieré interprets transport of the elements as fluoride or phosphate complexes. Transport as fluoride complexes was also considered essential for development of vapor-phase zircon in an altered rhyolite dome and for Zr enrichment with SiO_2 - and F-rich alteration of felsic to intermediate volcanic rocks, both in Idaho, U.S.A. (Ludington et al., 1980; Johnson and McIntyre, 1983).

A few examples of hydrothermal Zr mobility do not appear to be associated with alkalic or F-rich magmas or hydrothermal systems. These include zircon-rich hydrothermal barite beds in Kuroko-type volcanogenic massive-sulfide deposits in Japan (Kalogeropoulos, 1983). Patchy zircon and zircon overgrowths in shear zones were attributed to Zr mobility during prograde mylonitization (Wayne and Sinha, 1988). Wayne and Sinha did not specify the geochemical environment or evaluate the effect of fluid chemistry, but shear-zone fluids are generally H_2O-CO_2 mixtures; significant F concentrations are rare (Fyfe et al., 1978; Kerrich and Fyfe, 1981).

4. Discussion

The presence of zircon and other Zr-bearing minerals in the wide variety of hydrothermal alteration suites listed in the previous sections demonstrate that Zr can be mobile in hydrothermal systems. However, the degree of mobility, as indicated by concentrations of Zr in the end products of hydrothermal alteration, varies widely. Some of the best examples come from Trans-Pecos Texas where zircon is com-

mon in fluor spar deposits related to alkalic rhyolites, but Zr concentrations in these deposits range from a few tens of ppm to 38,000 ppm (Table 2). Basic factors that influence the post-magmatic mobility of Zr and other trace elements include initial concentration and mineralogical host of Zr in the igneous rock, the susceptibility of these sites to subsequent alteration, and the ability of the hydrothermal fluid to transport Zr. We primarily address the first two aspects.

Zr is incompatible in most rock-forming minerals and thus is concentrated in residual silicate liquids until zircon saturation occurs (Watson, 1979; Watson and Harrison, 1983). Crystallization of zircon, a common and highly stable accessory phase in most igneous systems, generally prohibits strong magmatic enrichment of Zr. Other crystallizing phases incorporate little Zr under conditions where zircon is stable.

Zircon is highly soluble in alkalic and F-rich magmas (Dietrich, 1968; Watson, 1979; Watson and Harrison, 1983; Keppler, 1991), therefore Zr is progressively enriched in differentiating magmas. Over a range of 0–6 wt% F, zircon solubility increases with the square of the F content, and the solubility of other refractory minerals, including rutile and thorite also increases (Keppler, 1991). For these reasons, alkalic rock systems generally have high Zr concentrations. Magmatic enrichment of Zr is evident in rocks of the Trans-Pecos Magmatic Province, which is both alkalic and F-rich, and particularly in peralkaline members such as in the Christmas Mountains (Table 1).

Zr in moderately alkalic and F-rich igneous rocks may still occur as zircon, but equilibrium concentrations of Zr in the melt are higher than in less alkalic magmas (Watson and Harrison, 1983). Zr concentrations are as high as 1000 ppm in the alkalic but peraluminous Sierra Blanca intrusions but still occurs mostly as zircon.

In more alkalic rocks, zircon crystallization may not occur at all, and Zr can eventually en-

ter other, late crystallizing phases. Microprobe analyses of sodic pyroxenes and amphiboles in zircon-poor alkalic rocks worldwide indicate that much whole-rock Zr occurs in them. Aegirine and arfvedsonite in peralkaline rocks of the Christmas Mountains area contain up to 3.1 and 0.95 wt% ZrO_2 , respectively (Table 3). Sodic pyroxenes (and sodic amphiboles to a lesser extent) show even greater enrichment elsewhere (Table 3), including up to 7.0 wt% ZrO_2 in several alkalic complexes and peralkaline rocks in Greenland (Larsen, 1976; Jones and Peckett, 1980; N.J.G. Pearce, 1989), and up to 14.3 wt% ZrO_2 in peralkaline quartz trachytes in Australia (Ewart, 1981; Duggan, 1988).

We suggest the mineralogical host for Zr in igneous rocks is a fundamental control on subsequent mobility. Zircon crystallization removes most Zr from the magma. Zircon is extremely stable, even during most hydrothermal alteration, which inhibits subsequent mobilization. In contrast, sodic pyroxenes and amphiboles are more easily broken down. Zr in these minerals would be more easily released to hydrothermal fluids.

Susceptibility of zircon to alteration can be enhanced by metamictization or mechanical fracturing during deformation. Metamictization, damage to the crystal lattice from decay of incorporated U and Th, increases zircon solubility (e.g., Woodhead et al., 1991). Older zircons and those with high U and Th concentrations are more likely to be metamict and susceptible to leaching. For example, magmatic zircons in the Sierra Blanca intrusions, although only 36 Ma old, contain up to 5.2 wt% UO_2 and 9.4 wt% ThO_2 and are uniformly corroded (Rubin et al., 1989a). Hydrothermal zircons in the fluor spar deposits at Sierra Blanca contain very low U and Th concentrations and are not metamict. Metamictization may have enhanced zircon solubility in the metamorphic source that Saxena (1966) invoked for authigenic zircon formation in sedimentary rocks. Fracturing during deformation

TABLE 3

Microprobe analyses (wt%) of selected clinopyroxenes (Cpx) and arvedsonites (Arf)

Mineral Source	Cpx [1]	Cpx [2]	Cpx [3]	Cpx [4]	Cpx [5]	Arf [1]	Arf [1]	Arf [2]	Arf [3]	Arf [6]	Arf [7]
SiO ₂	50.7	52.0	52.0	50.5	50.0	49.1	48.9	48.4	50.0	48.9	46.2
TiO ₂	0.98	0.82	1.51	0.36	0.77	1.13	1.41	0.98	1.50	1.43	n.d.
ZrO ₂	3.17	2.58	1.20	14.3	6.96	0.95	0.16	0.16	0.12	0.28	4.13
Al ₂ O ₃	0.11	0.18	0.23	0.35	0.45	0.20	0.39	0.63	0.27	0.28	1.88
FeO ^a	27.9	28.2	28.5	18.6	24.1	33.4	34.7	36.0	33.8	34.2	31.6
MnO	0.31	0.40	0.35	1.13	1.21	1.15	1.07	1.36	1.09	1.05	1.03
MgO	0.12	n.d.	n.d.	n.d.	0.20	0.04	0.16	0.25	n.d.	0.36	1.02
CaO	2.42	1.22	1.90	1.22	4.25	1.32	2.26	3.11	1.36	2.01	1.84
Na ₂ O	12.4	12.8	12.4	12.0	10.0	8.44	7.74	6.50	8.47	8.03	7.25
K ₂ O						1.46	1.31	1.27	1.47	1.31	2.32
F						2.21	1.68	2.00	2.60	2.56	n.a.
(F=O)						-0.93	-0.71	-0.84	-1.09	-1.08	
Total	98.1	98.1	98.1	98.5	97.9	98.5	99.1	99.8	99.6	99.3	97.3

n.d. = not detected; n.a. = not analyzed.

[1] = sample H86-85, peralkaline quartz trachyte, Christmas Mountains; [2] = sample H86-93, peralkaline quartz trachyte, Luna Vista sill (Christmas Mountains); [3] = sample H86-80, peralkaline rhyolite, West Corazones Peak (Christmas Mountains area); [4] = Duggan (1988); [5] = Jones and Peckett (1980); [6] = sample H81-30, peralkaline rhyolite, Adobe Walls (Christmas Mountains); [7] = Pearce (1989).

^aTotal Fe as FeO.

events, particularly those at high temperature, can also make zircons more susceptible to dissolution, especially if the zircons were already metamict (Wayne and Sinha, 1988).

The mineralogical host of other trace elements should also be important in influencing their subsequent mobility during hydrothermal alteration. A wide range of trace minerals, including apatite, monazite, euxenite, REE-fluorides, thorite, xenotime, columbite and changbaiite, all of which have been found at either Sierra Blanca or the Christmas Mountains, could hold many of the trace elements. Only Rb and Pb among the elements discussed here are commonly incorporated within major phases, e.g., alkali feldspar.

The composition of the hydrothermal solution is also important in Zr mobility, but we address this topic only indirectly. The low temperatures and salinities of fluid inclusions from the Christmas Mountains and Sierra Blanca demonstrate that hydrothermal fluids were dominantly meteoric water; they did not

separate directly from a melt and extract metals by liquid-melt partitioning (e.g., Webster, 1990). Thus the fluids probably derived their metals by leaching igneous source rocks. The high F concentrations in many alkalic magma systems means that associated hydrothermal fluids are F rich, which was obviously the case with the fluorspar deposits in Texas. Common experience demonstrates that HF easily dissolves most silicate minerals and is the only acid capable of dissolving zircon, albeit with difficulty (Dietrich, 1968; Krogh, 1973). Although we know of few data on aqueous speciation of Zr, its common association with fluorspar or other fluorine-rich deposits suggests it forms fluoride complexes (see also Gieré, 1990). Many other elements enriched in the Texas fluorspar deposits, including Be, Mo, U, Th, Y and REE, are either known to form, or have interpreted to be transported as, fluoride complexes (Barton, 1987; Keppler and Wyllie, 1990; Webster, 1990; Wood, 1990).

The differences in enrichment of Zr and

other elements among the fluor spar bodies in the Christmas Mountains, only partly related to concentration of the elements in the associated rhyolites, must reflect differences in the ability of the elements to enter a hydrothermal phase and their subsequent mobility. For example, U and Th are strongly partitioned into F-rich solutions, whereas only U is partitioned into Cl- or CO₂-rich solutions (Keppler and Wyllie, 1990). Other anions may play important roles where F is not abundant. Hydrothermal zircon in low-F, moderate-Al/alkali, magmatic and hydrothermal systems such as Ertsberg may be due to sulfate complexing. Anhydrite is a ubiquitous phase in the Ertsberg skarns, and Zr solubility has been shown to be elevated in sulfate-rich hydrothermal systems (Mottet et al., 1992). Most of the hydrothermal zircon has been observed at depth in the system, which is also where the highest concentrations of anhydrite are found. Although overall F abundance is low, most zircon that formed in the GBT complex skarns did so in the presence of the most F-rich phase (phlogopite).

Data from Trans-Pecos Texas bear on the combined influence of differences in mineralogy and attack by F-rich hydrothermal fluids. The greatest Zr mobility, as evidenced by the highest Zr concentrations in fluor spar deposits (Table 2), is associated with peralkaline rhyolites of the Christmas Mountains. Much of the Zr in these igneous rocks is within sodic pyroxenes or amphiboles, which are easily broken down during hydrothermal alteration. Although alteration of the rhyolites is relatively minor, intrusions related to fluor spar deposits, samples H90-74 (Paisano), H81-41 (Adobe Walls) and MGD-788 (North) (Table 1), have undergone argillic alteration with development of montmorillonite, a kaolinite-group mineral, and minor sericite. Primary mafic minerals are generally destroyed. Breakdown of arfvedsonite, which is enriched in F (Table 3), releases F as well as Zr. In contrast, fluor spar deposits at Sierra Blanca contain much

lower Zr concentrations (Table 2), although concentrations in the associated igneous rocks are nearly as high as those in the Christmas Mountains rhyolites (Table 1). The hydrothermal fluids at both localities were probably equally F rich and capable of complexing and transporting Zr. We suggest that Zr was much less easily extracted from the Sierra Blanca rhyolites because most of the Zr was in zircon, which was only moderately soluble.

5. Conclusions

Clearly, Zr can be mobile in hydrothermal systems developed in a broad range of igneous geochemical environments. These hydrothermal systems are mostly but not exclusively F rich and associated with alkalic, F-rich igneous suites. Zr is generally accompanied by a variety of mostly incompatible trace elements, including Be, REE, Y, Nb, Mo, U and Th, and also by other elements commonly considered immobile, such as Ti and Al. We interpret leaching of igneous source rocks to be the dominant source of Zr, and the Zr mineralogy of the igneous rock is an important factor in how much Zr can be mobilized. Rocks in which Zr occurs mostly as zircon probably release only a small fraction of their total Zr. In contrast, rocks where Zr occurs largely as aegirine or arfvedsonite can release a substantial portion of Zr. This mobility does not totally negate the use of Zr or other "immobile" elements as indicators of rock type or tectonic setting of altered rocks. Nevertheless, it does suggest caution, particularly for alkalic rock suites.

Acknowledgments

We thank Howard M. Harlan, Scott B. Petersen, Richard J. Thompson and Dan Robertson of Cyprus Minerals Company for access to the Sierra Blanca Peaks, and Freeport Indonesia, Inc., and Freeport McMoRan, Inc., for access and financial support in the Ertsberg District. This paper was significantly aided by

reviews by Daniel S. Barker, T. Mark Harrison and two anonymous reviewers. Thanks to Linda L. Davis for her assistance on the microprobe. Research was supported by the U.S. Department of the Interior's Mineral Institute program administered by the Bureau of Mines under allotment grant numbers G1164148 through G1194148 to the Texas Mining and Mineral Resources Research Institute. Presentation of results was assisted by grants from the Professional Development Fund of the Office of Graduate Studies and the Arno P. (Dutch) Wendler Professional Development Fund, Department of Geological Sciences, University of Texas at Austin.

References

- Ash, J.P. and Kyle, J.R., 1984. Fluid inclusion evidence for fluorite mineralization associated with peralkaline rhyolite intrusions, Paisano Mine, Trans-Pecos Texas. *Geol. Soc. Am., Abstr. Prog.*, 16: 433.
- Barker, D.S., 1987. Tertiary alkaline magmatism in Trans-Pecos Texas. In: J.G. Fulton and B.G.J. Upton (Editors), *Alkaline Igneous Rocks*. *Geol. Soc. London, Spec. Publ.*, 30: 415-431.
- Barton, M.D., 1987. Lithophile-element mineralization associated with Late Cretaceous two-mica granites in the Great Basin. *Geology*, 15: 337-340.
- Bowden, P., 1985. The geochemistry and mineralization of alkaline ring complexes in Africa (a review). *J. Afr. Earth Sci.*, 3: 17-39.
- Cameron, M., Cameron, K.L. and Carman, Jr., M.F., 1986. Alkaline rocks in the Terlingua-Big Bend area of Trans-Pecos Texas. *Univ. Texas at Austin, Bur. Econ. Geol. Guidebk.*, 23: 123-142.
- Christiansen, E.H., Burt, D.M., Sheridan, M.F. and Wilson, R.T., 1983. The petrogenesis of topaz rhyolites from the western United States. *Contrib. Mineral. Petrol.*, 83: 1-16.
- Christiansen, E.H., Sheridan, M.F. and Burt, D.M., 1986. The geology and geochemistry of Cenozoic topaz rhyolites from the western United States. *Geol. Soc. Am., Spec. Pap.* 205, 82 pp.
- Daugherty, F.W., 1982. Fluorspar deposits of Christmas Mountains district, Brewster County, Texas. In: *Industrial Rocks and Minerals of the Southwest*. N.M. Bur. Mines Mineral. Resour., Circ., 182: 85-88.
- Dietrich, R.V., 1968. Behavior of zirconium in certain artificial magmas under diverse *P-T* conditions. *Lithos*, 1: 20-29.
- Duggan, M.B., 1988. Zirconium-rich sodic pyroxenes in felsic volcanics from the Warrumbungle Volcano, central New South Wales, Australia. *Mineral. Mag.*, 52: 491-496.
- Dziedzic, A., 1984. Elk syenite intrusion. *Biul. Inst. Geol., Warsaw*, 347: 39-47.
- Ewart, A., 1981. The mineralogy and chemistry of the orogenic Tertiary silicic volcanics of S.E. Queensland and N.E. New South Wales. *J. Geophys. Res.*, 86: 10242-10256.
- Finlow-Bates, T. and Stumpfl, E.F., 1981. The behaviour of so-called immobile elements in hydrothermally altered rocks associated with volcanogenic submarine-exhalative ore deposits. *Miner. Deposita*, 16: 319-328.
- Floyd, P.A. and Winchester, J.A., 1975. Magma type and tectonic setting discrimination using immobile elements. *Earth Planet. Sci. Lett.*, 27: 211-218.
- Fyfe, W.S., Price, N.J. and Thompson, A.B., 1978. *Fluids in the Earth's Crust*. Elsevier, Amsterdam, 383 pp.
- Gieré, R., 1986. Zirconolite, allanite and hoegbomite in a marble skarn from the Bergell contact aureole: implications for mobility of Ti, Zr and REE. *Contrib. Mineral. Petrol.*, 93: 459-470.
- Gieré, R., 1990. Hydrothermal mobility of Ti, Zr and REE: examples from the Bergell and Adamello contact aureoles (Italy). *Terra Nova*, 2: 60-67.
- Gill, J.B., 1981. *Orogenic Andesites and Plate Tectonics*. Springer, New York, N.Y., 390 pp.
- Henry, C.D. and McDowell, F.W., 1986. Geochronology of the mid-Tertiary volcanic field, Trans-Pecos Texas. *Univ. Texas at Austin, Bur. Econ. Geol. Guidebk.*, 23: 99-122.
- Henry, C.D. and Price, J.G., 1984. Variations in caldera development in the Tertiary volcanic field of Trans-Pecos Texas. *J. Geophys. Res.*, 89: 8765-8786.
- Henry, C.D., Price, J.G. and Smyth, R.C., 1988. Chemical and thermal zonation in a mildly alkaline magma system, Infiernito Caldera, Trans-Pecos Texas. *Contrib. Mineral. Petrol.*, 98: 194-211.
- Henry, C.D., Price, J.G. and Miser, D.E., 1989. Geology and Tertiary igneous activity of the Hen Egg Mountain and Christmas Mountains quadrangles, Big Bend region, Trans-Pecos Texas. *Univ. Texas at Austin, Bur. Econ. Geol., Rep. Invest.*, 183, 105 pp.
- Henry, C.D., Price, J.G. and James, E.W., 1991. Mid-Cenozoic stress evolution and magmatism in the southern Cordillera, Texas and Mexico: transition from continental arc to intraplate extension. *J. Geophys. Res.*, 96: 13545-13560.
- Henry, C.D., Price, J.G., Duex, T.W. and James, E.W., 1992. Geology of the Infiernito caldera and magmatic evolution of the Chinati Mountains, Trans-Pecos Texas. *Univ. Texas at Austin, Bur. Econ. Geol., Rep. Invest.* 206, 56 pp.
- Jackson, N.J., Drysdall, A.R. and Stoesser, D.B., 1985. Alkali granite-related Nb-Zr-REE-U-Th mineralization in the Arabian Shield. In: C. Halls (Chairperson),

- High Heat Production (HHP) Granites, Hydrothermal Circulation and Ore Genesis. *Inst. Min. Metall.*, London, pp. 478-487.
- Johnson, K.M. and McIntyre, D.H., 1983. Disseminated gold-silver deposit in a rhyolite dome at the Sunbeam mine, Custer County, Idaho. *Geol. Soc. Am., Abstr. Prog.*, 15: 324-325.
- Jones, A.P. and Peckett, A., 1980. Zirconium-bearing aegirines from Motzfeldt, Greenland. *Contrib. Mineral. Petrol.*, 75: 251-255.
- Kalogeropoulos, S.I., 1983. Chemistry, and the role of zirconium in the formation of the Tsunokakezawa no. 1 orebody, Fukazawa mine, Japan. *Miner. Deposita*, 18: 535-541.
- Katchan, G., 1982. Mineralogy and geochemistry of the Ertsberg (*Gunung Bijih*) and Ertsberg East (*Gunung Bijih Timur*) skarns, Irian Jaya, Indonesia and the Ok Tedi skarns, Papua New Guinea. Ph.D. Thesis, University of Sydney, Sydney, N.S.W. (unpublished).
- Keppler, H., 1991. Influence on the solubility of high field strength trace elements in granitic melts. *Eos (Trans. Am. Geophys. Union)*, 72: 532-533 (abstract).
- Keppler, H. and Wyllie, P.J., 1990. Role of fluids in transport and fractionation of uranium and thorium in magmatic processes. *Nature (London)*, 348: 531-533.
- Kerrick, R. and Fyfe, W.S., 1981. The gold-carbonate association: source of CO₂, and CO₂ fixation reactions in Archean lode deposits. *Chem. Geol.*, 33: 265-294.
- Kinnaird, J.A., 1985. Hydrothermal alteration and mineralization of the alkaline anorogenic ring complexes of Nigeria. *J. Afr. Earth Sci.*, 3: 229-251.
- Krogh, T.E., 1973. A low contamination method for hydrothermal decomposition of zircon and extraction of U and Pb for isotopic age determination. *Geochim. Cosmochim. Acta*, 37: 485-494.
- Larsen, L.M., 1976. Clinopyroxenes and coexisting mafic minerals from the alkaline Illimaussaq intrusion, South Greenland. *J. Petrol.*, 17: 258-290.
- Ludington, S., Desborough, G. and Rostad, O., 1980. Unique low-pressure hydrothermal alteration at Big Southern Butte, Snake River Plain, Idaho. *Geol. Soc. Am., Abstr. Prog.*, 12: 279.
- McAnulty, W.N., 1974. Fluorspar in Texas. *Univ. Texas at Austin, Bur. Econ. Geol. Handbk.*, 3, 31 pp.
- McMahon, T.P. and McDowell, F.W., 1991. 3 Ma intermediate intrusions in the Ertsberg (*Gunung Bijih*) mining district, Irian Jaya, Indonesia. *Eos (Trans. Am. Geophys. Union)*, 72: 439 (abstract).
- Mottet, B., Pichavant, M., Bény, J.M. and Alary, J.A., 1992. Morphology of zirconia synthesized hydrothermally from zirconium chloride. *J. Am. Ceram. Soc.*, 75: 2515-2519.
- Nakamura, N., 1974. Determination of REE, Ba, Fe, Mg, Na, and K in carbonaceous and ordinary chondrites. *Geochim. Cosmochim. Acta*, 38: 757-773.
- Noble, D.C., Smith, V.C. and Peck, L.C., 1967. Loss of halogens from crystallized and glassy silicic volcanic rocks. *Geochim. Cosmochim. Acta*, 31: 215-223.
- Pearce, J.A. and Cann, J.R., 1973. Tectonic setting of basic volcanic rocks determined using trace element analyses. *Earth Planet. Sci. Lett.*, 19: 290-300.
- Pearce, N.J.G., 1989. Zirconium-bearing amphiboles from the Igaliko Dyke Swarm, South Greenland. *Mineral. Mag.*, 53: 107-110.
- Price, J.G., Henry, C.D., Barker, D.S. and Parker, D.F., 1987. Alkalic rocks of contrasting tectonic settings in Trans-Pecos Texas. In: E.M. Morris and J.D. Pasteris (Editors), *Mantle Metasomatism and Alkaline Magmatism*. *Geol. Soc. Am., Spec. Pap.*, 215: 335-346.
- Price, J.G., Rubin, J.N., Henry, C.D., Pinkston, T.L., Tweedy, S.W. and Koppenaar, D.W., 1990. Peraluminous rhyolites in a continental arc, Sierra Blanca Peaks, Trans-Pecos Texas. *Geol. Soc. Am., Spec. Pap.*, 246: 103-120.
- Rubin, J.N., 1991. Anhydrite- and phlogopite-rich Cu-Au skarns of the Ertsberg (*Gunung Bijih*) District, Irian Jaya, Indonesia. *Geol. Soc. Am., Abstr. Prog.*, 23: A415.
- Rubin, J.N., Price, J.G., Henry, C.D. and Koppenaar, D.W., 1987. Cryolite-bearing and rare metal-enriched rhyolite, Sierra Blanca Peaks, Hudspeth County, Texas. *Am. Mineral.*, 72: 1122-1130.
- Rubin, J.N., Henry, C.D. and Price, J.G., 1989a. Hydrothermal zircons and zircon overgrowths, Sierra Blanca Peaks, Texas. *Am. Mineral.*, 74: 865-869.
- Rubin, J.N., Price, J.G., Henry, C.D., Pinkston, T.L., Tweedy, S.W., Koppenaar, D.W., Peterson, S.B., Harlan, H.M., Miller, W.T., Thompson, R.J., Grabowski, R.B., Laybourn, D.P., Schrock, G.E., Johnson, A., Staes, D.G., Gaines, R.V. and Miller, F.H., 1989b. Mineralogy of beryllium deposits near Sierra Blanca, Texas. In: A.E. Torma and I.H. Gundiler (Editors), *Precious and Rare Metal Technologies*. Elsevier, Amsterdam, pp. 601-614.
- Rubin, J.N., Price, J.G., Henry, C.D. and Kyle, J.R., 1990. Geology of the beryllium-rare earth element deposits at Sierra Blanca, West Texas. In: J.R. Kyle (Editor), *Industrial Mineral Resources of the Delaware Basin, Texas and New Mexico*. *Soc. Econ. Geol. Guidebk.*, 8: 191-203.
- Saxena, S.K., 1966. Evolution of zircons in sedimentary and metamorphic rocks. *Sedimentology*, 6: 1-33.
- Smith, D.G.W., de St. Jorre, L., Reed, S.J.B. and Long, J.V.P., 1991. Zonally metamictized and other zircons from Thor Lake, Northwest Territories [Canada]. *Can. Mineral.*, 29: 301-309.
- Watson, E.B., 1979. Zircon saturation in felsic liquids: experimental results and applications to trace element geochemistry. *Contrib. Mineral. Petrol.*, 70: 407-419.
- Watson, E.B. and Harrison, T.M., 1983. Zircon saturation revisited: temperature and composition effects in a variety of crustal magma types. *Earth Planet. Sci. Lett.*, 64: 295-304.

- Wayne, D.M. and Sinha, A.K., 1988. Physical and chemical response of zircons to deformation. *Contrib. Mineral. Petrol.*, 98: 109-121.
- Weaver, S.D., Gibson, I.L., Houghton, B.F. and Wilson, C.J.N., 1990. Mobility of rare earth and other elements during crystallization of peralkaline silicic lavas. *J. Volcanol. Geotherm. Res.*, 43: 57-70.
- Webster, J.D., 1990. Partitioning of F between H₂O and CO₂ fluids and topaz rhyolite melt. *Contrib. Mineral. Petrol.*, 104: 424-438.
- Wood, S.A., 1990. The aqueous geochemistry of the rare-earth elements and yttrium, 1. Review of available low-temperature data for inorganic complexes and the inorganic REE speciation of natural waters. *Chem. Geol.*, 82: 159-186.
- Woodhead, J.A., Rossman, G.R. and Thomas, A.P., 1991. Hydrous species in zircon. *Am. Mineral.*, 76: 1533-1546.